applied sciences

Special Issue Reprint

Civil Structural Health Monitoring

Techniques, Systems and Applications

Edited by
Fei Kang and Yonglong Li

mdpi.com/journal/applsci

MDPI

Civil Structural Health Monitoring: Techniques, Systems and Applications

Civil Structural Health Monitoring: Techniques, Systems and Applications

Guest Editors

Fei Kang
Yonglong Li

MDPI

Basel • Beijing • Wuhan • Barcelona • Belgrade • Novi Sad • Cluj • Manchester

Guest Editors
Fei Kang
School of Infrastructure Engineering
Dalian University of Technology
Dalian
China

Yonglong Li
Sichuan Energy Internet Research Institute
Tsinghua University
Chengdu
China

Editorial Office
MDPI AG
Grosspeteranlage 5
4052 Basel, Switzerland

This is a reprint of the Special Issue, published open access by the journal *Applied Sciences* (ISSN 2076-3417), freely accessible at: https://www.mdpi.com/journal/applsci/special_issues/U9HANL9DX4.

For citation purposes, cite each article independently as indicated on the article page online and as indicated below:

Lastname, A.A.; Lastname, B.B. Article Title. *Journal Name* **Year**, *Volume Number*, Page Range.

ISBN 978-3-7258-9011-8 (Hbk)
ISBN 978-3-7258-9012-5 (PDF)
https://doi.org/10.3390/books978-3-7258-9012-5

© 2026 by the authors. Articles in this reprint are Open Access and distributed under the Creative Commons Attribution (CC BY) license. The reprint as a whole is distributed by MDPI under the terms and conditions of the Creative Commons Attribution-NonCommercial-NoDerivs (CC BY-NC-ND) license (https://creativecommons.org/licenses/by-nc-nd/4.0/).

Contents

About the Editors . . . . . **vii**

Fei Kang and Yonglong Li
Editorial for the Special Issue on Civil Structural Health Monitoring: Techniques, Systems and Applications
Reprinted from: *Appl. Sci.* **2026**, *16*, 2363, https://doi.org/10.3390/app16052363 . . . . . **1**

Peng Ding, Xiaogang Li, Sheng Chen, Xiangsheng Huang, Xiaohu Chen and Yong Qi
Load Effect Analysis Method of Cable-Stayed Bridge for Long-Span Track Based on Adaptive Filtering Method
Reprinted from: *Appl. Sci.* **2024**, *14*, 7057, https://doi.org/10.3390/app14167057 . . . . . **5**

Sizeng Zhao, Fei Kang, Lina He, Junjie Li, Yiqing Si and Yiping Xu
Intelligent Structural Health Monitoring and Noncontact Measurement Method of Small Reservoir Dams Using UAV Photogrammetry and Anomaly Detection
Reprinted from: *Appl. Sci.* **2024**, *14*, 9156, https://doi.org/10.3390/app14209156 . . . . . **21**

Bin Yan, Hexin Fu, Haiting Su and Benguang Hou
Influence of Boundary Conditions on the Three-Dimensional Temperature Field of a Box Girder in the Natural Environment: A Case Study
Reprinted from: *Appl. Sci.* **2025**, *15*, 1378, https://doi.org/10.3390/app15031378 . . . . . **52**

Youle Wang, Zhengjian Miao, Rui Song, Junchi Zhou, Yuheng Pan and Feng Wang
Inverse Analysis of Thermal Parameters of Arch Dam Concrete Based on Walrus Optimization Algorithm
Reprinted from: *Appl. Sci.* **2025**, *15*, 2155, https://doi.org/10.3390/app15042155 . . . . . **68**

Doron Hekič, Jan Kalin, Aleš Žnidarič, Peter Češarek and Andrej Anžlin
Model Updating of Bridges Using Measured Influence Lines
Reprinted from: *Appl. Sci.* **2025**, *15*, 4514, https://doi.org/10.3390/app15084514 . . . . . **89**

Guanglin Yin, Chaoning Lin, Taozhen Sheng, Wenbo Xue, Tongchun Li and Siyu Chen
Dynamic Inversion Method for Concrete Gravity Dam on Soft Rock Foundation
Reprinted from: *Appl. Sci.* **2025**, *15*, 4750, https://doi.org/10.3390/app15094750 . . . . . **115**

Hui Xie, Haoran Wang, Xingtong Zou, Yongcan Chen, Zhaowei Liu, Liyi Yang and Kang Liu
Research on Cracking Mechanism and Crack Extension of Diversion Tunnel Lining Structure
Reprinted from: *Appl. Sci.* **2025**, *15*, 9210, https://doi.org/10.3390/app15169210 . . . . . **129**

Xiaobian Wu, Weibo Zhang, Guangze Shen and Jinbao Sheng
Edge-Enhanced CrackNet for Underwater Crack Detection in Concrete Dams †
Reprinted from: *Appl. Sci.* **2025**, *15*, 10326, https://doi.org/10.3390/app151910326 . . . . . **150**

Guangze Shen, Jingxuan Zhang and Zhe Chen
MambaUSR: Mamba and Frequency Interaction Network for Underwater Image Super-Resolution
Reprinted from: *Appl. Sci.* **2025**, *15*, 11263, https://doi.org/10.3390/app152011263 . . . . . **166**

About the Editors

Fei Kang

Fei Kang is a professor at the School of Infrastructure Engineering, Dalian University of Technology. Mainly engaged in research on safety monitoring, health diagnosis, and numerical analysis of hydraulic structures, he has hosted and participated in over 30 national key research and development projects, National Natural Science Foundation of China, and enterprise-commissioned projects. He was selected as a National Young Talent and Elsevier China Highly Cited Scholar (2014–2025). Published over 100 papers in journals such as *Journal of Structural Engineering*, *Engineering Structures*, *Computers & Structures*, and *Automation in Construction*, he has also obtained 5 software copyrights and 5 patents. The research results have been successfully applied in multiple large- and medium-sized water conservancy and hydropower projects in China. He received the first prize of the Liaoning Provincial Natural Science Award and the Scott Sloan Outstanding Paper Award from the journal *Computers and Geotechnics*.

Yonglong Li

Yonglong Li is a professor of engineering in Sichuan Energy Internet Research Institute, Tsinghua University. His research interests include dam inspection robots, intelligent perception and control, and intelligent unmanned systems. He has long been dedicated to the research and development of special-purpose robots and artificial intelligence (AI) systems for the energy industry. He has led and participated in over 30 projects, including those under the National Key R&D Program of China, the National Natural Science Foundation of China, the Key R&D Program of Sichuan Province, and industry-commissioned research initiatives. He has received three provincial-/ministerial-level awards and one Gold Medal at the Geneva International Exhibition of Inventions. He has also formulated one group standard, filed over 30 patents, and published more than 40 academic papers. His achievements have been applied in over 10 major water conservancy and hydropower projects.

applied sciences

MDPI

Editorial

Editorial for the Special Issue on Civil Structural Health Monitoring: Techniques, Systems and Applications

Fei Kang [1,*] and Yonglong Li [2,*]

[1] School of Infrastructure Engineering, Dalian University of Technology, Dalian 116024, China
[2] Sichuan Energy Internet Research Institute, Tsinghua University, Chengdu 610213, China
* Correspondence: kangfei@dlut.edu.cn (F.K.); liyonglong@hotmail.com (Y.L.)

1. Introduction

Civil structures and infrastructure, including bridges, high-rise buildings, towers, dams, and tunnels, form the backbone of modern economies. Their long-term operational safety is vital to socioeconomic stability and the protection of public life and property [1–3]. As engineering projects grow in scale and complexity, structural deterioration due to material aging, environmental corrosion and extreme load conditions has emerged as a major threat to infrastructure safety and functionality [4–6]. In the era of smart technology, enabling intelligent diagnosis and prognosis of structural health throughout the entire lifecycle has become an urgent priority.

Recent advances in monitoring systems, sensor technologies, and artificial intelligence have promoted the integration of multi-source data and the adoption of intelligent algorithms, positioning structural health monitoring (SHM) at the forefront of addressing these challenges [7–9]. By synthesizing advanced sensing, numerical simulation, and machine learning, SHM systems establish an intelligent feedback loop of sensing–diagnosis–prediction, substantially improving monitoring efficacy and proactive maintenance.

This Special Issue is dedicated to presenting the latest research progress in civil structural health monitoring, encompassing areas such as damage detection, data processing algorithms, modeling and simulation, sensor development, and experimental validation.

2. Summary of the Special Issue Contents

The evolving discipline of civil structural health monitoring (SHM) lies at the intersection of sensor technology, data science, and civil engineering, aiming to ensure the safety, durability, and intelligent management of infrastructure. This Special Issue, entitled "Civil Structural Health Monitoring: Techniques, Systems and Applications," presents a curated collection of nine innovative studies that showcase the breadth and depth of contemporary SHM research. The contributions highlight sophisticated methodologies—ranging from signal processing and unmanned systems to artificial intelligence and physics-informed inverse analysis—applied to a diverse set of critical structures, including bridges, dams, and tunnels. Nine papers were ultimately included in this issue.

2.1. Bridge Infrastructure Monitoring: From Load Separation to Model Updating

The Special Issue begins with two advanced studies focused on bridges. In the first study, the complex challenge of monitoring long-span railway cable-stayed bridges is addressed. These bridges are subject to significant and overlapping load effects from trains and environmental temperature. A novel framework is proposed by employing an adaptive filtering method to meticulously separate these two response components

from continuous health monitoring data. Subsequently, the authors introduce dedicated analysis methods: a train load effect assessment based on influence lines and a temperature effect evaluation using correlation analysis. The application of this method to the Chongqing Nanjimen Railway Track Bridge demonstrates its effectiveness in providing an objective, real-time operational assessment, proving its utility for managing high-demand transport infrastructure.

Complementing this, the work by Hekič et al. explores the critical task of finite element model updating for an existing concrete roadway bridge. Utilizing long-term data from a Bridge Weigh-in-Motion system, the authors derive strain influence lines (ILs) induced by calibration vehicles. They then apply the Error-Domain Model Falsification methodology to update the bridge's numerical model based on these ILs, a method they compare against traditional frequency-based updating approaches. Their results are compelling: the IL-updated model shows excellent agreement (within 5%) with independently measured displacements, significantly outperforming conventional methods. This research underscores the high fidelity of traffic-load-response-based model updating for accurate digital twinning and long-term structural assessment.

2.2. Thermal Behavior and Inversion Analysis in Concrete Structures

Understanding thermal effects is paramount for concrete structures. The third study delves into the intricacies of the three-dimensional temperature field within box girders. Their study develops a comprehensive computational method that integrates key boundary conditions, including solar radiation, shading, and convective heat transfer. By analyzing the influence of parameters like atmospheric transparency and concrete's short-wave absorptivity, the research provides valuable guidelines for thermal design and material selection, ultimately aiming to mitigate detrimental thermal stresses.

Expanding on parameter identification, the fourth study tackles the inverse analysis of thermal parameters for mass concrete in arch dams. Recognizing the gap between laboratory-tested parameters and actual field conditions, the authors employ the novel Walrus Optimization Algorithm to inversely determine key parameters from measured temperature data. The algorithm's robustness is first validated against classical test functions and then successfully applied to a real arch dam case on the Jinsha River. This approach enhances the accuracy of thermal stress simulations during construction, offering a powerful tool for lifecycle management of massive concrete structures.

2.3. Dam Safety: From Surface Inspection to Foundation Degradation

Monitoring dam safety leverages both surface inspection and internal condition assessment. The next paper presents an integrated UAV-based system for small reservoir dams. The methodology combines Structure from Motion (SfM) for accurate georeferencing without ground control points, an improved YOLOv8 network for detecting small targets like pedestrians, and thermal imaging for seepage identification. This routine surveillance strategy exemplifies how automated, non-contact measurement can enhance operational safety and maintenance efficiency for distributed water-retaining structures.

Beneath the surface, the long-term behavior of dam foundations is critical. The sixth paper introduces a dynamic inversion method for concrete gravity dams on soft-rock foundations. Moving beyond static analysis, their improved Particle Swarm Optimization algorithm incorporates time-series monitoring data to inversely identify the deteriorating elastic modulus of the foundation rock. The study reveals a clear exponential decay trend in foundation stiffness over time, a factor crucial for accurate displacement prediction and long-term safety evaluation, thus informing proactive maintenance strategies.

https://doi.org/10.3390/app16052363

2.4. Tunnel and Underwater Structural Assessment

The Special Issue also covers the inspection of enclosed and submerged structures. Cracking mechanisms in diversion tunnel linings are investigated by using robotic 3D laser scanning. By analyzing defect distribution patterns and employing finite element analysis to simulate crack propagation under water pressure, the study identifies high-risk zones (e.g., the vault area) and quantifies stress increases due to cracking. These findings provide a scientific basis for targeted inspection and reinforcement in underground hydraulic tunnels.

Inspecting structures underwater presents unique challenges. The eighth paper proposes the Edge-Enhanced Underwater CrackNet (E2UCN), a dual-stage deep learning framework for crack detection on submerged dam surfaces. The method first employs a specially tailored Cycle-GAN to enhance underwater images with a focus on preserving crack edges and textures, overcoming the issues of low contrast and distortion. A subsequent YOLOv11 detector then achieves remarkably high precision in crack identification. This research offers a practical technological solution for intelligent inspection in deep-water environments.

Supporting such underwater vision tasks, the next study addresses the fundamental problem of image quality with "MambaUSR," a novel super-resolution network. By integrating a Vision State-Space Model (Mamba) with frequency-domain processing via a Fast Fourier Transform-based module, the method effectively restores global structure and recovers fine details in degraded underwater images, thereby providing higher-quality input data for any subsequent visual inspection or detection algorithm.

3. Conclusions

The papers in this Special Issue reflect a paradigm shift towards intelligent, integrated, and data-centric SHM systems. They demonstrate successful synergies between advanced sensing platforms (UAVs, ROVs, laser scanners, and dense sensor networks) and cutting-edge computational techniques (adaptive filtering, computer vision, metaheuristic optimization, and state-space models). Each contribution not only presents a methodological innovation but also validates it through rigorous application to real-world structures, bridging the gap between research and practice. We believe this collection will serve as a valuable resource for researchers, engineers, and asset managers, offering both innovative tools and profound insights for the next generation of civil structural health monitoring.

Acknowledgments: We extend our sincere appreciation to all the authors for their excellent contributions, the reviewers for their rigorous and constructive evaluations, and the editorial staff of *Applied Sciences* for their invaluable support in bringing this Special Issue to fruition.

Conflicts of Interest: The authors declare no conflicts of interest.

List of Contributions:

1. Ding, P.; Li, X.; Chen, S.; Huang, X.; Chen, X.; Qi, Y. Load Effect Analysis Method of Cable-Stayed Bridge for Long-Span Track Based on Adaptive Filtering Method. *Appl. Sci.* **2024**, *14*, 7057. https://doi.org/10.3390/app14167057.
2. Hekič, D.; Kalin, J.; Žnidarič, A.; Češarek, P.; Anžlin, A. Model Updating of Bridges Using Measured Influence Lines. *Appl. Sci.* **2025**, *15*, 4514. https://doi.org/10.3390/app15084514.
3. Yan, B.; Fu, H.; Su, H.; Hou, B. Influence of Boundary Conditions on the Three-Dimensional Temperature Field of a Box Girder in the Natural Environment: A Case Study. *Appl. Sci.* **2025**, *15*, 1378. https://doi.org/10.3390/app15031378.
4. Wang, Y.; Miao, Z.; Song, R.; Zhou, J.; Pan, Y.; Wang, F. Inverse Analysis of Thermal Parameters of Arch Dam Concrete Based on Walrus Optimization Algorithm. *Appl. Sci.* **2025**, *15*, 2155. https://doi.org/10.3390/app15042155.

5. Zhao, S.; Kang, F.; He, L.; Li, J.; Si, Y.; Xu, Y. Intelligent Structural Health Monitoring and Noncontact Measurement Method of Small Reservoir Dams Using UAV Photogrammetry and Anomaly Detection. *Appl. Sci.* **2024**, *14*, 9156. https://doi.org/10.3390/app14209156.
6. Yin, G.; Lin, C.; Sheng, T.; Xue, W.; Li, T.; Chen, S. Dynamic Inversion Method for Concrete Gravity Dam on Soft Rock Foundation. *Appl. Sci.* **2025**, *15*, 4750. https://doi.org/10.3390/app15094750.
7. Xie, H.; Wang, H.; Zou, X.; Chen, Y.; Liu, Z.; Yang, L.; Liu, K. Research on Cracking Mechanism and Crack Extension of Diversion Tunnel Lining Structure. *Appl. Sci.* **2025**, *15*, 9210. https://doi.org/10.3390/app15169210.
8. Wu, X.; Zhang, W.; Shen, G.; Sheng, J. Edge-Enhanced CrackNet for Underwater Crack Detection in Concrete Dams. *Appl. Sci.* **2025**, *15*, 10326. https://doi.org/10.3390/app151910326.
9. Shen, G.; Zhang, J.; Chen, Z. MambaUSR: Mamba and Frequency Interaction Network for Underwater Image Super-Resolution. *Appl. Sci.* **2025**, *15*, 11263. https://doi.org/10.3390/app152011263.

References

1. Zhou, H.; Wu, L.; Quan, Y.; Chen, W.; Li, Z.; Huang, Z.; Yin, X. Structural safety assessment of bridge via FSI and concrete damage plasticity under barge-bridge collision. *Structures* **2025**, *82*, 110586. [CrossRef]
2. Yi, G.; Zou, D.; Li, Y.; Chen, K.; Luo, X.; Gao, D. Application of high-accuracy cross-order algorithm in bending analysis of cutoff wall. *Comput. Geotech.* **2026**, *190*, 107744. [CrossRef]
3. Chen, K.; Guo, H.; Luo, X.; Zou, D.; Tian, S. A rapid prediction approach for the global deformation field of concrete-faced rockfill dams based on POD–MLP. *Eng. Anal. Bound. Elem.* **2026**, *183*, 106599. [CrossRef]
4. Kang, F.; Huang, B.; Wan, G. Automated detection of underwater dam damage using remotely operated vehicles and deep learning technologies. *Automat. Constr.* **2025**, *171*, 105971. [CrossRef]
5. Xu, Q.; Chen, J.; Wang, J.; Li, J.; Wang, Y. Velocity divergence—Generalized adaptive probability density evolution method. *Earthq. Eng. Struct. Dyn.* **2024**, *53*, 3678–3700. [CrossRef]
6. Zeng, X.; Xu, Q.; Chen, J.; Ye, M.; Wang, M. Dynamic reliability assessment of structural systems subjected to stochastic mainshock–aftershock sequences. *Eng. Struct.* **2026**, *351*, 122007. [CrossRef]
7. Bornholdt, M.; Herbrand, M.; Smarsly, K.; Zehetmaier, G. Digital-Twin-Based Structural Health Monitoring of Dikes. *CivilEng* **2025**, *6*, 39. [CrossRef]
8. Dagsever, F.; Sharif Khodaei, Z.; Aliabadi, M.H.F. WSN-Based Multi-Sensor System for Structural Health Monitoring. *Sensors* **2025**, *25*, 4407. [CrossRef] [PubMed]
9. Prakash, V.; Debono, C.J.; Musarat, M.A.; Borg, R.P.; Seychell, D.; Ding, W.; Shu, J. Structural Health Monitoring of Concrete Bridges Through Artificial Intelligence: A Narrative Review. *Appl. Sci.* **2025**, *15*, 4855. [CrossRef]

Disclaimer/Publisher's Note: The statements, opinions and data contained in all publications are solely those of the individual author(s) and contributor(s) and not of MDPI and/or the editor(s). MDPI and/or the editor(s) disclaim responsibility for any injury to people or property resulting from any ideas, methods, instructions or products referred to in the content.

applied sciences

MDPI

Article

Load Effect Analysis Method of Cable-Stayed Bridge for Long-Span Track Based on Adaptive Filtering Method

Peng Ding [1,2,3], Xiaogang Li [1,3,*], Sheng Chen [2], Xiangsheng Huang [1], Xiaohu Chen [2,3] and Yong Qi [2,3]

[1] School of Civil Engineering and Architecture, Chongqing University of Science & Technology, Chongqing 400074, China; dingpeng@tylin.com.cn (P.D.); 2022206095@cqust.edu.cn (X.H.)
[2] T. Y. Lin International Engineering Consulting (China) Co., Ltd., Chongqing 401121, China; chensheng@tylin.com.cn (S.C.); chenxiaohu@tylin.com.cn (X.C.); qiyong@tylin.com.cn (Y.Q.)
[3] Chongqing Key Laboratory of Energy Engineering Mechanics & Disaster Prevention and Mitigation, Chongqing University of Science & Technology, Chongqing 400074, China
* Correspondence: 2021058@cqust.edu.cn; Tel.: +86-135-9409-4526

Abstract: Aiming at the problems of large capacity, narrow transverse width, large excitation, high safety level, and difficulty in accurately grasping the working state of the cable-stayed bridge for the long-span track, this research obtains the structural response data in real time by establishing a health monitoring system. The adaptive filtering method was employed to separate the train load response and the temperature load response. Then, a train load effect analysis method based on the influence line and a temperature load effect analysis method based on the correlation were proposed to assess the operational status of the bridge in real time and objectively. The Chongqing Nanjimen Railway Track Bridge (hereinafter Chongqing Nanjimen track bridge) project was utilized as a case study to demonstrate the application of these methods. The results show that the adaptive filtering method can effectively separate the response of train and temperature loads. The normalized cross-correlation (NCC) results of the measured train load response and the influence line's finite element calculation show a high degree of fit between the measured values and the theory, proving that no significant anomalies are found in the bridge. There is a strong correlation between the ambient temperature difference and the Pearson correlation coefficient of structural response, which indicates that the Chongqing Nanjimen track bridge is currently in normal working condition.

Keywords: special cable-stayed bridge for track; adaptive filtering method; train effect; temperature effect; Pearson correlation coefficient

1. Introduction

As urbanization progresses, rail transit is undergoing a period of rapid development, with the construction of rail bridges in full swing. Cable-stayed bridges are becoming increasingly prevalent due to their distinctive shape, robust span capacity, and well-established construction technology.

The time-varying coupling of material property parameters, environmental factors, load action, and other factors makes the time-varying characteristics of the operation and maintenance state of the long-span track special bridge extremely complicated. Because of the characteristics of large traffic volume, narrow transverse width, large excitation, and high safety level, the working state of rail bridges is difficult to accurately control, especially for statically indeterminate rail cable-stayed bridges [1]. Meanwhile, the temperature of the bridge structure is not only subject to temporal fluctuations but also exhibits temperature disparities at all points within the structure. However, the temperature field is markedly uneven and a pronounced hysteresis phenomenon is evident. It is imperative to distinguish between load effects when evaluating the performance state of the bridge structure [2,3]. Therefore, it is important to figure out how to rely on a large amount of bridge measurement data, accurately perceive the changes in bridge performance after

separating temperature effects, and quickly and accurately evaluate the working status of large-span bridges, ensuring the safety of the bridge during its service stage. It is an urgent and difficult issue that the engineering community needs to overcome [4].

Scholars at home and abroad have made useful explorations in analyzing bridge structural performance and load effect. Chen Fang et al. [5] proposed a web-based and design-oriented structural health assessment system (SHES) for long-span bridges equipped with long-term structural health monitoring systems. Mosbeh R. Kaloop et al. [6] investigated using output-only structural health monitoring (SHM) to evaluate the reliability and safety of highway steel plate beams of Yuanxiao Bridge. Displacement, strain, and acceleration measurements are used to assess the behavior of the bridge under designed static, semi-static, and dynamic truck load effects. Chuang Chen et al. [7] designed and installed a long-term structural health monitoring system to monitor the behavior of the bridge during the huge fluctuations in temperature between summer and winter. X.Y.Li et al. [8] analyzed the data recorded by the suspension bridge structural health monitoring system (SHM) and developed a series of indicators for evaluating future changes in the structure's health status. Bjørn T. Svendsen et al. [9] proposed a data-based damage detection method for steel bridges, which obtained data from real bridges under different structural conditions and applied an unsupervised machine learning algorithm to evaluate the most detectable damage types. Ju Hanwen et al. [10] proposed a calculation method for vehicle-mounted impact parameters based on the deflection influence line. A correlation model of vehicle-mounted impact parameters, ambient temperature, and bridge deflection was established based on the GRU neural network. Li Xiaogang et al. [11] analyzed domestic and foreign norms and standards and proposed evaluation criteria for the service performance of long-span track bridges. Chenyu Zhou et al. [12] introduced an FE(finite element)-based adaptive enhanced Kalman filter (AAKF) B-WIM framework and adopted a new adaptive noise filter optimized by a genetic algorithm to realize accurate load recognition by combining finite element (FE) model update and bridge motion weighing (B-WIM). Premjeet Singh et al. [13] proposed a bridge state assessment technology, which used the vibration data collected by sensors, combined natural excitation technology (NExT) and empirical Fourier decomposition (EFD), and adopted a hybrid method to analyze the environmental vibration data of bridges and identify the bridge state for assessment. To separate vehicle-induced strain components from strain monitoring signals mixed with various loads, Danhui Dan et al. [14] proposed an online recursive sliding variational mode decomposition method. T. Hielscher et al. [15] proposed a robust end-to-end optical fiber sensor (FOS) monitoring prototype based on deep neural networks to convert FOS strain output into an interactive digital twin (DT) visualization in response to the scale of structural deterioration worldwide and the ineffectiveness of existing non-destructive assessment techniques. Xun Liu et al. [16] proposed a new method of real-time time-varying cable force identification. The method updates the cable vibration signal by sliding the window and uses adaptive chirped mode decomposition (ACMD) to identify the instantaneous frequency of the cable. Xiang Xu et al. [17] proposed a probabilistic anomaly detection method considering the uncertainty model, aiming at the multi-stage uncertainty modeling problem in the anomaly detection process of long-span bridges. To provide researchers with a clear perspective on the field of health monitoring, Anis Shafiqah Azhar et al. [18] reviewed the methods previously studied in the vibration characterization of SHM bridges. The future potential of the vibration-based approach as a structural characterization solution is significant, providing state-of-the-art data-driven measures for damage detection. The increased robustness of SHM also provides room for progress in the precise quantification and interpretation of vibration-based techniques, providing a way for future research to extend the vibration-based frontier. To sum up, scholars at home and abroad have conducted in-depth studies in the fields of bridge health monitoring systems and bridge condition evaluation, with fruitful results. However, there is little research on the load effect analysis of large-span dedicated track bridges based on health monitoring systems.

In view of this, this paper proposes the establishment of a dedicated track bridge health monitoring system with the objective of acquiring structural response data in real time. To address the specific characteristics of high frequency, large response, and periodicity of the train load effect, an adaptive filtering method is put forth to differentiate between train load and temperature load. The proposed system is validated through a real bridge test conducted on the Chongqing Nanjimen track bridge. The vertical displacement of the main beam, the longitudinal displacement of the main tower, and the stress of the main beam under the action of the train are studied and compared with the numerical simulation results. Meanwhile, the influence of ambient temperature on the aforementioned variables is analyzed. A linear regression equation was fitted by the least squares method, and the correlation strength and direction were determined by the Pearson correlation coefficient. Finally, the load effect analysis of the bridge was completed, providing scientific and technical support for the maintenance of the bridge in a healthy manner.

2. Project and Finite Element

2.1. Project Overview

The Chongqing Nanjimen track bridge is the key control engineering of the second phase of Chongqing Rail Transit Line 10, and it is the world's largest span railway special cable-stayed bridge. The main bridge adopts a five-span high–low tower double-cable-plane semi-floating system cable-stayed bridge. The longitudinal arrangement is 34.5 + 180.5 + 480 + 215.5 + 94.5 = 1005.0 m, and the cross-sectional arrangement is 2.8 m (cable area and access road) + 16.2 m (track zone) + 2.8 m (cable area and access road) = 21.8 m (without air nozzles). The main beam is of a steel-hybrid type, with a height of 3.3 m. The main structure of the steel beam is of the Q345qD variety, while the prefabricated bridge panel is of the C60 concrete variety. The main tower is constructed using a door frame structure comprising upper, middle, and lower beams. The P2 tower is 158 m tall, while the P3 tower is 227 m tall. The material used for the construction of these towers is C50 concrete. There are 16 pairs of cable-stayed cables at the P2 tower side and 27 pairs of cable-stayed cables at the P3 tower side. The cable-stayed cables are HDPE-sheathed with Φ7.0 mm galvanized high-strength and low-relaxation parallel steel wire. The tensile strength is not less than 1770 Mpa, and the tensile elastic modulus is not less than 195 GPa. Figures 1–3 show the overall layout of the bridge. The design of the special bridge for Chongqing Nanjimen track bridge adopts a train, with 6 sections in the near term and 7 sections in the long term. The axle weight is 150 kN, and the train loading is shown in Figure 4.

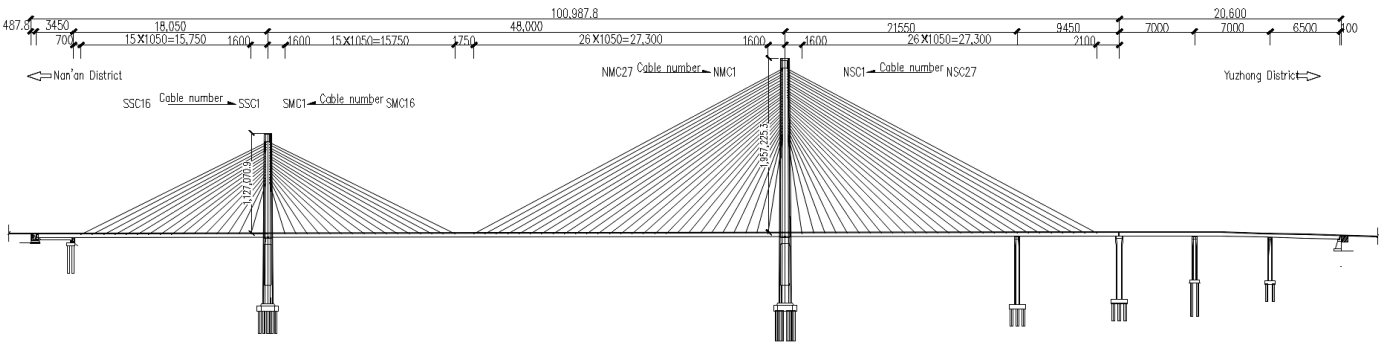


Figure 1. Bridge layout (unit: cm).

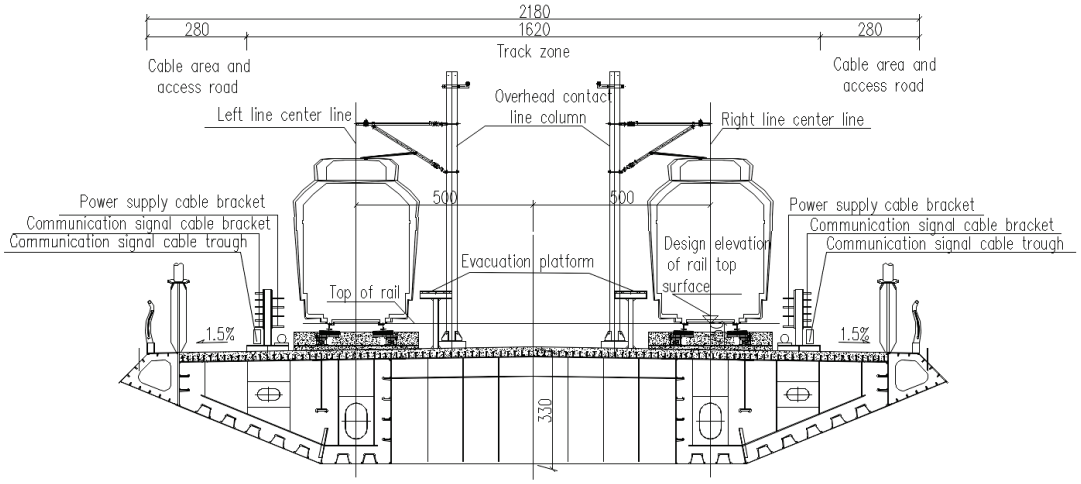


Figure 2. Cross-sectional layout (unit: cm).

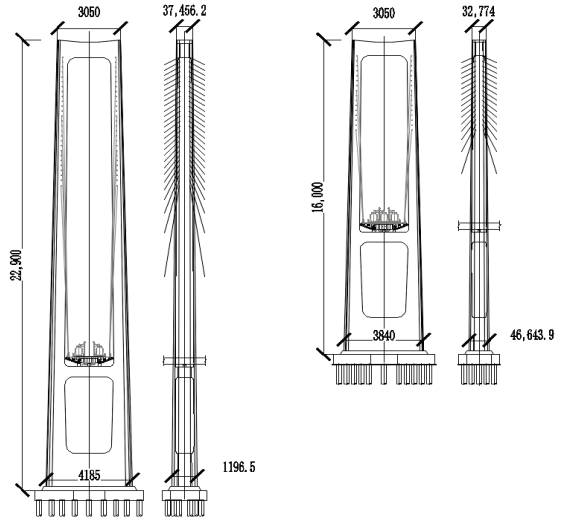


Figure 3. Section view of the main tower (unit: cm).

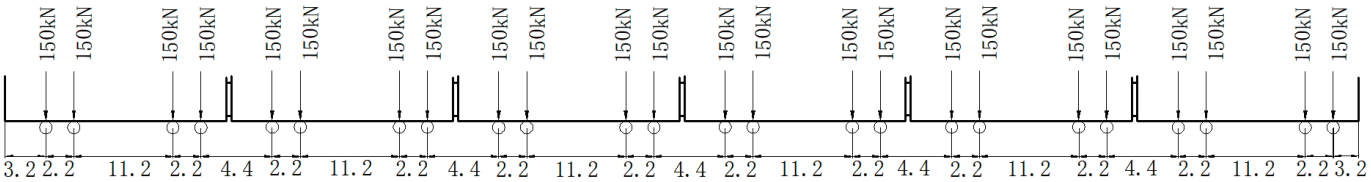


Figure 4. Loading diagram of the 6-car train (unit: m).

2.2. Health Monitoring System

The health monitoring system of the Chongqing Nanjimen track bridge structure is composed of five parts: 1. sensor module, 2. application module, 3. data analysis module, 4. data processing and management module, 5. data acquisition and transmission module. The overall distributed architecture (SOA) is the main one, and each component (subsystem) supports cluster deployment [19–21]. The system takes load and environment, overall static and dynamic response of the structure, and local response of the structure as the main monitoring categories, including temperature and humidity, wind speed and direction, vibration, deformation (displacement), angle, stress, cable force, and other monitoring items. The specific layout is shown in Figure 5 and details of the device of Figure 5 are shown in Table 1.

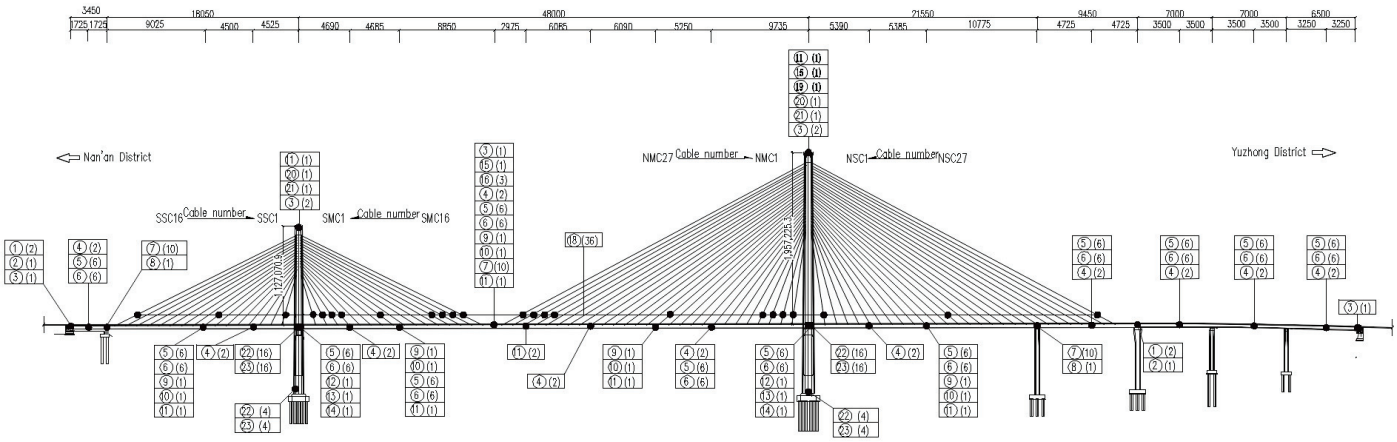


Figure 5. The overall layout of health monitoring points (unit: cm).

Table 1. Equipment information table of the health monitoring system.

Category	Monitoring Item	Number in Figure 5 *	Main Parameter	Device Type	Sampling Frequency
Load and environmental monitoring	Strike	⑫, ⑬, ⑭	Crash—Ship crash	Unidirectional acceleration sensor	20 Hz
	Temperature	⑯, ㉓	Temperature—Ambient temperature	Hygrograph	1/600 Hz
		⑥	Temperature—Temperature inside the box girder	Hygrograph	1/600 Hz
	Humidness	⑯, ㉓	Humidity—Ambient humidity	Hygrograph	1/600 Hz
			Humidity—Box girder inside wet	Hygrograph	1/600 Hz
	Rainfall	⑲	rainfall	Hyetometer	1/60 Hz
	Water level	⑰	Water level	Radar water level gauge	1 Hz
	Wind	⑮	Wind speed and direction	anemometer	1 Hz
Static and dynamic response monitoring of the whole structure	Vibration	⑨, ⑩	Vibration—Main beam vibration	Unidirectional acceleration sensor	20 Hz
		⑳, ㉑	Vibration—Tower vibration	Unidirectional acceleration sensor	20 Hz
	Amorphosis	④	Deformation—Vertical change in the main beam	Static level	1 Hz
		⑪	Deformation—Tower space deformation (GNSS)	GNSS deformation monitoring system	1 Hz
Static and dynamic response monitoring of the whole structure	Amorphosis	⑪	Deformation—Main beam space deformation (GNSS)	GNSS deformation monitoring system	1 Hz
		⑧	Deformation—Horizontal displacement of the pier	Inclinometer	1 Hz
		①	Deformation—Displacement of expansion joint	Fiber grating displacement meter	1 Hz
	Corner	②	Corner	inclinometer	1 Hz
Structure local response monitoring	Stress	⑤	Main beam stress	Fiber grating strain gauge	1 Hz
		㉒	Main tower stress	Fiber grating strain gauge	1 Hz
	Cable force	⑱	Cable force of the cable	Cable force accelerometer	20 Hz
				Transcore pressure sensor	1/60 Hz
	Structural fatigue	⑦	Fatigue of steel structure	Fiber grating strain gauge	1 Hz

* Note: ③ in the figure is video surveillance.

2.3. Finite Element Analysis

The general software MIDAS/Civil 2023 was used for the finite element analysis of Chongqing Nanjimen track bridge. There were 1085 nodes and 1504 units in the whole bridge, among which the inclined main tower and main beam were simulated by beam elements; the minimum length of the unit was 0.2 m, and a total of 1128 beam elements were simulated by the cable-stayed cable-only tension element. There was a total of 376 tension-only units. The bridge panels and main beams are simulated by the dual unit method. The bridge panels are made of C60 concrete with a 36,500 MPa elastic model; the bridge towers are made of C50 concrete with a 35,500 MPa elastic model; the steel beams are made of Q345qD steel with a 210,000 MPa elastic model, and the cable is made of 205,000 MPa galvanized high-strength low-relaxation galvanized parallel wire strands. The cable anchorage adopts a rigid connection; the bottom of the main tower adopts a general support solid connection, and the boundary constraint between the main beam and the main tower and bridge pier is an elastic connection. Train motion modeling method: Firstly, the axle load and distance of the vehicle load and the position of the left and right lanes are defined and the correlation between the two is established by defining the moving load condition. The number of iterations of load conditions is set to 20, and the convergence error is 0.001. The time-varying effect mainly considers creep, and the number of creep iteration calculations is set to 5 times, and the convergence error is 0.01. In the calculation of nonlinear analysis, the maximum number of iterations in each load step is set by the convergence criterion, which is 150 times, and the convergence error is 0.01. In the construction phase, nonlinear analysis and time-varying effect are considered, tangential assembly is considered for the main beam, and the cable force of the cable is controlled by external force, as shown in Figure 6.

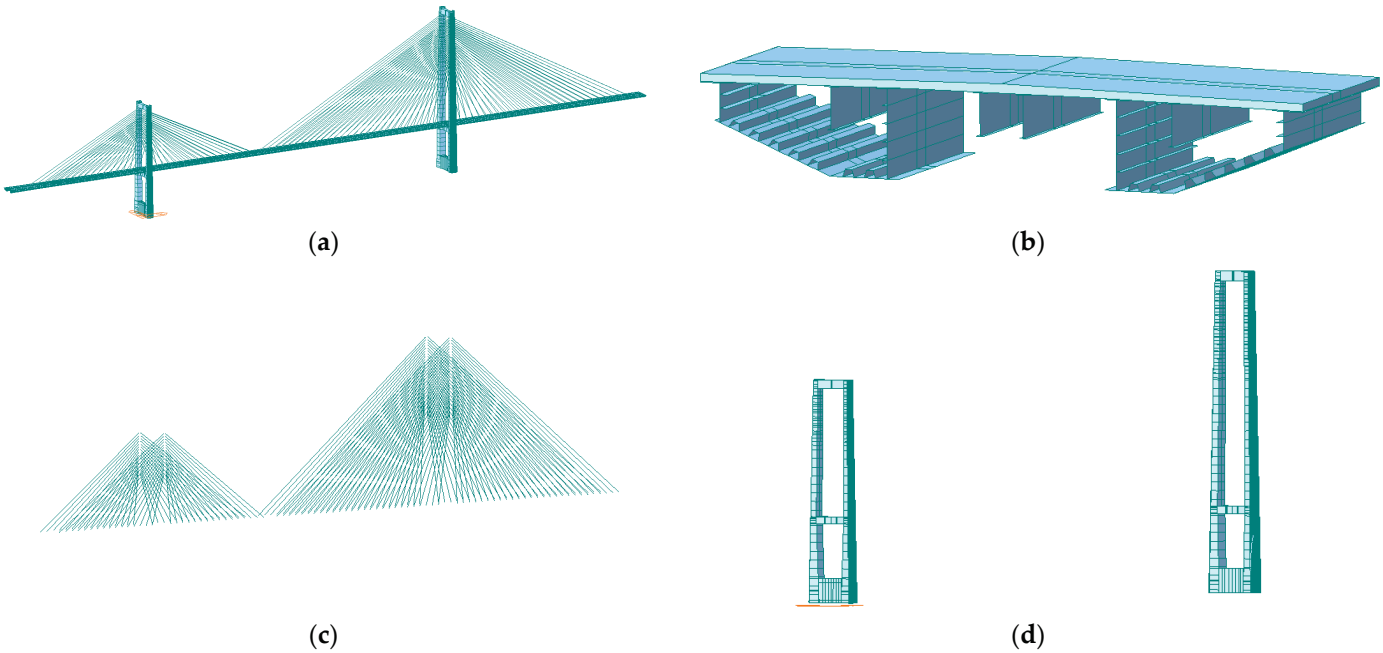


Figure 6. The overall finite element model of the Chongqing Nanjimen track bridge. (**a**) Discrete diagram of the overall finite element model. (**b**) Finite element model of the main girder section. (**c**) Finite element model of the stay cable section. (**d**) Finite element model of the main tower section.

3. Load Effect Analysis Method

The real-time structural response information obtained by the health monitoring system of the Chongqing Nanjimen track bridge is a composite value, including the train load effect, temperature load effect, and deterioration effect, wherein deterioration effect [22,23] is a long-term process, including shrinkage and creep of concrete, corrosion and rust of steel bars, etc. The response data obtained by the health monitoring system are real-time

data, which are mainly affected by train load and temperature effect. Therefore, the deterioration effect cannot be considered in load effect analysis. Considering that the signal frequency and amplitude of the train load effect and the temperature load effect are different, this paper adopts an adaptive filtering method to separate the train action from the temperature load effect. The specific principle is as follows:

1. According to the period T of the train crossing the bridge and the monitoring data acquisition frequency V, the number of data samples $N = T.V$ required for analysis is determined.
2. When the number of data samples N reaches the minimum value f_{min} and the median value f_z of the data sample is obtained, where data sample f generally refers to structural stress, displacement, and cable force. If $f_{min} = f_z$, the program preliminarily determines it as the train load effect data.
3. Based on the finite element model, the calculated value f_m under train load is obtained, and the limit value $f'_m = k * f_m f$ is set, where k is less than 1. The specific value is determined by the sample data, and the initial value f_c of the sample is obtained. If $|f_{min} - f_c| \geq f'_m$, it is confirmed that these data samples N are train load effect data.
4. After the train load effect data are extracted, the initial sample value f_c is subtracted to carry out initialization processing and remove the influence of temperature load.

Taking the vertical displacement of the main beam at the mid-span of the Chongqing Nanjimen track bridge on 1 November 2023 as an example, the train load effect and temperature load effect are separated through the above steps and the results are shown in Figures 7–9.

It can be seen from Figures 7–9 that the signal separation method proposed in this paper is effective. At 16:50:49, the deflection caused by the train load is −88.3 mm, the deflection caused by the temperature load is −179.9 mm, while the measured vertical displacement of the main beam is −266.7 mm, with an error of 0.56%. At 3:24:00, the deflection generated by the train load is 0 mm, the deflection generated by the temperature load is −51.5 mm, while the measured vertical displacement value of the main beam is −50.0 mm, with an error of 3.0%, meeting the requirements.

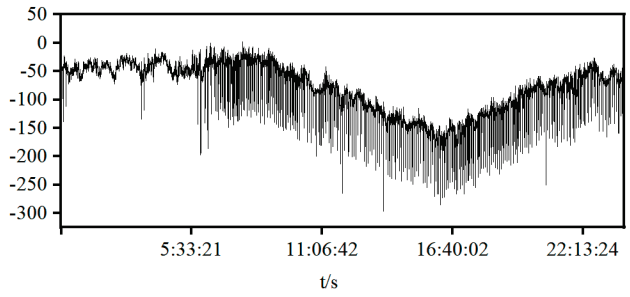


Figure 7. Measured vertical displacement of the main beam (unit: mm).

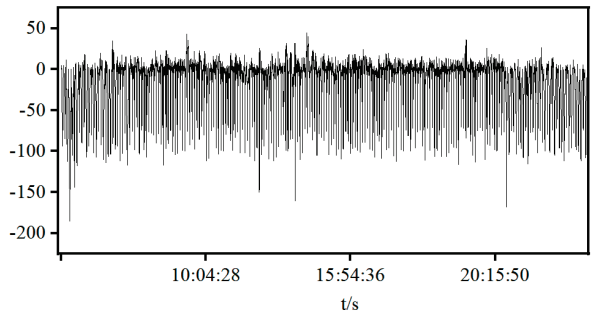


Figure 8. Vertical displacement of the main beam under train load (unit: mm).

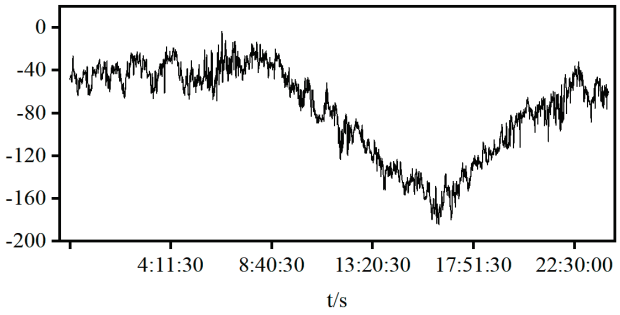


Figure 9. Vertical displacement of the main beam under temperature load (unit: mm).

In conclusion, the composite structural response data derived from the health monitoring system are inadequate for the accurate and effective evaluation of bridge behavior. To achieve load effect analysis, it is essential to differentiate between the train load and temperature load and utilize the data after the temperature effect has been isolated for targeted analysis of the operational state of the bridge under the influence of the train. This will facilitate the assessment of the bridge's performance and provide technical support for the scientific management and maintenance of the bridge.

4. Load Effect Separation Experiment

4.1. Analysis of Train Load Effect Based on Influence Line

The stiffness or elastic modulus of the bridge structure will change after damage. As an inherent characteristic of the bridge, the influence line [24–29] will also have different degrees of influence with the change in the structural characteristics of the bridge.

The Chongqing Nanjimen track bridge's health monitoring system enables the real-time acquisition of response data, including vertical displacement of the main beam, longitudinal displacement of the main tower, and stress of the main beam, during the operation of a train. Considering that the train is running at a constant speed during the crossing of the bridge (the impact of different speeds is minimal) and the duration is brief (the effect of temperature and wind is stable), bridge influence lines of various indexes can be obtained through monitoring data analysis and compared with the finite element analysis results to achieve a bridge state assessment. The analysis results are shown in Figures 10–14.

As can be seen from Figures 10–14, based on the response data such as vertical displacement of the main beam, longitudinal displacement of the main tower, and stress of the main beam collected by the health monitoring system of the Chongqing Nanjimen track bridge, the temperature load is removed by the above separation method and the response data under the action of the train load are obtained. A comparison of the influence line obtained by Midas/Civil 2023 simulation with the measured maximum vertical displacement of the main beam reveals that the measured maximum vertical displacement of the main beam is 92.00 mm and the theoretical maximum is 92.4 mm, both of which occur at 67.80 m from the left side of the span. The measured maximum longitudinal displacement of the P2 main tower is 34.00 mm, and the theoretical maximum is 34.4 mm, both of which occur at 106.28 m from the left side of the span. The measured maximum longitudinal displacement of the P3 main tower is 18.80 mm, and the theoretical maximum is 19.20 mm, both of which occur at 11.42 m from the left side of the span. The measured maximum stress of the main beam roof is -0.70 Mpa, and the theoretical maximum stress is -0.70 Mpa at 67.80 m from the left side of the span. The measured maximum stress of the main beam floor is 3.80 Mpa; the theoretical maximum stress is -0.70 Mpa, and the stress is 9.32 m from the left side of the span.

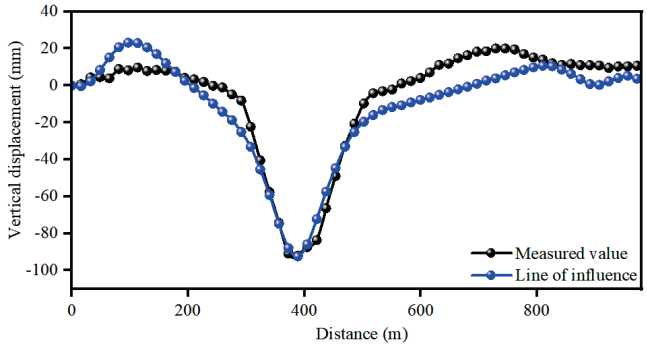


Figure 10. Comparative analysis of vertical displacement of the main beam and finite element influence line.

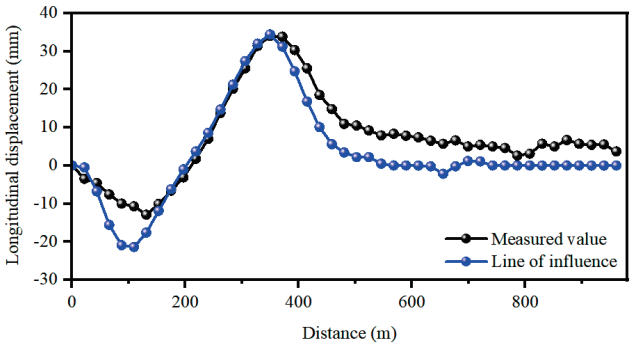


Figure 11. Comparative analysis of longitudinal displacement of P2 tower top and finite element influence line.

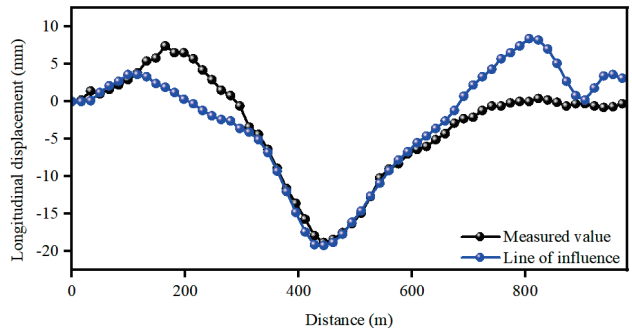


Figure 12. Comparative analysis of longitudinal displacement of P3 tower top and finite element influence line.

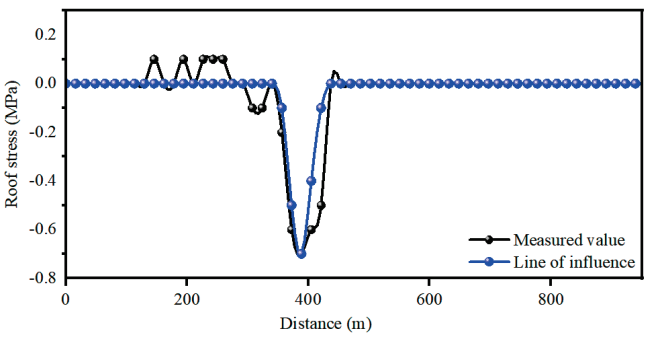


Figure 13. Comparative analysis of roof stress and finite element influence line in the center section of the main beam closing section.

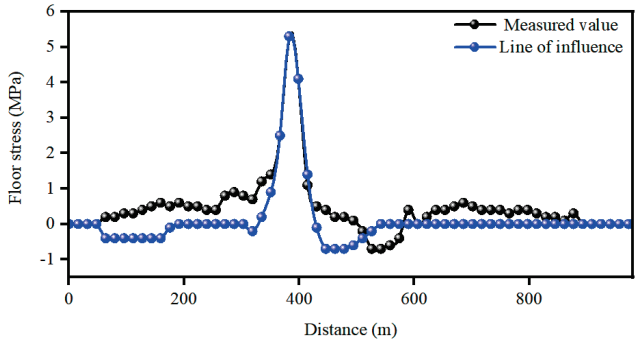


Figure 14. Comparative analysis of the stress of the bottom plate of the center section of the main beam and the influence line of the finite element.

Meanwhile, normalized cross-correlation (NCC) was employed to assess the degree of similarity between the two entities [30,31].

For each lag (k), we calculated the number of normalized cross-relations:

$$R(k) = \frac{\sum_{i=1}^{n}(y_1(i) - \overline{y}_1)\cdot(y_2(i+k-n) - \overline{y}_2)}{\sqrt{\sum_{i=1}^{n}(y_1(i) - \overline{y}_1)^2}\cdot\sqrt{\sum_{i=1}^{n}(y_2(i+k-n) - \overline{y}_2)^2}} \quad (1)$$

where

n—Sample size;

$\overline{y}_1$, $\overline{y}_2$—Mean of samples y_1 and y_2, respectively.

The larger the NCC value, the better the fitting. As can be seen from Table 2, the normalized cross-correlation values are 0.9457, 0.9531, 0.8873, 0.9098, and 0.9101 indicating a high degree of fitting between the measured values and the theory. In summary, the structural response under train load and the influence line results of finite element calculation have small errors and a high fitting degree and no significant anomalies are found on the bridge, which proves that the data obtained through the health monitoring system can achieve the load effect analysis of the bridge and provide technical support for the scientific management and maintenance of the bridge.

Table 2. Normalized relationship between measured and theoretical values (NCC).

Serial Number	Structural Response Parameter	NCC	Similarity
1	Vertical displacement of the main beam	0.9457	High
2	Longitudinal displacement of the main tower (P2 side)	0.9531	High
3	Longitudinal displacement of the main tower (P3 side)	0.8873	High
4	Roof stress in the span of the main beam	0.9098	High
5	Middle floor stress of main beam span	0.9101	High

4.2. Analysis of Temperature Load Effect Based on Correlation

The cable-stayed bridge dedicated to the long-span track has an obvious response to temperature load. Therefore, an accurate analysis of the correlation between ambient temperature, displacement of the main beam and main tower, cable-stayed cable force, and main beam stress is of great significance for accurately identifying the structural state of the bridge and ensuring the operation safety of the bridge [32,33]. In this paper, the linear regression equation is fitted by the least squares method and the Pearson correlation coefficient [34,35] is used to determine the strength and direction of its correlation. The formula is shown as follows:

$$R = \frac{\sum_{i=1}^{n}(X_i - \overline{X})(Y_i - \overline{Y})}{\left[\sqrt{\sum_{i=1}^{n}(X_i - \overline{X})^2} * \sqrt{\sum_{i=1}^{n}(Y_i - \overline{Y})^2}\right]} \quad (2)$$

where

RPearsoncorrelationcoefficient;

X_i, Y_i—Values of X and Y variables for the ith sample;

$\overline{X}$, $\overline{Y}$—Sample average of X variable and Y variable;

n—Sample size.

According to the stress characteristics of the track bridge, one-day monitoring data with small and stable wind speed in the bridge area are selected to separate the train load response data and the correlation between daily temperature difference and vertical displacement of the main beam, longitudinal displacement of the main tower, longitudinal displacement of the main beam, cable force of the cable, and stress of the main beam is analyzed, as shown in Table 3 and Figures 15–23.

Table 3. Results of correlation analysis between ambient temperature and structural response.

Serial Number	Structural Response Parameter	Pearson Correlation Coefficient R	Strength of Correlation
1	Vertical displacement of the main beam	−0.9634	strong
2	Longitudinal displacement of the main tower (P2 side)	0.9384	strong
3	Longitudinal displacement of the main tower (P3 side)	−0.8951	strong
4	Longitudinal displacement of the main beam (A0 side)	−0.9421	strong
5	Longitudinal displacement of the main beam (P5 side)	−0.7853	strong
6	SMC1 Cable	−0.8980	strong
7	NMC1 Cable	−0.9625	strong
8	Roof stress in the span of the main beam	0.9658	strong
9	Middle floor stress of main beam span	0.9326	strong

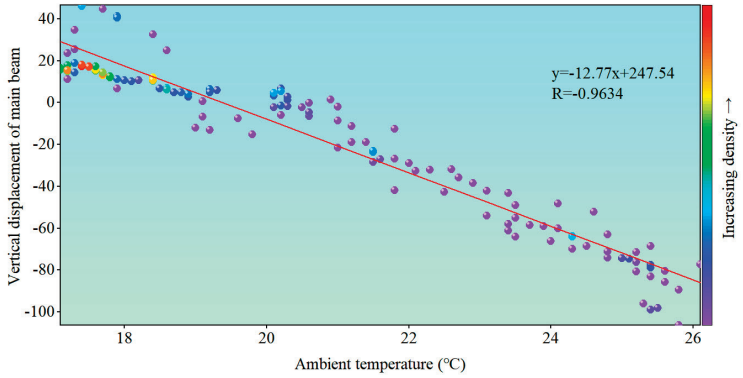


Figure 15. Correlation between ambient temperature and vertical displacement of the main beam (unit: mm).

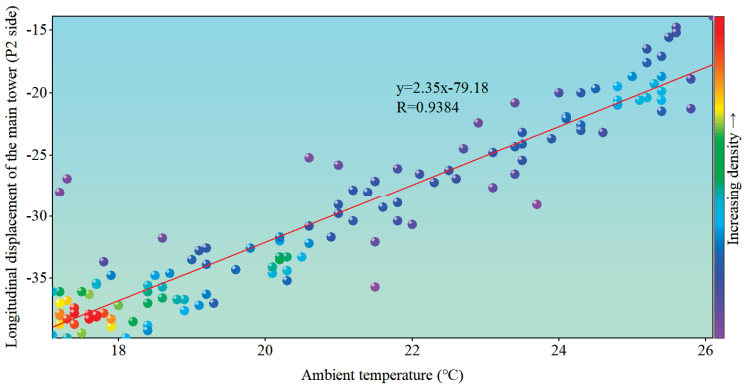


Figure 16. Correlation between ambient temperature and longitudinal displacement of the main tower at P2 side (unit: mm).

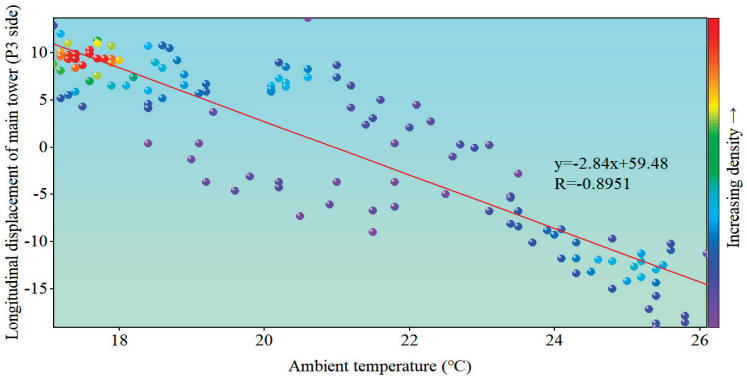


Figure 17. Correlation between ambient temperature and longitudinal displacement of the main tower at P3 side (unit: mm).

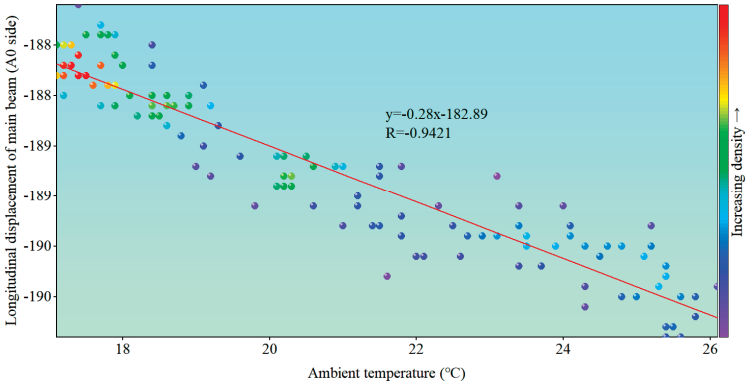


Figure 18. Correlation between ambient temperature and longitudinal displacement of the main beam on the A0 side (unit: mm).

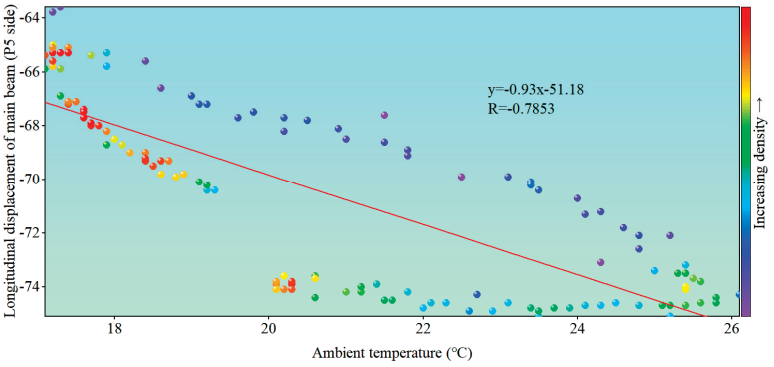


Figure 19. Correlation between ambient temperature and longitudinal displacement of the main beam on the P5 side (unit: mm).

Figures 15–23 show the following: The ambient temperature has a strong negative correlation with the vertical displacement of the main beam, the longitudinal displacement of the main tower (A0 side, P3 side, and P5 side), and the Pearson correlation coefficient $R < -0.7$ of the SMC1 stay cable and NMC1 stay cable. When the temperature rises, the vertical displacement of the main beam, the longitudinal displacement of the P3 main tower, and the longitudinal displacement of the A0 side main beam show a downward torsion trend. The SMC1 and NMC1 cable bodies become longer, and the tension becomes smaller. The Pearson correlation coefficient $R > 0.7$ shows a strong positive correlation between the longitudinal displacement of the main tower (P2 side), the roof stress in the main beam span, and the stress in the middle floor of the main beam span. When the temperature

rises, the longitudinal displacement of the main tower (P2 side) shows an upward bending trend, and the roof stress in the main beam span and the stress in the middle floor of the main beam span increase. The results show that temperature has a significant effect on the cable-stayed bridge with a long-span track and there is a significant correlation with the response of each part of the structure.

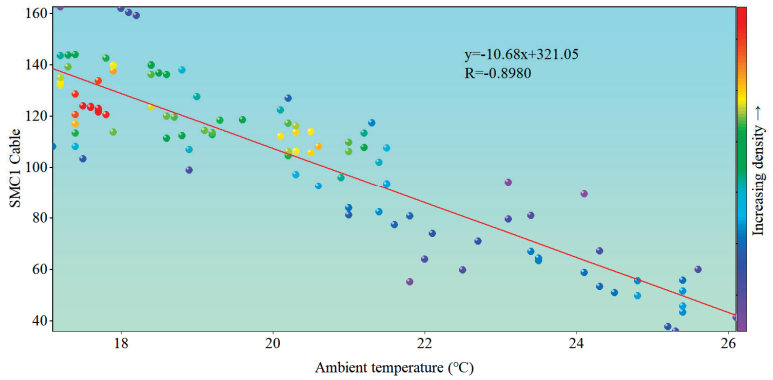


Figure 20. Correlation between ambient temperature and the SMC1 cable (unit: kN).

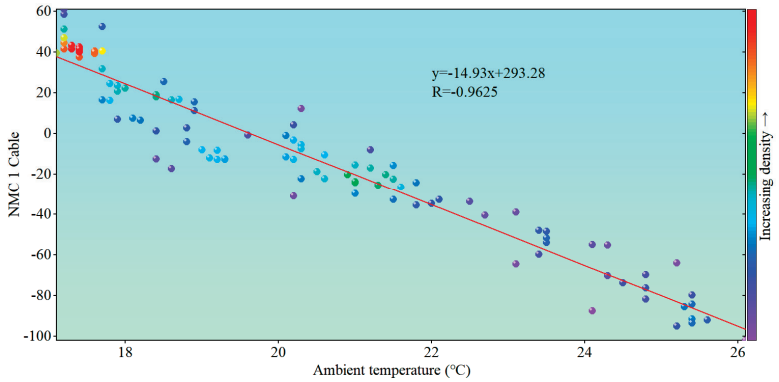


Figure 21. Correlation between ambient temperature and NMC1 cable (unit: kN).

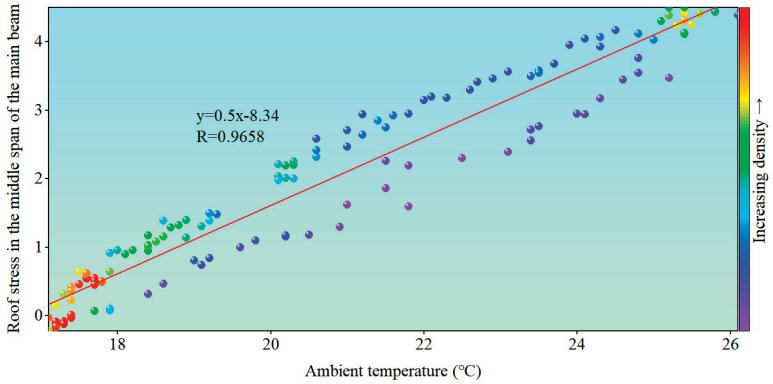


Figure 22. Correlation between ambient temperature and roof stress in the middle span of the main beam (unit: MPa).

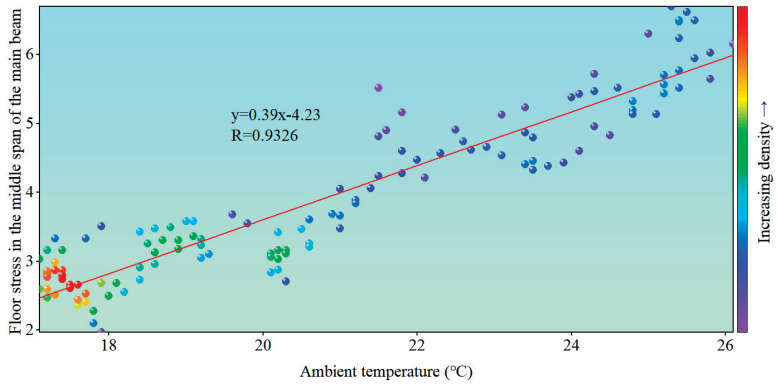


Figure 23. Correlation between ambient temperature and floor stress in the middle span of the main beam (unit: MPa).

5. Conclusions and Prospects

Based on the characteristics of track bridges, such as large volume, narrow transverse width, large excitation, high safety level, and clear load response, this paper proposes for the first time a method to obtain temperature load and train load from the composite response data of track bridge through an adaptive filter separation monitoring system. Relying on the structural health monitoring system of the Chongqing Nanjimen track bridge to analyze the load effect of train and temperature effects, this paper obtains the following conclusions:

1. The adaptive filtering load effect separation method proposed in this paper is both feasible and effective. Based on the characteristics of high frequency, large response, and periodicity of train load effect, a method for separating load effect is proposed. Through the signal separation of the composite structure response data obtained by the monitoring system, the respective effects of train load and temperature load at the same time are obtained, which provides scientific support for the state evaluation of the bridge and makes the evaluation results more accurate and reliable.
2. The measured values of the structural influence line of the vertical displacement of the main beam, the longitudinal displacement of the main tower, and the stress index of the main beam under the action of train load are compared with the theoretical influence line obtained by simulation, based on the train load effect analysis method of the influence line. The normalized cross-correlation (NCC) of the two indexes was found to be 0.9457, 0.9531, 0.8873, 0.9098, and 0.9101. This demonstrated a very high degree of fit, indicating that no significant anomalies were found in the bridge and verifying the direct evaluation of the structural state of the line affected by the train load.
3. The impact of ambient temperature on the cable-stayed bridge with a long-span track is profound, and there is a clear correlation between the response of each structural component. The temperature exhibits a strong negative correlation with the vertical displacement of the main beam, longitudinal displacement of the main tower (A0 side, P3 side, and P5 side), and Pearson correlation coefficient $R < -0.7$ of the stay cable. Conversely, the longitudinal displacement of the main tower (P2 side), roof stress in the main beam span, and floor stress in the main beam span exhibit a strong positive correlation coefficient $R > 0.7$. It has been demonstrated that the structural state can be evaluated indirectly by temperature load correlation.

Based on the bridge health monitoring system, the load effect analysis and evaluation of long-span track special bridge structure are studied to some extent, but there are still the following deficiencies:

1. Comprehensive consideration of long-term effects: In addition to the load effect, the durability of the long-span track special cable-stayed bridge is also an important consideration. Therefore, in the future, a durability analysis will be carried out by mon-

itoring the corrosion and fatigue of bridge materials to ensure the long-term safe operation of the bridge.

2. Optimize the monitoring system: In the future, the combination of artificial intelligence and big data analysis technology with the establishment of a decision support system will facilitate more accurate real-time monitoring, analysis, and prediction of the load effect of long-span track special cable-stayed bridges. Through systematic data management and analysis, the efficiency and safety of bridge operation and maintenance will be enhanced.

Author Contributions: P.D. Conceptualization, methodology, software, investigation, and writing—original manuscript; X.L. Conceptualization, methodology, formal analysis, and writing—review, and editing; S.C. Resources, visualization, and supervision; X.H. Writing—original manuscript, verification, and investigation; X.C. Resources, verification, investigation, and data management; Y.Q. Resources, writing—review and editing, and data management. All authors have read and agreed to the published version of the manuscript.

Funding: This work was supported by the Open Fund of Chongqing Key Laboratory of Energy Engineering Mechanics and Disaster Prevention and Mitigation (EEMDPM2021201) and the Chongqing University of Science and Technology research funding project (CKRC2021074).

Data Availability Statement: All of the data and models that were generated or used during the study are available from the corresponding author by request.

Conflicts of Interest: Author Mr. Sheng Chen was employed by the company T. Y. Lin International Engineering Consulting (China) Co., Ltd. The remaining authors declare that the research was conducted in the absence of any commercial or financial relationships that could be construed as a potential conflict of interest.

References

1. Li, X.; Luo, H.; Ding, P.; Chen, X.; Tan, S. Prediction Study on the Alignment of a Steel-Concrete Composite Beam Track Cable-Stayed Bridge. *Buildings* **2023**, *13*, 882. [CrossRef]
2. Tan, H.; Qian, D.; Xu, Y.; Yuan, M.; Zhao, H. Analysis of Vertical Temperature Gradients and Their Effects on Hybrid Girder Cable-Stayed Bridges. *Sustainability* **2023**, *1053*, 1013. [CrossRef]
3. Tan, D.-M.; Guo, T.; Gan, Q.-L. Separation of Temperature Effect in Monitored Deflection of Bridges Based on VMD-SVD. *Bridge Constr.* **2023**, *53*, 87–94.
4. Wang, L.-B.; Wang, Q.-L.; Zhu, Z.; Zhao, Y. Current Status and Prospects of Research on Bridge Health Monitoring Technology. *Zhongguo Gonglu Xuebao/China J. Highw. Transp.* **2021**, *34*, 25–45.
5. Fang, C.; Xu, Y.L.; Hu, R.; Huang, Z. A web-based and design-oriented structural health evaluation system for long-span bridges with structural health monitoring system. *Struct. Control Health Monit.* **2021**, *29*, e2879. [CrossRef]
6. Kaloop, M.R.; Eldiasty, M.; Hu, J.W. Safety and reliability evaluations of bridge behaviors under ambient truck loads through structural health monitoring and identification model approaches. *Measurement* **2022**, *187*, 110234. [CrossRef]
7. Chen, C.; Wang, Y.; Kaloop, M.R.; Wang, T.; Ma, J. Continuous Box-Girder Bridge Condition Assessment Based on Structural Health Monitoring System: A Case Study. In Proceedings of the 2020 International Conference on Intelligent Transportation, Big Data & Smart City (ICITBS), Vientiane, Laos, 11–12 January 2020; pp. 734–740.
8. Li, X.Y.; Guan, Y.H.; Law, S.S.; Zhao, W. Monitoring abnormal vibration and structural health conditions of an in-service structure from its SHM data. *J. Sound Vib.* **2022**, *537*, 117185. [CrossRef]
9. Svendsen, B.T.; Frøseth, G.T.; Øiseth, O.; Rønnquist, A. A data-based structural health monitoring approach for damage detection in steel bridges using experimental data. *J. Civ. Struct. Health Monit.* **2022**, *12*, 101–115. [CrossRef]
10. Hanwen, J.; Yang, D.; Aiqun, L. Correlation model of deflection-temperature-vehicle load monitoring data for bridge structures. *J. Vib. Shock* **2023**, *42*, 79–89.
11. Li, X.; Gao, M.; Zhou, J.; Chen, X.; Tan, S. Permanent deformation limits of long-span track cable-stayed bridges based on service performance analysis. *Sage J.* **2021**, *40*, 1215–1226. [CrossRef]
12. Zhou, C.; Butala, M.D.; Xu, Y.; Demartino, C.; Spencer, B.F. FE-based bridge weigh-in-motion based on an adaptive augmented Kalman filter. *Mech. Syst. Signal Process.* **2024**, *218*, 111530. [CrossRef]
13. Singh, P.; Bana, D.; Sadhu, A. Improved bridge modal identification from vibration measurements using a hybrid empirical Fourier decomposition. *J. Sound Vib.* **2024**, *590*, 118598. [CrossRef]
14. Dan, D.; Zeng, G.; Pan, R.; Yin, P. Block-wise recursive sliding variational mode decomposition method and its application on online separating of bridge vehicle-induced strain monitoring signals. *Mech. Syst. Signal Process.* **2023**, *198*, 110389. [CrossRef]

15. Hielscher, T.; Khalil, S.; Virgona, N.; Hadigheh, S.A. A neural network based digital twin model for the structural health monitoring of reinforced concrete bridges. *Structures* **2023**, *57*, 105248. [CrossRef]
16. Liu, X.; Yang, J.; Zhuo, W.; Lin, K.; Lin, Y. Real-time identification of time-varying cable force for cable-stayed bridges based on vibration monitoring. *Measurement* **2024**, *231*, 114590. [CrossRef]
17. Xu, X.; Shi, C.; Ren, Y.; Fan, Z.; Guo, Z.; Zeng, X.; Jin, Y.; Huang, Q. Probabilistic anomaly detection considering multi-level uncertainties for cable-stayed bridges. *Structures* **2023**, *58*, 105448. [CrossRef]
18. Azhar, A.S.; Kudus, S.A.; Jamadin, A.; Mustaffa, N.K.; Sugiura, K. Recent vibration-based structural health monitoring on steel bridges: Systematic literature review. *Ain Shams Eng. J.* **2024**, *15*, 102501. [CrossRef]
19. Fang, F.; Lv, K.; Qiu, L. Design of GMM Damage Alarm Software Based on Embedded Structural Health Monitoring System. *Trans. Nanjing Univ. Aeronaut. Andastronautics* **2023**, *40*, 62–68.
20. Yi, T.H.; Zheng, X.; Yang, D.H.; Li, H.N. Lightweight design method for structural health monitoring system of short-and medium-span bridges. *J. Vib. Eng.* **2023**, *36*, 458–466.
21. Yu, J.; Peng, Z.; Meng, X.; Xie, Y. GNSS-based Rea-time Vibration Monitoring and Dynamic Response Analysis of a Long-span SuspensionBridge under an Extreme Typhoon Event. *China J. Highw. Transp.* **2024**, 1–14. Available online: http://kns.cnki.net/kcms/detail/61.1313.U.20240222.1338.002.html (accessed on 6 August 2024).
22. Xiaopeng, L.Z.F. Study of Degradation Effects of Perforation and Welding on Fatigue Performance of Steel Deck. *Bridge Constr.* **2020**, *50*, 8–13.
23. Miao, P.; Yokota, H.; Zhang, Y. Deterioration prediction of existing concrete bridges using a LSTM recurrent neural network. *Struct. Infrastruct. Eng.* **2023**, *19*, 475–489. [CrossRef]
24. Tang, L.; Wu, T.; Mao, R.; Zhou, Z. Curvature Influence Line Area Difference Method for Damage Location of Bridge Structures. *Yingyong Jichu Yu Gongcheng Kexue Xuebao/J. Basic Sci. Eng.* **2022**, *30*, 541–553.
25. Zhang, C.; Zhu, J.; Zhou, S. Integration of multi-point influence line information for damage localization of bridge structures. *J. Civ. Struct. Health Monit.* **2024**, *14*, 449–463. [CrossRef]
26. Zhou, Y.; Zhang, L.; Hu, J.; Hao, G. Measurement of Bridge lnfluence Lines Based on Machine Vision and lnterval Affine Algorithm. *China J. Highw. Transp.* **2024**, *37*, 142–151.
27. Wang, Y.; Jing, G.G.; Wang, B. Online Structural Analysis and State Evaluation Method for Bridge Health Monitoring System. *Bridge Constr.* **2014**, *44*, 25–30.
28. Zheng, X.; Yi, T.H.; Yang, D.H.; Li, H.N. Stiffness Estimation of Girder Bridges Using Influence Lines Identified from Vehicle-Induced Structural Responses. *J. Eng. Mech.* **2021**, *147*, 04021012. [CrossRef]
29. Zhao, H.; Wei, B.; Jiang, L.; Xiang, P.; Zhang, X.; Ma, H.; Xu, S.; Wang, L.; Wu, H.; Xie, X. A velocity-related running safety assessment index in seismic design for railway bridge. *Mech. Syst. Signal Process.* **2023**, *198*, 110305. [CrossRef]
30. Dong, C.-Z.; Bas, S.; Necati Catbas, F. A completely non-contact recognition system for bridge unit influence line using portable cameras and computer vision. *Smart Struct. Syst.* **2019**, *24*, 617–630.
31. Dong, C.Z.; Celik, O.; Catbas, F.N.; O'Brien, E.J.; Taylor, S. Structural displacement monitoring using deep learning-based full field optical flow methods. *Struct. Infrastruct. Eng.* **2020**, *16*, 51–71. [CrossRef]
32. Hu, J.; Zheng, Q.-G.; Zhang, W.-M. Study of Combined Effects of Wind and Thermal Loads on Changtai Changjiang River Bridge. *Bridge Constr.* **2020**, *50*, 42–47.
33. Abid, S.R. Three-dimensional finite element temperature gradient analysis in concrete bridge girders subjected to environmental thermal loads. *Cogent Eng.* **2018**, *5*, 1447223. [CrossRef]
34. Huang, H.-B.; Yi, T.-H.; Li, H.-N.; Liu, H. Strain-Based Performance Warning Method for Bridge Main Girders under Variable Operating Conditions. *J. Bridge Eng.* **2020**, *25*, 04020013. [CrossRef]
35. Saccenti, E.; Hendriks, M.H.W.B.; Smilde, A.K. Corruption of the Pearson correlation coefficient by measurement error and its estimation, bias, and correction under different error models. *Sci. Rep.* **2020**, *10*, 438. [CrossRef] [PubMed]

Disclaimer/Publisher's Note: The statements, opinions and data contained in all publications are solely those of the individual author(s) and contributor(s) and not of MDPI and/or the editor(s). MDPI and/or the editor(s) disclaim responsibility for any injury to people or property resulting from any ideas, methods, instructions or products referred to in the content.

applied sciences

MDPI

Article

Intelligent Structural Health Monitoring and Noncontact Measurement Method of Small Reservoir Dams Using UAV Photogrammetry and Anomaly Detection

Sizeng Zhao [1], Fei Kang [2,*], Lina He [3], Junjie Li [1,2,*], Yiqing Si [4] and Yiping Xu [5]

[1] College of Water Conservancy and Hydropower Engineering, Hohai University, Nanjing 210098, China; zhaosizeng@hhu.edu.cn
[2] School of Hydraulic Engineering, Faculty of Infrastructure Engineering, Dalian University of Technology, Dalian 116024, China
[3] School of Earth Sciences and Engineering, Hohai University, Nanjing 211100, China; hlnyh@hhu.edu.cn
[4] Chongqing Surveying and Design Institute Co. Ltd. of Water Resources, Electric Power and Architecture, Chongqing 401120, China
[5] Chongqing Water Resources and Electric Engineering College, Chongqing 402160, China
* Correspondence: kangfei@dlut.edu.cn (F.K.); lijunjie@dlut.edu.cn (J.L.); Tel.: +86-0411-84708516 (F.K.); Fax: +86-0411-84708501 (J.L.)

Abstract: This study proposes a UAV-based remote measurement method for accurately locating pedestrians and other small targets within small reservoir dams. To address the imprecise coordinate information in reservoir areas after prolonged operations, a transformation method for converting UAV coordinates into the local coordinate system without relying on preset parameters is introduced, accomplished by integrating the Structure from Motion (SfM) algorithm to calculate the transformation parameters. An improved YOLOv8 network is introduced for the high-precision detection of small pedestrian targets, complemented by a laser rangefinder to facilitate accurate 3D locating of targets from varying postures and positions. Furthermore, the integration of a thermal infrared camera facilitates the detection and localization of potential seepage. The experimental validation and application across two real small reservoir dams confirm the accuracy and applicability of the proposed approach, demonstrating the efficiency of the proposed routine UAV surveillance strategy and proving its potential to establish electronic fences and enhance maintenance operations.

Keywords: computer vision; noncontact measurement; small reservoir dam; unmanned aerial vehicle; structural health monitoring; deep learning

1. Introduction

Reservoirs and dams are essential infrastructures for flood protection, water supply storage and distribution, energy generation, and other purposes. Small reservoir dams have consistently represented a substantial portion of hydraulic infrastructures given their construction cost advantages, applicability to certain locations, and convenient access due to proximity [1]. During long-term operation, the safety of the dam is often affected by several factors, such as structural aging and loading [2]. To monitor dam health and plan operational responses accurately, many researchers have conducted numerical simulations or model experiments for dam maintenance analysis [3,4]. However, these methods mainly focus on large hydraulic facilities, and, considering the cost constraints and efficiency, small reservoir dams have received limited attention [5]. Due to the lack of sufficient automated monitoring systems or inspection personnel, numerous small reservoir dams are often considered vulnerable structures in flood defense systems.

The safety of pedestrians in the reservoir dam area is a focal point for managers [6]. However, unlike conventional damage, pedestrians exhibit both spatiotemporal randomness and mobility. Furthermore, in contrast to large-scale hydraulic structures, small

reservoir dams often serve as thoroughfares, leading to frequent appearances or crossings by pedestrians. During routine inspections, it is essential to promptly detect and locate pedestrians, issuing timely warnings when they venture into areas outside the designated pathways. In the event of changes in water levels, the prompt determination of pedestrian presence in areas like river channels becomes imperative. Identifying areas with frequent pedestrian activity allows management to implement targeted measures. Although deploying an extensive array of cameras could accomplish these objectives, the associated construction and maintenance costs are impractical for small reservoir dams. Therefore, efficiently achieving accurate pedestrian detection and three-dimensional (3D) positioning is a crucial measure for ensuring the safety of individuals in reservoir areas. Seepage has a significant impact on the structural safety of small reservoirs, primarily those composed of earth–rock dams [7]. Due to the concealed and spatiotemporal randomness of seepage, the conventional methods struggle to identify it. Recently, several contact measurement methods have been adopted to explore the internal features, including ground-penetrating radar [8], electrical resistivity measurement [9], and other sensing techniques [10]. However, for small reservoir dams, the cost of detection is a significant consideration. More importantly, rapidly and accurately pinpointing the location of leaks in the dam is also challenging. Consequently, an efficient and cost-effective method is needed to address both seepage and pedestrian detection and localization in small reservoir dams.

Recently, computer vision has been recognized as an important method for structural health monitoring, and, with the development of both aerial and terrestrial vehicles to carry the requisite instruments and sensors, computer vision has been widely applied in the fields of damage detection and noncontact measurements [11–13]. Jiang used a single panoramic camera to measure full-field structural deformation and accurately calculate the displacement of specified nodes, proving the practicality of computer vision in noncontact measurements [14]. Xu proposed a visualization method for simulating the seismic dynamic responses of buildings based on aerial photography, and the resulting realistic visualization results provide a basis for decision making during sudden disasters [15].

To obtain images more flexibly and comprehensively, unmanned aerial vehicles (UAVs) are widely adopted and integrated with positioning systems to monitor structural health [16,17]. Narazaki applied a comprehensive inspection method to automatically recognize and localize critical structural components, and the results confirmed the significant potential of image processing methods for efficient post-earthquake structural inspection [18]. Xu proposed a 3D reconstruction method for bridge geometry measurements based on UAV images that improved the computational efficiency without reducing the accuracy [19]. For construction safety, Chen presented a homography-based method for measuring the vibration of a bridge model, and the effectiveness was validated against the fixed-camera-based method [20]. In addition to visible light, infrared thermography can also enable the detection of temperature fields. Zhou combined passive infrared thermography and deep learning to identify embankment leakages automatically; the results indicated the practicality and flexibility of UAVs for seepage detection [21]. Qin conducted research on urban evapotranspiration using UAVs, demonstrating the potential of UAVs for urban environmental planning applications [22]. Zhong also used UAVs to analyze urban temperatures at the microscale and proposed a method for analyzing the spatial variations in urban thermal environments [23]. These studies demonstrate the valuable utility of UAVs in facilitating high-precision noncontact measurements, and the introduction of 3D reconstruction methods enables damage localization and change detection [24–26].

A key challenge for UAV-photogrammetry-based structural health monitoring involves the accurate estimation of the relative pose and position between the image and the target, such as the registration from a 2D image to 3D coordinates [27–29]. Chen fine-tuned the rough pose estimated by photogrammetry and solved the challenging indoor localization problem [30]. Tan presented a simplified coordinate transformation method to transform damage positions in the real world to coordinates in a building information modeling (BIM) model, enabling an efficient method for detecting and locating struc-

tural damage in high buildings [31]. Ren proposed a method to reduce the systematic errors in the vertical axis direction of the 3D reconstruction results based on GPS data [32]. Coordinate transformation is a crucial technique for achieving target localization and measurements. Lasers are often incorporated into noncontact measurement methods and introduce another dimensional constraint [33–35]. Zhuge developed a method for precisely measuring bridge deflection with a laser combined with a UAV [36]. Xu combined laser scanning data to monitor the dimensional accuracy of prefabricated components and enhance the quality management efficiency [37]. In summary, compared with the traditional methods, UAVs equipped with different measurement and sensing devices can efficiently detect and accurately locate multiple types of targets in a noncontact manner. The flexibility and efficiency of UAVs integrated with sensors have been demonstrated in various applications, and they can provide rapid and automated structural assessment as well as route planning in advance [11].

Small reservoir dams possess distinct characteristics. Due to inadequate recognition of the emphasis and limited financial resources, they often lack automated monitoring systems, necessitating UAVs as a supplementary measure. However, the absence of control points and terrain deformation complicate the establishment of a correspondence between UAV positions and the coordinates of small reservoir dams. Consequently, this limitation obstructs the precise 3D localization of observed entities such as pedestrians, which is elaborated upon subsequently:

1. UAVs typically rely on the World Geodetic System-1984 (WGS-84) coordinate system, which uses longitude (*L*), latitude (*B*), and altitude (*H*). This coordinate system is not commonly utilized in dam construction. While conversion parameters are publicly available, within the scope of small reservoirs, the transformation precision may be insufficient for precise positioning.
2. Coordinate transformations typically require simultaneous measurements of the coordinates in both coordinate systems for multiple control points. However, the control points for small reservoir dams that have been in operation for many years may not have been adequately preserved, making it difficult to accurately determine their positions in the dam coordinate system.
3. Both the pedestrian and seepage locations in small reservoirs are highly random, requiring methods capable of accurately determining the 3D positions of targets from 2D images photographed in arbitrary positions and angles, as shown in Figure 1.

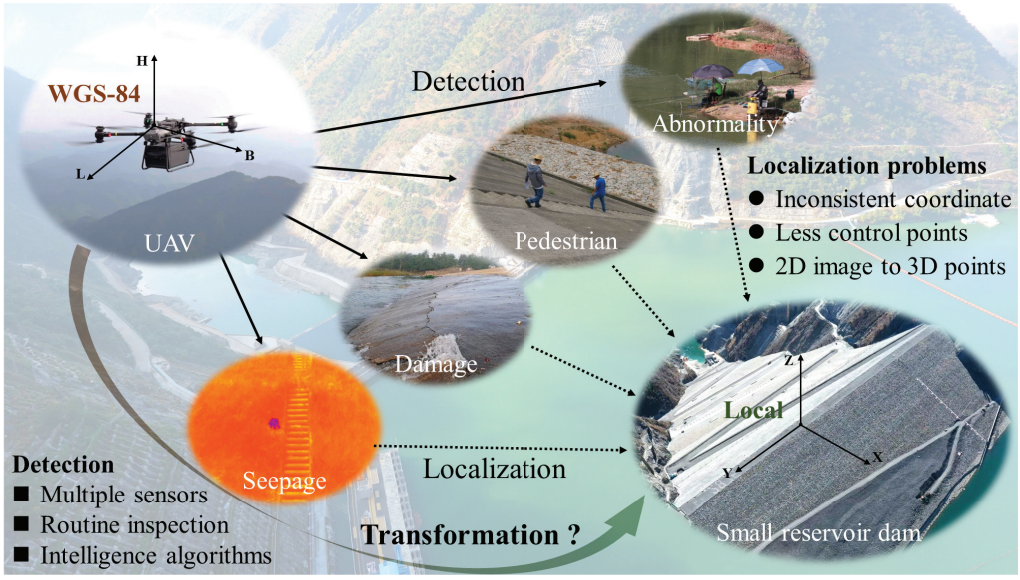


Figure 1. Target 3D localization challenges with UAV inspection.

Moreover, the accurate identification of pedestrians is crucial during UAV inspections, but the small pixel size of pedestrians can lead to poor accuracy using the conventional detection algorithms. Therefore, achieving rapid target localization in the dam coordinate system and accurate pedestrian detection need to be guaranteed during UAV inspection.

This study introduces an effective method for coordinate transformation and non-contact measurement to detect and localize pedestrian targets. UAV coordinates are decomposed into planar coordinates projected onto the Gauss–Krüger plane and altitude coordinates. By incorporating ground control points (GCPs) to establish a local coordinate system, a correspondence between the UAV coordinates and local dam coordinates is proposed using the Structure from Motion (SfM) algorithm. Subsequently, a combination of a four-parameter model and the altitude fitting method is introduced, establishing a rapid and accurate approach for coordinate transformation. Integrated with laser rangefinder measurements, this methodology enables the 3D localization of targets regardless of the photographing position and posture. To enhance pedestrian detection accuracy, an improved YOLOv8 network incorporating attention modules is introduced, bolstering the feature extraction capability for small targets. The precision of the proposed method is validated by applying it to two existing earth–rock dams. By comparing the 3D point cloud generated after the coordinate transformation with the laser scanning results, it accurately identified and positioned various seepage locations and pedestrians. The results of this study provide both the theoretical and technical frameworks required for the routine inspection of small reservoir dams using UAV photogrammetry.

The remainder of this paper is organized as follows. Section 2 describes the theory and method of coordinate transformation. Section 3 discusses the coordinate calculation method based on the SfM algorithm and the detection method for pedestrians and dam seepages. The experimental results and application case studies are analyzed in Section 4. Finally, the conclusions are presented in Section 5.

2. 3D Localization of UAV Targets in the Dam Local Coordinate System

The objective of UAV inspection is to identify and locate different objects, thereby determining the structural locations of these objects based on the coordinate system of the dam. Therefore, an efficient and convenient coordinate transformation and positioning method suitable for small reservoir dams must be developed.

2.1. Coordinate Transformation Methods

Since UAVs use WGS-84 coordinate system while local coordinate system or spatial Cartesian coordinate system is often employed during dam construction, coordinate transformation methods are required to convert between different coordinate systems [38,39]. As shown in Figure 2, WGS-84 coordinate system can be transformed into the spatial Cartesian coordinate system through the seven-parameter method expressed in Equation (1), which is generally employed when the conversion range is large. The UAV coordinate system can then be projected onto the dam planar coordinate system using the reference parameters, as shown in Figure 3a.

$$\mathbf{P}_j = (1 + m_1) \begin{bmatrix} 1 & -\kappa & -\varphi \\ \kappa & 1 & -\omega \\ \varphi & \omega & 1 \end{bmatrix} \mathbf{P}_i + \begin{bmatrix} \Delta X \\ \Delta Y \\ \Delta Z \end{bmatrix} \quad (1)$$

where $\mathbf{P}_i$ (X_i, Y_i, Z) and $\mathbf{P}_j$ (X_j, Y_j, Z_j) are the 3D coordinate points matched in the two coordinate systems; m_1 indicates a scale factor; (ω, φ, κ) and (ΔX, ΔY, ΔZ) represent three Euler angle rotation parameters and three translation parameters, respectively. It can be observed that a minimum of three high-precision control points with two sets of coordinates are required for computation when employing the seven-parameter method. Furthermore,

when calculating plane and altitude conversions separately, the four-parameter method can be adopted, as depicted in Figure 3b and described as

$$\mathbf{p}_j = (1 + m_2)\begin{bmatrix} \cos\theta & -\sin\theta \\ \sin\theta & \cos\theta \end{bmatrix}\mathbf{p}_i + \begin{bmatrix} \Delta x \\ \Delta y \end{bmatrix} \tag{2}$$

where $\mathbf{p}_i$ (x_i, y_i) and $\mathbf{p}_j$ (x_j, y_j) represent the planar coordinate points; m_2 also indicates a scale factor; θ denotes the rotation angle of the coordinate axis. Meanwhile, altitude h_j and h_i can be transformed based on the altitude anomaly Δh, as shown in Figure 3c and expressed as

$$h_j = h_i - \Delta h. \tag{3}$$

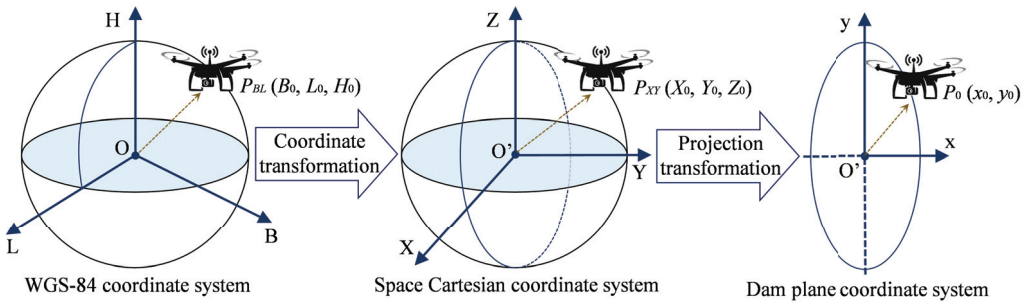


Figure 2. Conventional coordinate transformation process between UAV and dam coordinate systems.

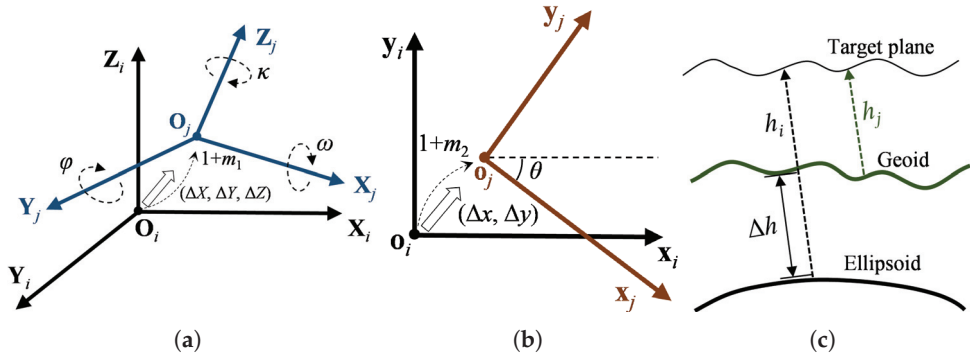


Figure 3. Geometric models for coordinate transformation in different dimensions. (**a**) Seven-parameter model. (**b**) Four-parameter model. (**c**) Altitude conversion.

The altitude anomaly Δh is a variable that varies from one geographic location to another due to the non-uniform nature of Earth's surface. Then, coordinate transformation can be achieved when there are a sufficient number of control points with precision coordinates in both coordinate systems.

However, despite the efficiency of the seven-parameter method in achieving coordinate transformation, it presents challenges when the center of the local coordinate system is established at the dam crest, which is significantly distant from the center of the reference ellipsoid. In such scenarios, the rotation (ω, φ, κ) and translation (ΔX, ΔY, ΔZ) parameters tend to become relatively large when using the seven-parameter method. This can lead to a singularity in the coefficient matrix when attempting to solve for these parameters using the least-squares method, resulting in suboptimal and biased solutions, along with substantial errors post-conversion [40]. Simultaneously, in the conventional altitude transformation method, there is a reliance on altitude anomaly Δh. However, as the planar position undergoes changes, the height difference between the reference ellipsoid and the geoid also varies. This renders the fixed altitude anomaly Δh inadequate for accurately representing altitude transformation in the reservoir area. Hence, it becomes imperative to explore

coordinate transformation methods and frameworks tailored to the distinctive environment of small reservoir dams.

2.2. SfM-Based UAV to Dam Coordinate Registration

While UAVs are equipped with positioning capabilities, the absence of a sufficient number of high-precision control points results in the lack of a reference for conventional coordinate transformation methods. The SfM algorithm can calculate the spatial relationship between a UAV and target points through multiple images in a noncontact manner, thereby generating a 3D point cloud or a real scene model [18,41]. The coordinates of a point P (X, Y, Z) in space can be calculated by multiple cameras using the principle of triangulation:

$$s_n \begin{bmatrix} u_n \\ v_n \\ 1 \end{bmatrix} = \mathbf{K}_{3\times4}[\mathbf{R}|\boldsymbol{t}]_{4\times4} \begin{bmatrix} X \\ Y \\ Z \\ 1 \end{bmatrix}_{84} \tag{4}$$

where $\boldsymbol{u}_n$ (u_n, v_n) is the projection of point P in image n; $\mathbf{K}$ and $[\mathbf{R} \mid \mathbf{t}]$ are the intrinsic matrix and extrinsic matrix, respectively; and s_n is a scale factor. To calculate the relationship between images, the pixel points $\boldsymbol{u}_n$ should be constrained by the fundamental matrix $\mathbf{F}$ with ${\boldsymbol{u}_n}^T\ \mathbf{F}\ \boldsymbol{u}_{n-1} = 0$ according to the epipolar constraint, and further decomposed into ${\boldsymbol{u}_n}^T\ \mathbf{K}^{-T}\ \mathbf{E}\ \mathbf{K}^{-1}\ \boldsymbol{u}_{n-1} = 0$ to resolve the essential matrix $\mathbf{E}$ when $\mathbf{K}$ is known. Finally, bundle adjustment is employed to optimize the camera parameters and positions by minimizing the reprojection error [42]:

$$g(C, X) = \sum_{n=1}^{all} \sum_{m=1}^{all} \omega_{nm} \|\boldsymbol{u}_{nm} - \mathbf{project}(\mathbf{C}_n, P_m)\|^2 \tag{5}$$

where $||\boldsymbol{u}_{nm}$-$\mathbf{project}(\mathbf{C}_n, P_m)||$ represents the difference between the pixel point m from image n and the projection position of space point P, $\mathbf{C}_n$ includes several parameters; $\omega_{nm} = 1$ indicates the point is observed. With a sufficient number of images captured by a UAV, the 3D coordinates of the target point can be calculated.

However, the 3D points generated by the SfM algorithm have no corresponding spatial relationship with respect to the location of the small reservoir dam, and the lack of a sufficient number of high-precision control points hinders the application of traditional coordinate transformation methods [33], as shown in Figure 4a. This paper introduces the ground control points (GCPs) associated with dam local coordinate system to establish the foundation for transformation. GCPs are usually measured by a total station or other equipment to obtain the 3D coordinates in a specific coordinate system. Corresponding to each UAV image capturing a GCP with location (X_{UAV}, Y_{UAV}, Z_{UAV}), the projection point (u, v) and GCP position (X_{GCP}, Y_{GCP}, Z_{GCP}) are on a single line and expressed as

$$\begin{cases} u - u_0 + k_u = -f\dfrac{a_1(X_{GCP} - X_{UAV}) + b_1(Y_{GCP} - Y_{UAV}) + c_1(Z_{GCP} - Z_{UAV})}{a_2(X_{GCP} - X_{UAV}) + b_2(Y_{GCP} - Y_{UAV}) + c_2(Z_{GCP} - Z_{UAV})} = -f\dfrac{\overline{X}}{\overline{Z}} \\ v - v_0 + k_v = -f\dfrac{a_3(X_{GCP} - X_{UAV}) + b_3(Y_{GCP} - Y_{UAV}) + c_3(Z_{GCP} - Z_{UAV})}{a_2(X_{GCP} - X_{UAV}) + b_2(Y_{GCP} - Y_{UAV}) + c_2(Z_{GCP} - Z_{UAV})} = -f\dfrac{\overline{Y}}{\overline{Z}} \end{cases} \tag{6}$$

where (u_0, v_0) is the center point of image; (k_u, k_v) denotes the correction values for system errors such as distortion; f represents focal length; and $\mathbf{R} = \begin{bmatrix} a_1 & a_2 & a_3 \\ b_1 & b_2 & b_3 \\ c_1 & c_2 & c_3 \end{bmatrix}$ is the direction cosine for the three external orientation angles (ω, φ, κ). Meanwhile, given the offset between the camera photographic center and the GPS position, there exists a displacement described as $\Delta\boldsymbol{t} = [\Delta X, \Delta Y, \Delta Z]^T$, as shown in Figure 4b. When using UAVs to capture

several GCPs, the internal and external parameters can be calculated based on the SfM algorithm, and Equation (6) simplifies to

$$\begin{cases} u = (u_0 - f\dfrac{\overline{X}}{\overline{\overline{Z}}} - k_u) + D_X \\ v = (v_0 - f\dfrac{\overline{Y}}{\overline{\overline{Z}}} - k_v) + D_Y \end{cases} \tag{7}$$

where D_X and D_Y are the correction factors for the true values during iterative process. Therefore, the first-order term resulting from the Taylor series expansion of Equation (7) is expressed as

$$\begin{bmatrix} u \\ v \end{bmatrix} = \begin{bmatrix} \dfrac{\partial u}{\partial X_{UAV}} & \dfrac{\partial u}{\partial Y_{UAV}} & \dfrac{\partial u}{\partial Z_{UAV}} & \dfrac{\partial u}{\partial \omega} & \dfrac{\partial u}{\partial \varphi} & \dfrac{\partial u}{\partial \kappa} \\ \dfrac{\partial v}{\partial X_{UAV}} & \dfrac{\partial v}{\partial Y_{UAV}} & \dfrac{\partial v}{\partial Z_{UAV}} & \dfrac{\partial v}{\partial \omega} & \dfrac{\partial v}{\partial \varphi} & \dfrac{\partial v}{\partial \kappa} \end{bmatrix} \begin{bmatrix} \Delta X \\ \Delta Y \\ \Delta Z \\ \Delta \omega \\ \Delta \varphi \\ \Delta \kappa \end{bmatrix} - \begin{bmatrix} u_0 - f\dfrac{\overline{X}}{\overline{\overline{Z}}} - k_u \\ v_0 - f\dfrac{\overline{Y}}{\overline{\overline{Z}}} - k_v \end{bmatrix}. \tag{8}$$

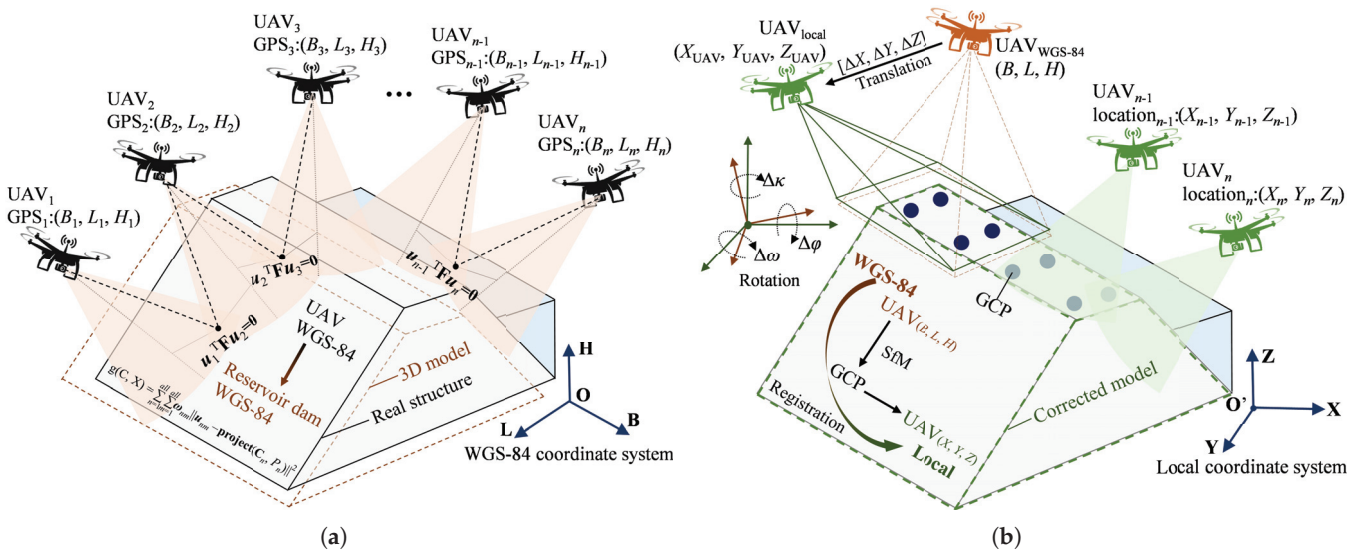


Figure 4. The registration process between UAV and dam coordinates based on the SfM algorithm. (**a**) UAV image-based SfM processes without GCPs. (**b**) UAV coordinates transformed to local coordinate system.

For a massive collection of UAV images, the average of the correction factors can serve as a representative value for the discrepancy between the computed external orientation elements using GCPs and the UAV GPS data. Thus, multiple sets of coordinates (B, L, H) from the UAV internal positioning system can be matched with their corresponding coordinates (X, Y, Z) within the local coordinate system of the small reservoir dam, which provides precise and low-cost spatial referencing.

The correspondence between UAV coordinates and small reservoir dam coordinates can be established by deploying GCPs and utilizing SfM algorithms. Two transformation modes can be considered, including GCP-coordinate-based transformation and UAV-coordinate-based transformation. The GCP-coordinate-based transformation is based on the coordinates of GCPs in both systems. However, GCPs are typically placed at the dam crest, leading to minimal vertical changes, and the GCP-coordinate-based approach might become trapped in a local optimum for vertical transformations, which could result in an increase in overall errors, as shown in Figure 5. Consequently, for a comprehensive coordinate transformation, this paper adopts the UAV-coordinate-based method, which involves

the transformation of the UAV coordinate system at various altitudes and positions into the local coordinate system.

After applying the SfM algorithm, corrections were made to the UAV parameters, and multiple control points with coordinates in two coordinate systems were established. This process laid the foundation for proposing the coordinate transformation method in the subsequent steps.

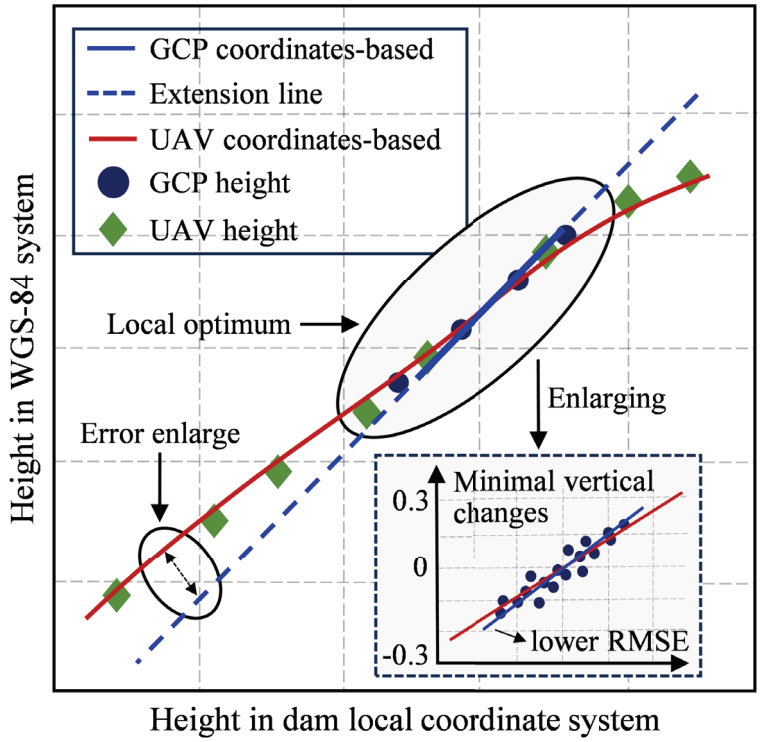


Figure 5. Altitude conversion methods and corresponding error trends.

2.3. Proposed UAV Inspection and Localization Framework

In the distinctive environment of small reservoir dams, precise locating of targets on the surface is paramount based on UAV coordinates and collected data. This section introduces a framework for high-precision noncontact measurement of targets, combining established coordinate transformation formulas with the previously identified challenges.

2.3.1. Projection from WGS-84 to Plan Coordinate

B and L represent spatial positions on the surface of a three-degree sphere and are measured in degrees, in contrast to the typical linear units commonly employed in the local coordinate system. The process of projection onto a plane is introduced to determine the relationship between the UAV system and the local reference [39]. The Gauss–Kruger projection method is widely adopted in topographic surveys given its minimal distortion in terms of length and area. Hence, this study employs the Gauss–Kruger method to project (B_0, L_0) of the UAV into a planar Cartesian coordinate system (x_{proj}, y_{proj}) before transformation:

$$\begin{bmatrix} x_{proj} \\ y_{proj} \end{bmatrix} = f_{proj}(N, e) \begin{bmatrix} B_0 \\ L_0 \end{bmatrix} \tag{9}$$

where N is the radius of the Meridian circle and e is the first eccentricity of the reference ellipsoid. The process is shown in Figure 6b. By using the projection method, the 3D coordinates can be separated into both plane and elevation components. This alignment corresponds to the GCP coordinates measured using a total station on the small reservoir dam.

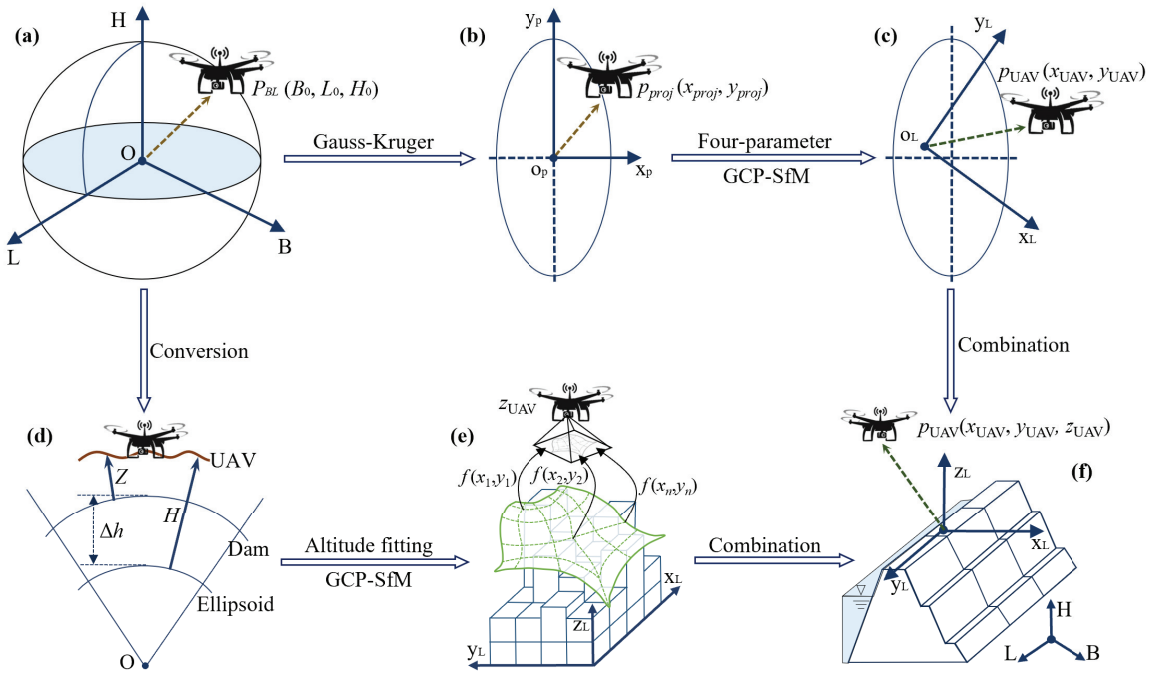


Figure 6. The process of transforming UAV WGS-84 coordinates to dam local coordinates. (**a**) WGS-84 coordinate system. (**b**) Projection to plane. (**c**) Convert to local. (**d**) Altitude transformation. (**e**) Altitude adjustment. (**f**) UAV transformation coordinates.

2.3.2. Transforming UAV Coordinate to Dam Coordinate

After projection conversion, coordinate registration can be achieved by including the UAV altitude information, as described in Section 2.2. Considering image distortion and other influences, based on the four-parameter model in Equation (3), the scale factor m_2 is revised by applying m_x and m_y separately in different directions [31], and the transformation parameters are calculated based on coordinates in both coordinate systems, as shown in Figure 6c:

$$\begin{bmatrix} x_{UAV} \\ y_{UAV} \end{bmatrix} = \begin{bmatrix} 1+m_x & 0 \\ 0 & 1+m_y \end{bmatrix} \begin{bmatrix} \cos\theta & -\sin\theta \\ \sin\theta & \cos\theta \end{bmatrix} \begin{bmatrix} x_{proj} \\ y_{proj} \end{bmatrix} + \begin{bmatrix} \Delta x \\ \Delta y \end{bmatrix}. \quad (10)$$

The altitude anomaly mainly consists of two parts: the elevation difference between the geoid height used by the UAV and the normal height and the height difference between the reference surface of the dam local coordinate system and the normal height reference surface. However, considering the influence of the gravity field, the altitude difference between the reference ellipsoid and the geoid varies with the topography, which can have a minor impact on the altitude conversion. Additionally, since GCPs have relatively small changes in the vertical direction, some parameters are required to correct the converted altitudes. Therefore, as shown in Figure 6e, for small reservoir dams, the altitude fitting method is introduced to perform polynomial fitting for the altitude anomaly Δh [43,44], and Equation (3) can be expanded as

$$z_{UAV}(H,x,y) = H + \alpha_0 + \alpha_1 x + \alpha_2 y + \alpha_3 xy + \alpha_4 x^2 + \alpha_5 y^2 \quad (11)$$

where $\alpha_0 \sim \alpha_5$ are the conversion fitting coefficients from WGS-84 altitude H to local altitude Z_{UAV} in the small reservoir dam area. Finally, through the modified four-parameter method and the altitude fitting method, the transformation from UAV WGS-84 to dam local coordinate system can be achieved as shown in Figure 6f. The developed method establishes the correspondence between the UAV and the dam structural position in space, enabling target localization.

2.3.3. Target 3D Localization

After obtaining the coordinates of the UAV in the dam local coordinate system, the position of specific targets within the small reservoir dam can be determined. However, during routine inspections, it is difficult for UAVs to maintain a strictly vertical orientation relative to the target plane, and a spatial angle between UAV and the target is introduced. Furthermore, the target 3D spatial position cannot be solely determined based on 2D projection coordinates (u, v) [27,45,46]. To address this complexity, the use of a laser rangefinder is introduced in this study, adding an additional constraint that establishes the connection between the UAV optical center and a pixel point on the image. The position of target point $(x_{tar}, y_{tar}, z_{tar})$ can be calculated as

$$\begin{bmatrix} x_{tar} \\ y_{tar} \\ z_{tar} \end{bmatrix} = \begin{bmatrix} x_{UAV} \\ y_{UAV} \\ z_{UAV} \end{bmatrix} + d \begin{bmatrix} -\sin\beta\cos\gamma \\ \cos\beta\cos\gamma \\ -\sin\gamma \end{bmatrix} \tag{12}$$

where d refers to the measurement distance of the laser rangefinder; β and γ are the capturing angles, as shown in Figure 7. Meanwhile, as UAV inspections often involve vertical photography, a single capture combined with distance measurements can determine the 3D positions of any pixel point (u_i, v_i) within the dam coordinate system. This approach is particularly advantageous for flat areas such as the dam crest, and the pixel point position can be expressed as

$$\begin{bmatrix} x_{tar-i} \\ y_{tar-i} \end{bmatrix} = \frac{d\lambda}{f} \begin{bmatrix} (u_i - u_0) \times \sin\psi \\ (v_i - v_0) \times \cos\psi \end{bmatrix} + \begin{bmatrix} x_{tar} \\ y_{tar} \end{bmatrix} \tag{13}$$

where λ is the unit pixel length; (u_0, v_0) is the position of pixel center; ψ is the angle between the u-axis of the image and the x-axis of the dam coordinate system. Finally, the position of the target point within the dam coordinate system can be rapidly measured using the UAV integrated with a rangefinder.

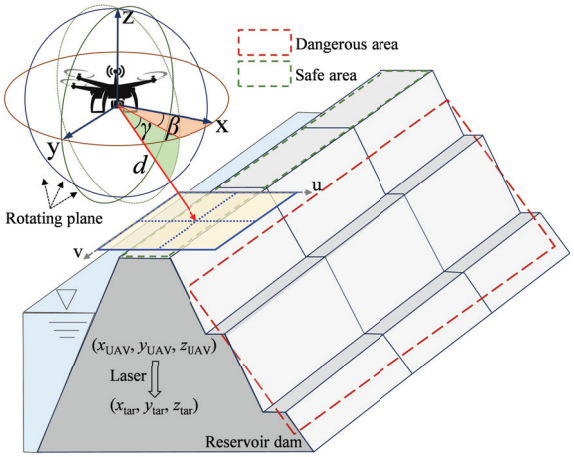


Figure 7. Target 3D localization using a UAV integrated with a laser rangefinder.

Overall, when the calculation of conversion parameters is inaccurate, the proposal is to use a combination of plane and altitude transformations to improve accuracy. For altitude transformations, altitude fitting method can be effective in addressing inaccuracies. A method for target localization based on ranging results during noncontact measurements is established. The approach proposed in this section enables accurate positioning of target points through UAV photogrammetry.

3. Small Pedestrian Target Intelligent Detection Algorithm

To achieve UAV automatic inspection and 3D localization, in addition to the proposed noncontact measurement method, it is also necessary to implement fast and intelligent pedestrian identification algorithms. However, unlike conventional targets, pedestrians captured by UAV cameras usually occupy a small portion of the pixel and lack facial features, and the relevant datasets are smaller, making target detection very challenging for conventional methods. Therefore, it is necessary to develop pedestrian detection methods tailor-made for UAV inspections of small reservoir dams.

3.1. YOLOv8 Detection Algorithm Basic Architecture

The YOLO network is one of the most widely adopted object detection algorithms for UAV image detection, and it is suitable for deployment on UAV platforms to achieve real-time detection [47,48]. YOLOv8, like YOLOv5, was developed and continues to be updated by Ultralytics and provides about notable enhancements in detection speed and accuracy [49]. The input image with size of (w, h, c) is down-sampled five times in the backbone, resulting in dimensions of ($w/32$, $h/32$, c_{set}). These features are then transferred to the neck structure, which is primarily employed for feature fusion and up-sampling. This facilitates the amalgamation of features from different scales, leading to a more comprehensive understanding of the target. The detection part is the head structure, which can classify the target, predict the bounding box, generate three scale detection results, and finally describe the position of the target in image.

YOLOv8 is composed of a similar network architecture to YOLOv5, making it possible to directly compare their performance when using similar parameters. This also enables an effective evaluation of how newly added modules enhance the network's capabilities. Furthermore, compared with YOLOv5, several improvements are adopted in YOLOv8. A C2f module is used to replace the C3 module to obtain more abundant gradient flow information while maintaining a lightweight architecture. At the end of backbone, the spatial pyramid pooling fast (SPPF) module is retained from original YOLOv5 to ensure running speed during the fusion of global and local features. The feature pyramid network (FPN) and path aggregation network (PAN) are also introduced in the neck, but one convolution operation is removed to achieve a lightweight model. The head is designed as a decoupled structure, which separates the prediction of target classification and bounding box regression into different branches. The advantage of this structure lies in simplifying the training and optimization process of the network, enhancing the model trainability and inference efficiency. In the context of object detection, the model directly learns to predict object locations and scales without relying on predefined anchors. With these improvements, YOLOv8 achieves higher detection speed and accuracy, making it more suitable for real-time detection in UAV routine inspections [50].

3.2. Proposed Pedestrian Detection Network

To enhance the detection of small pedestrians lacking distinct facial features, some improvements should be implemented in the YOLOv8 model. In this study, the ConvNeXt v2 [51,52] module and ODConv (Omni-Dimensional Dynamic Convolution) [53] module are introduced to enhance feature extraction capabilities. The network architecture is modified to incorporate a tiny detection head, and the Wise-IoU loss function is added to comprehensively improve the network ability in detecting small pedestrians. The specific details are described as follows.

3.2.1. Additional Modules

The ConvNeXt module is a pure convolutional neural network that performs better in terms of accuracy than a transformer and is widely adopted by various detection tasks [54]. ConvNeXt v2 is proposed by adding a global response normalization (GRN) step to increase the feature contrast between channels and enhance performance. Effective detection of small targets typically requires a model with a good receptive field and strong

representation capabilities for small-sized objects. The improvements in ConvNeXt v2 primarily focus on the depth structure of the network, which may contribute to improving the receptive field and enhancing the detection capabilities for small targets. Based on ConvNeXt, a global response normalization (GRN) step was added to ConvNeXt v2, which can increase the feature contrast between channels and enhance performance. The architecture of ConvNeXt v2 is shown in Figure 8. In contrast to conventional bottleneck structures, a 7×7 depthwise convolution is adopted in the first step, followed by layer normalization. Then, features are passed into convolutional layers and a GRN block applied on each patch. The module ultimately concludes with the convolutional layer and drop path. ConvNeXt can maintain the efficiency of convolution without complex modules, and the weights of small objects are increased to make the network focus more on training.

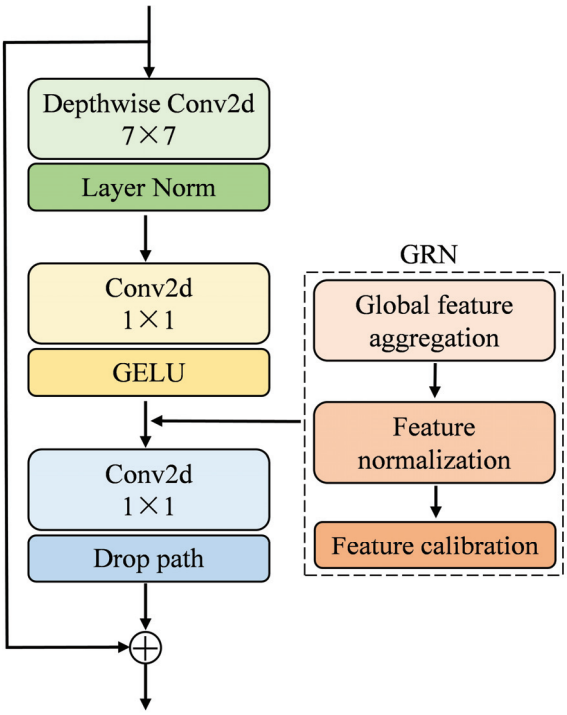


Figure 8. The ConvNeXt v2 module architecture.

This study also modifies the convolutional part of YOLOv8. Considering the characteristics of low resolution and limited information content, small targets are susceptible to being overlooked or falsely detected during the detection process, thus requiring the digging of deeper image features. ODConv adopts a parallel strategy and multi-dimensional attention mechanism of the convolutional kernel space, which provides an advantage when dealing with low-resolution images that contain limited information, thus obtaining full-dimensional convolutional kernel attention, as shown in Figure 9. This allows the network to better understand target features and improve detection accuracy for small targets. Specifically, in addition to the conventional assignment of dynamic attributes to convolution through the number of kernels (α_{wi}), attention is also introduced in the spatial dimension (α_{si}), input channel dimension (α_{ci}), and output channel dimension (α_{fi}), which can be expressed as follows:

$$f_{out} = f_{in} \sum \left(\alpha_{wi} \bullet \alpha_{fi} \bullet \alpha_{ci} \bullet \alpha_{si} \bullet W_i \right) \tag{14}$$

where W_i is the convolutional kernel i; f_{in} and f_{out} denote the input and output features, respectively. The four types of attentions are complementary to each other, providing rich contextual clues and significantly enhancing the feature extraction capability of con-

volutional operations; therefore, it is introduced into the detection network for small pedestrian targets.

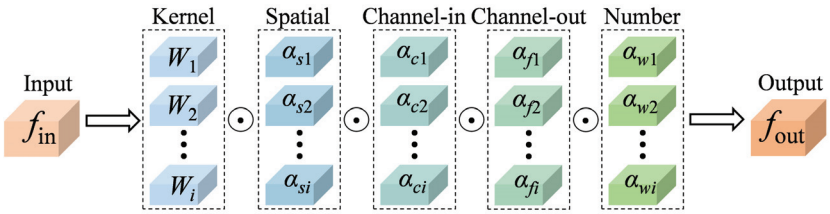


Figure 9. Schematic representation of the ODConv architecture.

3.2.2. Architecture of the Proposed Network

Although the YOLOv8 network performs well on most datasets, specific modifications are needed to further improve detection accuracy, particularly when dealing with small objects that occupy a low number of pixels in images captured by UAVs. The most widely adopted and effective method is the addition of another detection head specifically for tiny objects, preventing their features from being overwhelmed by continuous convolution operations [55–57]. Meanwhile, given the imperative to preserve the real-time detection performance of the network, this study refrained from adding too many complex modules to every layer in the backbone and neck.

The architecture of the proposed network is shown in Figure 10. In the shallow layers of the backbone, the conventional convolution and C2f modules are replaced by ODConv and ConvNeXt to enhance the detection of small targets in large images. In the neck structure, layers 15, 18, and 21 are replaced with ConvNeXt to improve the fusion of shallow and deep features, making the small head and the newly added tiny head more sensitive to small targets. The proposed network is primarily designed for small targets in UAV images, and it enhances the ability to extract features from shallow layers without significantly increasing the number of parameters, making it more suitable for real-time detection in UAV inspections.

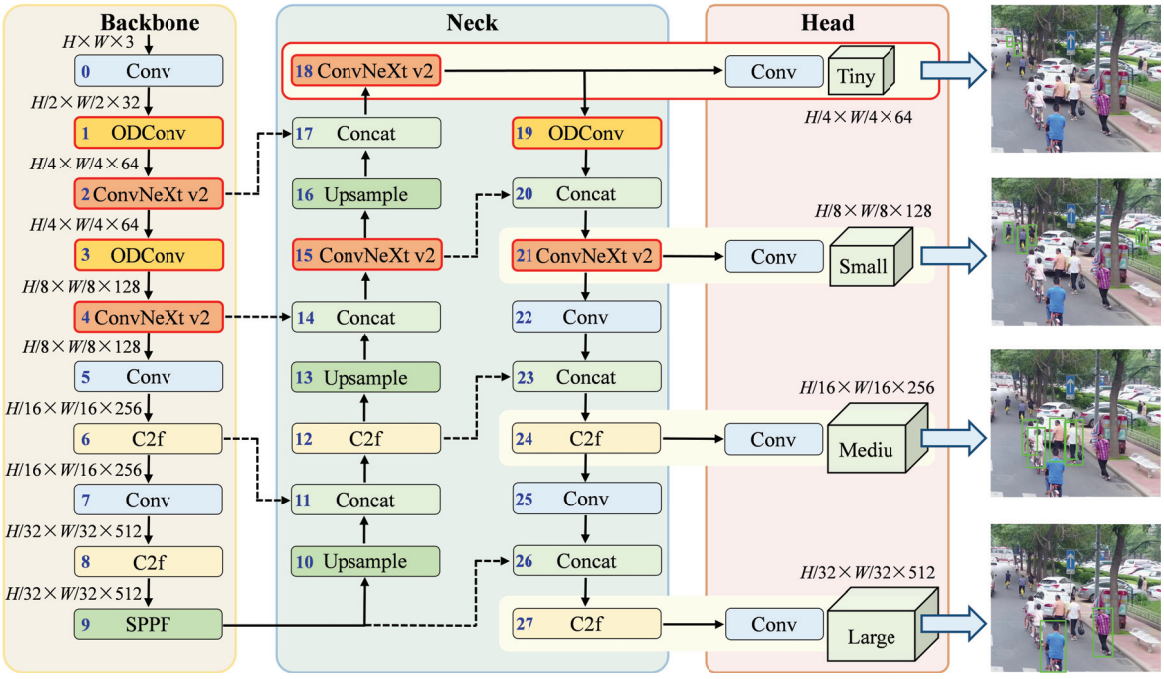


Figure 10. Architecture of the proposed small pedestrian detection network with a tiny head. The main modified part is enclosed in the red box. Modules 0 to 9 are the backbone of the network, while modules 10 to 27 are the Neck structure of the network.

3.2.3. Loss Function

The loss function is a crucial component in the training process of deep learning models. The loss function reduces gradients so that the model parameters can be upgraded. An appropriate loss function can significantly enhance the detection accuracy of a network. YOLOv8 adopts CIoU (Complete Intersection over Union) to calculate the regression loss of bounding boxes. However, for pedestrian targets captured in UAV images, where the pixel proportion is relatively small, CIoU does not consider the balance between hard and easy samples, leading to the inability to learn some useful information [58].

To address this issue, a modified loss function called WIoU (Wise Intersection over Union) is introduced [59]. WIoU v3 incorporates a dynamic non-monotonic mechanism and includes a well-designed gradient gain allocation strategy. This strategy reduces the occurrence of large gradients or harmful gradients in extreme samples. The loss method focuses more on samples of moderate quality, thereby improving the network model generalization ability and overall performance, expressed as

$$L_{\mathrm{WIoUv3}} = \frac{\beta_{\mathrm{v3}}}{\delta_{\mathrm{v3}}\alpha_{\mathrm{v3}}^{\beta_{\mathrm{v3}}-\delta_{\mathrm{v3}}}} \exp\left(\frac{(x-x_{gt})^2+(y-y_{gt})^2}{(W_g^2+H_g^2)}\right)(1-IoU) \tag{15}$$

where α_{v3}, β_{v3}, δ_{v3} are the parameters indicating the quality and dynamically optimizing the anchor boxes; (W_g, H_g) is the smallest size of the bounding box; and (x, y) and (x_{gt}, y_{gt}) are the center of the predicted box and truth box, respectively. The addition of WIoU v3 into the network training process allows the network to focus more on recognizing and challenging small targets, and dynamically optimizes the loss weights, thereby improving the detection performance.

3.3. Evaluation Metrics

To evaluate the performance of the developed network, the mean average precision (*mAP*) is calculated and represents the average precision when the *IoU* threshold is 50%. Moreover, some indexes including *Precision*, *Recall*, and *F*1 are introduced and expressed as

$$Precision = \frac{TP}{TP+FP} \tag{16}$$

$$Recall = \frac{TP}{TP+FN} \tag{17}$$

$$F1 = \frac{2Precision \times Recall}{Precision + Recall} \tag{18}$$

where *TP* refers to the true positives that have been correctly predicted; *FP* represents the true negative sample; *FN* indicates the number of incorrect predictions.

3.4. Coordinate Transformation and Target Localization Procedure

First, GCPs are established and measured at the dam crest, and then images are captured by the UAV camera. The SfM algorithm is subsequently applied to create a correspondence between the UAV planar projected coordinates and altitudes within the local dam coordinate system. The developed method is then introduced to calculate the parameters for the plane and altitude transformation. Finally, small pedestrians are detected by the improved YOLOv8 algorithm and located, with the laser rangefinder ascertaining their presence within potentially hazardous areas. The entire procedure effectively translates 2D pixels into 3D coordinates through coordinate transformation, target detection, and localization. The main steps are processed on Windows workstation; details are as follows and summarized in Figure 11:

Step 1: Data acquisition. Gathering GCP coordinates through instruments and capturing small reservoir dam images using UAV photography.

Step 2: Coordinate registration. Employing the SfM algorithm to align the Gauss–Kruger planar projected coordinates and altitudes with dam local positions.

Step 3: Coordinate transformation. Calculating the transformation parameters of the four-parameter model and applying the altitude fitting formula using the developed method.

Step 4: Pedestrian detection. Utilizing the improved YOLOv8 algorithm to detect pedestrians in UAV inspection images.

Step 5: Target localization. Locating pedestrians within the dam coordinate system by combining captured angles and distances using a laser rangefinder.

Step 6: Position analysis. Determining if pedestrians are within hazardous areas based on their position in the local coordinate system of the small reservoir dam.

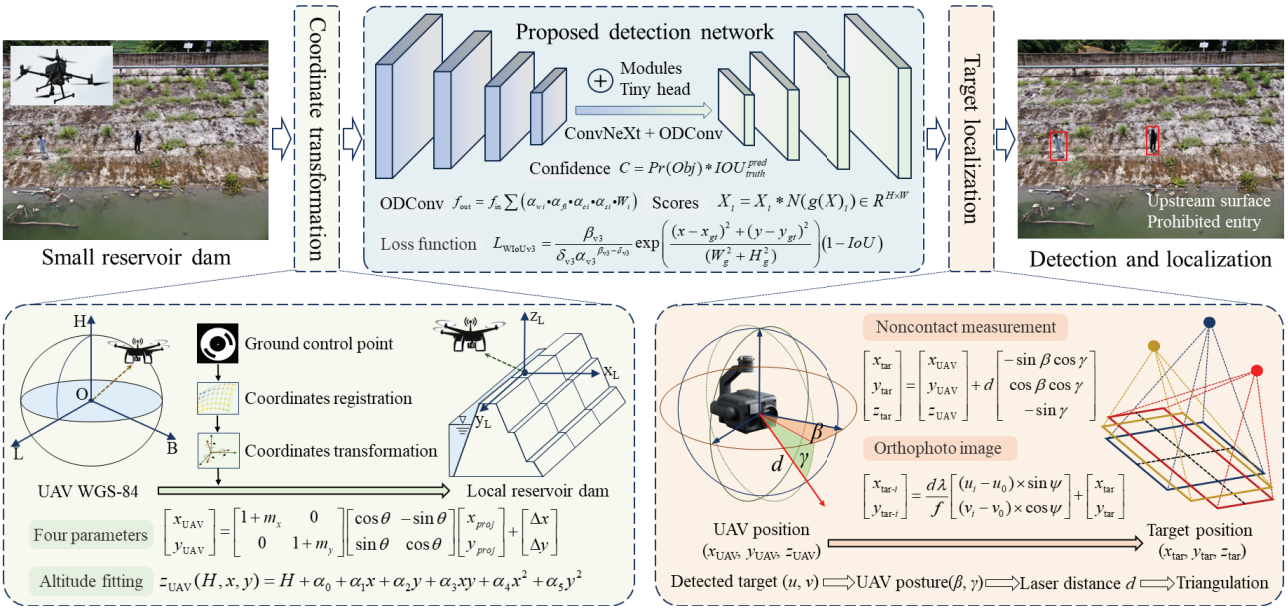


Figure 11. UAV coordinate transformation and detected target 3D localization in a small reservoir dam.

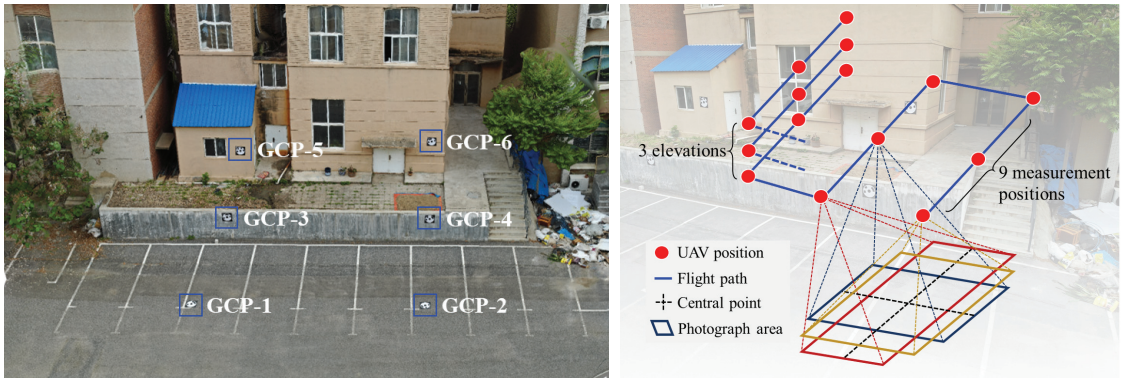
4. Experimental Performance Analysis and Practical Implementation

4.1. Accuracy Analysis of UAV Coordinate Transformation

To analyze and evaluate the impact of the developed coordinate transformation method on the 3D localization accuracy of targets, random point coordinate measurements and analyses were conducted. The images were captured using a DJI M300 RTK UAV, and the SfM algorithm was applied using Agisoft Metashape version 2.0.1 [60]. A workstation running on Windows with an Intel i7-13700F CPU was used, which can integrate its computational power with pre-defined spatial coordinates of the inspection area and produce inspection results directly.

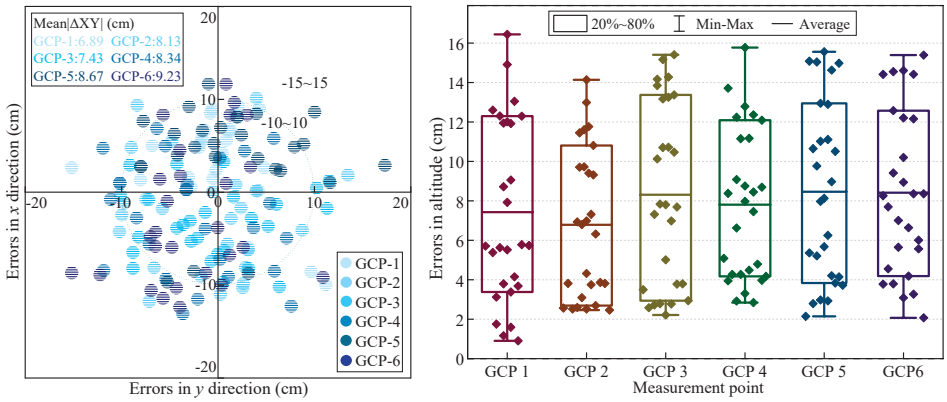
As shown in Figure 12a, six GCPs are placed in the measurement area and their 3D coordinates in the local coordinate system are measured using a total station. A total of 53 images were captured, and, after using the common Gauss–Kruger projection parameters in the transformation library (PROJ), the planar coordinates and altitudes were registered using the SfM algorithm. The parameters described in Section 2.3 could then be calculated. Subsequently, utilizing the transformation parameters and laser rangefinder measurement values, the UAV was used to capture and measure the 3D coordinates of GCPs at various locations. Each GCP was measured nine times from different directions at the same elevation, and these measurements were conducted at three distinct elevations, as shown in Figure 12b. To obtain the most accurate results, professional operators precisely aligned the center of the image with the center of the control point during each measurement. Although this process is time-consuming, it ensures more accurate outcomes. The error

of each measured GCP is shown in Figure 13; the overall in-plane error is generally less than 20 cm, with most values not exceeding 10 cm, and the error remains consistent across the different measurement positions, as in Figure 13a. For altitude, the errors fluctuate greatly, but the average values are less than 10 cm, as in Figure 13b. Some measurement results exhibit larger errors, attributed to significant angles or longer distances during capture, as well as inaccuracies in laser rangefinding. The measurement results in different directions are shown in Table 1, where the errors in the planar directions, x and y, are about 5 cm, while the average error in the altitude direction z is 7.868 cm. This is mainly influenced by the accuracy of the SfM algorithm in calculating the feature points in the altitude direction and the accuracy of the UAV self-positioning. It can be seen that the proposed method can accurately measure the 3D coordinates of the target point in the local coordinate system in a noncontact manner. However, it should be noted that the experiment only used six GCPs in a small area and did not fully exploit the advantages of the altitude fitting method. In a larger-scale measurement process where more GCPs are introduced, the developed method would produce better results.



(**a**) (**b**)

Figure 12. Evaluation scenario and measurement process of the developed method. (**a**) 3D model of experimental area with 6 GCPs. (**b**) Target measurements in 27 various positions.



(**a**) (**b**)

Figure 13. GCP errors measured from each position. (**a**) Errors in planar measurement. (**b**) Errors in altitude measurement.

Table 1. The measurement errors of the 6 GCPs in each direction (cm).

Point	Mean ΔX	Mean ΔY	Mean ΔZ	Mean ΔXYZ
GCP 1	3.343	5.140	7.425	10.829
GCP 2	5.080	5.128	6.789	11.403
GCP 3	5.010	4.217	8.312	11.767

Table 1. *Cont.*

Point	Mean ΔX	Mean ΔY	Mean ΔZ	Mean ΔXYZ
GCP 4	5.473	5.075	7.807	11.999
GCP 5	5.017	5.943	8.464	12.709
GCP 6	4.679	6.912	8.414	12.999
Total	4.767	5.402	7.868	11.951

4.2. Small Pedestrian Detection Results Based on the Developed Improved YOLOv8

To accurately detect small pedestrian targets on the dam, the developed network was trained and compared with the other networks. A total of 22,400 annotated images were included in the dataset, which were derived from several public datasets, such as WiderPerson [61], VisDrone [62], and COCO [63], and cropped to the appropriate size. The dataset was divided into training, validation, and testing with a ratio of 7:2:1, resulting in 15,680 images for training, 4480 images for validation, and 2240 images for testing. The dataset includes multi-scale targets, ranging from small pedestrians captured from a distance to larger ones photographed up close. The image sizes used during training and testing vary, further enhancing the robustness of the network. Meanwhile, considering the dataset conditions, the training image size was modified to 960 × 960 for improved detection accuracy and better performance. The initial learning rate was set to 0.01, the SGD optimization algorithm was adopted, and the optimizer weight decay was 0.0005. The entire training process was conducted using a Linux system equipped with an RTX 2080 Ti GPU and 128 GB of RAM.

The training process is shown in Figure 14; four other networks are involved, including YOLOv5s, original YOLOv8s, and YOLOv8s with tiny detection heads. All the networks were trained using 200 epochs to ensure convergence. The evaluation results for each trained model are presented in Table 2, and the developed algorithm exhibited the best $F1$ and *mAP* values, reaching up to 70.4 and 78.4%, respectively. These values represent $F1$ and *mAP* improvements of 1.5 and 2.3%, respectively, compared to the original YOLOv8s network. Additionally, with the introduction of the WIoU loss function, the *mAP* value increased by 0.3%. Some detection results are shown in Figure 15, where the developed network excels in accurately identifying pedestrians of various sizes as well as small targets that were ignored by the other models. The developed network can cover targets of all sizes, as shown in Figure 15a, significantly improving the detection accuracy for small targets in Figure 15b–e and reducing the false positives in Figure 15f. These results substantiate the effectiveness of introducing additional modules for enhancing detection capabilities. Moreover, to objectively assess the network generalization ability, the K-Fold Cross-Validation method was utilized, dividing the data of 15,680 images into five parts. The proposed method was then iteratively trained on four parts and validated on the remaining part. The results of the five training iterations are presented in Table 3, with an average *mAP* of 78.2 and $F1$ of 70.5. Additionally, the training results showed no significant differences across the different folds, indicating that the proposed model exhibits a strong level of generalization. To further analyze the robustness of the proposed method, the trained model was utilized to detect the background images, as shown in Figure 16. Although these background images do not contain pedestrians, they feature other disturbances of similar size. The test results confirm that the proposed network did not generate any false detections, further indicating its robust performance.

To evaluate the effectiveness of the proposed method, all the compared networks were kept consistent in terms of the parameters. Additionally, since the Ray Tune method did not significantly improve the network's accuracy during hyperparameter optimization, this study employed the default hyperparameters of YOLOv8. The experimental results are expressed in Table 4; it can be seen from the table that all three modules have a positive impact on the model optimization. With the adoption of ConvNeXt v2, *mAP* increased by 0.9%, and the use of ODConv and a tiny head resulted in a further *mAP* improvement of 1.2%. This is attributed to the fact that ConvNeXt v2 is mainly applied to the backbone

network, contributing more to feature extraction. Additionally, while the tiny head alone only increased *mAP* by 0.3%, it is evident that combining it with ODConv yields better performance. Finally, to analyze the network sensitivity, some layers are replaced with 1×1 convolutional modules. Despite the variations in texture among the different images, the results from a substantial number of validation images indicate that replacing all the layers from zero to six in the backbone significantly hampers the detection of small pedestrian targets within the images.

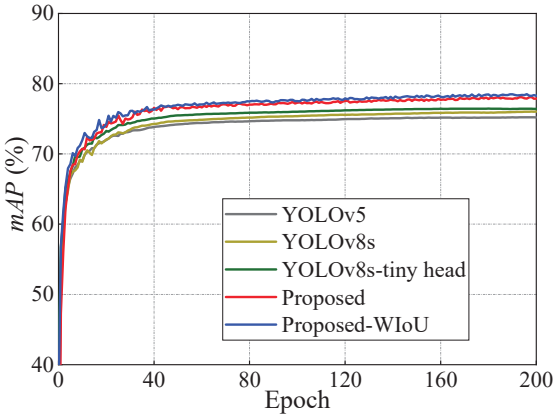


Figure 14. Training process *mAP* curves for the different networks.

Table 2. Comparison of comprehensive evaluation results of different models (%).

Network	*Precision*	*Recall*	*F1*	*F1* Improved	*mAP*	*mAP* Improved
YOLOv5s	70.6	67.1	68.8	-	75.3	-
YOLOv8s	68.3	69.5	68.9	-	76.1	-
YOLOv8s-tiny head	68.8	69.2	69.0	0.1	76.4	1.3
Proposed	69.7	70.7	70.2	1.3	78.1	2.0
Proposed-WIoU	70.0	70.8	70.4	1.5	78.4	2.3

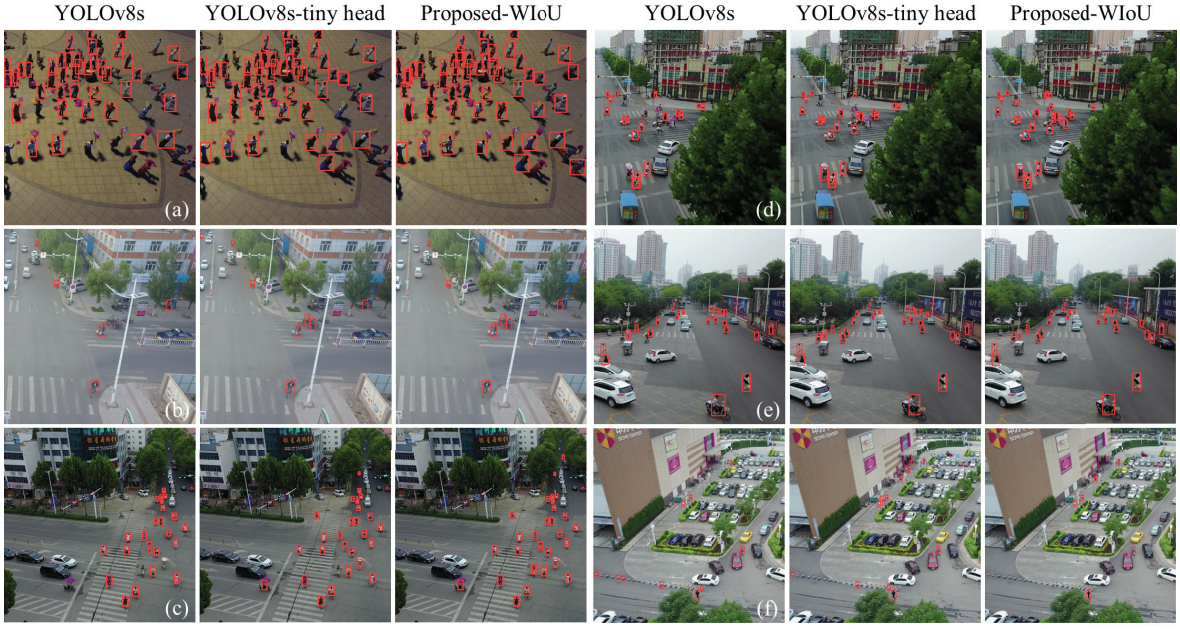


Figure 15. Small pedestrian detection results of different networks. To visually demonstrate the detection performance, the relevant confidence values are not displayed. Some large target pedestrians appear in (**a**,**b**), while smaller targets appear in (**c**–**f**).

Table 3. Cross-validation results with k = 5 (%).

Evaluation Metrics	Division 1	Division 2	Division 3	Division 4	Division 5	Average
*F*1	70.6	71.0	70.2	70.3	70.2	70.5
mAP	78.1	78.6	77.9	78.0	78.4	78.2



Figure 16. Examples of added background images.

Table 4. Results of ablation experiments (%).

ConvNeXt v2	ODConv	Tiny Head	*Precision*	*Recall*	*F*1	*mAP*	Speed (ms)
-	-	-	68.3	69.5	68.9	76.1	10.3
√	-	-	68.8	70.1	69.4	77.0	14.4
√	√	-	69.1	70.2	69.6	77.7	14.8
-	√	-	69.0	69.2	69.1	76.7	10.5
-	√	√	68.9	70.3	69.6	77.3	16.0
-	-	√	68.8	69.2	69.0	76.4	15.7
√	√	√	69.7	70.7	70.2	78.1	18.2

Note: √ means adopting the module; - means without the module.

Moreover, to further verify the performance of the proposed network, multiple one-stage and two-stage object detection models were trained in this study, and the results are described in Table 5. In general, the one-stage object detection models exhibit superior performance compared to the two-stage models. On one hand, this superiority is attributed to the effective structures and modules utilized by single-stage algorithms; on the other hand, this might be due to the incorporation of supervised signals regarding relationships directly into the feature maps, which made the learned context information richer.

Table 5. Comparison of comprehensive evaluation results of different models (%).

Category	Network	*Precision*	*Recall*	*F*1	*mAP*	Speed (ms)
One-stage	YOLOv5s	70.6	67.1	68.8	75.3	11.4
	YOLOv8s	68.3	69.5	68.9	76.1	10.3
	Proposed-WIoU	70.0	70.8	70.4	78.4	18.2
	SSD	61.5	62.4	61.9	70.8	13.7
Two-stage	Faster-R-CNN	48.4	52.4	50.3	57.3	47.5
	Mask R-CNN	51.9	57.2	54.4	61.5	62.4
	Cascade R-CNN	60.1	58.7	59.4	64.2	56.7

4.3. Small Reservoir Dam Inspection and Localization Using UAV—Case 1

4.3.1. Analysis of UAV Measurement Accuracy after Coordinate Transformation

The developed method was first applied to a small earth–rock dam, as shown in Figure 17a. The dam has a height of 13 m, and the length of the crest is 75 m. Moreover,

the dam serves as a road that can support traffic. After prolonged operation, the downstream surface of the dam was covered with weeds, and there was a lack of comprehensive monitoring data. To establish the local coordinate system of the dam efficiently and economically, 14 GCPs were set up on the dam crest, and their 3D coordinates were measured using a Leica total station (Figure 17b). The UAV used is a DJI M300 RTK (Figure 17c) equipped with an H20T camera that consists of optical imaging, infrared thermal imaging, and laser ranging capabilities. To enhance the positioning accuracy, the UAV network RTK mode was implemented.



(**a**) (**b**) (**c**)

Figure 17. Photos of the small reservoir dam and measurement equipment for Case 1. (**a**) Overall scene of the dam. (**b**) Total station and one GCP. (**c**) M300 RTK UAV and H20T camera.

To adapt to a larger range of UAV inspections, a total of 1215 images were taken to calculate the coordinate transformation parameters, including images from locations far from the dam. The 14 GCPs were then remeasured from 14 random positions, and the results are presented in Table 6. Similar to the experimental results, the errors in the planar direction are smaller than those in the altitude direction, measuring 7.47 cm and 9.49 cm, respectively, verifying the broad applicability of the developed method. However, the measurement error for GCP 4 is significantly high and is attributed to water accumulation on the ground causing significant errors in the laser ranging results.

Table 6. Measurement errors of 14 GCPs on the dam crest for Case 1 (cm).

No	ΔX	ΔY	ΔXY	ΔZ
GCP 1	−3.49	−8.92	9.58	−10.56
GCP 2	−4.77	−0.04	4.77	−6.77
GCP 3	−10.12	0.05	10.12	7.67
GCP 4	15.77	−2.80	16.01	−16.00
GCP 5	−7.63	−6.07	9.75	12.68
GCP 6	−0.28	5.47	5.48	2.82
GCP 7	−7.53	−6.64	10.04	−6.12
GCP 8	−8.18	−9.85	12.80	0.31
GCP 9	−10.02	2.37	10.29	7.67
GCP 10	−2.17	−7.71	8.01	8.70
GCP 11	−3.27	−11.73	12.18	9.96
GCP 12	1.28	−3.28	3.52	−5.22
GCP 13	−3.43	−11.20	11.72	6.66
GCP 14	−8.36	−1.65	8.52	3.42
Mean |Δ|	6.16	5.56	7.47	9.49

A 3D reconstruction of the dam area was created to further evaluate the accuracy of the developed method. The point clouds generated before and after applying coordinate transformation are compared with the results from laser scanning, as shown in Figure 18. To eliminate noise interference, the point cloud data from the trees near the dam were removed. It can be observed that the point cloud generated after coordinate transformation is closer to the laser scanning results, as shown in Figure 18b, with most of the points

having distances within 10 cm. However, there are still some large errors, mainly caused by the poor performance of the SfM algorithm in generating point clouds on the downstream surface covered with weeds. The point cloud comparison results indicate that the coordinate transformation method can improve the localization accuracy and enable a UAV-based routine inspection method.

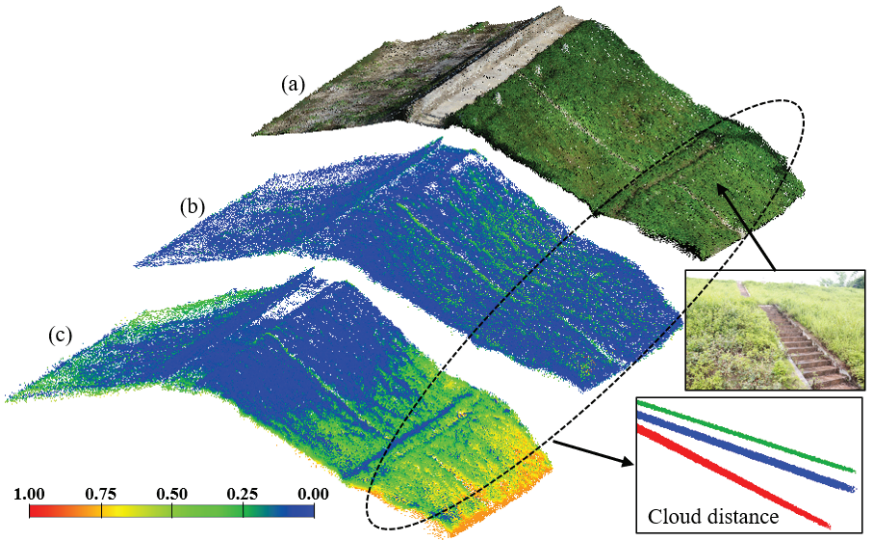


Figure 18. Point clouds generated from UAV images of a laser scan for Case 1. (**a**) Laser scan. (**b**) Transformed points. (**c**) No transformation.

4.3.2. 3D Localization of Pedestrians in Small Reservoir Dams

The developed noncontact method in combination with an improved YOLOv8 detection algorithm enables the analysis of whether pedestrians are present in hazardous areas. Some detection and localization results are shown in Figure 19. Based on the measured coordinates in the dam coordinate system, it is possible to determine the structural positions of pedestrians. For example, if a pedestrian appears near the downstream surface close to the reservoir area, an alert can be triggered. Additionally, virtual electronic fences can be constructed to promptly detect pedestrians in hazardous situations [64]. Compared to manual inspection, the proposed method offers the advantages of efficiency and low cost and is particularly suitable for small reservoir dams without automated monitoring devices.

4.3.3. Potential Seepage Detection and Localization

For small earth–rock dams, seepage is a major cause for alarm. Given that the data collection occurred during the summer, the temperature in the deeper layers of the reservoir is expected to be lower than the ambient temperature. Based on this, the primary criterion for determining seepage occurrence in this study is the manual identification of whether low-temperature areas appear on the downstream face. The UAV camera is equipped with an infrared thermal imaging sensor, capable of detecting the temperature field on the dam surface. A total of 770 infrared images were captured within the dam area, and a 3D model was generated as shown in Figure 20a. It can be observed that there are two anomalous areas on the dam surface, as indicated by the infrared image, where the temperature is lower than the surrounding environment, as shown in Figure 20b,c. However, not all the low-temperature areas can be conclusively identified as seepage. For instance, the temperature at the drainage channels at the bottom of the dam is also low due to the presence of accumulated water in Figure 20d. Combining the proposed method enables the 3D localization of this position. Nevertheless, certain locations may display temperature anomalies, as shown in Figure 20e. By incorporating their positional information, it can be analyzed that these locations do not fall within the dam area, thus avoiding false alarms. Considering that the detection of seepage still requires further analysis of the internal

conditions of the dam, to maintain rigor, in the absence of additional measurements such as osmotic pressure, this study refers to the occurrence of seepage as potential seepage.

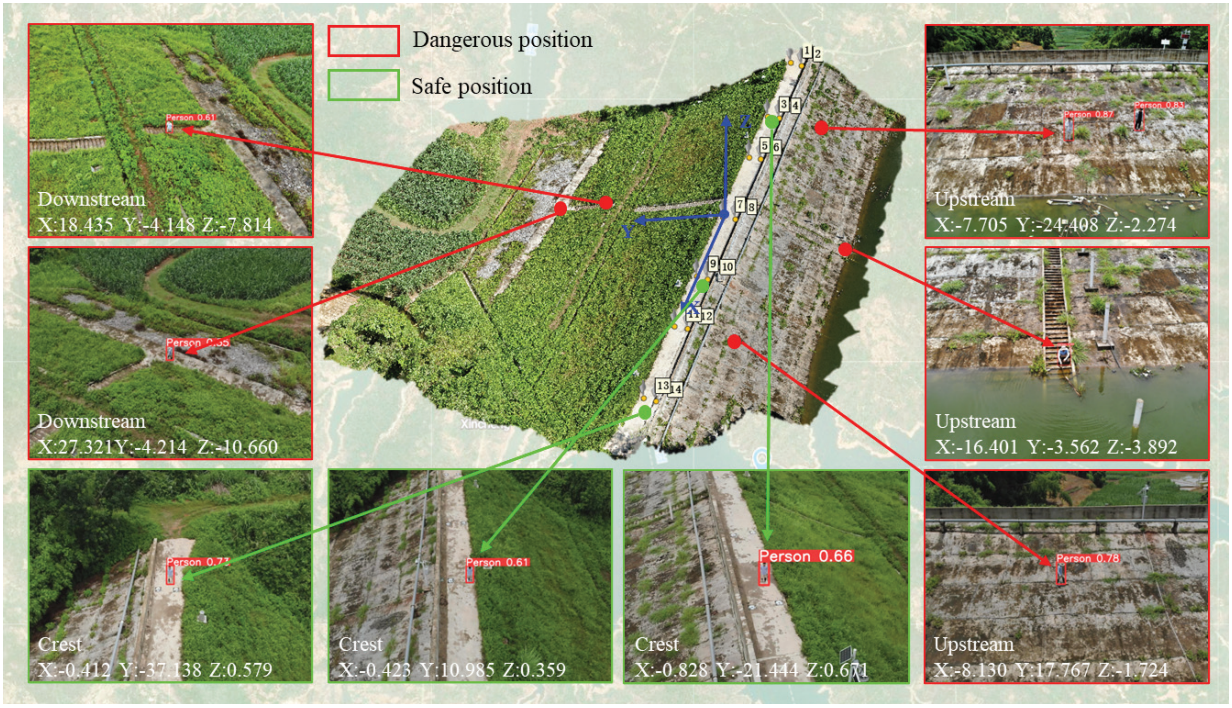


Figure 19. The 3D localization of pedestrians in the dam coordinate system and the analysis of their positions within the dam structure for Case 1.

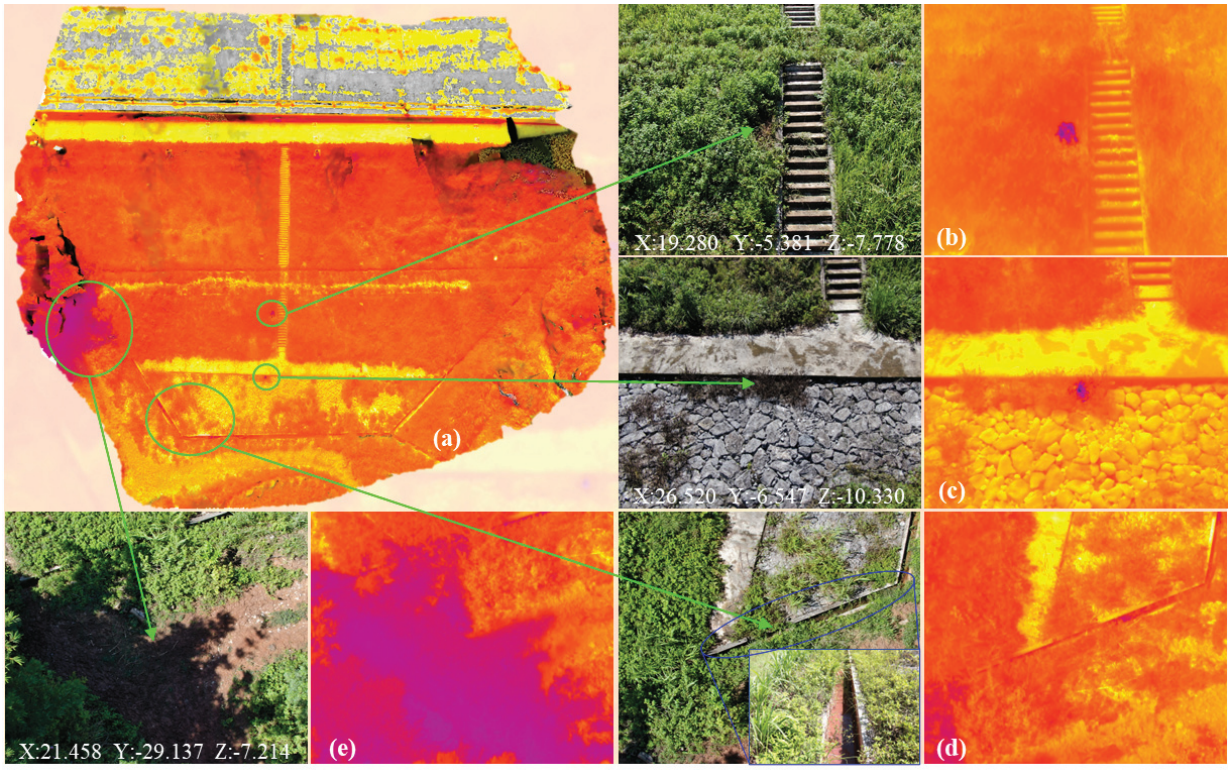


Figure 20. Detection and localization of potential seepage regions based on infrared thermography for Case 1. (**a**) Overall image. (**b**–**e**) Details of visible light and infrared images.

4.4. Small Reservoir Dam Inspection and Localization Using UAV—Case 2

4.4.1. Coordinate Transformation and Measurement Accuracy Analysis

To validate the broad applicability of the proposed method, the coordinate transformation approach was applied to another earth–rock dam. This dam has a maximum height of 21.12 m and a length of 108 m (Figure 21). Similarly, 14 GCPs were placed on the dam crest, utilizing the same UAV and measurement equipment as in Case 1. The origin of the dam local coordinate system was established at the crest.



Figure 21. Photograph of the small reservoir dam for Case 2.

A total of 1688 UAV images were captured for the purposes of coordinate transformation and 3D reconstruction. Following the coordinate transformation, noncontact measurements were carried out on the 14 GCPs from 14 distinct positions. The resulting measurement errors are detailed in Table 7. The average error in the plane is 7.19 cm, while the average error in the altitude direction 8.44 cm, demonstrating a consistent trend where the accuracy of the planar positioning surpasses that of the vertical positioning. The measurement results for Case 2 indicate that the proposed method is applicable to different dam environments.

Table 7. Measurement errors of 14 GCPs on the dam crest for Case 2 (cm).

No	ΔX	ΔY	ΔXY	ΔZ
GCP 15	0.22	−0.01	0.22	3.07
GCP 16	7.59	−4.81	8.98	6.62
GCP 17	12.67	−7.11	14.53	8.59
GCP 18	7.58	−3.94	8.55	8.22
GCP 19	1.51	1.57	2.17	2.50
GCP 10	6.28	−1.90	6.56	14.64
GCP 21	−0.51	−7.40	7.41	4.17
GCP 22	3.31	−2.06	3.89	9.80
GCP 23	−2.88	−2.19	3.62	5.71
GCP 24	−7.20	−1.98	7.47	11.76
GCP 25	−4.43	2.41	5.04	11.02
GCP 26	−11.54	6.84	13.41	14.85
GCP 27	−10.53	1.63	10.66	9.65
GCP 28	−7.84	2.23	8.15	7.56
Mean |Δ|	6.01	3.29	7.19	8.44

The dam laser scanning data are shown in Figure 22a, with the point cloud of trees near the reservoir removed. Using the scan results as a reference, the results between the point clouds generated by the SfM algorithm before and after coordinate transformation can be compared, as shown in Figure 22b,c. Although the model generated directly from the GCPs can depict the shape and structural dimensions, the point cloud generated after the coordinate transformation is noticeably closer to the scanning results. Most of the distances are less than 20 cm, and the errors are distributed relatively evenly from the dam crest to the bottom. In addition, there are some high error points near the crest, mainly caused by noise points such as weeds. Overall, accurate measurement results can be obtained after coordinate transformation for Case 2.

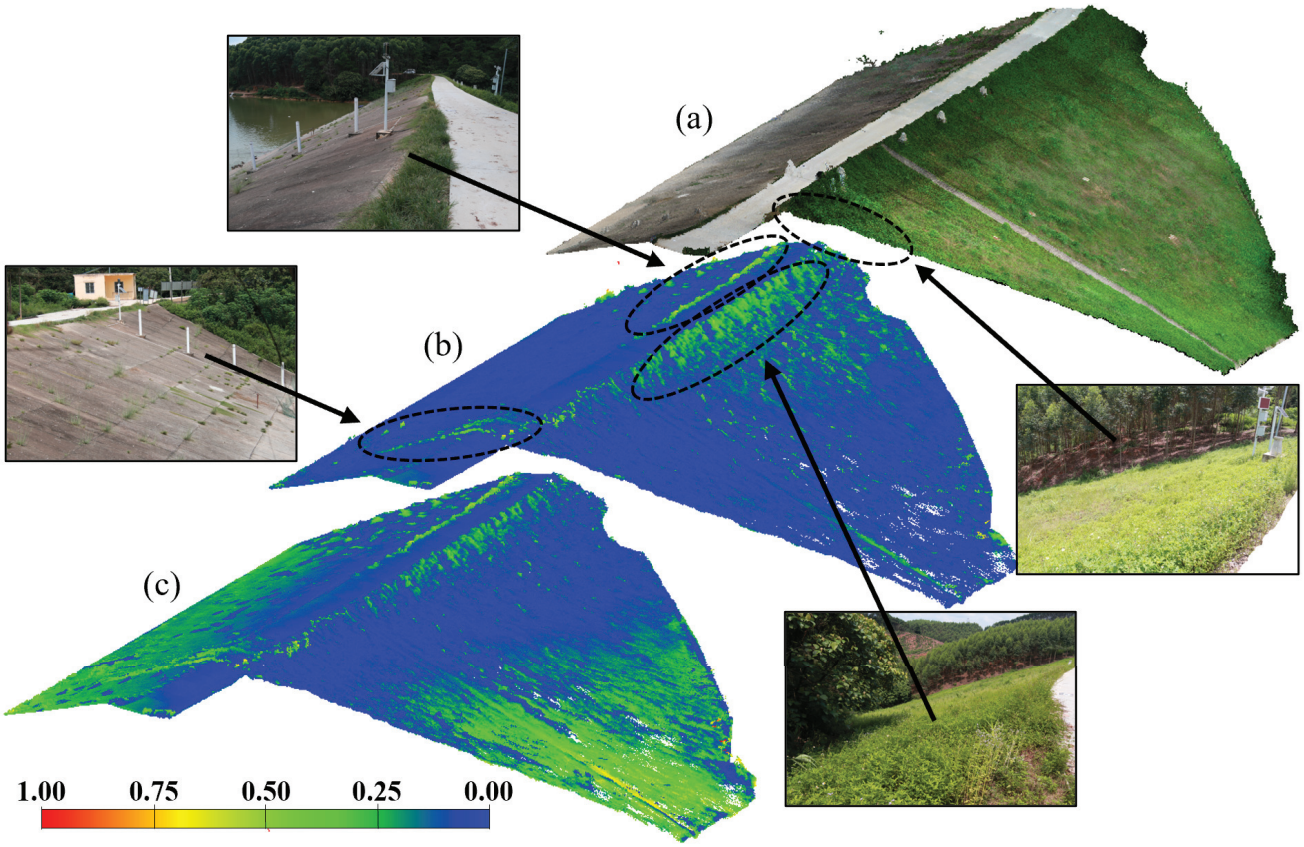


Figure 22. Point clouds generated from UAV images and a laser scan for Case 2. (**a**) Laser scan. (**b**) Transformed points. (**c**) No transformation.

4.4.2. Pedestrian Detection and Localization in Local Coordinate System

Combined with the improved YOLOv8 detection algorithm, several pedestrians at various locations on the surface of the dam can be detected and localized within the local coordinate system and specific structural positions, as shown in Figure 23. Based on the calculated 3D coordinates, it was determined that some pedestrians were present near the reservoir. When the UAV is equipped with a speaker, it can be used to promptly emit an alert. Additionally, since the dam serves a road, pedestrians detected on the crest will not trigger an alarm, thereby establishing a virtual electronic fence. With continuous monitoring, the system can record the prolonged presence of pedestrians, enabling safety management in small dam environments.

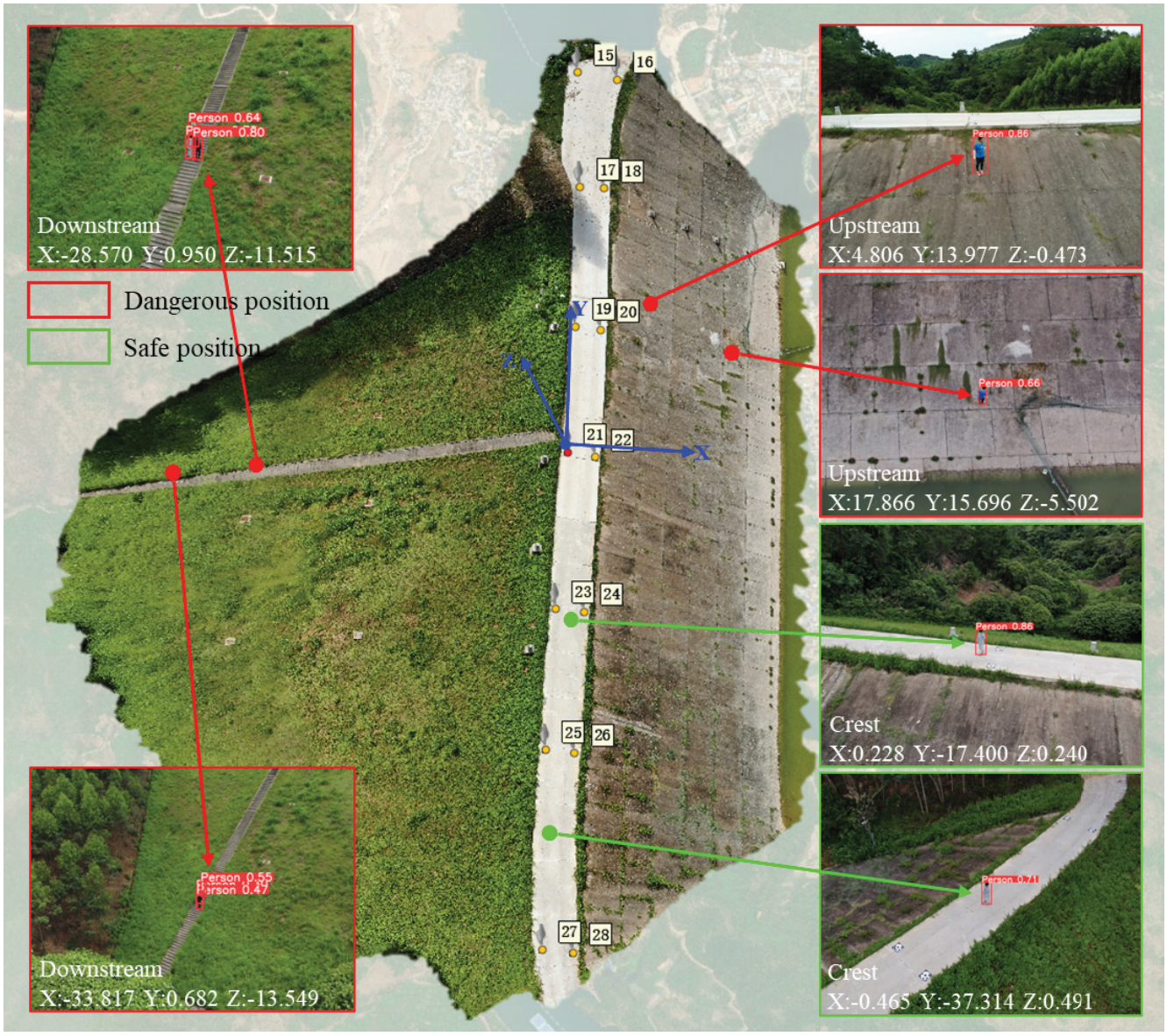


Figure 23. 3D localization of pedestrians in the dam coordinate system and the analysis of their positions within the structure for Case 2.

4.4.3. Potential Seepage Detection Using Infrared Thermography

Infrared thermal images of the dam area were collected by the UAV to assess the surface seepage. A total of 875 infrared images were used to generate the 3D model, as shown in Figure 24a. There are a total of three areas with lower temperatures, which were manually identified as potential seepage points, as shown in Figure 24b–d, all distributed near the bottom of the dam. Comparing the thermal infrared imaging with the water-filled channel reveals similar temperature values, indicating that this area requires special attention. After multiple data collections by the UAV, it is possible to determine whether an area has experienced anomalies by analyzing the temperature or texture variations at the same location at different time periods. These two cases demonstrate the applicability of the proposed method for long-term UAV inspection and localization.

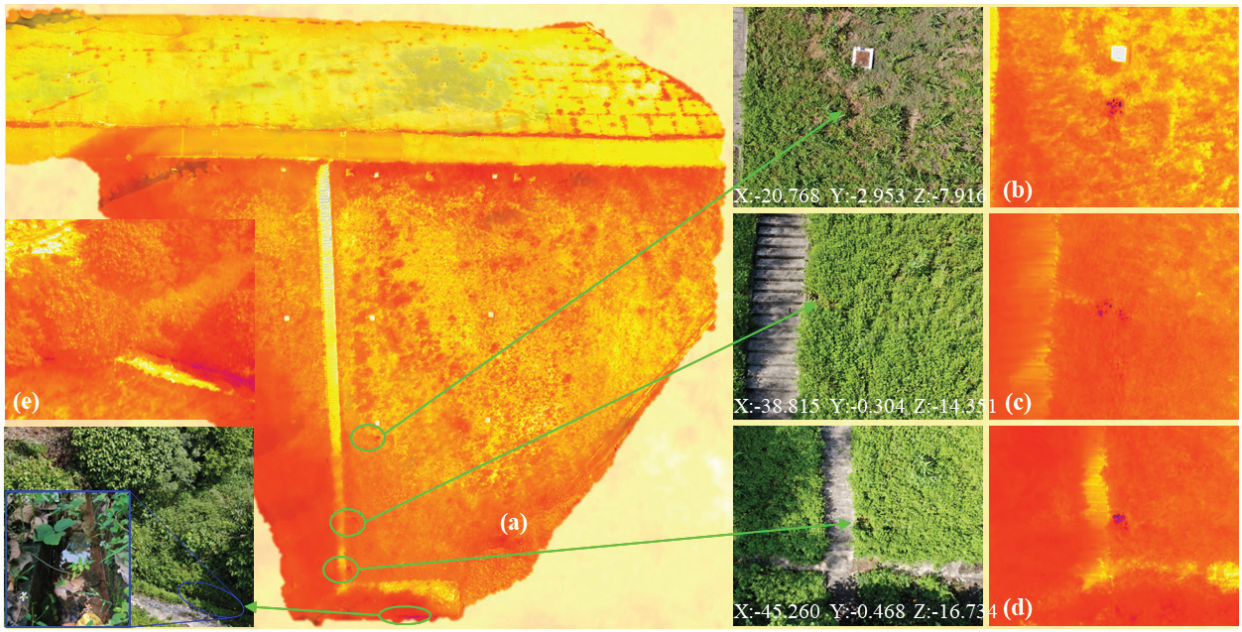


Figure 24. Detection and localization of potential seepage regions based on infrared thermography for Case 2. (**a**) Overall image. (**b**–**e**) Details of visible light and infrared images.

5. Conclusions

This paper proposed a UAV coordinate transformation and pedestrian localization method designed for small reservoir dams. It effectively addressed the problems associated with the absence of sufficient control points and terrain deformation, which complicate the establishment of a coordinate system due to the absence of geographic information. The precision and applicability of the proposed method were verified by experimental validation and application in two case studies, demonstrating its cost-effectiveness in accurately detecting pedestrians and identifying structural anomalies within small reservoir dams. The major contributions of the study include the following:

1. A coordinate transformation method for converting two coordinate systems without reference points using the SfM algorithm was developed. The UAV 3D coordinates were projected onto a plane using the Gauss–Kruger method and then transformed to the local coordinate system of the small reservoir dam through four-parameter plane transformation and an altitude fitting. The coordinate registration was calculated by the SfM algorithm with the introduction of several GCPs. After the transformation, the dam point cloud generated from the UAV images closely matched the laser scanning results, with errors mostly below 0.2 m and minimal sensitivity to changes in altitude.
2. An improved YOLOv8 algorithm for the accurate detection of small pedestrians in UAV images was also conceived. To detect targets with a limited number of pixels, a tiny head channel was introduced into the original structure. Additionally, ConvNeXt v2 modules and the ODConv algorithm were integrated into the small target detection sections of the backbone, thereby enhancing the feature extraction capability. The *mAP* value of the improved YOLOv8 network can reach up to 78.4%, an improvement of 2.8% compared to the original network. Therefore, the method is more accurate and efficient at detecting small pedestrians in practical scenarios.
3. Combined with laser rangefinding, the developed method enables noncontact 3D measurement of the target by UAV photogrammetry. To convert 2D coordinates to actual 3D coordinates, the capturing distance and camera pose were determined, and the coordinates of the target point were calculated based on the UAV position. The experimental results indicate an overall positioning error of less than 0.2 m, and, in two case studies,

the measured plane and altitude average errors were both less than 0.1 m. Moreover, both pedestrians and potential seepage points can be accurately located.

Compared to the current UAV inspection approaches, the proposed method in this study is suitable for small reservoir dams. From a methodological perspective, unlike 3D reconstruction [25], the proposed method does not require excessive time to capture 3D coordinates in complex structural areas or rely on other structural features for coordinate transformation. The proposed approach only requires a single coordinate transformation, making it more suitable for evaluating the safety of identified individuals in small reservoir dam inspections. In terms of accuracy, the proposed method incorporates a laser rangefinder, effectively converting 2D pixels into 3D coordinates. When relying solely on measurement methods based on the spatial relationship between the image and the structure, the error could be around 1 m. However, in this study, the positioning error was within 0.2 m, which meets the inspection positioning requirements for small reservoir dams. For practicality, the method developed in this research requires minimal additional equipment. The coordinate system of the small reservoir dam does not need to be pre-established; the UAV coordinates can be transformed using ground control point coordinates alone. This is particularly important for meeting the low-cost demands of small reservoir dam inspections. Additionally, the proposed method enables the creation of a virtual electronic fence for small reservoir dams, as illustrated in Figure 25. Thus, compared to the current state-of-the-art methods, the proposed approach is more suitable for small reservoir dams, supporting safety management and guiding disaster prevention strategies [65,66].

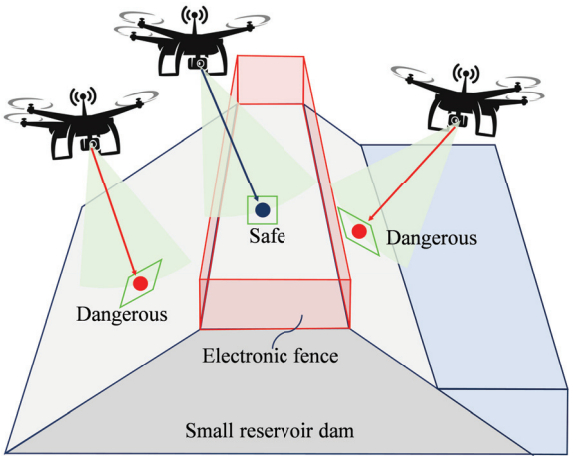


Figure 25. Schematic diagram of electronic fence for small reservoir dams using UAVs.

However, the method presented in this paper still has some limitations. First, the positioning accuracy of the UAV is dictated by satellite signals. Although the study adopted the network RTK mode to enhance the signal strength, fluctuations in positioning can lead to significant measurement errors [67]. Second, the localization results for pedestrians were determined at their midpoint and do not correspond to their positions on the dam surface. This could introduce interference when assessing the critical positions of pedestrians in danger zones. Finally, the detection of seepage is still based on empirical judgment and lacks a theoretical baseline and standardized discernment criteria based on temperature anomaly recognition [68].

In future research, detection algorithms for various types of damages should be developed, and they should be mapped to real-time digital models [69]. For network optimization, significant computational resources should be invested to fine-tune the network architecture and hyperparameters while also increasing the dataset size to further enhance the pedestrian detection accuracy. Additionally, methods that integrate image and LiDAR data should be considered to quickly detect targets while simultaneously determining the corresponding point cloud locations, thereby enabling the detection of multiple targets on complex geometric surfaces. In the application of edge devices, ensuring

smooth data transmission is a crucial issue that needs to be addressed. Additionally, there is a need to consider and mitigate the problem of data transmission delays caused by network instability. Moreover, inspection results for different time periods should be compared, and the progression of damages should be analyzed [70] to identify the rate of change without requiring initial conditions [71], enabling long-term dam health monitoring. With sufficient data, it should be possible to predict the dam response and the evolution of damages [72].

Author Contributions: Conceptualization, J.L.; methodology, L.H.; validation, Y.S.; formal analysis, Y.X.; writing—original draft preparation, S.Z.; writing—review and editing, F.K.; funding acquisition, J.L., F.K., S.Z. and Y.X. All authors have read and agreed to the published version of the manuscript.

Funding: This work was supported by Chongqing Water Conservancy Science and Technology Project (CQSLK-2023025), the National Key R & D Program of China (2022YFB4703401 and 2022YFB4703404), the National Natural Science Foundation of China (52079022 and 52409156), the Water Conservancy Science and Technology Project of Jiangsu Province (2022062), China Postdoctoral Science Foundation (2024M750740), the Natural Science Foundation of Jiangsu Province (BK20241518), the Guangxi Key R&D Program Project (GUIKE AB19245054), and the Fundamental Research Funds for the Central Universities (DUT21TD106).

Institutional Review Board Statement: No ethical approvals are required.

Informed Consent Statement: Informed consent was obtained from all subjects involved in the study.

Data Availability Statement: The datasets presented in this article are not readily available because authors do not have the relevant permissions.

Conflicts of Interest: Author Yiqing Si was employed by the company Chongqing Surveying and Design Institute Co. Ltd. of Water Resources. The remaining authors declare that the research was conducted in the absence of any commercial or financial relationships that could be construed as a potential conflict of interest.

References

1. Habets, F.; Molénat, J.; Carluer, N.; Douez, O.; Leenhardt, D. The cumulative impacts of small reservoirs on hydrology: A review. *Sci. Total Environ.* **2018**, *643*, 850–867. [CrossRef] [PubMed]
2. Kang, F.; Li, J.; Zhao, S.; Wang, Y. Structural health monitoring of concrete dams using long-term air temperature for thermal effect simulation. *Eng. Struct.* **2019**, *180*, 642–653. [CrossRef]
3. Gong, J.; Zou, D.; Kong, X.; Liu, J.; Qu, Y. An approach for simulating the interaction between soil and discontinuous structure with mixed interpolation interface. *Eng. Struct.* **2021**, *237*, 112035. [CrossRef]
4. Chen, X.; Li, D.; Tang, X.; Liu, Y. A three-dimensional large-deformation random finite-element study of landslide runout considering spatially varying soil. *Landslides* **2021**, *18*, 3149–3162. [CrossRef]
5. Arvor, D.; Daher, F.R.; Briand, D.; Dufour, S.; Rollet, A.J.; Simoes, M.; Ferraz, R.P. Monitoring thirty years of small water reservoirs proliferation in the southern Brazilian Amazon with Landsat time series. *ISPRS J. Photogramm. Remote Sens.* **2018**, *145*, 225–237. [CrossRef]
6. Mignot, E.; Dewals, B. Hydraulic modelling of inland urban flooding: Recent advances. *J. Hydrol.* **2022**, *609*, 127763. [CrossRef]
7. Zhou, R.; Su, H.; Wen, Z. Experimental study on leakage detection of grassed earth dam by passive infrared thermography. *NDT E Int.* **2022**, *126*, 102583. [CrossRef]
8. Sedláček, J.; Bábek, O.; Grygar, T.M.; Lend'áková, Z.; Pacina, J.; Štojdl, J.; Hošek, M.; Elznicová, J. A closer look at sedimentation processes in two dam reservoirs. *J. Hydrol.* **2022**, *605*, 127397. [CrossRef]
9. Guo, Y.; Cui, Y.a.; Xie, J.; Luo, Y.; Zhang, P.; Liu, H.; Liu, J. Seepage detection in earth-filled dam from self-potential and electrical resistivity tomography. *Eng. Geol.* **2022**, *306*, 106750. [CrossRef]
10. Kim, S.Y.; Kwon, D.Y.; Jang, A.; Ju, Y.K.; Lee, J.S.; Hong, S. A review of UAV integration in forensic civil engineering: From sensor technologies to geotechnical, structural and water infrastructure applications. *Measurement* **2023**, *224*, 113886. [CrossRef]
11. Spencer, B.F., Jr.; Hoskere, V.; Narazaki, Y. Advances in computer vision-based civil infrastructure inspection and monitoring. *Engineering* **2019**, *5*, 199–222. [CrossRef]
12. Zhu, Y.; Tang, H. Automatic damage detection and diagnosis for hydraulic structures using drones and artificial intelligence techniques. *Remote Sens.* **2023**, *15*, 615. [CrossRef]
13. Guzman-Acevedo, G.M.; Quintana-Rodriguez, J.A.; Vazquez-Becerra, G.E.; Garcia-Armenta, J. A reliable methodology to estimate cable tension force in cable-stayed bridges using Unmanned Aerial Vehicle (UAV). *Measurement* **2024**, *229*, 114498. [CrossRef]
14. Jiang, S.; Wang, Y.; Zhang, J.; Zheng, J. Full-field deformation measurement of structural nodes based on panoramic camera and deep learning-based tracking method. *Comput. Ind.* **2023**, *146*, 103840. [CrossRef]

15. Xu, Z.; Wu, Y.; Lu, X.; Jin, X. Photo-realistic visualization of seismic dynamic responses of urban building clusters based on oblique aerial photography. *Adv. Eng. Inform.* **2020**, *43*, 101025. [CrossRef]
16. Wu, Y.; Meng, F.; Qin, Y.; Qian, Y.; Xu, F.; Jia, L. UAV imagery based potential safety hazard evaluation for high-speed railroad using Real-time instance segmentation. *Adv. Eng. Inform.* **2023**, *55*, 101819. [CrossRef]
17. Feng, S.; Gao, M.; Jin, X.; Zhao, T.; Yang, F. Fine-grained damage detection of cement concrete pavement based on UAV remote sensing image segmentation and stitching. *Measurement* **2024**, *226*, 113844. [CrossRef]
18. Narazaki, Y.; Hoskere, V.; Chowdhary, G.; Spencer, B.F., Jr. Vision-based navigation planning for autonomous post-earthquake inspection of reinforced concrete railway viaducts using unmanned aerial vehicles. *Autom. Constr.* **2022**, *137*, 104214. [CrossRef]
19. Xu, Y.; Zhang, J. UAV-based bridge geometric shape measurement using automatic bridge component detection and distributed multi-view reconstruction. *Autom. Constr.* **2022**, *140*, 104376. [CrossRef]
20. Chen, G.; Liang, Q.; Zhong, W.; Gao, X.; Cui, F. Homography-based measurement of bridge vibration using UAV and DIC method. *Measurement* **2021**, *170*, 108683. [CrossRef]
21. Zhou, R.; Wen, Z.; Su, H. Automatic recognition of earth rock embankment leakage based on UAV passive infrared thermography and deep learning. *ISPRS J. Photogramm. Remote Sens.* **2022**, *191*, 85–104. [CrossRef]
22. Qin, L.; Yan, C.; Yu, L.; Chai, M.; Wang, B.; Hayat, M.; Shi, Z.; Gao, H.; Jiang, X.; Xiong, B.; et al. High-resolution spatio-temporal characteristics of urban evapotranspiration measured by unmanned aerial vehicle and infrared remote sensing. *Build. Environ.* **2022**, *222*, 109389. [CrossRef]
23. Zhong, X.; Zhao, L.; Wang, J.; Zhang, X.; Nie, Z.; Li, Y.; Ren, P. A retrieval method for land surface temperatures based on UAV broadband thermal infrared images via the three-dimensional look-up table. *Build. Environ.* **2022**, *226*, 109793. [CrossRef]
24. Zhou, X.; Zhu, Q.; Zhang, Q.; Du, Y. The full-field displacement intelligent measurement of retaining structures using UAV and 3D reconstruction. *Measurement* **2024**, *227*, 114311. [CrossRef]
25. Zhao, S.; Kang, F.; Li, J.; Ma, C. Structural health monitoring and inspection of dams based on UAV photogrammetry with image 3D reconstruction. *Autom. Constr.* **2021**, *130*, 103832. [CrossRef]
26. Chen, S.; Fan, G.; Li, J. Improving completeness and accuracy of 3D point clouds by using deep learning for applications of digital twins to civil structures. *Adv. Eng. Inform.* **2023**, *58*, 102196. [CrossRef]
27. Szostak, B.; Specht, M.; Burdziakowski, P.; Stateczny, A.; Specht, C.; Lewicka, O. Methodology for performing bathymetric measurements of shallow waterbodies using an UAV, and their processing based on the SVR algorithm. *Measurement* **2023**, *223*, 113720. [CrossRef]
28. Lee, G.; Moon, S.; Hwang, J.; Chi, S. Development of a real-time noise estimation model for construction sites. *Adv. Eng. Inform.* **2023**, *58*, 102133. [CrossRef]
29. Jiang, S.; Wu, Y.; Zhang, J. Bridge coating inspection based on two-stage automatic method and collision-tolerant unmanned aerial system. *Autom. Constr.* **2023**, *146*, 104685. [CrossRef]
30. Chen, J.; Li, S.; Lu, W. Align to locate: Registering photogrammetric point clouds to BIM for robust indoor localization. *Build. Environ.* **2022**, *209*, 108675. [CrossRef]
31. Tan, Y.; Li, G.; Cai, R.; Ma, J.; Wang, M. Mapping and modelling defect data from UAV captured images to BIM for building external wall inspection. *Autom. Constr.* **2022**, *139*, 104284. [CrossRef]
32. Ren, C.; Jiao, Y.; Liu, Y.; Shang, H. Optimal camera focal length detection method for GPS-supported bundle adjustment in UAV photogrammetry. *Measurement* **2024**, *228*, 114329. [CrossRef]
33. Chen, J.; Lu, W.; Lou, J. Automatic concrete defect detection and reconstruction by aligning aerial images onto semantic-rich building information model. *Comput.-Aided Civ. Infrastruct. Eng.* **2023**, *38*, 1079–1098. [CrossRef]
34. Wu, C.; Chen, B. An automatic measurement system for the wall thickness of corrugated plate based on laser triangulation method. *Adv. Eng. Inform.* **2023**, *55*, 101814. [CrossRef]
35. Lenda, G.; Marmol, U. Integration of high-precision UAV laser scanning and terrestrial scanning measurements for determining the shape of a water tower. *Measurement* **2023**, *218*, 113178. [CrossRef]
36. Zhuge, S.; Xu, X.; Zhong, L.; Gan, S.; Lin, B.; Yang, X.; Zhang, X. Noncontact deflection measurement for bridge through a multi-UAVs system. *Comput.-Aided Civ. Infrastruct. Eng.* **2022**, *37*, 746–761. [CrossRef]
37. Xu, Z.; Kang, R.; Lu, R. 3D reconstruction and measurement of surface defects in prefabricated elements using point clouds. *J. Comput. Civ. Eng.* **2020**, *34*, 04020033. [CrossRef]
38. Tan, Y.; Li, S.; Liu, H.; Chen, P.; Zhou, Z. Automatic inspection data collection of building surface based on BIM and UAV. *Autom. Constr.* **2021**, *131*, 103881. [CrossRef]
39. Liu, D.; Chen, J.; Hu, D.; Zhang, Z. Dynamic BIM-augmented UAV safety inspection for water diversion project. *Comput. Ind.* **2019**, *108*, 163–177. [CrossRef]
40. Chang, G.; Xu, T.; Wang, Q. Error analysis of the 3D similarity coordinate transformation. *GPS Solut.* **2017**, *21*, 963–971. [CrossRef]
41. Lee, E.; Park, S.; Jang, H.; Choi, W.; Sohn, H.G. Enhancement of low-cost UAV-based photogrammetric point cloud using MMS point cloud and oblique images for 3D urban reconstruction. *Measurement* **2024**, *226*, 114158. [CrossRef]
42. Triggs, B.; McLauchlan, P.F.; Hartley, R.I.; Fitzgibbon, A.W. Bundle adjustment—A modern synthesis. In Proceedings of the Vision Algorithms: Theory and Practice: International Workshop on Vision Algorithms, Corfu, Greece, 21–22 September 1999; Springer: Berlin/Heidelberg, Germany, 2000; pp. 298–372. [CrossRef]
43. Claessens, S.J. Efficient transformation from Cartesian to geodetic coordinates. *Comput. Geosci.* **2019**, *133*, 104307. [CrossRef]

44. Kern, A.; Bobbe, M.; Khedar, Y.; Bestmann, U. OpenREALM: Real-time mapping for unmanned aerial vehicles. In Proceedings of the 2020 International Conference on Unmanned Aircraft Systems (ICUAS), Athens, Greece, 1–4 September 2020; pp. 902–911. [CrossRef]
45. Han, Y.; Wu, G.; Feng, D. Vision-based displacement measurement using an unmanned aerial vehicle. *Struct. Control Health Monit.* **2022**, *29*, e3025. [CrossRef]
46. Jiang, S.; Zhang, J.; Gao, C. Bridge Deformation Measurement Using Unmanned Aerial Dual Camera and Learning-Based Tracking Method. *Struct. Control Health Monit.* **2023**, *2023*, 4752072. [CrossRef]
47. Hui, Y.; Wang, J.; Li, B. STF-YOLO: A small target detection algorithm for UAV remote sensing images based on improved SwinTransformer and class weighted classification decoupling head. *Measurement* **2024**, *224*, 113936. [CrossRef]
48. Li, Y.; Bao, T.; Li, T.; Wang, R. A robust real-time method for identifying hydraulic tunnel structural defects using deep learning and computer vision. *Comput.-Aided Civ. Infrastruct. Eng.* **2023**, *38*, 1381–1399. [CrossRef]
49. Jocher, G.; Chaurasia, A.; Qiu, J. YOLO by Ultralytics. Available online: https://github.com/ultralytics/ultralytics (accessed on 11 March 2024).
50. Talaat, F.M.; ZainEldin, H. An improved fire detection approach based on YOLO-v8 for smart cities. *Neural Comput. Appl.* **2023**, *35*, 20939–20954. [CrossRef]
51. Liu, Z.; Mao, H.; Wu, C.Y.; Feichtenhofer, C.; Darrell, T.; Xie, S. A convnet for the 2020s. In Proceedings of the IEEE/CVF Conference on Computer Vision and Pattern Recognition, New Orleans, LA, USA, 18–24 June 2022; pp. 11976–11986. [CrossRef]
52. Woo, S.; Debnath, S.; Hu, R.; Chen, X.; Liu, Z.; Kweon, I.S.; Xie, S. Convnext v2: Co-designing and scaling convnets with masked autoencoders. In Proceedings of the IEEE/CVF Conference on Computer Vision and Pattern Recognition, Vancouver, BC, Canada, 17–24 June 2023; pp. 16133–16142. [CrossRef]
53. Li, C.; Zhou, A.; Yao, A. Omni-dimensional dynamic convolution. *arXiv* **2022**, arXiv:2209.07947. [CrossRef]
54. Zhang, Z.; Liu, Y.; Xue, W. MS-IRTNet: Multistage information interaction network for RGB-T semantic segmentation. *Inf. Sci.* **2023**, *647*, 119442. [CrossRef]
55. Zhu, X.; Lyu, S.; Wang, X.; Zhao, Q. TPH-YOLOv5: Improved YOLOv5 based on transformer prediction head for object detection on drone-captured scenarios. In Proceedings of the IEEE/CVF International Conference on Computer Vision, Montreal, QC, Canada, 11–17 October 2021; pp. 2778–2788. [CrossRef]
56. Zhao, S.; Kang, F.; Li, J. Concrete dam damage detection and localisation based on YOLOv5s-HSC and photogrammetric 3D reconstruction. *Autom. Constr.* **2022**, *143*, 104555. [CrossRef]
57. Wang, G.; Chen, Y.; An, P.; Hong, H.; Hu, J.; Huang, T. UAV-YOLOv8: A small-object-detection model based on improved YOLOv8 for UAV aerial photography scenarios. *Sensors* **2023**, *23*, 7190. [CrossRef] [PubMed]
58. Li, X.; Chen, J.; He, Y.; Yang, G.; Li, Z.; Tao, Y.; Li, Y.; Li, Y.; Huang, L.; Feng, X. High-through counting of Chinese cabbage trichomes based on deep learning and trinocular stereo microscope. *Comput. Electron. Agric.* **2023**, *212*, 108134. [CrossRef]
59. Tong, Z.; Chen, Y.; Xu, Z.; Yu, R. Wise-IoU: Bounding box regression loss with dynamic focusing mechanism. *arXiv* **2023**, arXiv:2301.10051.
60. Agisoft Metashape. Available online: www.agisoft.com (accessed on 11 March 2023).
61. Zhang, S.; Xie, Y.; Wan, J.; Xia, H.; Li, S.Z.; Guo, G. Widerperson: A diverse dataset for dense pedestrian detection in the wild. *IEEE Trans. Multimed.* **2019**, *22*, 380–393. [CrossRef]
62. Du, D.; Zhu, P.; Wen, L.; Bian, X.; Lin, H.; Hu, Q.; Peng, T.; Zheng, J.; Wang, X.; Zhang, Y.; et al. VisDrone-DET2019: The vision meets drone object detection in image challenge results. In Proceedings of the IEEE/CVF International Conference on Computer Vision Workshops, Seoul, Republic of Korea, 27–28 October 2019. [CrossRef]
63. Lin, T.Y.; Maire, M.; Belongie, S.; Hays, J.; Perona, P.; Ramanan, D.; Dollár, P.; Zitnick, C.L. Microsoft coco: Common objects in context. In Proceedings of the Computer Vision–ECCV 2014: 13th European Conference, Zurich, Switzerland, 6–12 September 2014. [CrossRef]
64. Luo, H.; Liu, J.; Fang, W.; Love, P.E.; Yu, Q.; Lu, Z. Real-time smart video surveillance to manage safety: A case study of a transport mega-project. *Adv. Eng. Inform.* **2020**, *45*, 101100. [CrossRef]
65. Liu, G.; Zhong, Z.; Ma, K.; Bo, W.; Zhao, P.; Li, Y.; Zhang, Z.; Zhang, P. Field experimental verifications of 3D DDA and its applications to kinematic evolutions of rockfalls. *Int. J. Rock Mech. Min. Sci.* **2024**, *175*, 105687. [CrossRef]
66. Chen, D.; Huo, L.; Song, G. High resolution bolt pre-load looseness monitoring using coda wave interferometry. *Struct. Health Monit.* **2022**, *21*, 1959–1972. [CrossRef]
67. He, L.; He, X.; Huang, Y.; Yang, C. A new approach for estimating geocenter motion based on BDS-3 plane-specific orbit error correction model. *GPS Solut.* **2023**, *27*, 204. [CrossRef]
68. Cheng, C.; Shang, Z.; Shen, Z. Automatic delamination segmentation for bridge deck based on encoder-decoder deep learning through UAV-based thermography. *NDT E Int.* **2020**, *116*, 102341. [CrossRef]
69. He, Z.; Wang, Y.H.; Zhang, J. Generative Structural Design Integrating BIM and Diffusion Model. *arXiv* **2023**, arXiv:2311.04052.
70. Liu, X.; Li, Z.; Sun, L.; Khailah, E.Y.; Wang, J.; Lu, W. A critical review of statistical model of dam monitoring data. *J. Build. Eng.* **2023**, *80*, 108106. [CrossRef]

71. Ni, F.; Zhang, J.; Taciroglu, E. Development of a moving vehicle identification framework using structural vibration response and deep learning algorithms. *Mech. Syst. Signal Process.* **2023**, *201*, 110667. [CrossRef]
72. Yuan, D.; Gu, C.; Wei, B.; Qin, X.; Gu, H. Displacement behavior interpretation and prediction model of concrete gravity dams located in cold area. *Struct. Health Monit.* **2023**, *22*, 2384–2401. [CrossRef]

Disclaimer/Publisher's Note: The statements, opinions and data contained in all publications are solely those of the individual author(s) and contributor(s) and not of MDPI and/or the editor(s). MDPI and/or the editor(s) disclaim responsibility for any injury to people or property resulting from any ideas, methods, instructions or products referred to in the content.

applied sciences

MDPI

Article

Influence of Boundary Conditions on the Three-Dimensional Temperature Field of a Box Girder in the Natural Environment: A Case Study

Bin Yan [1,2], Hexin Fu [1,*], Haiting Su [3] and Benguang Hou [1]

[1] School of Civil Engineering, Central South University, Changsha 410075, China; binyan@csu.edu.cn (B.Y.); benguanghou@csu.edu.cn (B.H.)
[2] National Engineering Research Center of High-Speed Railway Construction Technology, Changsha 410075, China
[3] College of Mechanical and Architectural Engineering, Taishan University, Taian 271000, China; suhaiting1988@gmail.com
* Correspondence: fuhexin@csu.edu.cn

Abstract: The inhomogeneous distribution of temperature in bridges causes stresses and strains inside the structure, thus affecting the safety and durability of bridges. Therefore, the study of temperature action in bridge structures is crucial; boundary conditions of the temperature field are critical to study them. In this study, the calculation method of the boundary conditions for the three-dimensional temperature field of box girders in the natural environment is investigated by taking box girders as the object, which integrates the solar radiation, environmental radiation, structural shading effect, and convective heat transfer between the inner and outer surfaces of box girders. The effects of the atmospheric transparency coefficient and concrete short-wave absorptivity on the temperature field distribution of box girders were also investigated. It is shown that the calculation results obtained by the method in this study are in good agreement with the measured results, and the method can effectively simulate the three-dimensional temperature field of the box girder. The atmospheric transparency coefficient and the short-wave absorptivity of concrete have a significant effect on the temperature field distribution of box girders, and materials with lower short-wave absorptivity can be used in the design of box girders to reduce the structural temperature.

Keywords: box girder; three-dimensional temperature field; boundary conditions; solar radiation; convective heat transfer

1. Introduction

Bridges enable people to cross rivers, canyons, or other obstacles easily. However, the natural environments of different regions differ significantly, and different meteorological conditions pose higher challenges to the safety and durability of bridge structures. Bridges are exposed to natural environments for long periods of time, and large temperature changes may lead to stress concentrations, localized failures, or even overall damage, reducing their service performance [1,2].

With the continuous and in-depth exploration of scholars in various countries, there are numerous studies related to the temperature action of bridge structures. One study [3] used temperature data to establish a probabilistic statistical model of the relationship between climatic conditions and high pier temperatures by monitoring the temperature of a high pier in a real project (2 years) and simulating long-term temperatures (50 or 100 years)

through the model. Another study [4] placed the test box girder on the roof of the house for solarization and temperature testing of the box girder for 3 months. The experimental data were analyzed and later validated by COMSOL modeling. The temperature field in other environments was simulated for validating the model. Another study [5] conducted temperature monitoring of three-cell concrete box girders for one year and developed temperature prediction equations for these using instantaneous air temperature, solar radiation, and wind speed. A different study [6] investigated the temperature distribution pattern of a combination girder under typical weather conditions based on a six-year temperature dataset and derived the distribution map and standard value of the most critical temperature gradient through statistical analysis. Another study [7] derived and established a vertical discrete dimensional reduction model for steel–concrete composite bridges by simplifying the temperature field of the bridge into a vertical temperature gradient for rapid calculation of temperature loads. Another study [8] calibrated the temperature gradient loading factors for different risk levels using a first-order reliability approach and considered sources of uncertainty such as material, fabrication, and loading effects. Another study [9] simulated the long-term temperature field at a site based on weather station observation data and obtained representative values with a 50-year return period by substituting the data into a generalized Pareto model through the temperature gradient model in the design specification; spatial interpolation was used to draw a map of the temperature action contours, and the contour map was simplified to obtain the map of the temperature action zones.

Some scholars have achieved the prevention and monitoring of structural health of bridges under temperature effects by simulating or predicting the temperature field of bridges. One study [10] analyzed the temperature distribution and related responses of a suspension bridge using structural health monitoring as well as field tests and numerical analysis. A modeling system was developed to predict the effect of temperature on the bridge and its effectiveness was demonstrated by comparing the observed data with the predicted values. A different study [11] presented a model for predicting extreme temperatures of bridge structures. A probabilistic model of structural temperature was developed by combining experimental and environmental data; and the average structural temperatures for 50 and 100 years were predicted. Another study [12] proposed a temperature gradient pattern calculation method that considered condition dependence and the entire design service life. The temperature gradient pattern of the box girder throughout its service life was predicted. Another study [13] identified the main meteorological parameters affecting the temperature gradient through correlation analysis, considered the different mechanisms by which different meteorological conditions affect the temperature gradient, and established a correlation model between the temperature gradient and the meteorological parameters.

In the temperature effect study of the structure, the boundary conditions of the temperature field must be clarified first, and the treatment of the boundary conditions directly affects the accuracy of the calculation results. One study [14] firstly calculated the temperature field boundary conditions with the formula before correction and then calculated the temperature field boundary conditions with the formula after correction, and compared the two. Then, ANSYS V19.2 was used to establish the temperature field simulation model. The modified temperature field boundary conditions were applied to the model, the calculated structural temperature was extracted, and the measured values in the field were compared with the numerical simulation values. A different study [15] carried out a comprehensive comparative analysis of the established box girder temperature field calculation formula and values, explored the reasonable range of values of the radiation heat transfer coefficient to facilitate engineering applications, the influence of the temperature difference between the bridge and the environment and the wind speed on the convective heat transfer coefficient, as

well as the influence of the external atmospheric temperature values of the different parts of the box girder on the influence law of the internal temperature field of the box girder. Existing studies are less related to the boundary conditions of the temperature field of bridge structures. There is a lack of research on the boundary conditions of three-dimensional temperature fields. Research on the boundary conditions of the three-dimensional temperature field of box girders in the natural environment is urgently needed.

Based on the thermodynamics theory, this study discusses the calculation method of boundary conditions for the three-dimensional temperature field of a box girder in the natural environment, which considers the solar radiation, environmental radiation, structural shading effect, and convective heat transfer between the inner and outer surfaces of the box girder. Taking a box girder of a section of railroad line as an example, the boundary condition calculation method in the paper was used to analyze the temperature field distribution of the structure and was verified with measured temperature data. Finally, the effects of the atmospheric transparency coefficient and concrete short-wave absorptivity on the temperature field distribution of box girder are also discussed.

2. Boundary Conditions for Solar Radiation

2.1. Solar Constant

The solar constant is the amount of solar heat received per unit area in a plane perpendicular to the Sun's rays at the average distance of the Earth from the Sun. The equation for calculating the solar constant I is given below:

$$I = \frac{L}{4\pi d^2} \tag{1}$$

where L is the total radiant power of the Sun, which is 3.846×10^{26} W.

With the movement of the Sun and the Earth, the distance from the Sun to the Earth changes, and the solar constant changes accordingly. In order to take into account the positional relationship between the Sun and the Earth, a time correction coefficient is introduced to correct the value of the solar constant at different times, which is expressed as follows:

$$I_0 = I \cdot \left[1 + 0.033\cos\left(\frac{360N}{365}\right)\right] \tag{2}$$

where N is the daily ordinal number, calculated from 1 January (the same below).

2.2. Cape of the Sun

The radiation received from the Sun by structures in natural environments is directly related to the relative position of the Sun and the Earth, and the following concepts for the relevant solar angles are introduced to characterize the relative positions of the Sun and the structures, which contain the angle of declination δ, the angle of solar time ω, the angle of solar altitude h, and the angle of solar azimuth γ_z.

2.2.1. Angle of Declination δ

The angle of declination refers to the line between the center of the Sun and the center of the Earth and the equatorial plane formed by the line angle. In the spring and the autumnal equinoxes when the center line of the Sun and the Earth coincide with the equatorial plane, the angle of declination is zero; in the summer and winter solstices when the angle of declination is the largest, up to $\pm 23.45^\circ$. The magnitude of the angle of declination δ can be calculated by the following equation:

$$\delta = 23.45\sin\left[\frac{360}{365}(284 + N)\right] \tag{3}$$

2.2.2. Solar Time Angle ω

The solar time angle is the angle between the line connecting the center of the Sun and the Earth and the calculation plane, assuming that the solar time angle is positive in the morning. The solar time angle ω can be expressed as a linear function of the true solar time t as follows:

$$\omega = (12 - t) \times 15^\circ \tag{4}$$

The Sun–Earth center distance and the relative position of the Sun–Earth are constantly changing, so the apparent solar time and the calculation of the solar time between the relative error, so the true solar time t can be calculated by the following equation:

$$t = t_s \pm \frac{L - L_s}{15} + t_d \tag{5}$$

where t_s is the standard time of the region, China adopts Beijing time (East 8 time zone); L, L_s are the longitude of the location of the structure and the longitude of the standard time of the region, respectively; and t_d is the time difference, which is calculated as follows:

$$t_d = \frac{9.87\sin 2\theta_N - 7.53\cos\theta_N - 1.5\sin\theta_N}{60} \tag{6}$$

where θ_N is the day angle of the daily ordinate change, calculated by the equation $\theta_N = 360(N - 81)/364$.

In summary, the apparent solar time angle ω is given by:

$$\omega = \left(12 - t_s - \frac{L - L_s}{15} + \frac{9.87\sin 2\theta_N - 7.53\cos\theta_N - 1.5\sin\theta_N}{60}\right) \times 15^\circ \tag{7}$$

2.2.3. Solar Altitude Angle h

Solar altitude angle refers to the structure and the Sun's center line and the horizontal plane of the line angle, the Sun's incidence direction, and the angle of the horizontal plane. The solar altitude angle h changes with time, and the relationship between the angles can be seen in Figure 1, which is calculated as follows:

$$\sin h = \cos\varphi\cos\delta\cos\omega + \sin\varphi\sin\delta \tag{8}$$

where φ is the geographic latitude, normalized to north latitude; δ is the solar declination angle; and ω is the solar time angle.

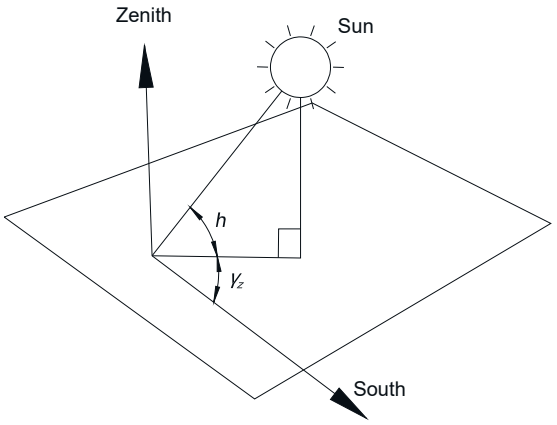


Figure 1. Solar altitude angle and azimuth angle.

2.2.4. Solar Azimuth γ_z

Solar azimuth refers to the angle between the projection of incident light on the ground and the due south direction, and it is specified that the solar azimuth γ_z is positive when it deviates from the east, and its specific calculation equation is as follows:

$$\sin \gamma_z = \frac{\cos \delta \sin \omega}{\cos h} \tag{9}$$

where δ is the solar declination angle; ω is the solar time angle; and h is the solar altitude angle.

2.2.5. Solar Incidence Angle θ

The solar incidence angle θ is the angle between the incident light and the plane normal. The solar incidence angle of any plane with the structure of the plane normal to the tilt angle β and azimuth γ. The geometric relationship between the three shown in Figure 2. The solar incidence angle can be calculated using the following equation:

$$\cos \theta = \sin \beta \sin h + \cos \beta \cos h \cos(\gamma_z - \gamma) \tag{10}$$

where β is the angle between any plane normal and the horizontal plane; h is the solar altitude angle; γ_z is the solar azimuth angle; and γ is the azimuth of any out-of-plane normal.

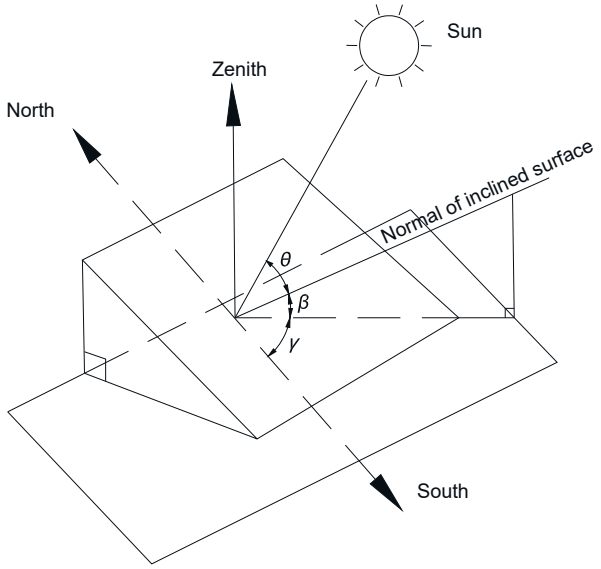


Figure 2. Angle of incidence of the Sun in an arbitrary plane.

2.3. Boundary of Solar Radiation Intensity

2.3.1. Direct Solar Radiation

Based on the above theoretical basis, the direct solar radiation reaching the Earth's surface can be expressed in the following equation:

$$I_s = I_0 \cdot P^{1/\sin h} \tag{11}$$

where P is the atmospheric transparency coefficient and h is the solar altitude angle.

Assuming that the north, west, and up directions of the Sun correspond to the x, y, and z directions in the Cartesian coordinate system, the direction vector of the Sun in

three-dimensional coordinates can be obtained based on the Sun angle calculated above, and the conversion relationship between the Sun angle and the direction vector is:

$$i_x = -\cos(90^\circ - h)\sin\gamma_z \tag{12}$$

$$i_y = \sin(90^\circ - h)\sin\gamma_z \tag{13}$$

$$i_z = -\cos\gamma_z \tag{14}$$

Because of the shading effect, the direct solar radiation does not cover the entire structure. The shading effect is illustrated in Figure 3. Shading increases the structural temperature gradient and internal stresses, leading to more complex numerical analyses [16]. The solar irradiated and shaded areas are divided by the solar radiation direction vector.

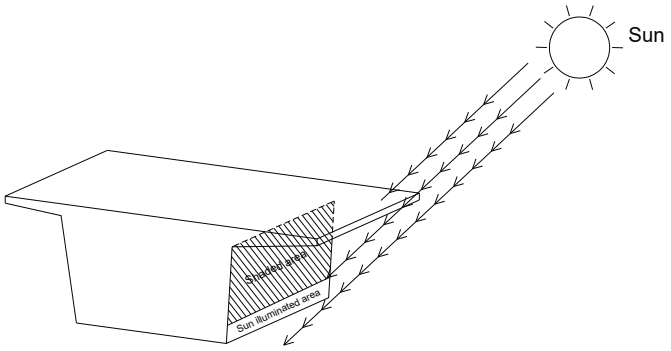


Figure 3. Solar radiation shading effect.

The direct solar radiation in the shaded region is 0 and the direct solar radiation received in the sunlit region is I_D:

$$I_D = I_s\cos\beta \tag{15}$$

2.3.2. Atmospheric Scattering Radiation

A portion of the solar radiant energy is absorbed by the atmosphere during its transfer to the Earth's surface, and a portion of this absorbed energy returns to the surface, it has been found that this portion of the energy is closely related with the surface inclination angle [17], and is not strongly related with the azimuthal angle of the structure surface, and the intensity of the scattering on the horizontal plane has been obtained as:

$$I_{dH} = (0.271I_0 - 0.294I_D)\sin h \tag{16}$$

The intensity of the Sun-scattered radiation in a cross-section with an arbitrary inclination angle β is:

$$I_d = \frac{1+\cos\beta}{2} I_{dH} \tag{17}$$

2.3.3. Surface-Reflected Radiation

A portion of the energy radiated by the Sun at the surface will be reflected by the surface and then projected the surface of the bridge structure. The equation used is the following:

$$I_f = \frac{\xi[I_D\sin h + I_{dH}][1-\cos\beta]}{2} \tag{18}$$

where ξ is the ground reflection coefficient, generally taken as 0.2.

In summary, the solar shortwave radiation projected onto the surface of a structure can be categorized as direct solar radiation, atmospheric scattering, and surface reflection, and the total solar radiant energy q_s on any surface is given in the following equation:

$$q_s = a_t\Big(I_D + I_d + I_f\Big) \tag{19}$$

where a_t is the short-wave radiation absorptivity of concrete.

3. Boundary of Convective Heat Transfer

The convective heat transfer between the surface of the concrete box girder and the outside atmosphere follows Newton's law of cooling, as follows:

$$q_c = h_c(T_a - T) \tag{20}$$

where h_c is the convective heat transfer coefficient.

The convective heat transfer coefficient is calculated according to the convective heat transfer coefficient correlation equation in the literature [18]. In the case of no wind or very small wind speed, the outer surface of the box girder and the atmosphere are mainly characterized by natural convection heat transfer. The convective heat transfer coefficient can be calculated using the following equation:

$$h = \begin{cases} \frac{k}{L}\left(0.68 + \frac{0.67(\cos\varphi Ra_L)^{1/4}}{\left(1+\left(\frac{0.492k}{\mu C_p}\right)^{9/16}\right)^{4/9}}\right) & if\ Ra_L \le 10^9 \\ \frac{k}{L}\left(0.825 + \frac{0.387{Ra_L}^{1/6}}{\left(1+\left(\frac{0.492k}{\mu C_p}\right)^{9/16}\right)^{8/27}}\right)^2 & if\ Ra_L > 10^9 \end{cases} \tag{21}$$

where L is the characteristic length (the horizontal plane is the ratio of area to perimeter, the inclined plane is the height), k is the coefficient of thermal conductivity, φ is the angle between the calculation surface and the vertical plane, μ is the dynamic viscosity, C_p is the specific heat capacity, Ra_L is the Rayleigh number, which can be calculated by the following equation:

$$Ra_L = \frac{g\alpha_p\rho^2 C_p|T - T_{ext}|L^3}{k\mu} \tag{22}$$

where g is the gravitational acceleration, α_p is the coefficient of thermal expansion, ρ is the density, T is the structural temperature, and T_{ext} is the atmospheric temperature.

When the wind speed is large, and there is forced convection heat transfer between the outer surface of the box beam and the atmosphere, the convection heat transfer coefficient can be calculated using the following equation:

$$h = \begin{cases} 2\frac{k}{L}\frac{0.3387Pr^{1/3}Re_L^{1/2}}{\left(1+\left(\frac{0.0468}{Pr}\right)^{2/3}\right)^{1/4}} & if\ Re_L \le 5\times10^5 \\ 2\frac{k}{L}Pr^{1/3}\Big(0.037Re_L^{4/5} - 871\Big) & if\ Re_L > 5\times10^5 \end{cases} \tag{23}$$

where L is the length of the calculation surface; Pr is the Prandtl number, calculated by the formula $Pr = \mu C_p/k$; Re_L is the Reynolds number, calculated by the formula $Re_L = \rho UL/\mu$, where U is the external fluid flow rate, which is the wind speed in the natural environment.

The inside of the box girder is a closed space, and the inner surface of the box girder mainly carries out internal natural convection heat transfer with the gas inside the box, which can be calculated by the following equation:

$$h = \frac{k}{H}\frac{1}{24}Ra_L \tag{24}$$

where H is the height of the internal region and L is the width of the internal region.

4. Boundary of Radiative Heat Transfer

Radiant heat transfer of box girders in the natural environment mainly consists of absorption and reflection, and the absorbed radiant heat includes atmospheric scattering and ground diffuse reflection.

4.1. Environmental Radiation

The atmospheric radiant heat G_a received by the bridge structure is calculated by the following equation:

$$G_a = \varepsilon_a \sigma T_{ext}^4 \tag{25}$$

where $\mathcal{E}_a$ is the atmospheric radiation coefficient, which is usually taken as 0.82, and σ is the blackbody radiation constant, which has a value of 5.67×10^{-8} W/(m^2·K^4).

The heat radiated from the surface by the surface with an inclination angle of β is calculated by the following equation:

$$U_\beta = \frac{\sigma T_{ext}^4 (1 - \cos\beta)}{2} \tag{26}$$

4.2. Structural Exothermic Radiation

Structure absorbs external radiant heat simultaneously and also radiates heat to the outside. The radiant heat E_l can be calculated according to the following equation:

$$E_l = a_l \sigma T^4 \tag{27}$$

where a_l is the long-wave radiation absorptivity and emissivity of concrete.

In summary, the total amount of radiative heat transfer q_r of concrete can be expressed as:

$$q_r = a_l \left(G_a + U_\beta\right) - E_l \tag{28}$$

5. Engineering Background and Verification

5.1. Engineering Background

A 32 m simply supported girder bridge of a passenger dedicated line in the literature [19] was taken as an example of calculation. The bridge was located at longitude 117.97° E, latitude 28.45° N, and the bridge azimuth was 6.92°. The cross-sectional dimensions of the box girder are shown in Figure 4. The girder was made of C50 concrete material, which has a thermal conductivity of 10.8 kj/(h·K·m). The thermal conductivity of air was 0.0864 kj/(h·K·m), the atmospheric transparency coefficient was 0.8, and the wind speed was 2.5 m/s. The short-wave absorptivity and emissivity of concrete was 0.6, and the long-wave absorptivity and albedo were 0.85. The reflectivity of the ground surface was 0.18.

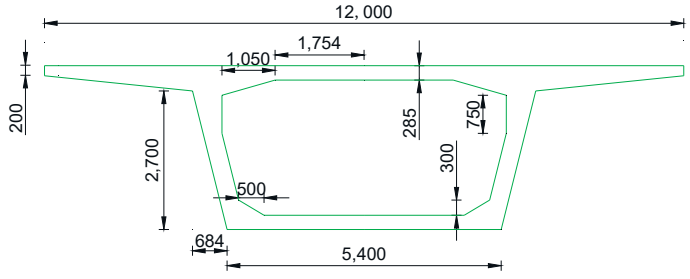


Figure 4. Cross-section of the box girder (unit: mm).

The temperature change during the day is usually influenced by the Sun; the temperature reaches its maximum value during the day and its minimum value at night. In general, the variation in the temperature during the day can be described by a sinusoidal function with the function equation:

$$T_{ext} = \frac{T_{max} + T_{min}}{2} + (T_{max} - T_{min})\sin(At - B) \tag{29}$$

where T_{max} is the daily maximum temperature; T_{min} is the daily minimum temperature; A is the angular frequency, $A = 2\pi/T$; and B is the phase offset, which is used to adjust the starting point of the waveform, and the temperature is lowest at 3:00 a.m. in the calculation time.

The model calculated once every hour and the calculation results gradually stabilized after multiple iterations. One week of analysis met the requirements of temperature field simulation [20]. The calculation period was from 27 December 2013 to 2 January 2014, and the daily maximum and minimum temperatures and the atmospheric sine function are shown in Table 1. Figure 5 shows a plot of the atmospheric sine function for the seven days of the calculation period.

Table 1. Air temperatures during the calculation time.

Day/Month	Maximum Temperature	Minimum Temperature	Atmospheric Sine Function
27/12	6	−1	$T_{ext1} = 3.5\sin\left(\frac{\pi t}{12} - \frac{\pi}{4}\right) + 2.5$
28/12	9	−1	$T_{ext2} = 5\sin\left(\frac{\pi t}{12} - \frac{\pi}{4}\right) + 4$
29/12	9	−4	$T_{ext3} = 6.5\sin\left(\frac{\pi t}{12} - \frac{\pi}{4}\right) + 2.5$
30/12	12	−3	$T_{ext4} = 7.5\sin\left(\frac{\pi t}{12} - \frac{\pi}{4}\right) + 4.5$
31/12	14	0	$T_{ext5} = 7\sin\left(\frac{\pi t}{12} - \frac{\pi}{4}\right) + 7$
1/1	17	0	$T_{ext6} = 8.5\sin\left(\frac{\pi t}{12} - \frac{\pi}{4}\right) + 8.5$
2/1	19	0	$T_{ext7} = 9.5\sin\left(\frac{\pi t}{12} - \frac{\pi}{4}\right) + 9.5$

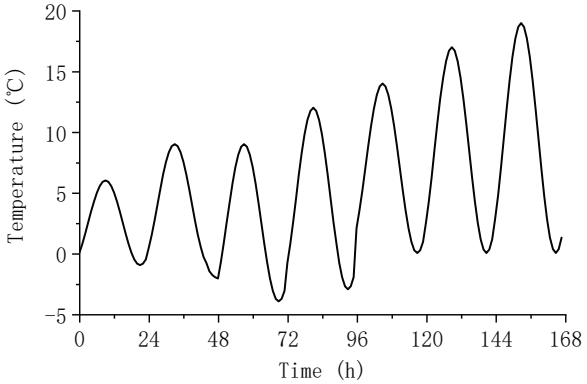


Figure 5. Atmospheric sine function.

Combined with the boundary condition calculation method introduced above and the engineering background of the example, the outer surface of the box girder applied solar radiation, external natural convection, and radiative heat transfer boundaries. The internal cavity applied internal natural convection boundaries. The three-dimensional temperature field finite element model of the box girder was established using COMSOL V6.1 software, as shown in Figure 6.

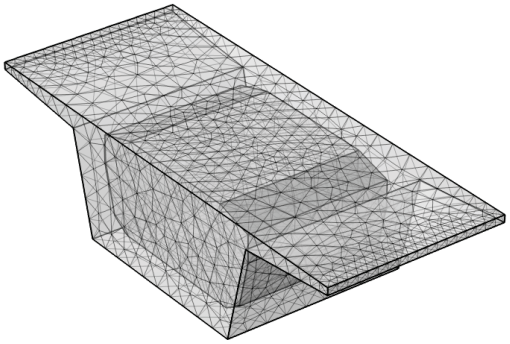


Figure 6. Three-dimensional temperature field finite element model of the box girder.

5.2. Validation of Results

The above boundary conditions and parameters were used to simulate the temperature field of the box girder. Data from the middle 5 days were selected for analysis; the first and last days were removed to reduce the influence of boundary effects. Comparison of the finite element results (FEM) and experimental data (EXP) of the key points of the box girder top plate, web plate, and bottom plate was conducted. The locations of key points are shown in Figure 7, and the results are compared in Figures 8–10.

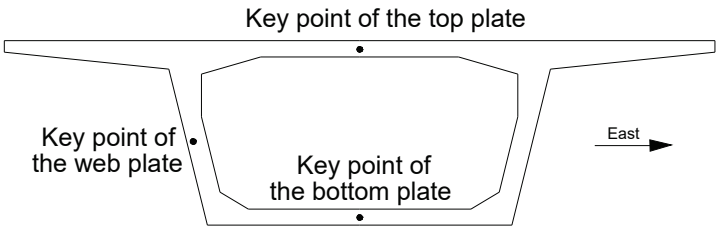


Figure 7. Map of key point locations.

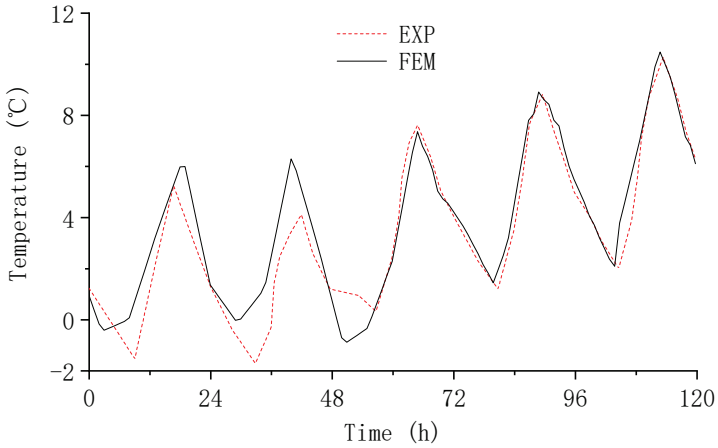


Figure 8. Critical point temperatures of the top plate.

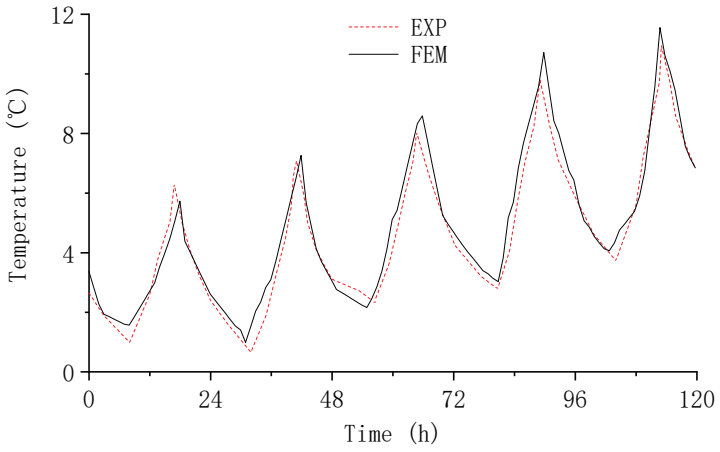


Figure 9. T Critical point temperatures of the web plate.

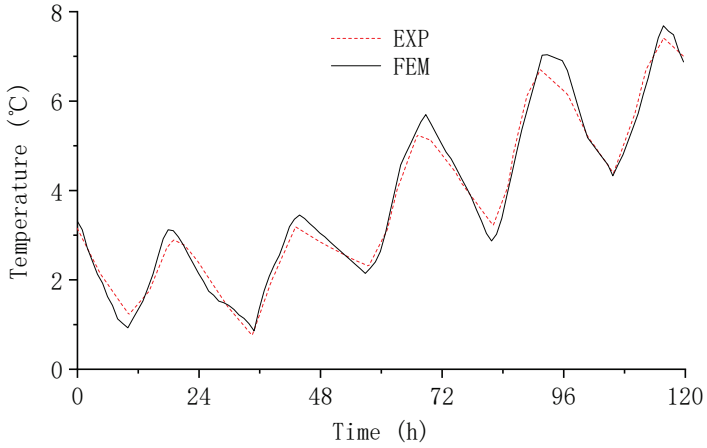


Figure 10. Critical point temperatures of the bottom plate.

As can be seen from Figures 8–10, the calculated and measured results of the temperature distribution at each key point of the box girder have a good coincidence. The temperature at the key point of the top plate had a slight difference in the first two days, and the maximum error between the calculated value and the measured value was 2.4 °C. In the last three days, the calculated value and the measured value matched well, and the maximum error was only 0.3 °C. The temperature at the key point of the web plate was 0.5 °C, and the maximum error between the calculated value and the measured value was 0.5 °C. The maximum error between the calculated and measured values of the key point temperature of the web plate was 0.5 °C. The maximum error between the calculated and measured temperatures of the key points of the bottom plate was 0.8 °C. Under comprehensive consideration, the error between the calculated and measured results was small; thus, the boundary condition calculation method used in this paper can effectively simulate the three-dimensional temperature field distribution of the box girder.

6. Influence of Boundary Condition Parameters on the Temperature Field Distribution

6.1. Impact of Atmospheric Transparency

The atmospheric transparency coefficient is a parameter that measures the ability of the atmosphere to transmit solar radiation, which affects the size of the bridge structure by the direct radiation and scattered radiation from the Sun. This paper analyzed the atmospheric transparency coefficient P by setting it to five values of 0.9, 0.8, 0.7, 0.6, and 0.5 to explore the effect of atmospheric transparency on the temperature field distribution of

the box girder structure. Figures 11–13 show the temperature maps of key points of the box girder at different atmospheric transparency coefficients.

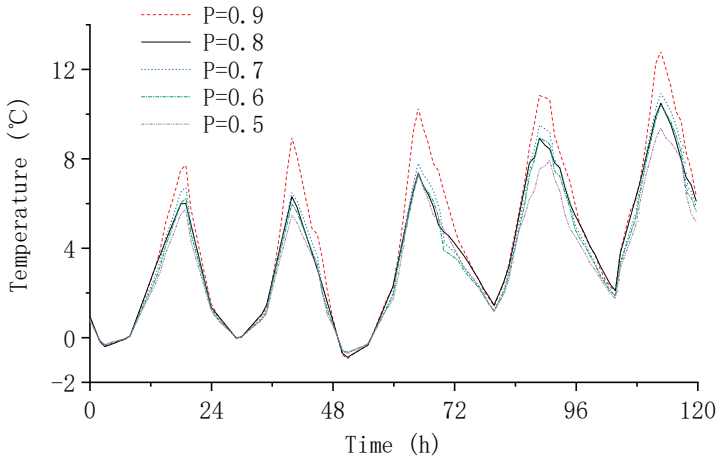


Figure 11. Critical point temperatures of the top plate for different atmospheric transparency coefficients.

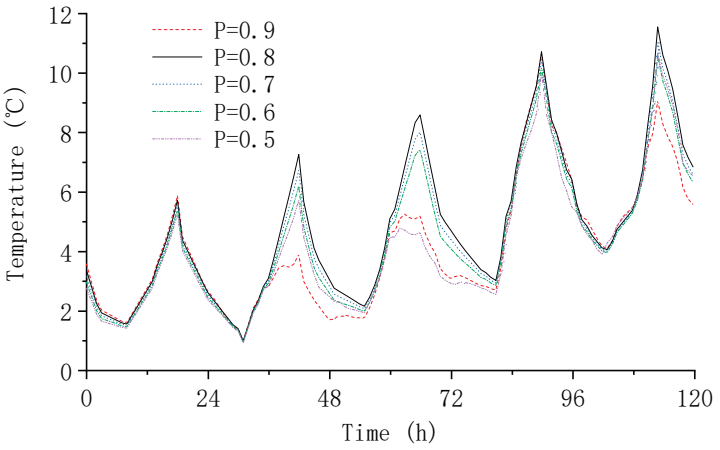


Figure 12. Critical point temperatures of the web plate for different atmospheric transparency coefficients.

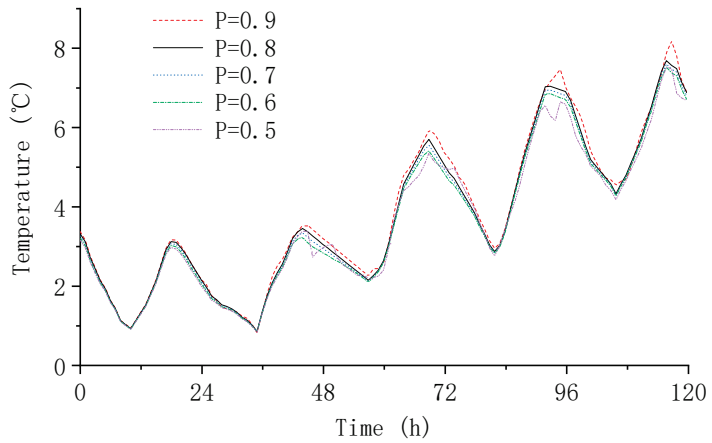


Figure 13. Critical point temperatures of the bottom plate for different atmospheric transparency coefficients.

As shown in Figure 11, because the atmospheric transparency directly affects the magnitude of solar radiation received by the box girder, the top plate irradiated by the Sun reflects a large correlation with the atmospheric transparency in the temperature distribution. The daily maximum temperature at the key point of the top plate is greatly

affected by the change in atmospheric transparency, and it increases with the increase in the atmospheric transparency coefficient. When the atmospheric transparency coefficient increases from 0.8 to 0.9, the daily maximum temperature of the key point of the roof plate on the third day increases from 7.3 °C to 10.3 °C, with an increase of 41.1%. The daily minimum temperature and the change pattern of temperature were less affected.

The daily maximum temperature of the key point temperature of the web plate increases with the increase in the atmospheric transparency coefficient from 0.5 to 0.8. However, when the atmospheric transparency coefficient increases to 0.9, the daily maximum temperature decreases abruptly, which is presumed to be due to the fact that the web plate is subjected to both direct solar radiation and scattered radiation, and the effect of scattered radiation decreases significantly when the atmospheric transparency coefficient reaches 0.9, which leads to a decrease in the daily maximum temperature.

Because the bottom plate is always in the shaded area, the temperature distribution at the key point of the bottom plate is minimally affected by the atmospheric transparency. As can be seen from Figure 13, the temperature curves at the key points of the bottom plate at different atmospheric transparency coefficients basically overlap, and the daily maximum temperature at the key points of the bottom plate only changes slightly when P = 0.9 and P = 0.5, and the value of the key point temperature change ranges from −0.8 °C to 0.6 °C. The temperature distribution at the key points of the bottom plate is also affected by the atmospheric transparency coefficient.

In summary, atmospheric transparency has the greatest effect on the top plate temperature, and the maximum daily temperature of the top plate increases with the increase in the atmospheric transparency coefficient. Atmospheric transparency also has less influence on the temperature of the web plate and has the least influence on the temperature of the bottom plate. When the atmospheric transparency coefficient is too large or too small, the maximum daily temperature of the web plate will appear to decrease abruptly.

6.2. Influence of Short-Wave Absorptivity in Concrete

Short-wave absorptance of concrete refers to the proportion of short-wave radiation (mainly solar radiation) absorbed by concrete material. In this study, the influence of the short-wave absorptance of concrete on the temperature field distribution of a box girder structure was explored by setting the short-wave absorptance of concrete to four values of 0.8, 0.6, 0.4, and 0.2. Figures 14–16 show the temperature diagrams of key points of the box girder at different short-wave absorptivity.

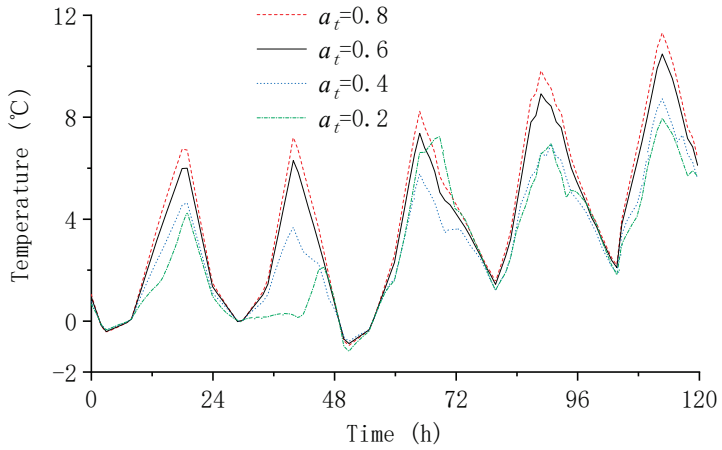


Figure 14. Critical point temperatures of the top plate for different short-wave absorptivity.

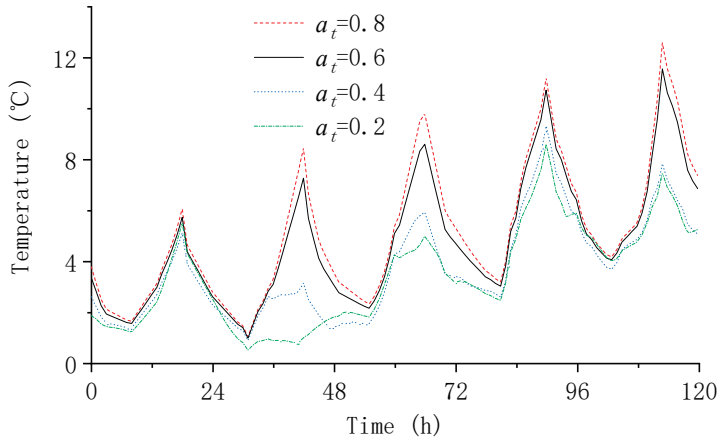


Figure 15. Critical point temperatures of the web plate for different short-wave absorptivity.

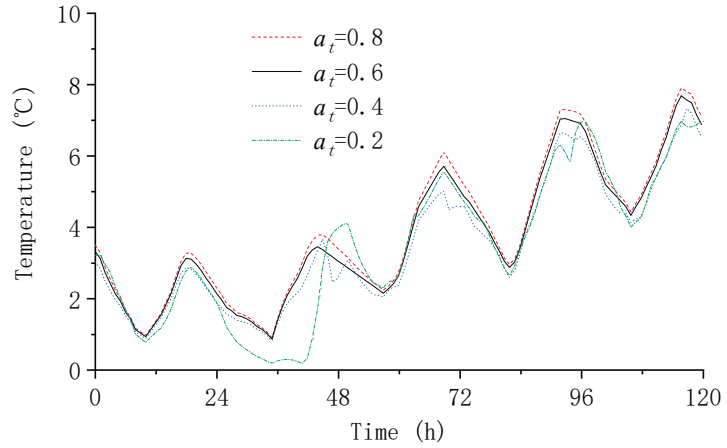


Figure 16. Critical point temperatures of the bottom plate for different short-wave absorptivity.

As can be seen in Figures 14 and 15, the short-wave absorptivity of concrete has a more significant effect on the temperatures of the top and web plate. When the short-wave absorptivity decreased from 0.6 to 0.4, the temperatures of the top and web plate decreased significantly. The maximum decrease in the temperature of the top plate reached 41.8%, and the maximum decrease in the temperature of the web plate reached 57.1%.

As can be seen in Figure 16, the bottom plate temperature is less affected by the short-wave absorptivity. Although there is a small decrease in the bottom plate temperature as the short-wave absorptivity decreases, the regularity is not obvious.

In summary, the short-wave absorptivity of concrete can significantly affect the temperature distribution of concrete box girders, and the temperatures of the top plate and web plate decrease with the decrease in the short-wave absorptivity of concrete. When designing box girders, the structural temperature can be reduced covering the structural surface with materials with low short-wave absorptivity.

7. Discussion

In order to explore the boundary conditions for the three-dimensional temperature field of box girders in natural environments, a series of studies were carried out in this paper.

Firstly, based on the theoretical basis of engineering thermodynamics, three kinds of temperature field boundary conditions of solar radiation, convective heat transfer, and radiative heat transfer of box girder under natural environment were investigated, respec-

tively, which comprehensively considered the factors of direct solar radiation, atmospheric scattering, ambient radiation, structural shading effect, and convective heat transfer.

Secondly, taking a box girder of a section of railroad line as an example, the boundary condition calculation method in this study was used to establish a finite element model. The structural temperature field distribution was analyzed and verified with measured temperature data. The calculation results are in good agreement with the measured results, and the model can effectively simulate the three-dimensional temperature field distribution of the box girder.

Finally, the effects of the atmospheric transparency coefficient and concrete short-wave absorptivity on the temperature field distribution of box girders are discussed. The atmospheric transparency has the greatest effect on the temperature of the top slab and the least effect on the temperature of the bottom slab. The daily temperature maximum of the top plate increases with the increase in the atmospheric transparency coefficient. Atmospheric transparency also has a certain influence on the temperature of the web plate. When the atmospheric transparency coefficient is too large or too small, the daily maximum temperature of the web plate will appear to decrease abruptly. The short-wave absorptivity of concrete can significantly affect the temperature distribution of the concrete box girder, and the temperature of the top plate and web plate decreases with the decrease in the short-wave absorptivity of concrete. When designing box girders, the structural temperature can be reduced covering the structural surface with materials that have low short-wave absorptivity.

Author Contributions: Conceptualization, B.Y.; methodology, B.Y.; software, H.F.; validation, B.Y., H.F. and H.S.; formal analysis, H.F.; writing—original draft preparation, B.Y., H.F. and H.S.; writing—review and editing, H.F., H.S. and B.H. All authors have read and agreed to the published version of the manuscript.

Funding: This research was funded by the National Natural Science Foundation of China (grant number 52278470) and the Natural Science Foundation of Hunan Province (grant number 2022JJ30741).

Institutional Review Board Statement: Not applicable.

Informed Consent Statement: All authors are aware of and agree with the publication of the paper.

Data Availability Statement: The original contributions presented in this study are included in the article. Further inquiries can be directed to the corresponding author.

Acknowledgments: The authors would like to thank the National Natural Science Foundation of China (Project No. 52278470) and the Natural Science Foundation of Hunan Province (Project No. 2022JJ30741).

Conflicts of Interest: The authors declare no conflicts of interest.

References

1. Peeters, B.; De, R. One-year monitoring of effects versus damage the Z24-Bridge: Environmental events. *Earthq. Eng. Struct. Dyn.* **2001**, *30*, 149–171. [CrossRef]
2. Ni, Y.; Hua, X.; Fan, K.; Ko, J.M. Correlating modal properties with temperature using long-term monitoring data and support vector machine technique. *Eng. Struct.* **2005**, *27*, 1762–1773. [CrossRef]
3. Dai, G.; Wang, F.; Ge, H.; Xiao, Y.; Rao, H. Temperature pattern and extreme value of concrete high pier of high-speed railway bridge. *Tiedao Kexue Yu Gongcheng Xuebao* **2023**, *20*, 961–972.
4. Huang, S.; Cai, C.; Zou, Y.; He, X.; Zhou, T.; Zhu, X. Experimental and Numerical Investigation on the Temperature Distribution of Composite Box-girders with Corrugated Steel Webs. *Struct. Control. Health Monit.* **2022**, *29*, e3123. [CrossRef]
5. Zhang, F.; Liu, J.; Gao, L. Experimental Investigation of Temperature Gradients in a Three-Cell Concrete Box-Girder. *Constr. Build. Mater.* **2022**, *335*, 127413.
6. Zhang, P.; Wang, C.; Wu, G.; Wang, Y. Temperature Gradient Models of Steel-Concrete Composite Girder Based on Long-Term Monitoring Data. *J. Constr. Steel Res.* **2022**, *194*, 107309. [CrossRef]

7. Fan, J.; Li, B.; Liu, C.; Liu, Y.-F. An Efficient Model for Simulation of Temperature Field of Steel-Concrete Composite Beam Bridges. *Structures* **2022**, *43*, 1868–1880. [CrossRef]
8. Elshoura, A.; Okeil, A. Calibration of Temperature Gradient Load Factor for Service Limit State Design of Concrete Slab-on-Girder Bridges. *J. Bridge Eng.* **2022**, *27*, 04022112. [CrossRef]
9. Liu, Y.; Ma, Z.; Liu, J.; Zhu, W.; Wang, X.; Li, M. Temperature action and zoning of concrete jointless bridge in Shanxi. *J. Traffic Transp. Eng.* **2022**, *22*, 85–103.
10. Zhu, Y.; Sun, D.; Shuang, M. Investigation of temperature-induced effect on rail-road suspension bridges during operation. *J. Constr. Steel Res.* **2024**, *215*, 108542. [CrossRef]
11. Dai, G.; Wang, F.; Chen, Y.; Ge, H.; Rao, H. Modelling of extreme uniform temperature for high-speed railway bridge piers using maximum entropy and field monitoring. *Adv. Struct. Eng.* **2023**, *26*, 302–315. [CrossRef]
12. Zhang, L.; Zhou, L.; Bu, J.; Liu, Q.; Wei, B.; Zhao, C.B.; Chai, W. Temperature gradient estimation of long-span concrete box girders using average conditional exceedance rate function. *Struct. Infrastruct. Eng.* **2024**, 1–15. [CrossRef]
13. Yang, D.; Guan, Z.; Yi, T.; Li, H.-N.; Liu, H. Structural temperature gradient evaluation based on bridge monitoring data extended by historical meteorological data. *Struct. Health Monit.* **2024**, *23*, 1800–1815. [CrossRef]
14. Zhang, H.; Liu, D.; Zhao, W.; Ding, S.; Liu, Y.; Yang, J.; Lu, W. Boundary Condition and Distribution Study of Temperature Field of Rail-Cum-Road Steel Truss Girder. *Zhongguo Tiedao Kexue* **2023**, *44*, 91–101.
15. Zhao, R.; Wang, Y. Studies on Temperature Field Boundary Conditions for Conerete Box girder Bridges Under Solar Radiation. *Zhongguo Gonglu Xuebao* **2016**, *29*, 52–61.
16. Zhu, J.; Chen, K.; Meng, Q. Fine Analysis Method for Spatial Temperature Field of Long-Span Suspension Bridge. *Tianjin Daxue Xuebao* **2018**, *51*, 339–347.
17. Peng, Y. Studies on Theory of Solar Radiation Thermal Effects on Concrete Bridges with Application. Ph.D. Dissertation, Southwest Jiaotong University, Chengdu, China, 2007.
18. Incropera, F.; DeWitt, D.; Bergman, T.; Lavine, A.S. *Fundamentals of Heat and Mass Transfer*, 6th ed.; John Wiley & Sons: Hoboken, NJ, USA, 2006.
19. Liu, Y.; Su, H.; Dai, G. Study on Temperature Fields of Simply-supported Box Girder under Solar Radiation in Passenger Dedicated Lines Based on Meteorological Conditions. *Tiedao Xuebao* **2019**, *14*, 154–159.
20. Dai, G.; Zheng, P.; Yan, B.; Xiao, X.N. Longitudinal Force of CWR on Box Girder under Solar Radiation. *Zhejiang Daxue Xuebao* **2013**, *47*, 609–614.

Disclaimer/Publisher's Note: The statements, opinions and data contained in all publications are solely those of the individual author(s) and contributor(s) and not of MDPI and/or the editor(s). MDPI and/or the editor(s) disclaim responsibility for any injury to people or property resulting from any ideas, methods, instructions or products referred to in the content.

applied sciences

MDPI

Article

Inverse Analysis of Thermal Parameters of Arch Dam Concrete Based on Walrus Optimization Algorithm

Youle Wang [1,2,3], Zhengjian Miao [1,2,3], Rui Song [4], Junchi Zhou [4], Yuheng Pan [5] and Feng Wang [4,*]

[1] Changjiang Survey Planning Design and Research Co., Ltd., Wuhan 430010, China; wyl98517@tju.edu.cn (Y.W.); miaozhengjian@cjwsjy.com.cn (Z.M.)
[2] State Key Laboratory of Water Resources Engineering and Management, Wuhan 430072, China
[3] National Dam Safety Research Center, Wuhan 430010, China
[4] College of Hydraulic & Environmental Engineering, China Three Gorges University, Yichang 443002, China; 202308590221027@ctgu.edu.cn (R.S.); 202308590221122@ctgu.edu.cn (J.Z.)
[5] College of Natural Resources and Environment, Northwest A&F University, Yangling 712100, China; panyuheng@arizona.edu
* Correspondence: wangfengctgu@ctgu.edu.cn; Tel.: +86-15997598162

Abstract: In the simulation of concrete thermal stress fields, thermal parameters are crucial for calculating the concrete temperature field. In actual construction, due to the adjustment of the concrete mixing ratio and the changing external environment (temperature fluctuations, cooling conditions, solar radiation, thermal insulation measures, etc.), there are significant differences between the thermal parameters obtained in tests and the actual working conditions, which affect the simulation accuracy. Therefore, the inverse analysis of concrete thermal parameters under real working conditions can be carried out based on the measured temperature data. A method for inverse analysis of thermal parameters of arch dams using the walrus optimization algorithm (WaOA) is proposed. To verify the accuracy of the inversion parameters, twelve classical test functions are used to compare the three algorithms to evaluate their fitness. The efficiency difference is analyzed by nonparametric methods such as Fredman and Wilcoxon rank sum test. The results consistently indicate that the walrus optimization algorithm performs better. Furthermore, the WaOA is utilized for the parameter inversion of an arch dam in the downstream area of the Jinsha River. We bring the inversion results into different dam sections to calculate the temperature field during construction, which effectively verifies the efficient solution ability of the WaOA for the inverse analysis of concrete thermal parameters under complex engineering backgrounds.

Keywords: parameter inversion; walrus optimization algorithm; massive concrete; finite element method; circulating water cooling

1. Introduction

During the construction phase of the concrete arch dam, because of the superposition effect of the hydration heat release of the concrete itself and the external environment temperature, the temperature inside the dam will rise sharply. Then, a significant temperature gradient will be formed inside the dam body, accompanied by a large temperature stress. When the thermal stress exceeds the limit of the tensile strength of the concrete, it may induce temperature cracking [1–3] and affect the quality of pouring blocks. To predict real-time and accurate monitoring of arch dam temperature behavior information, it is insufficient to collect data only by current instruments. Therefore, it is necessary to introduce the simulation technology to forecast the forthcoming evolutionary tendency of the dam's temperature, building an accurate concrete temperature field model, and then

analyze the stress state of the dam [4–6]. The simulation of the temperature field and stress field is affected by many factors. The most important are the characteristic parameters of construction materials. The thermal conductivity coefficient, temperature rise coefficient, surface heat transfer coefficient, and adiabatic temperature rise of different structures are different. The actual thermodynamic parameters of the same concrete structure are different due to different environmental conditions [7–10] (including temperature, humidity, wind speed, etc.). The choice of traditional thermal parameters is often faced with the challenges of high cost and difficulty in accurately fitting the onsite construction conditions. It is difficult to ensure the accuracy of simulation calculation. Therefore, by using the field measured data to carry out parameter inversion analysis, we can obtain more accurate thermal parameter values. It can also improve the accuracy of the simulation calculation model of the concrete thermal stress field.

Parameter inverse analysis is a problem that requires searching through a large space of multiparameter combinations. Usually, the problem of parameter inversion analysis is converted into an optimization issue. The objective function is minimized by multiple iterations [11]. However, some traditional optimization methods often have problems such as locally optimal solution, being time-consuming, and having low accuracy for complex numerical models [12]. Therefore, searching for efficient optimization algorithms has become a popular topic. In recent years, the inversion of thermal parameters for dams has captured the interest of numerous scholars and has been thoroughly investigated. Pei et al. [10] utilized an enhanced genetic algorithm to conduct the inversion of the thermal parameters of concrete arch dams. Han et al. [13] set up a thermal model for concrete by taking the degree of hydration into account, and inversed the specific heat and thermal conductivity of fly-ash concrete by BP neural network. Zhao et al. [14] developed an inversion program relying on the particle swarm optimization algorithm (PSO) to invert the thermal resistance parameters of early cement paste. Shi et al. [15] used a genetic algorithm to inverse the thermal parameters, and used the inversed parameters to predict the temperature change of concrete within 300 days. According to the temperature data that were monitored by the DTS system, Su et al. [16] inverted the thermal diffusion coefficient and surface heat transfer coefficient of concrete, and inserted the results into the finite element model to conduct the calculation. It turned out that the simulation outcomes were highly consistent with the calculation results.

As a population-based optimization strategy, with the utilization of random operators by meta-heuristic algorithms (MAs), the global search capability is enhanced and the local optimal trap can be effectively avoided. It is straightforward to carry out and features low computational complexity. It is widely used in engineering fields [17]. The walrus optimization algorithm [18] is a new meta-heuristic algorithm proposed by Pavel Trojovský et al. in 2023, which mimics the behavior of walruses when they are feeding, migrating, escaping, and fighting against predators in nature. As a creature with social and natural behaviors, the walrus shows significant spatial displacement characteristics when preying on and avoiding natural enemies. Because of its unique characteristics, the WaOA has higher global search capability and efficiency, and shows excellent optimization performance for most benchmark test functions. Through applying a series of benchmark test functions (including unimodal, multimodal functions, and CEC 2015 and CEC 2017 test function sets), the researchers carried out the test on the performance of the WaOA, and compared it with ten other well-known meta-heuristic algorithms, like the genetic algorithm (GA), particle swarm optimization (PSO), gravitational search algorithm (GSA), etc., fully demonstrating its superior exploration and development capabilities. In addition, the algorithm was also utilized to solve engineering design problems and practical engineering optimization problems in the CEC 2011 test function set. This paper conducts

a comparison involving WaOA, the sand cat swarm optimization algorithm (SCSO), the ant lion optimization algorithm (ALO), and the seagull optimization algorithm (SOA), and 12 standard functions are selected for testing. Two nonparametric statistical methods, the Friedman test and the Wilcoxon rank sum test, serve to guarantee the reliability of the evaluation results. The test results show that the WaOA performs well in most benchmark test functions and has the best performance.

Based on the field-measured temperature dataset of C40 concrete of a dam in the downstream area of Jinsha River, this study comprehensively considers the combined impacts of the fluctuation in external environmental temperature and water-cooling effect, and applies the WaOA to the inversion analysis of the thermal parameters of the dam concrete. By formulating specific engineering optimization problems, the performance of the WaOA is evaluated in depth, and it offers a reference for the inversion of thermal parameters of arch dam concrete.

2. Walrus Optimization Algorithm

The walrus optimization algorithm (WaOA) simulates the walrus population behavior to achieve efficient optimization. The core idea is to balance global exploration and local exploration. In the early stage of the algorithm, the global search is enhanced by the leader and the random disturbance factor. The migration strategy maintains the diversity of the population. In the local development stage, the dynamic neighborhood radius adjustment mechanism is used to improve the convergence accuracy. This collaborative mechanism makes the algorithm perform well in complex multipeak problems. With these advantages, the WaOA solves high-dimensional, multiconstraint, and nonlinear problems in the field of mechanical structure optimization. It minimizes the cost under safety constraints in safety-sensitive fields such as pressure vessels. However, the existing research focuses on multifocus structure optimization. In this study, the WaOA is applied to the inversion of thermal parameters of concrete for the first time. By constructing a mapping relationship and using its dynamic neighborhood adjustment mechanism to break through the limitations of traditional algorithms, the optimization is transformed into an objective function solution. It improves the inversion accuracy and provides a new method for parameter optimization of complex engineering systems.

2.1. Initialization of the Algorithm

In the WaOA, every walrus stands for a prospective solution to the optimization problem. The candidate value of the problem variable directly corresponds to its position. Thus, each walrus can be considered as a vector, and the entire walrus population can be mathematically modeled through the population matrix. In the initial phase of the WaOA, the population matrix is randomly generated according to Equation (1).

$$X = \begin{bmatrix} X_1 \\ \vdots \\ X_i \\ \vdots \\ X_N \end{bmatrix}_{N\times m} = \begin{bmatrix} x_{1,1} & \cdots & x_{1,j} & \cdots & x_{1,m} \\ \vdots & \ddots & \vdots & \ddots & \vdots \\ x_{i,1} & \cdots & x_{i,j} & \cdots & x_{i,m} \\ \vdots & \ddots & \vdots & \ddots & \vdots \\ x_{N,1} & \cdots & x_{N,j} & \cdots & x_{N,m} \end{bmatrix}_{N\times m} \quad (1)$$

In the formula, X is a walrus population; X_i refers to the ith walrus; $X_{i,j}$ stands for the jth decision variable value recommended by the ith walrus; N and m represent the number of walrus and decision variables, respectively.

Each walrus symbolizes a candidate solution to the problem. The objective function of the problem can be assessed in light of the recommended value for the decision variable. Equation (2) presents the estimated value of the objective function derived from the walrus.

$$F = \begin{bmatrix} F_1 \\ \vdots \\ F_i \\ \vdots \\ F_N \end{bmatrix}_{N\times 1} = \begin{bmatrix} F(X_1) \\ \vdots \\ F(X_i) \\ \vdots \\ F(X_N) \end{bmatrix} \tag{2}$$

In the formula, F represents the objective function vector; F_i represents the objective function value based on the ith walrus calculation.

The objective function value is the core index used to evaluate the candidate solution. The candidate solutions that make the objective function achieve the optimal value are called the optimal members; others are called the worst members. The update of the objective function value in each iteration determines the update of the best and worst members.

2.2. Feeding Strategy

During the feeding phase, the strongest and longest-tusked walrus will guide other members of the population to forage. The length of the walrus tusk bears a resemblance to the quality of the objective function value of the candidate solution, and the candidate solution with the optimal objective function value is deemed the strongest walrus within the group. This search pattern adopted by the walrus scans diverse regions within the search space, thereby augmenting the global search capability of the WaOA. The mathematical model of updated walrus position is shown in Equations (3) and (4).

$$x_{i,j}^{P_1} = x_{i,j} + rand_{i,j}\cdot(SW_j - I_{i,j}\cdot x_{i,j}) \tag{3}$$

$$X_i = \begin{cases} X_i^{P_1}, & F_i^{P_1} < F_i \\ X_i, & else \end{cases} \tag{4}$$

In the formula, $X_i^{P_2}$ represents the new position of the ith walrus on the basis of the first stage; $X_{i,j}^{P_2}$ is its jth dimension; $F_i^{P_1}$ is its objective function value; $rand_{i,j}$ is a random number in the interval [0,1]; SW is the best candidate solution for the strongest walrus; $I_{i,j}$ is an integer randomly selected between 1 and 2. $I_{i,j}$ is used to enhance the probing ability of the algorithm. When $I_{i,j}$ is 2, the position change of the walrus is more significant and the range is wider.

2.3. Migration Strategy

Walruses have a natural behavior of migrating to outcrops or rocky beaches because of the rising temperatures in late summer. The WaOA utilizes this behavior to direct the walrus within the search space and locate the most suitable area. Mathematical modeling of this behavior mechanism is carried out by Equations (5) and (6). The model presumes that each walrus migrates to the location of another walrus (randomly selected) within the search space. A new position is generated on the basis of Equation (5), and then, in accordance with Equation (6), if it enhances the value of the objective function, the prior position of the walrus will be replaced.

$$x_{i,j}^{P_2} = \begin{cases} x_{i,j} + rand_{i,j}\cdot\left(x_{k,j} - I_{i,j}\cdot x_{i,j}\right), F_k < F_i \\ x_{i,j} + rand_{i,j}\cdot\left(x_{i,j} - x_{k,j}\right), else \end{cases} \tag{5}$$

$$X_i = \begin{cases} X_i^{P_2}, F_i^{P_2} < F_i \\ X_i, else \end{cases} \tag{6}$$

In the formula, $X_i^{P_2}$ represents the new position of the ith walrus generated on the basis of the second stage; $X_{i,j}^{P_2}$ is its jth dimension; $F_i^{P_2}$ is its objective function value; X_k represents the position of selected walrus to migrate the ith walrus towards it. $k \in \{1, 2, \ldots, N\}$ and $k \neq i$; $x_{k,j}$ is its jth dimension; F_k is its objective function value.

2.4. Avoid Predator Strategy

Simulating the natural behavior of a walrus changing its position to avoid predators effectively improves the local search capability of the WaOA. During the simulation, we set each walrus to have a dynamic neighborhood centered on its current position. At the beginning, with the aim of thoroughly probing the search space, the neighborhood radius is configured to be at its maximum. As the iteration increases, the neighborhood radius is gradually reduced in order to accurately approximate the optimal solution. It improves the local search capability. To realize this process, the concept of local lower/upper limits is introduced in the WaOA to dynamically adjust the neighborhood radius. A neighborhood is set around each walrus, and a new position is randomly generated initially according to Equation (7), and then its field is shrunk according to Equation (8). In cases where the value of the objective function is enhanced, the prior position will be substituted in accordance with Equation (9).

$$x_{i,j}^{P_3} = x_{i,j} + \left(lb_{local,j}^t + \left(ub_{local,j}^t - rand \cdot lb_{local,j}^t \right) \right) \tag{7}$$

$$Localbounds: \begin{cases} lb_{local,j}^t = \frac{lb_j}{t} \\ ub_{local,j}^t = \frac{ub_j}{t} \end{cases} \tag{8}$$

$$X_i = \begin{cases} X_i^{P_3}, F_i^{P_3} < F_i \\ X_i, else \end{cases} \tag{9}$$

In the formula, $X_i^{P_3}$ represents the new location of the ith walrus generated on the basis of the third stage; $x_{i,j}^{P_3}$ is its jth dimension, $F_i^{P_3}$ is its objective function value; t is the number of iterations; lb_j^t and ub_j^t are the lower limit and upper limit of the jth variable; $lb_{local,j}^t$ and $ub_{local,j}^t$ are the local lower limit and upper limit of the jth variable.

After the first iteration of the WaOA, the walrus position is updated and the value of the objective function is calculated following a three-stage strategy. Then, iterative optimization following the steps of the WaOA is performed until the number of iterations is appropriate. Finally, the WaOA outputs the optimal candidate solution as the final solution. The flowchart illustrating the execution of the WaOA is presented in Figure 1.

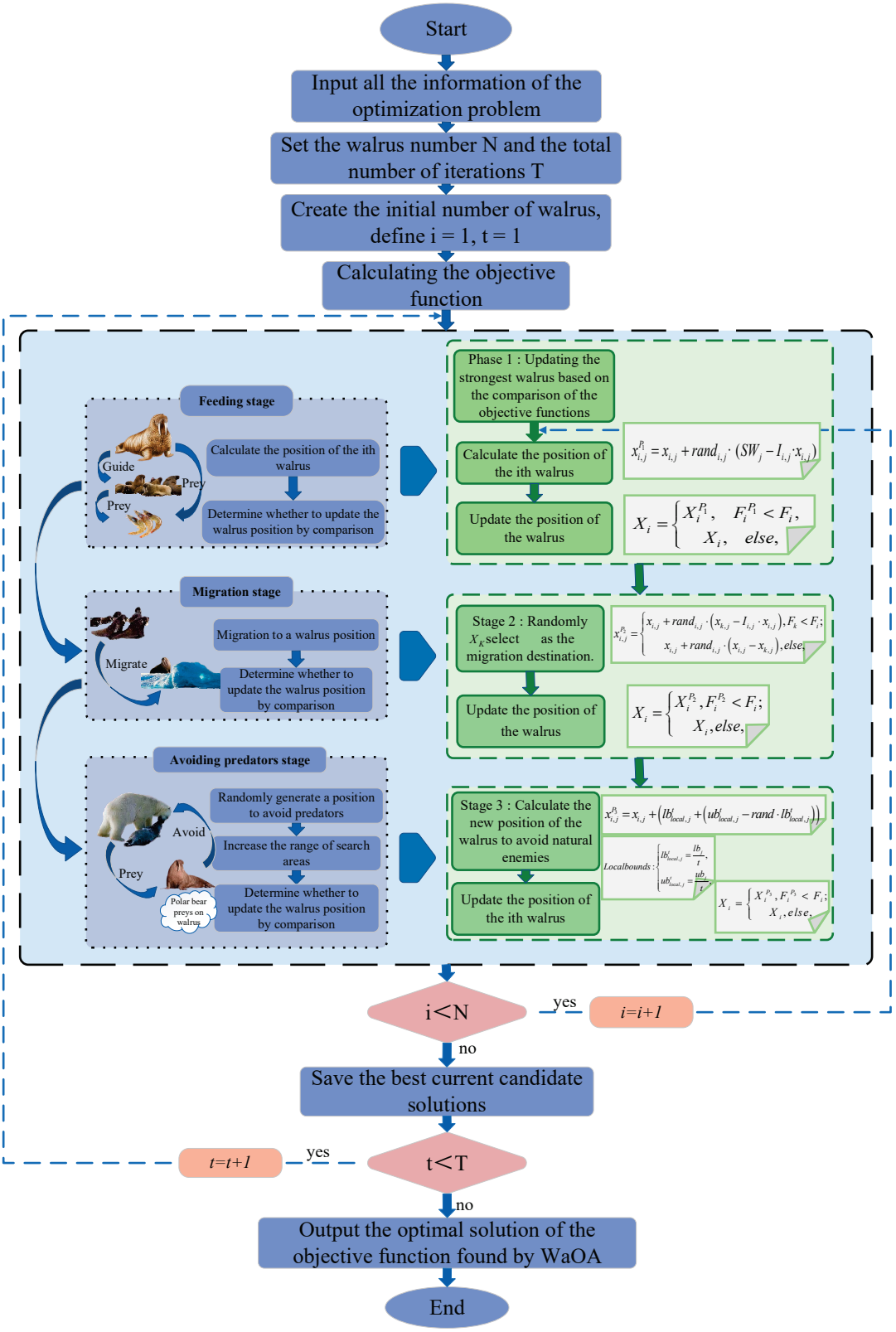


Figure 1. Flowchart of the WaOA.

3. Numerical Experiments and Analysis

3.1. Benchmark Function

In the process of developing and improving optimization algorithms, benchmark function testing is highly valued [7]. Twelve benchmark functions are selected for the

simulation test, as shown in Table 1. The definition domain limits the search space, and the theoretical values reflect the optimal solutions. F1–F6 are unimodal functions that possess only one global optimal solution, without a local optimum. They are utilized to test the convergence speed and development behavior of the algorithm. F7–F12 are multimodal functions, which possess global optimum as well as several local optimal solutions. The number grows exponentially as the dimension increases, which can be utilized to examine the capability of the algorithm to break away from local optimal and global search capability [8,9]. One of the advantages of the multimodal function is that it has high similarity with the search space of practical problems [4]. Figure 2 displays the diagram of the search space of the WaOA in benchmark functions F7–F12.

Table 1. Test function.

Number	Name	Benchmark Functions	Dim	Range	$f_{\min}$
F1	Sphere	$f_1(x) = \sum_{i=1}^{Dim} x_i^2$	30	[−100,100]	0
F2	Schwefel 2.22	$f_2(x) = \sum_{i=1}^{Dim} \lvert x_i \rvert + \prod_{i=1}^{Dim} \lvert x_i \rvert$	30	[−10,10]	0
F3	Schwefel 1.2	$f_3(x) = \sum_{i=1}^{Dim} \left(\sum_{j-1}^{i} x_i \right)^2$	30	[−100,100]	0
F4	Schwefel 2.21	$f_4(x) = \max_i \{ \lvert x_i \rvert, 1 \le i \le D \}$	30	[−100,100]	0
F5	Rosenbrock	$f_5(x) = \sum_{i=1}^{Dim-1} \left[100(x_{i+1} - x_i^2)^2 + (x_i - 1)^2 \right]$	30	[−30,30]	0
F6	Step	$f_6(x) = \sum_{i=1}^{Dim} \left([x_i + 0.5] \right)^2$	30	[−100,100]	0
F7	Quartic	$f_7(x) = \sum_{i=1}^{Dim} i \times x_i^4 + random[0,1)$	30	[−1.28,1.28]	0
F8	Schwefel 12.26	$f_8(x) = \sum_{i=1}^{Dim} -x_i \sin\left(\sqrt{x_i}\right)$	30	[−500,500]	−12,569.5
F9	Rastrigin	$f_9(x) = \sum_{i=1}^{Dim} \left[x_i^2 - 10\cos(2\pi x_i + 10) \right]$	30	[−5.12,5.12]	0
F10	Ackley	$f_{10}(x) = -20\exp\left(-0.2\sqrt{\frac{i}{Dim}\sum_{i=1}^{Dim} x_i^2} \right) - \exp\left(\frac{1}{Dim}\sum_{i=1}^{Dim} \cos(2\pi x_i) \right) + 20 + e$	30	[−32,32]	0
F11	Griewank	$f_{11}(x) = \frac{1}{4000}\sum_{i=1}^{Dim} x_i^2 - \prod_{i=1}^{Dim} \cos\left(\frac{x_i}{\sqrt{i}} \right) + 1$	30	[−600,600]	0
F12	Generalized penalized	$f_{12}(x) = \frac{\pi}{Dim}\left\{ 10\sin(\pi y_1) + \sum_{i=1}^{Dim-1} (y_i - 1)^2 \left[1 + 10\sin^2(\pi y_{i+1}) \right] + (y_{Dim} - 1)^2 \right\} + \sum_{i=1}^{Dim} u(x_i, 10, 100, 4)$, $y_i = 1 + \frac{x_i + 1}{4}$, $u(x_i, a, k, m) = \begin{cases} k(x_i - a)^m & x_i > a \\ 0 & -a < x_i < a \\ k(-x_i - a)^m & x_i < -a \end{cases}$	30	[−50,50]	0

The theoretical optimal value of function F8 presents the feature tightly related to its dimension. Meanwhile, it changes along with the change of the dimension. The ideal value of F8 ought to be $f_{\min} = -418.9872 \times \dim$. When the dimension denotes 30, the optimal value should be −12,569.5 [11].

Regarding the function F12,

$$y_i = 1 + \frac{x_i+1}{4},$$
$$u(x_i, a, k, m) = \begin{cases} k(x_i - a)^m & x_i > a \\ 0 & -a < x_i < a \\ k(-x_i - a)^m & x_i < -a \end{cases} \tag{10}$$

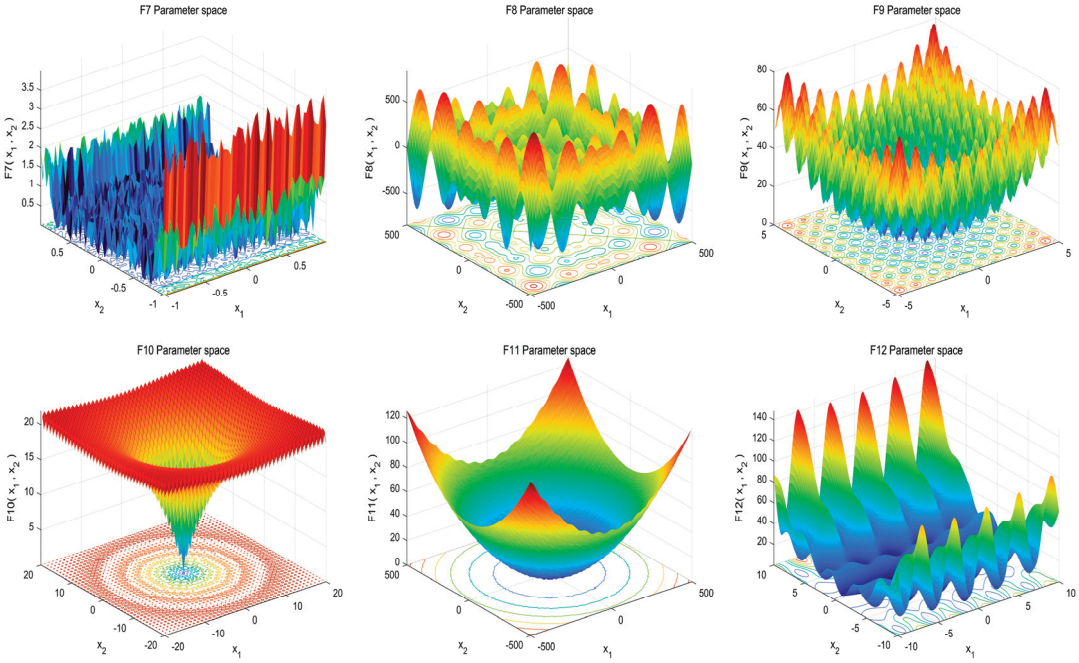


Figure 2. Search space diagram of the WaOA in benchmark functions.

3.2. Algorithm Parameter Setting

All algorithm tests are carried out in MATLAB R2022a software. The test setup consists of Windows 11, an AMD Ryzen 7 5800H 3.20 GHz processor, and 16 GB of RAM (MAXSUN, Yichang, China). To guarantee the fairness of the comparison, it is necessary to uniformly set all algorithms to the same variables uniformly. For the specific parameters of various algorithms, we refer to the relevant literature and adopt the parameter values recommended in the standard version of the algorithm. The parameters are configured as presented in Table 2.

Table 2. Different algorithm parameter settings.

Algorithms	Parameters	Values
For all algorithms	Population size	30
	Iterations	500
Walrus optimization algorithm (WaOA)	No specific parameters	
Sand cat swarm optimization algorithm (SCSO)	S_M	2
	Roulette selection	[0,360]
Seagull optimization algorithm (SOA)	Control parameter A	[0,2]
	f_c	2
Ant lion optimization algorithm (ALO)	Random number F	[0.2,0.8]
	Probability factor P_{CR}	0.8

3.3. Algorithm Performance Calculation

The meta-heuristic algorithm has the feature of random search. It usually obtains the approximate optimal solution, which may be different from the global optimal solution. The calculation results may be different each time [10]. In order to reduce the randomness bias, we perform twenty independent operations on each test function. The mean and standard deviation of fitness values serve as the metrics for evaluating algorithm performance. The mean value is utilized to verify the convergence rate and solution accuracy of the algorithm, while the standard deviation is employed to reveal the stability. Table 3 shows the test results of four different algorithms after 20 independent repeated experiments.

Table 3. Performance comparison of four algorithms.

Function	WaOA		SCSO		ALO		SOA	
	Mean	Std	Mean	Std	Mean	Std	Mean	Std
F1	5.50×10^{-283}	0.00	1.49×10^{-113}	4.61×10^{-113}	1.08×10^{-3}	7.18×10^{-4}	1.70×10^{-11}	3.42×10^{-11}
F2	3.89×10^{-144}	1.36×10^{-143}	8.07×10^{-61}	2.86×10^{-61}	5.64×10^{1}	4.81×10^{1}	2.38×10^{-8}	3.19×10^{-8}
F3	7.22×10^{-215}	0.00	1.84×10^{-100}	4.47×10^{-100}	4.93×10^{3}	2.13×10^{3}	2.00×10^{-5}	2.85×10^{-5}
F4	3.40×10^{-135}	1.10×10^{-134}	7.31×10^{-52}	2.62×10^{-51}	1.71×10^{1}	5.10×10^{0}	5.37×10^{-3}	1.55×10^{-2}
F5	0.00	0.00	28.2	0.70	4.62×10^{2}	4.83×10^{2}	2.84×10^{1}	4.2×10^{-1}
F6	0.00	0.00	2.04	0.56	2.26×10^{-3}	1.93×10^{-3}	3.18×10^{0}	3.66×10^{-1}
F7	5.04×10^{-5}	3.97×10^{-5}	2.34×10^{-4}	2.25×10^{-4}	2.47×10^{-1}	8.50×10^{-2}	3.04×10^{-3}	1.50×10^{-3}
F8	-8.57×10^{3}	6.04×10^{2}	-6.31×10^{3}	1.08×10^{3}	-5.46×10^{3}	5.92×10^{1}	-5.02×10^{3}	3.50×10^{2}
F9	0.00	0.00	0.00	0.00	8.15×10^{1}	2.17×10^{1}	2.94×10^{0}	4.58×10^{0}
F10	2.22×10^{-15}	1.78×10^{-15}	4.44×10^{-16}	1.97×10^{-31}	6.03×10^{0}	2.72×10^{0}	2.00×10^{1}	1.50×10^{-3}
F11	0.00	0.00	0.00	0.00	5.24×10^{-2}	3.02×10^{-2}	2.33×10^{-2}	3.80×10^{-2}
F12	1.57×10^{-32}	5.47×10^{-48}	9.83×10^{-2}	4.61×10^{-2}	1.49×10^{1}	6.96×10^{0}	3.53×10^{-1}	1.79×10^{-1}

As shown in Table 3, the WaOA manages to find the optimal results in the majority of test functions. Particularly, on the functions F5, F6, F9, and F11, the theoretical optimal value 0 can be realized. It shows that the WaOA is very competitive among the eight algorithms. However, the optimization accuracy of the WaOA on function F10 is slightly worse than that of the SCSO. This phenomenon can be reasonably explained by the famous No Free Lunch (NFL) theorem; it means there is no universal algorithm that can show optimal performance on all test functions [19]. It emphasizes the close relationship between algorithm performance and problem characteristics.

However, relying on the data in Table 3 solely is not sufficient to fully evaluate the optimization effect of the WaOA on the benchmark function. In order to further understand its performance, the convergence curves on different functions for the WaOA and other algorithms are plotted, as shown in Figure 3.

As can be seen more intuitively from the Figure 3, the WaOA demonstrates excellent convergence speed and accuracy in the majority of test functions, and it can discover the optimal value more rapidly. Via the thorough analysis of the table data and the fitness curve, we can conclude that, among the four algorithms, the WaOA performs best and is capable of achieving better results.

3.4. Nonparametric Tests

Conducting a thorough analysis of the algorithm data is also a crucial part of the conclusion [20]. Nonparametric tests can provide significant results when disparities exist among the algorithms. In this paper, the Friedman test [21,22] is used to rank the algorithms. The top performance is assigned a rank of 1, the second-best one is given a rank of 2, and this ranking method continues accordingly [23]. The results of Friedman's test calculations for the four algorithms are presented in Table 4.

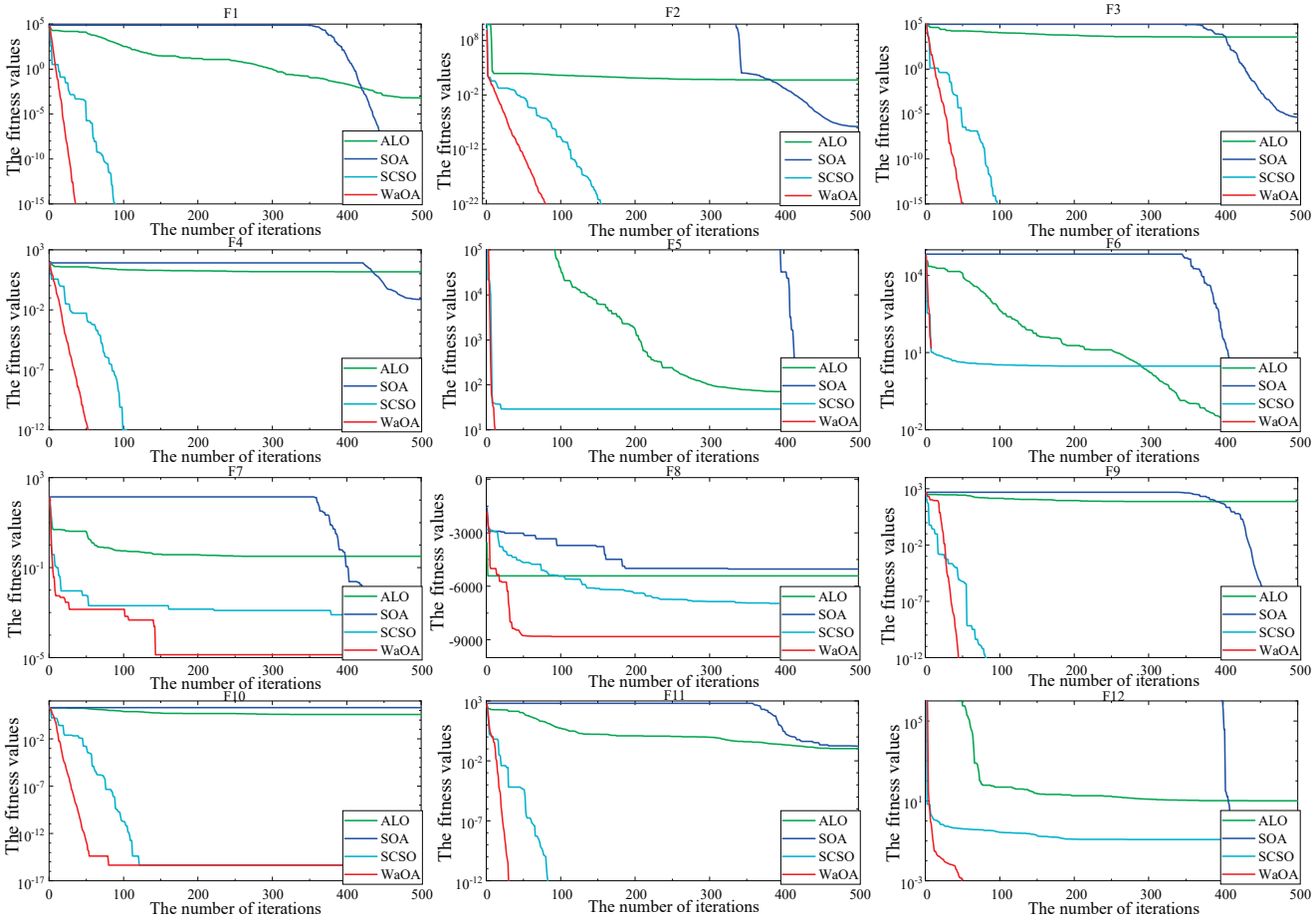


Figure 3. Algorithm fitness iteration curve.

Table 4. Friedman test results.

Algorithm	Freidman Rank	Ranking
WaOA	1.16	1
ALO	3.65	4
SOA	3.20	3
SCSO	1.98	2

It can be seen from Table 4 that the WaOA ranks first among the four algorithms, and the Freidman rank is 1.16, which suggests that it has excellent comprehensive performance.

When analyzing the performance of the algorithm, we apply the Wilcoxon rank sum test method and set the significance level p at 0.05. Under this setting, when the p-value is below 0.05, it shows that the WaOA differs significantly from other algorithms. On the contrary, it is not significant [24]. Table 5 lists the p-values of the WaOA in relation to the other three algorithms.

As shown in Table 5, the p-value of the majority of the algorithms is below 0.05 compared to the WaOA, regardless of unimodal or multimodal functions. It indicates that the WaOA has more obvious advantages. In functions F9 and F11, the p-values of the WaOA relative to the SCSO are both 1. According to the fitness curve, although the WaOA has better convergence speed and accuracy than the SCSO on these two functions in the early stage, due to the great global optimization ability of the SCSO, the WaOA cannot perform much better than the SCSO on these two functions with a sufficient number of iterations.

Generally speaking, the WaOA attains an effective equilibrium between global search and local search strategies. Compared with other algorithms, it shows better convergence speed and solution accuracy, reflecting its excellent optimization performance.

Table 5. *p*-values of the Wilcoxon rank sum test for different algorithms on functions F1–F12.

Function	ALO	SOA	SCSO
F1	8.86×10^{-5}	8.86×10^{-5}	8.86×10^{-5}
F2	8.86×10^{-5}	8.86×10^{-5}	8.86×10^{-5}
F3	8.86×10^{-5}	8.86×10^{-5}	8.86×10^{-5}
F4	8.86×10^{-5}	8.86×10^{-5}	8.83×10^{-5}
F5	8.86×10^{-5}	8.86×10^{-5}	8.86×10^{-5}
F6	8.86×10^{-5}	8.86×10^{-5}	8.86×10^{-5}
F7	8.86×10^{-5}	8.86×10^{-5}	3.38×10^{-4}
F8	8.86×10^{-5}	8.86×10^{-5}	1.40×10^{-4}
F9	8.86×10^{-5}	8.86×10^{-5}	1
F10	8.86×10^{-5}	8.86×10^{-5}	0.002
F11	8.86×10^{-5}	8.86×10^{-5}	1
F12	8.86×10^{-5}	8.86×10^{-5}	8.86×10^{-5}

4. Basic Principle of Thermal Parameter Inversion

4.1. Parameter Selection

The hydration heat of cement is a vital factor for the variation in internal thermal stress. During the calculation process of the temperature field, the adiabatic temperature rise θ of the concrete is customarily utilized as the principal parameter. Adiabatic temperature rise is the temperature growth that is directly brought about by all the heat released by the adequate hydration process of cementitious materials in concrete when there is no heat loss in the ideal state of completely isolating the external heat exchange [25].

The calculation of adiabatic temperature rise depends on a series of thermal characteristic parameters of concrete. It is often expressed in hyperbolic form, and the expression is as follows:

$$\theta(\tau) = \theta_0 \frac{\tau}{n + \tau} \tag{11}$$

Within the formula, $\theta(\tau)$ is the adiabatic temperature rise function of concrete; θ_0 is the final adiabatic temperature rise of concrete; τ is the age of concrete; n is the parameter of temperature rise law.

Although the results obtained by the hyperbolic formula demonstrate a high degree of coincidence with the experimental data, the calculation process is relatively complicated. In view of this, Zhu Bofang proposed a straightforward and efficient exponential approach to calculate the adiabatic temperature rise of concrete. The expression is as follows:

$$\theta(\tau) = \theta_0 s(1 - e^{-m_1\tau}) + \theta_0(1 - s)(1 - e^{-m_2\tau}) \tag{12}$$

The parametric relationship of Equation (12) is as follows:

$$m_1 = \frac{1.45}{n}, m_2 = 0.10m_1 \tag{13}$$

In Equations (12) and (13), m_1, m_2 represent the hydration heat dissipation coefficient of concrete. As constants without units, they dominate the slope change of the temperature rise curve in the primary stage and the advanced stage during the evolution of the concrete's temperature. It means that they affect the rate of concrete temperature rise; s is a coefficient related to the concrete material. Most of the s values in the practical application were 0.60.

In this paper, the combined exponential formula that is applicable for operation is adopted as the expression for the adiabatic temperature rise of concrete during the parameter inversion calculation process. The inversion coefficient m_1 is transformed by Equation (13) to obtain the parameter n. The expression of the final result is formulated as a hyperbolic form that can be easily organized.

The chief parameters of thermal performance during the calculation of the temperature field of the concrete are final adiabatic temperature rise θ_0, temperature rising law parameters n, surface heat transfer coefficient β, thermal conductivity λ, thermal diffusivity α, density of concrete ρ, and specific heat c. It merits attention that the number of inversion parameters has a substantial impact on the accuracy and speed of inversion. The more parameters there are, the more inappropriateness is increased and the lower the accuracy is. Therefore, the inversed thermal parameters should be preferentially selected to be sensitive to external factors and more crucial for the computation of the concrete temperature field.

The concrete density ρ, specific heat c, and thermal diffusivity α vary little with external factors, and more accurate results can be obtained through laboratory tests. Moreover, the thermal conductivity λ can be established based on the formula $\alpha = \lambda / c\rho$.

Considering that concrete is a material of poor thermal conduction, the final adiabatic temperature rise is regarded as a thermal parameter that varies considerably after the pouring block is affected by various external factors. In addition, θ_0 is also affected by the variety of concrete cement, the amount of cement, the variety and dosage of mixed materials, etc., and there are differences between the laboratory test environment and the onsite construction conditions, so it is necessary to invert θ_0. In Equations (12) and (13), the temperature rising law parameter n also exerts a significant influence on temperature calculation. After the completion of pouring, in order to ensure its quality, it is necessary to implement thermal insulation coverage on the surface or adopt a watering spray to maintain appropriate temperature conditions. For the block surface with different thermal insulation measures, we should use the different surface heat transfer coefficient β to simulate, and β needs to be inverted.

In summary, we select the final adiabatic temperature rise θ_0, surface heat transfer coefficient β, and temperature rising law parameter n as the inversion parameters.

4.2. Calculation of Concrete Temperature

Setting cooling water pipes inside mass concrete is one of the most significant measures for controlling its temperature. A large amount of hydration heat generated inside the concrete is taken away by cooling water [5]. In an average sense, Zhu Bofang regarded the cooling water pipe as a negative heat source and proposed the equivalent heat conduction equation. The expression is as follows [26,27]:

$$T(t) = T_{\omega i} + (T_i - T_{\omega i})\phi_i(t) + \theta_0\psi_i(t) \tag{14}$$

$$\phi_i(t) = e^{-p_i t} \tag{15}$$

$$\psi_i(t) = \frac{sm_1}{m_1 - p_i}\left(e^{-p_i - m_1 t_i} - e^{-m_1(t+t_i)}\right) + \frac{(1-s)m_2}{m_2 - p_i}\left(e^{-p_i - m_2 t_i} - e^{-m_2(t+t_i)}\right) \tag{16}$$

In Equations (14)–(16), $T(t)$ is the average temperature of concrete; $T_{\omega i}$ is the cooling circulating water temperature of the ith stage; T_i is the concrete temperature at the beginning of the water supply of the ith stage; $\phi_i(t)$ is the water cooling function when the ith stage is accessing water; $\psi_i(t)$ is the temperature rise function of water cooling when the ith stage is accessing water; p_i is the water cooling parameter. s, m_1, m_2 are the same as in Equations (12) and (13).

4.3. The Objective Function

With the aim of reducing the gap between the calculated temperature and the measured temperature of the simulated concrete to the minimum, by using the ordinary least squares, the mathematical expression model of the objective function is formulated as follows:

$$Q(x) = \sum_{j=1}^{p} \sum_{i=1}^{q} \left(\frac{T_{ij}' - T_{ij}}{T_{ij}} \right)^2 \tag{17}$$

$$x = (x_1, x_2, x_3, \cdots x_D) \in [L_d, U_d] \tag{18}$$

In the formula, $Q(x)$ is the objective function of the optimization problem; x is the feasible solution of the optimization problem. Each solution is a D-dimensional vector; D is the number of parameters of the intelligent optimization problem; L_d and U_d are the upper and lower bounds of the solution space; T_{ij}' and T_{ij} are the calculated value of finite element temperature and the measured value of field temperature at the j position of concrete at time i; p is the entirety number of measuring points; and q is the total duration.

In MATLAB R2010a, the parameter inversion is converted into an optimization problem through the application of the objective function. The thermal parameters are iteratively optimized by the WaOA algorithm, and then introduced into ANSYS 12.1 for temperature field simulation. When the fitness values of the objective function fulfil the convergence condition, the optimal thermal parameter values are outputted. Figure 4 shows the flowchart of MATLAB calling ANSYS for computation.

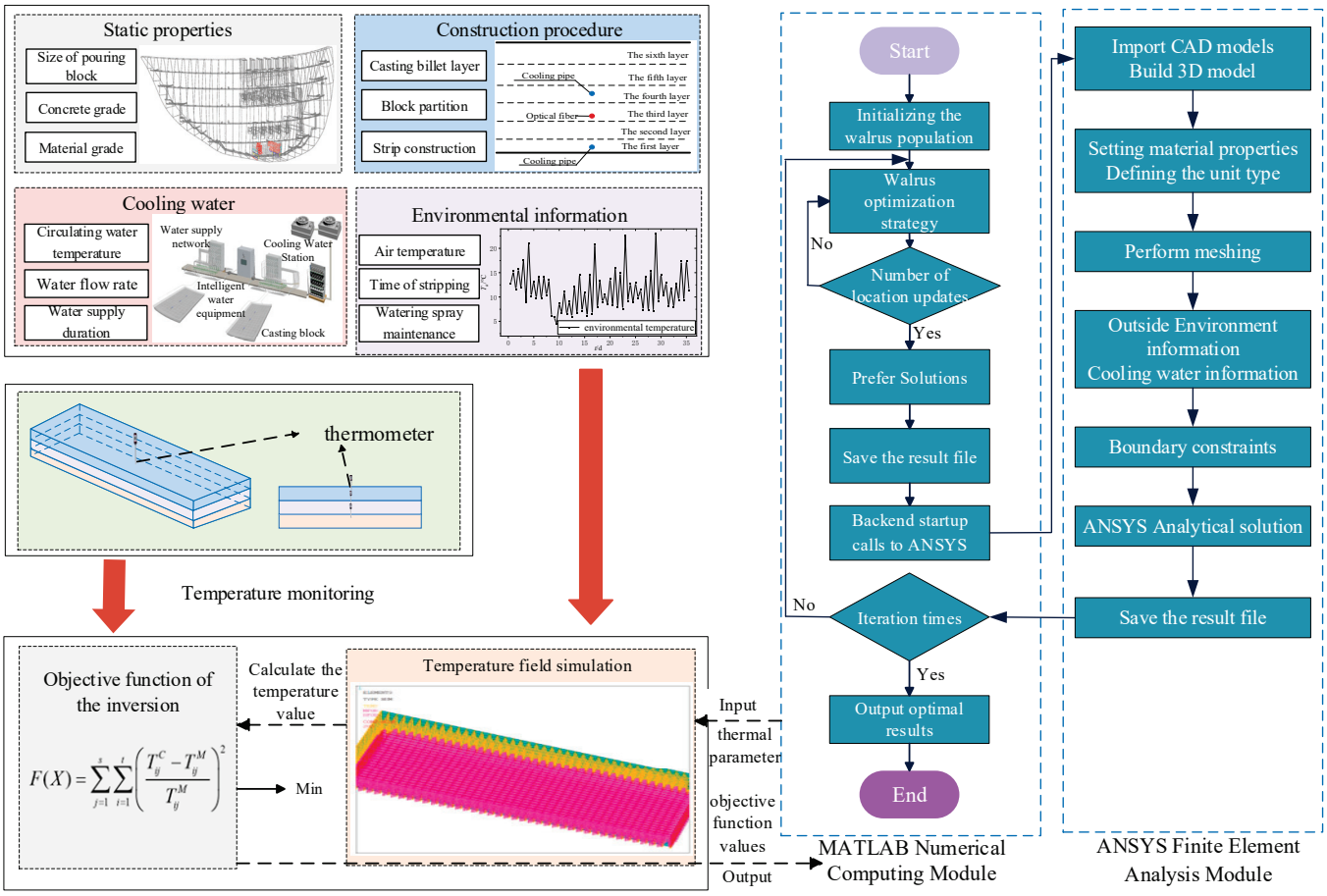
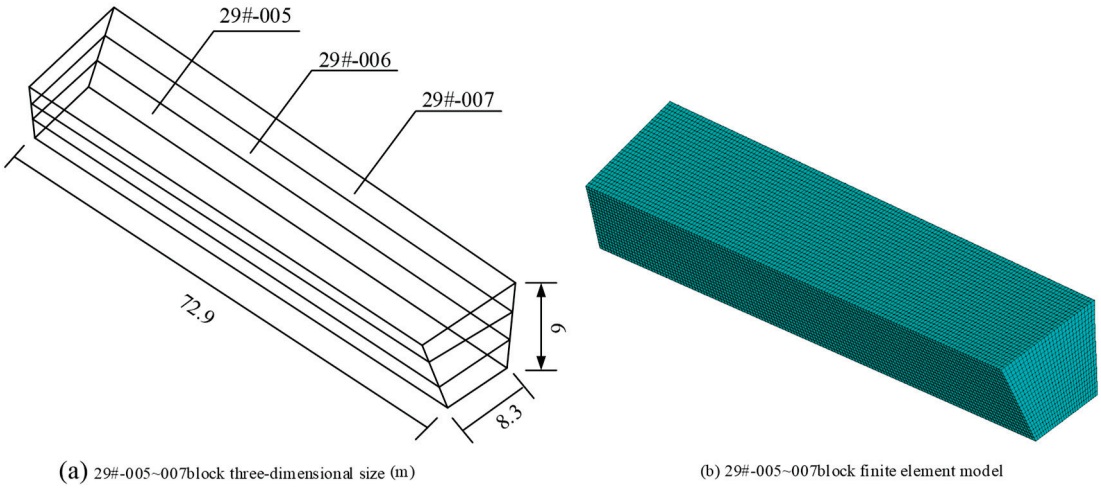


Figure 4. Flowchart of MATLAB calling ANSYS for computation.

5. The Application Example

A hydropower station lies in the downstream section of Jinsha River, spanning Sichuan and Yunnan provinces. The controlling watershed of the hydropower station is large, located in the subtropical monsoon region. The initial installed capacity is 16,000 MW, boasting an annual power generation of 6409 million kW/h.

Figure 5 shows the information of the 29#-005~007 concrete pouring block of an arch dam in the downstream section of Jinsha River. It can be seen that the thickness of each pouring block amounts to three meters, and it consists of six blank layers that is half a meter thick. The concrete strength grade is C40. The finite element model is discretized using hexahedral eight-node isoparametric elements. There are 37,800 elements and 42,718 nodes built in total. According to the design value of concrete in this area and the laboratory test value provided by Changjiang River Scientific Research Institute [28], the range of inversion parameters is as follows: $\theta_0 \in [20, 30]$°C, $n \in [1.5, 5]$, $\beta \in [100, 900]$kJ/(m^2·h·°C).



(a) 29#-005~007block three-dimensional size (m)

(b) 29#-005~007block finite element model

Figure 5. Information on pouring block 29#-005 to 007.

The other parameters refer to the laboratory test values of the Changjiang River Scientific Research Institute. During simulation calculation, the C40 concrete density ρ equals 2601 kg/m^3, the value of the specific heat c equals 0.851 kJ/(kg·°C), and the value of the thermal diffusivity α equals 0.0708 m^2 / h.

The boundary conditions of the model include the following: the transverse joint surfaces on both sides of the pouring block are set as adiabatic boundary conditions, while the third type of temperature boundary conditions (i.e., convection boundary conditions) are imposed on the top surface along with the upstream and downstream surfaces of the pouring block. With the aim of emulating the effect of water pipe cooling, the equivalent heat conduction model of water pipe cooling is utilized. Meanwhile, with the application of the birth and death element technology of ANSYS, the pouring sequence of various concrete pouring blocks can be accurately simulated and controlled [29]. Once the pouring of the first concrete block commences, the finite elements of the first block are activated, while those of the others are terminated. When the second begins, the first and the second block concrete finite elements are activated, and the third is killed. According to the actual project progress, the pouring sequence of each pouring block is precisely regulated. With the aim of removing the interference, the measured temperature data of the bottom block do not participate in the inversion calculation.

The time step of temperature calculation is set at 0.5 d, and the overall time spans 30 d. The actual interval time among different blocks is decided in line with the pouring progress. The time, circulating water temperature, and water flow rate data of cooling

water gained are in accordance with the intelligent water-cooling system of this dam, as depicted in Figures 6 and 7. The average temperature of every 0.5 d is designated as the ambient temperature, as depicted in Figure 8.

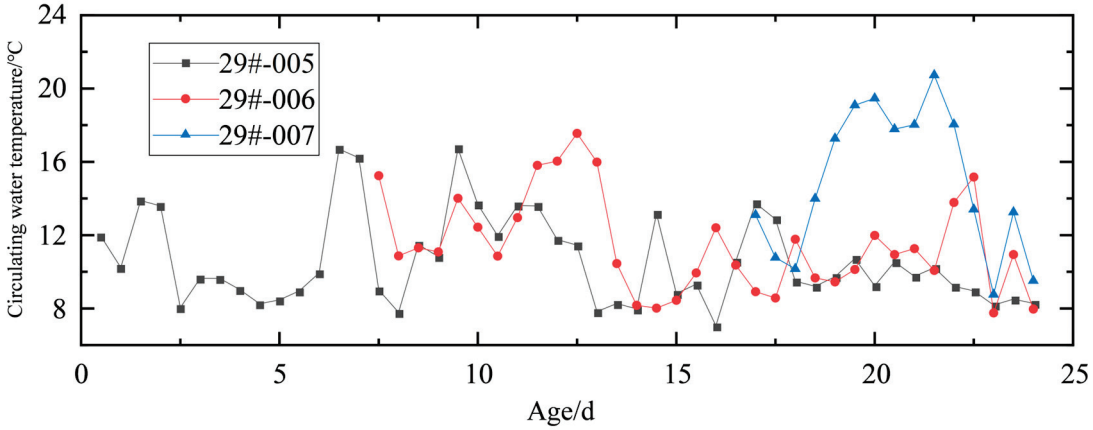


Figure 6. Circulating water temperature.

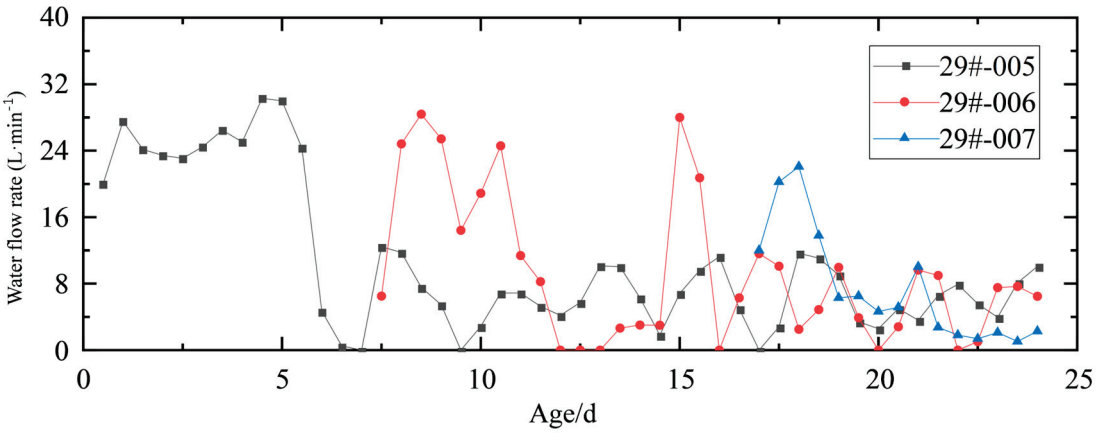


Figure 7. Water flow rate.

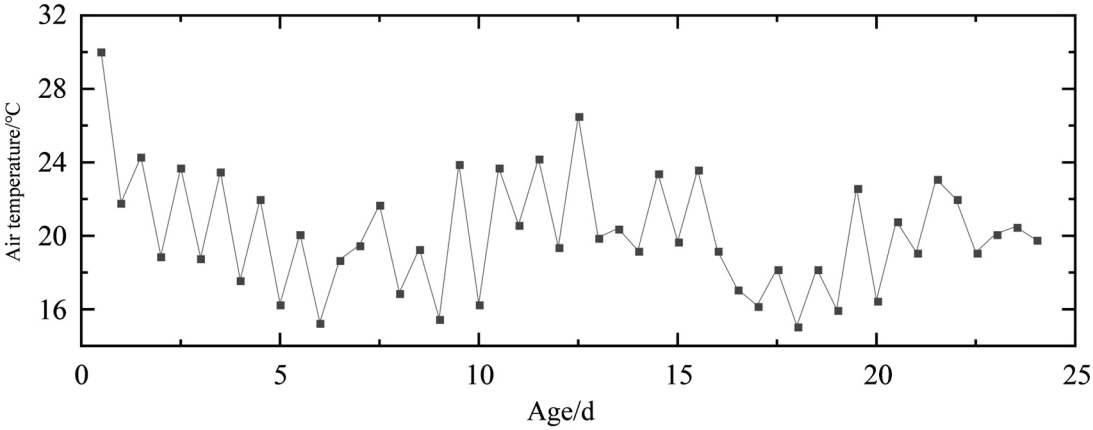


Figure 8. Ambient air temperature.

For a thorough assessment of the performance of the WaOA in practical applications, the four algorithms described in Chapter 2 are included in the parameter inversion calculation. Taking the time factor into account, the population is set at thirty, and the iteration number amounts to forty. Figure 9 illustrates the change of the fitness value of different algorithms in relation to the number of iterations.

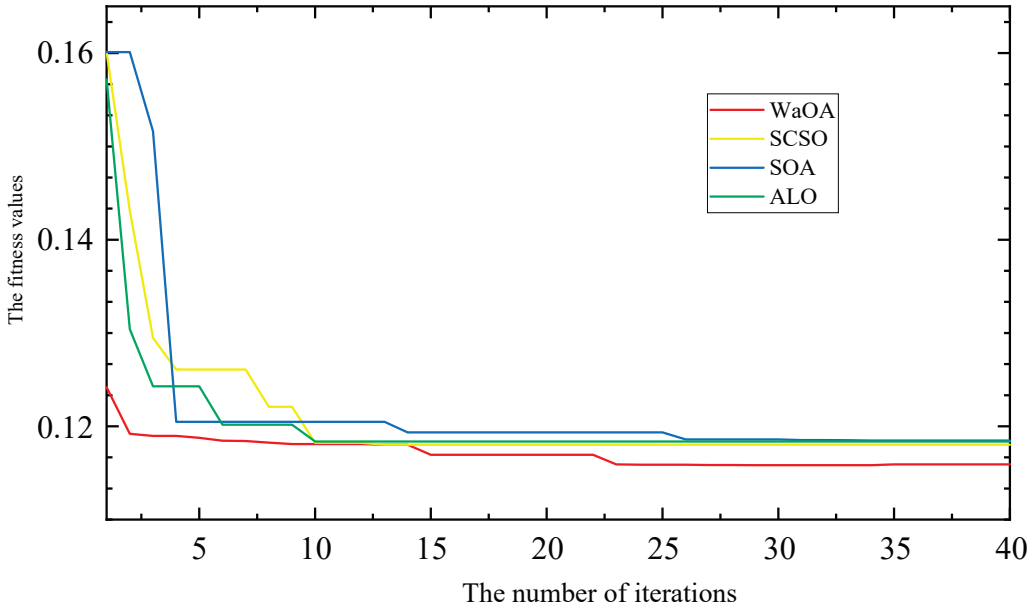


Figure 9. Fitness iteration curve.

From Figure 9, it is observable that as the iteration proceeds, the fitness values exhibit a downward trend. However, the WaOA converges at a notably faster pace and boasts the highest convergence accuracy among the four algorithms. Table 6 shows the inversion results of the WaOA after forty iterations.

Table 6. Inversion value of thermal parameters.

Parameter	Surface Heat Transfer Coefficient kJ/(m²·h·°C)	Adiabatic Temperature Rise
C40 inversion value	742.7	$\theta(t) = \frac{24.2t}{t+2.83}$

With reference to the thermal parameters that were acquired through inversion in Table 6, the numerical simulation of temperature field is carried out for the 29#-006~007 pouring block. Figure 10 presents the comparison of the measured temperature and the calculated temperature data throughout the time.

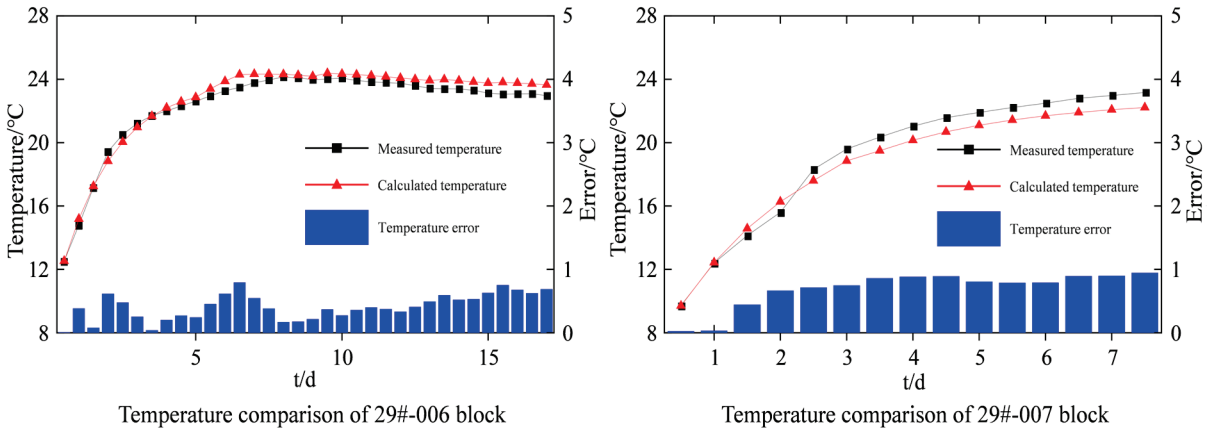


Figure 10. Temperature comparison chart for pouring block 29#-006 to 007.

Apparently, the predicted value of the concrete temperature obtained by numerical simulation is highly consistent with the measured data in the field. The maximum error

is controlled within 1 °C. It is proved that the thermal parameter values obtained by inversion have high reliability. The chief factor contributing to the error may be that it is tough to accurately define the initial temperature of concrete which imposes a certain effect on the results of the temperature rise stage. Meanwhile, owing to the instability of the cooling water flow onsite, the intermittent water flow causes the fluctuation of water flow at different times. It also exerts an influence on the calculation results. In terms of calculation, it is beneficial to enhance the accuracy of the calculation results by maintaining the continuous and smooth transition of the water flow and avoiding the occurrence of intermittent water cut-off.

Tables 7 and 8 show the construction date of the 29#-005~007 and 27#-024~026 pouring blocks of an arch dam in the lower reaches of Jinsha River. Although these pouring blocks are not carried out simultaneously, their pouring time intervals are relatively short. Both of them used the C40 grade concrete materials. In a similar period of time, the concrete pouring process, aggregate gradation, and slump used by them are consistent. At the same time, the temperature conditions and the heat preservation measures taken during this period are also the same. Based on this, we propose a conjecture: in the adjacent time period, is the thermal parameters of the concrete of the same grade poured in the adjacent dam section consistent?

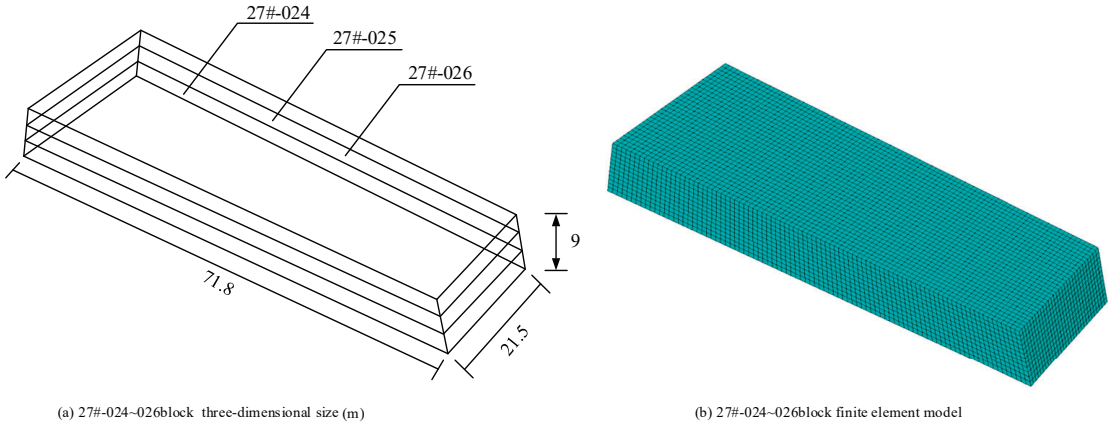
Table 7. Construction sequence of pouring block 29#-005~007.

Pouring Block	29#-005	29#-006	29#-007
Start	2019-10-09 06:00	2019-10-16 05:28	2019-10-25 21:15
End	2019-10-10 04:03	2019-10-17 06:29	2019-10-27 00:43

Table 8. Construction sequence of pouring block 27#-024~026.

Pouring Block	27#-024	27#-025	27#-026
Start	2019-07-04 22:50	2019-07-21 05:31	2019-07-28 05:37
End	2019-07-06 06:29	2019-07-22 09:10	2019-07-29 09:38

Figure 11 shows the information on pouring bay 27#-024 to 026. The grid cell of the finite element model is an eight-node hexahedral isoparametric cell, which is made up of 32,400 elements and 36,673 nodes in total.



(a) 27#-024~026block three-dimensional size (m)

(b) 27#-024~026block finite element model

Figure 11. Information on pouring block 27#-024 to 026.

Using the field-measured water information and ambient temperature data, the thermal parameters of C40 concrete in the 29#-005~007 block obtained by inversion in Table 6 are applied to the finite element numerical simulation model of the 27#-024~026 block.

Through the calculation, the calculated temperature values of the 27#-025 and the 026 blocks are obtained, and compared with the measured temperature onsite. The results of the comparison are demonstrated in Figure 12.

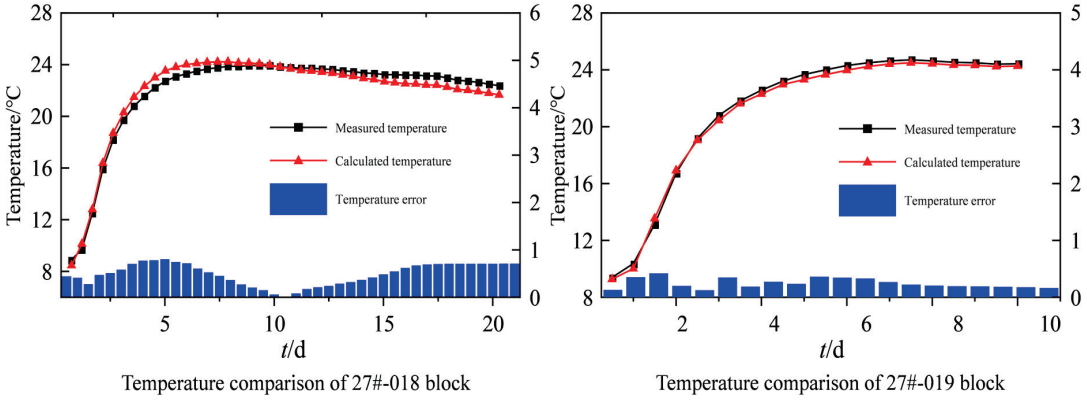


Figure 12. Temperature comparison chart for pouring block 27#-025 to 026.

As can be seen from the comparison results of Figure 12 that the variation trends of the calculated temperature and the measured temperature are in high accordance, and the maximum temperature deviation is controlled within 1 °C, which indicates that the numerical simulation method has high accuracy.

According to the research report of the Changjiang River Scientific Research Institute on the concrete mix proportion test of the dam of the hydropower station [28], the thermal parameters of the C40 strength grade concrete obtained through inversion are compared with the values from laboratory tests, as demonstrated in Table 9. Figure 13 shows the comparison of the curve of the adiabatic temperature rise of concrete as its age changes.

Table 9. Comparison of adiabatic temperature rise.

Strength Grade	Data Sources	Adiabatic Temperature Rise (°C)
C40	29#-005~007	$\theta(t) = \frac{24.2t}{t+2.83}$
	Laboratory test value	$\theta(t) = \frac{25.2t}{t+3.26}$

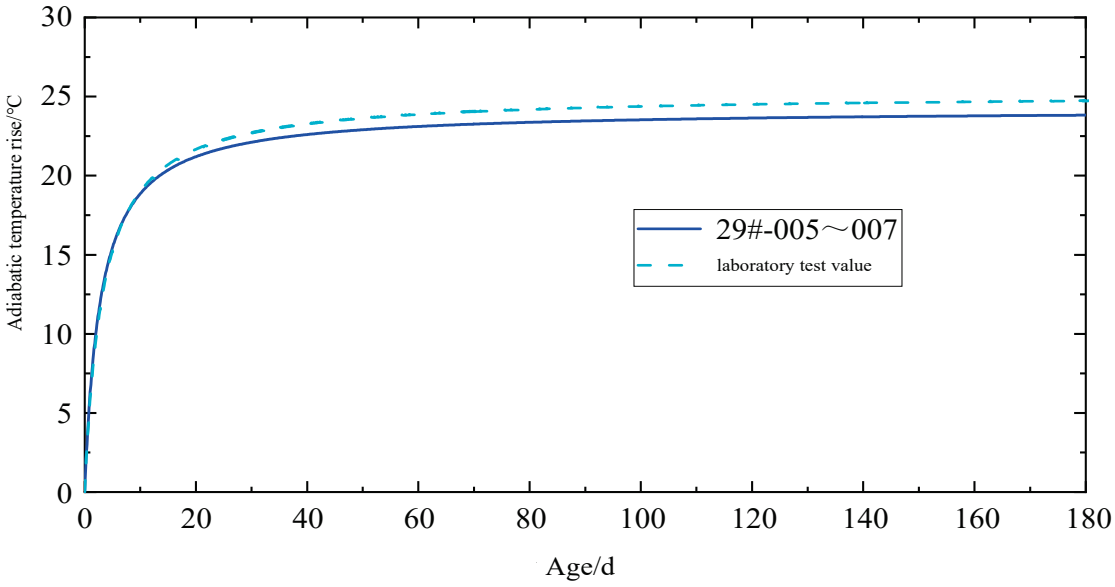


Figure 13. Relationship curve between adiabatic temperature rise and age of C40 concrete.

The Figure 13 reveals that the final adiabatic temperature rise of C40 concrete gained through the inversion process is a bit lower than the laboratory test value, and the error range is within 0.9 °C. The fitness curve obtained by inversion is roughly the same as the laboratory test results, which fully demonstrates that the inversion possesses high accuracy and reliability. Table 10 shows the design parameters of a dam in the downstream section of Jinsha River [28]. Obviously, in the laboratory test, the water–binder ratio of concrete ranges from 0.42 to 0.46. However, the water–binder ratio of concrete that is poured at the actual site typically reaches 0.5. We observe that the adiabatic temperature rise of concrete acquired through inversion is of a lower level than that obtained by laboratory standard tests. This variability may be attributed to the lower amount of cement used in the actual casting, resulting in an elevation of the water–binder ratio of the concrete, which in turn leads to the final adiabatic temperature rise being slightly less than the experimental values.

Table 10. Design parameters of dam concrete for Baihetan Hydropower Station.

Strength Grade	Design Age (d)	Strength Guarantee	Frost Resistance Grade	Impermeability Grade	Tensile Strength (MPa)	Ultimate Tensile Value ($\times 10^{-6}$)	Maximum Water-Binder Ratio Allowed	Gradation
C35	180	85%	$\geq F_{90}300$	$\geq W_{90}14$	≥ 3.0	≥ 100	0.46	Three and four
C40			$\geq F_{90}300$	$\geq W_{90}15$	≥ 3.2	≥ 105	0.42	Four

6. Conclusions

(1) In order to make the conclusion more credible, this study not only uses twelve standard benchmark functions as test sets, but also further tests its performance with three different algorithms, and implements nonparametric tests when evaluating the performance of the WaOA. The results show that the WaOA, as a new meta-heuristic algorithm, possesses the features of simple structure, ease of implementation, and fewer parameters. It can strike a fine balance between the exploration stage and the development stage of the algorithm, and shows significant advantages in performance, which can provide help for subsequent practical engineering calculation problems.

(2) By combining the inverse analysis theory with the finite element calculation of the temperature field, a numerical model for inverse analysis of thermal parameters relying on the WaOA is established, and the thermal parameters of C40 concrete of an arch dam in the lower reaches of Jinsha River are inverted. By comparing the measured and calculated temperature curves of typical measuring points, it is observable that the overall temperature change trend of the two shows a high degree of conformity, and the error stays below 1 °C. It suggests that the thermal parameters acquired through inversion can reflect the real thermal characteristics of concrete materials. Further verification shows that the inversion parameters are applied to different dam section models with adjacent pouring blocks and similar pouring time. High consistency is shown between the measured and calculated temperature values, and the maximum error is limited within 1 °C. The practicability and reliability of the inversion parameters are, thus, proved, and theoretical guidance is provided for subsequent research.

Author Contributions: Research and review, Y.W.; research and writing, Z.M.; review and modification, J.Z., R.S. and Y.P.; conceptualization and review, F.W. All authors have read and agreed to the published version of the manuscript.

Funding: This research was supported by National Natural Science Foundation of China (Grant No. 51809154), Joint supported by Hubei Provincial Natural Science Foundation-Innovative Development of Three Gorges of China (No. 2023AFD189), Independent Innovation Project of Changjiang Survey, Planning, Design and Research Co., Ltd. (No. CX2021Z56), (No. CX2023S024). and Open Research Fund of Key Laboratory of Reservoir and Dam Safety Ministry of Water Resources (Grant No. YK323009).

Institutional Review Board Statement: Not applicable.

Informed Consent Statement: Not applicable.

Data Availability Statement: The datasets presented in this article are not readily available because authors do not have the relevant permissions. Requests to access the datasets should be directed to wangfengctgu@ctgu.edu.cn.

Conflicts of Interest: Author Youle Wang and Zhengjian Miao are employed by the company Changjiang Survey Planning Design and Research Co., Ltd. The remaining authors declare that the research was conducted in the absence of any commercial or financial relationships that could be construed as a potential conflict of interest.

References

1. Javanmardi, F.; Léger, P. Grouting of cracks in concrete dams: Numerical modelling and structural behaviour. *Prog. Struct. Eng. Mater.* **2005**, *7*, 161–173. [CrossRef]
2. Li, B.; Wang, Z.; Jiang, Y.; Zhu, Z. Temperature control and crack prevention during construction in steep slope dams and stilling basins in high-altitude areas. *Adv. Mech. Eng.* **2018**, *10*, 1687814017752480. [CrossRef]
3. Zhao, Y.; Li, G.; Fan, C.; Pang, W.; Wang, Y. Effect of Thermal Parameters on Hydration Heat Temperature and Thermal Stress of Mass Concrete. *Adv. Mater. Sci. Eng.* **2021**, *2021*, 5541181. [CrossRef]
4. Lim, C.-K.; Kim, J.-K.; Seo, T.-S. Prediction of concrete adiabatic temperature rise characteristic by semi-adiabatic temperature rise test and FEM analysis. *Constr. Build. Mater.* **2016**, *125*, 679–689. [CrossRef]
5. Cheng, J.; Li, T.C.; Liu, X.; Zhao, L.H. A 3D discrete FEM iterative algorithm for solving the water pipe cooling problems of massive concrete structures. *Int. J. Numer. Anal. Methods Geomech.* **2016**, *40*, 487–508. [CrossRef]
6. Castilho, E.; Schclar, N.; Tiago, C.; Farinha, M.L.B. FEA model for the simulation of the hydration process and temperature evolution during the concreting of an arch dam. *Eng. Struct.* **2018**, *174*, 165–177. [CrossRef]
7. Nadimi-Shahraki, M.H.; Zamani, H. DMDE: Diversity-maintained multi-trial vector differential evolution algorithm for non-decomposition large-scale global optimization. *Expert Syst. Appl.* **2022**, *198*, 116895. [CrossRef]
8. Mirjalili, S.; Mirjalili, S.M.; Hatamlou, A. Multi-Verse Optimizer: A nature-inspired algorithm for global optimization. *Neural Comput. Appl.* **2016**, *27*, 495–513. [CrossRef]
9. He, Q.; Lin, J.; Xu, H. Hybrid Cauchy mutation and uniform distribution of grasshopper optimization algorithm. *Control. Decis.* **2021**, *36*, 1558–1568. (In Chinese) [CrossRef]
10. Pei, L.; Chen, J.K.; Wu, Z.Y.; Li, Y.L.; Zhang, H. Response surface genetic algorithm of back analysis of concrete thermal parameters. *Mater. Res. Innov.* **2015**, *19* (Suppl. S8), S8-840–S8-845. [CrossRef]
11. Dhiman, G.; Kumar, V. Seagull optimization algorithm: Theory and its applications for large-scale industrial engineering problems. *Knowl.-Based Syst.* **2019**, *165*, 169–196. [CrossRef]
12. Wolpert, D.H.; Macready, W.G. No free lunch theorems for optimization. *IEEE Trans. Evol. Comput.* **1997**, *1*, 67–82. [CrossRef]
13. Han, Y.; Fu, S.; Wang, S.; Xie, Z. Study on Adiabatic Temperature Rise Reflecting Hydration Degree of Concrete. *Adv. Mater. Sci. Eng.* **2018**, *2018*, 1435049. [CrossRef]
14. Zhao, H.; Fan, G.; Wei, Z.; Wang, J.; Huang, D. Investigation of thermal conductivity and related parameters of early-age cement paste. *Int. J. Heat Mass Transf.* **2020**, *155*, 119798. [CrossRef]
15. Shi, N.; Zhang, R.; Huang, D. Thermal stress analyses and reinforcement design of massive RC structures. *Eur. J. Environ. Civ. Eng.* **2015**, *19*, 901–916. [CrossRef]
16. Su, H.; Li, J.; Hu, J.; Wen, Z. Analysis and Back-Analysis for Temperature Field of Concrete Arch Dam During Construction Period Based on Temperature Data Measured by DTS. *IEEE Sens. J.* **2013**, *13*, 1403–1412. [CrossRef]
17. Xu, P.A.; Lin, Q.; Hao, S.P.; Zhang, L.H. Twin-delayed-based Deep Deterministic Policy Gradient Method Integrating Gravitational Search. *J. Softw.* **2023**, *34*, 5191–5204. [CrossRef]
18. Trojovský, P.; Dehghani, M. A new bio-inspired metaheuristic algorithm for solving optimization problems based on walruses behavior. *Sci. Rep.* **2023**, *13*, 8775. [CrossRef] [PubMed]

19. Abdel-Basset, M.; El-Shahat, D.; Jameel, M.; Abouhawwash, M. Exponential distribution optimizer (EDO): A novel math-inspired algorithm for global optimization and engineering problems. *Artif. Intell. Rev.* **2023**, *56*, 9329–9400. [CrossRef]
20. Carrasco, J.; García, S.; Rueda, M.M.; Das, S.; Herrera, F. Recent trends in the use of statistical tests for comparing swarm and evolutionary computing algorithms: Practical guidelines and a critical review. *Swarm Evol. Comput.* **2020**, *54*, 100665. [CrossRef]
21. Friedman, M. The Use of Ranks to Avoid the Assumption of Normality Implicit in the Analysis of Variance. *J. Am. Stat. Assoc.* **1937**, *32*, 675–701. [CrossRef]
22. Hutchinson, T.P. On the generalised friedman test. *Comput. Stat. Data Anal.* **1996**, *21*, 473–476. [CrossRef]
23. García, S.; Fernández, A.; Luengo, J.; Herrera, F. Advanced nonparametric tests for multiple comparisons in the design of experiments in computational intelligence and data mining: Experimental analysis of power. *Inf. Sci.* **2010**, *180*, 2044–2064. [CrossRef]
24. Wang, M.; Heidari, A.A.; Chen, M.; Chen, H.; Zhao, X.; Cai, X. Exploratory differential ant lion-based optimization. *Expert Syst. Appl.* **2020**, *159*, 113548. [CrossRef]
25. Zhou, Y. *Study on Hydration Heat and Temperature Control Measures of Mass Concrete*; Chongqing Jiaotong University: Chongqing, China, 2020; (In Chinese). [CrossRef]
26. Huang, Y.Y.; Zhou, S.W.; Fu, X.K.; Zhou, Y.H. Dynamic Forecasting Model of Concrete Casting Warehouse in Middle-late Cooling Age. *Adv. Eng. Sci.* **2013**, *45*, 34–38. (In Chinese) [CrossRef]
27. Zhou, J.B.; Huang, Y.Y.; He, X.P.; Tian, K.P. Dynamic Prediction of Concrete Temperature for the Plugging of Bottom Diversion Outlet of Xiangjiaba Hydropower Project. *J. Chang. River Sci. Res. Inst.* **2015**, *32*, 119–122. (In Chinese)
28. Yang, H.Q.; Dong, Y.; Xiao, K.T. *Experimental Study on Concrete Mix Proportion of Baihetan Hydropower Station*; Changjiang River Scientific Research Institute: Wuhan, China, 2015. (In Chinese)
29. Zhang, H.D. Application to ANSYS Unit Technical Software to Structural Design and Construction. *Build. Constr.* **2008**, *9*, 824–825+833. (In Chinese)

Disclaimer/Publisher's Note: The statements, opinions and data contained in all publications are solely those of the individual author(s) and contributor(s) and not of MDPI and/or the editor(s). MDPI and/or the editor(s) disclaim responsibility for any injury to people or property resulting from any ideas, methods, instructions or products referred to in the content.

applied sciences

MDPI

Article

Model Updating of Bridges Using Measured Influence Lines

Doron Hekič [1,2,*], Jan Kalin [1], Aleš Žnidarič [1], Peter Češarek [2] and Andrej Anžlin [1]

[1] Department of Structures, Slovenian National Building and Civil Engineering Institute, Dimičeva ulica 12, 1000 Ljubljana, Slovenia; jan.kalin@zag.si (J.K.); ales.znidaric@zag.si (A.Ž.); andrej.anzlin@zag.si (A.A.)
[2] Faculty of Civil and Geodetic Engineering, University of Ljubljana, Jamova cesta 2, 1000 Ljubljana, Slovenia; peter.cesarek@fgg.uni-lj.si
* Correspondence: doron.hekic@zag.si

Abstract: In developing a digital twin of a real structure, finite element model updating (FEMU) is essential for refining the model's response based on measured data, enabling the detection of structural damage or hidden reserves over time. This case study focused on a 40-year-old multi-span concrete roadway bridge, equipped with permanent bridge weigh-in-motion (B-WIM) and structural health monitoring (SHM) systems. Bridge responses from two calibration vehicles were used to derive strain influence lines (ILs) from mid-span B-WIM strain transducers mounted on the main girders. The error-domain model falsification (EDMF) methodology was applied to perform strain IL-based FEMU and the more conventional frequency-based, MAC-based, and combined frequency and MAC-based FEMU. Boundary conditions and three Young's modulus adjustment factors, representing different groups of structural elements, were updated. The strain IL-based updated FE model, with averages of 35% and 50% stiffness increases for the two main girders, showed strong agreement with independently measured mid-span vertical displacements. Maximum values deviated not more than 5%. In contrast, the frequency and MAC-based updated FE model underestimated displacements by 25–30%. These findings highlight the potential of using B-WIM for FEMU and SHM on such types of bridges, particularly when the response under traffic load is of interest.

Keywords: finite element model updating (FEMU); calibration; bridge; bridge weigh-in-motion (B-WIM); structural health monitoring (SHM); error-domain model falsification (EDMF); influence line (IL)

1. Introduction

The average age of bridges all around the world, particularly in developed economies, is increasing and great numbers are approaching the end of their design lives [1]. As they are often poorly maintained and monitored and are exposed to natural disasters, such as earthquakes and floods, which cause erosion under their supports, we are observing more and more collapses, many of which have caused fatalities. Nearly half of the reported bridge failures worldwide have occurred in the last 20 years [2]. Comparing the expanding global economy and the number of reported bridge collapses results in a firm correlation (Figure 1).

Without systematic inspections, monitoring, timely interventions, and implementation of new technologies, even nominally robust systems gradually deteriorate, culminating in higher collapse rates. Recognising this linkage justifies the current research efforts into new technologies, such as structural health monitoring (SHM), finite element model updating (FEMU), and bridge weigh-in-motion (B-WIM), especially as transport networks become

ever more extensive and critical to economic development. Tackling these issues requires better and more robust predictions of bridge behaviour. One approach that copes with these requirements is FEMU, where finite element (FE) models are updated to match the analytical and measured responses.

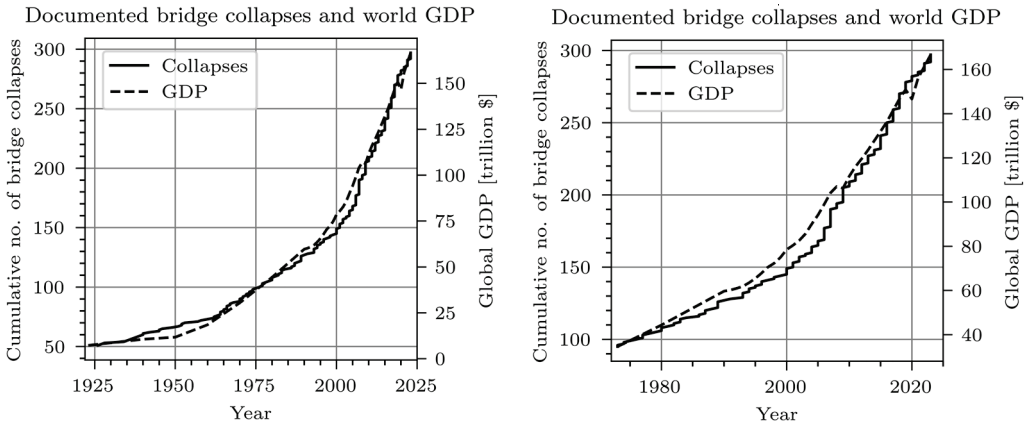


Figure 1. Correlation between bridge collapses [2] and world GDP [3] in the last 100 (**a**) and 40 years (**b**).

In structural dynamics, FEMU traces back to the early efforts of reconciling FE simulations with measured vibration data to refine predictions of real-world structural behaviour. Mottershead and Friswell [4] conducted a deep survey on the topic, systematising key approaches for parameter selection, objective function formulation, and optimisation strategies. Early on, most FEMU applications focused on natural frequencies and mode shapes to capture global structural responses. Over time, researchers recognised that purely vibration-based data sometimes lacked sensitivity to localised parameters (e.g., small-scale stiffness or boundary nuances). This realisation gradually led to new data types, such as displacements and strains [5–10], being integrated into the FEMU process, helping to address the inherent limitations of purely modal data. Building on these foundations, the current generation of FEMU techniques harnesses large-scale test data under various loading scenarios. One promising approach is using measured influence lines (ILs). IL-based approaches reflect global and local responses with minimal instrumentation, allowing for more precise FEMU. Using ILs in FEMU can more accurately describe local boundary conditions, subtle stiffness variations, and stress distribution patterns.

The literature proposes various signal-processing and inverse analysis techniques to extract an IL from measured bridge responses under moving loads: spatial-domain, frequency-domain, and decomposition-based methods. O'Brien et al. [11] introduced a bridge IL identification method through spatial domain modelling. This approach quantifies the connection between vehicle axle load, IL coefficients, and bridge response at different vehicular positions. Alternatively, one can achieve response normalisation in the frequency domain, restoring the IL using the inverse Fourier transformation. Yan & Yuen [12] developed a method that utilises static response transfer ratio functions to identify IL from a probabilistic frequency domain viewpoint. Similarly, Frøseth et al. [13] identified IL in the frequency domain based on the principle that the convolution of the moving load and IL results in the bridge response. An adaptive enhanced variational mode decomposition (AEVMD) method was presented for extracting the bridge's quasi-static response [14]. This method combines the pre-processed conjugate gradient least squares (PCGLS) algorithm to determine the IL. Although both spatial and frequency domain methods effectively create mathematical models for IL identification, they remain vulnerable to dynamic interference. In contrast [15], a non-linear optimisation approach,

drawing from a substantial number of random vehicles in traffic flow with unknown axle loads to define the shape of the influence line, has a notable advantage since the inherent dynamic responses of both the bridge and vehicles influence the IL shape less. This can skew results based solely on a limited number of pre-weighed vehicles. This paper follows this aspect of leveraging continuous advances in sensor technology, signal processing, and data-driven optimisation to enhance IL-based FEMU, ensuring more precise and robust methodologies for bridge health monitoring and structural safety assessment.

This paper builds on previous work on using strain ILs obtained from B-WIM measurements. Strain ILs are essential for B-WIM algorithms to calculate accurate axle loads [15]. Algorithms have been developed to calculate strain ILs from all heavy gross vehicle crossings. Hundreds are statistically evaluated to obtain reliable information on bridge performance under moving loads [16]. In the past, these B-WIM-calculated strain ILs have already been used to calibrate the analytical models of simple short-span bridges. In this study, we first enhanced the strain IL calculation methodology to account for quantities better suited to bridge analyses. Then, we used the results to update the case study bridge and compared the FEMU results with more traditional frequency and mode shape-based FEMU results. For the FEMU, we replaced the traditional methods, such as Bayesian model updating and residual minimisation, with the EDMF methodology. Lastly, we validated the FE model response with measured displacements under calibration vehicle passages.

The novelty of the proposed method lies in integrating measured strain ILs, derived from B-WIM data, into the FEMU process, representing an important advancement over traditional approaches that rely solely on modal parameters, like frequencies, MAC values, or on maximum strains under traffic load. It offers a cost-effective alternative to displacement-based methods, which were independently validated to yield comparable results in terms of response prediction. Methodologically, this study replaces more demanding Bayesian updating and residual minimisation with the error-domain model falsification (EDMF) approach. This falsification-based framework identifies plausible variable values of the FE model by systematically eliminating FE models that fail to match experimental data within defined uncertainty bounds. This makes it more robust to systematic uncertainties and model biases and increasingly recognised for its accuracy and practical effectiveness in structural identification. These methodological contributions not only simplify the FEMU process, but also enhance the role of B-WIM in structural identification and long-term SHM.

2. Materials and Methods

2.1. Description of the Case Study Bridge

The case study Tomačevo roadway bridge was built in 1982 and crosses the Sava River near the Slovenian capital Ljubljana (LJ). Its superstructure is a seven-span continuous post-tensioned double-T section supported by circular piers on deep foundations (Figure 2).

The bridge consists of two parallel independent structures. The right one (Figure 3a,b inside the red rectangles) carries traffic in the LJ direction and the left one in the opposite (northeast) direction. This paper focuses on the right structure, denoted as the *bridge* throughout this paper.

The superstructure was cast in place with sliding formwork technology. Cross girders at the abutments connect longitudinal main girders. The bridge is bounded by modular expansion joints at both abutments, where the superstructure is supported by guided unidirectional pot bearings. The superstructure passes continuously above piers, supported by round elastomeric bearings. No major rehabilitation works have been performed on the bridge since its completion, apart from the expansion joint replacement in 1990 and the asphalt layer and steel safety barrier replacement in 2018.

The bridge is in good condition, with typical damages and defects, such as local insufficient cover layer and consequent spalling of concrete, clogged expansion joints, and corroded bearings. Drainage is inadequately implemented and maintained in several places, especially near the abutments, which has caused accelerated deterioration of concrete and bearings, as shown in Figure 4.



Figure 2. Aerial view of the Tomačevo bridge, with an arrow indicating the traffic flow in the Ljubljana (LJ) direction.



(**a**) (**b**)

Figure 3. View under the Tomačevo bridge towards LJ (**a**) and opposite direction (**b**). Red arrows indicate traffic direction and red rectangles the right structure, considered in this paper.



(**a**) (**b**)

Figure 4. Water leakage at the abutments (**a**) and a corroded guided unidirectional pot bearing (**b**).

Side, plan, and cross-section views of the bridge are shown in Figure 5. Typical elements are labelled with abbreviations, such as MG1, representing Main Girder 1, CG, representing the Cross Girder, and similar to other elements, described in more detail in Table 3.

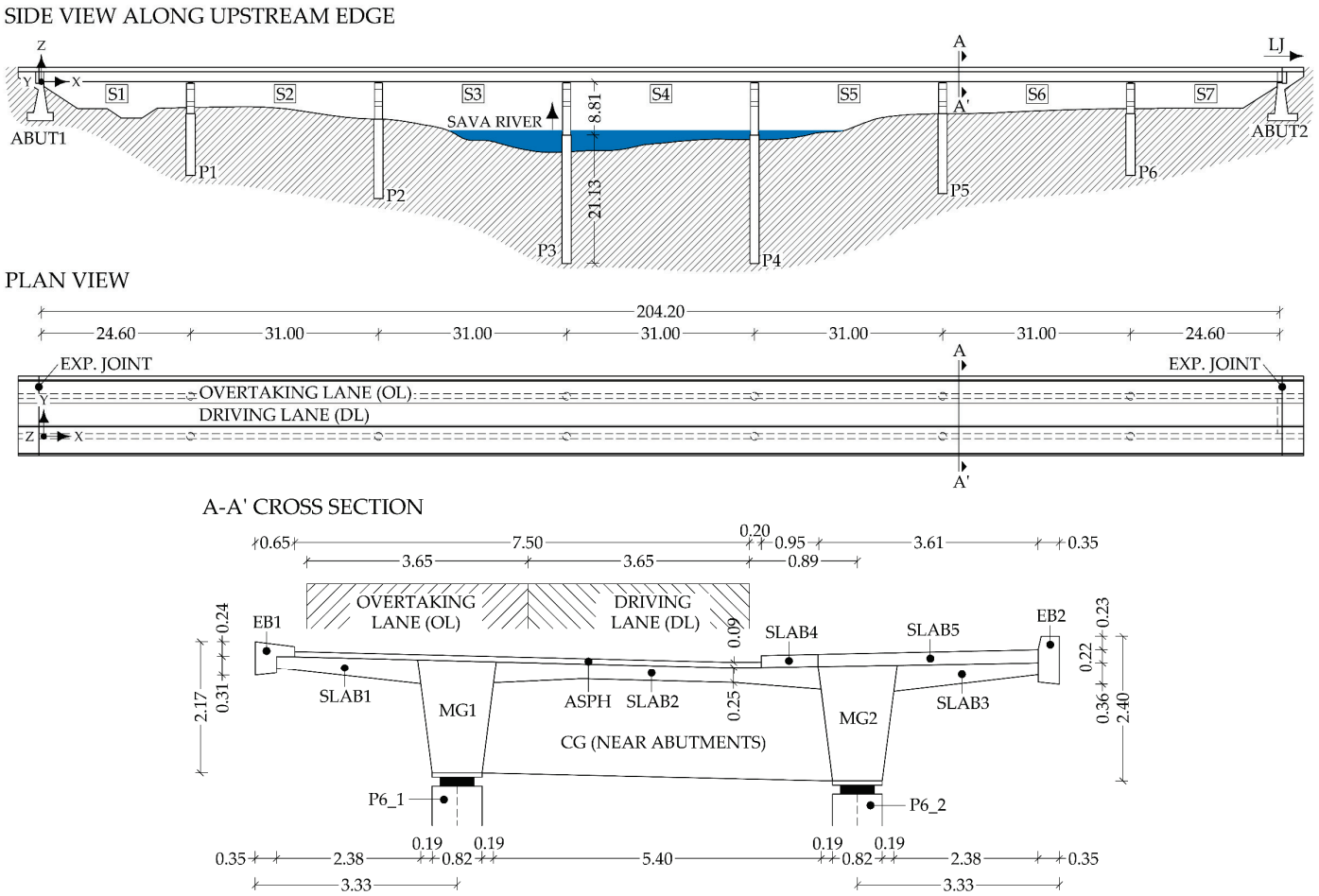


Figure 5. Plan view, side view, and cross-section view of the bridge. Typical elements are labelled with abbreviations, described more in detail in Table 3.

2.2. Measurements

The Tomačevo bridge is a B-WIM and SHM living-lab facility designed to develop and test new technologies, sensors, and methods. The measurements setup on the bridge varied over time, but for this study, the following sensors, shown in Figure 6, were considered:

- Fourteen Dewesoft-type IOLITEi 3xMEMS-ACC tri-axial MEMS accelerometers (Dewesoft, Trbovlje, Slovenia) measuring the ambient and traffic-induced vibrations and to determine the modal parameters of the bridge;
- Two inductive strain transducers (denoted in the paper as B-WIM sensors) measuring traffic-induced strains on both girders, and to obtain input for the B-WIM measurements;
- Two linear variable differential transformers (denoted as LVDTs or. displacement sensors) (HBK, Darmstadt, Germany) measuring traffic-induced vertical displacements on both main girders;
- Two temperature sensors, T_OUT (Dewesoft, Trbovlje, Slovenia)measuring environmental temperature and T_IN, measuring the temperature approximately 5 cm inside the main girder MG1.

DewesoftX 2023.5 data acquisition software [17] was used for data recording with a 500 Hz sampling frequency.

Besides the sensors that measure the mid-span strains on main elements such as girders and slabs, B-WIM systems generally require additional sensors to detect the axles and calculate the vehicle's speed. In the lateral direction, they are installed on the elements and locations close to the vehicle's wheel track to capture clear spikes, representing individual axles. One pair of such strain sensors was installed on the SLAB1 and one on the SLAB2 element.

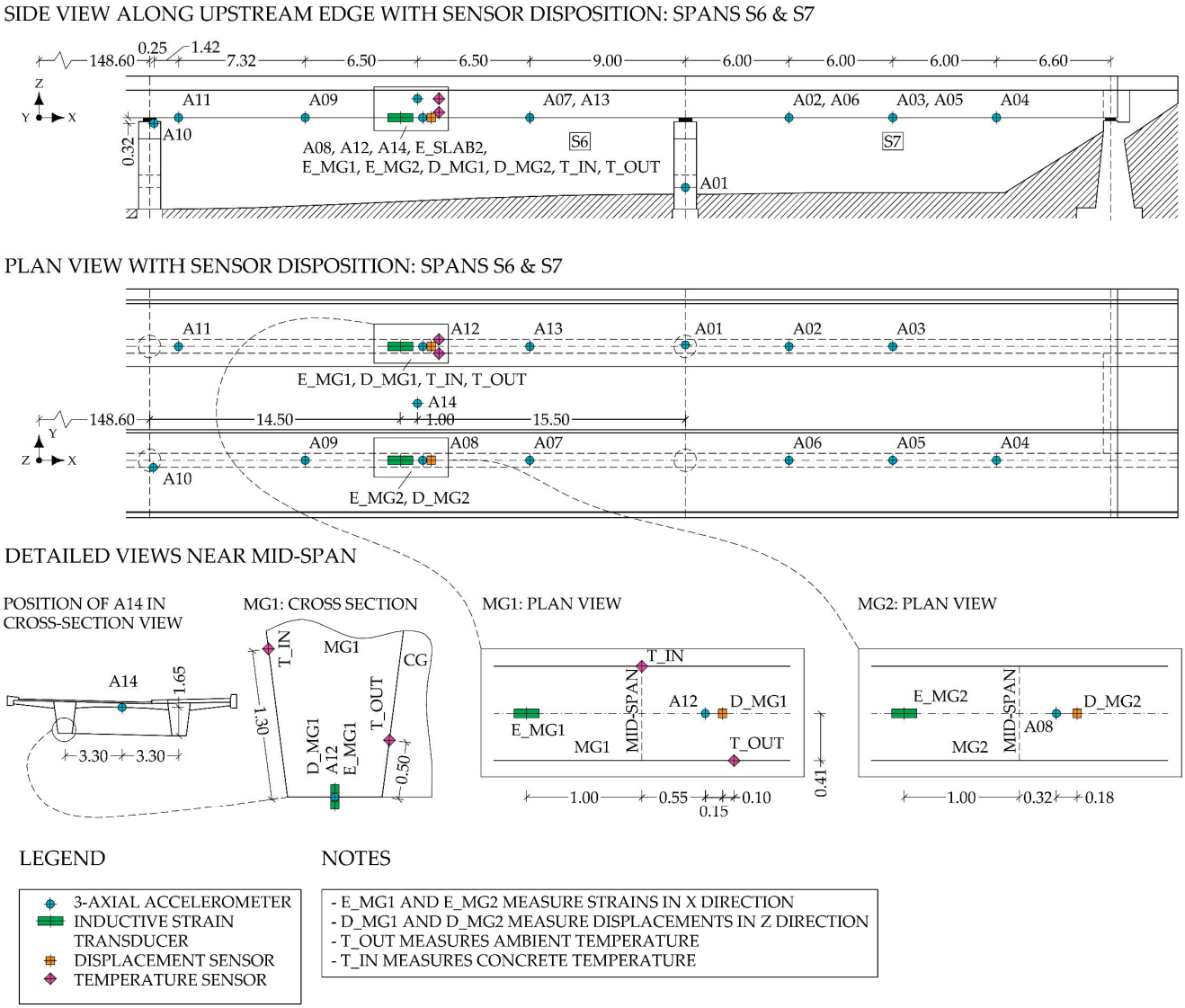


Figure 6. Disposition of the sensors used in this paper. Typical elements are labelled with abbreviations, described more in detail in Table 3.

2.2.1. Strain and Displacement Measurements Under the Calibration Vehicle Crossings

Strains and displacements were measured in May 2024 at night to avoid congestion and minimise the presence of other vehicles on the bridge. The environmental conditions were similar both nights; for the time of the experimental campaign, the difference between the measured average temperatures of the first (18.2 °C) and second (17.7 °C) nights was 0.5 °C. Two statically pre-weighed calibration vehicles were used (Figure 7), a tri-axle rigid truck, denoted as V1, and a two-axle tractor with a three-axle semi-trailer, denoted as V2.

Both vehicles were fully loaded on the first night and empty on the second night. Their axle loads, spacing, and gross vehicle weight (GVW) are shown in Table 1.



(**a**) (**b**)

Figure 7. Calibration vehicles: V1 (**a**) and V2 (**b**).

Table 1. Axle loads, axle spacing, and gross vehicle weights (GVW) of the calibration vehicles.

	1st Axle		2nd Axle		3rd Axle		4th Axle		5th Axle	
Vehicle [1]	**Load (kN)**	**Spacing (m)**	**Load (kN)**	**Spacing (m)**	**Load (kN)**	**Spacing (m)**	**Load (kN)**	**Spacing (m)**	**Load (kN)**	**GVW (kN)**
V1_F	68.67	3.42	73.58	1.37	71.61	/	/	/	/	213.86
V1_E	57.88	3.42	37.28	1.37	36.30	/	/	/	/	131.45
V2_F	69.65	3.60	90.25	2.82	64.75	1.31	61.80	1.31	59.84	346.29
V2_E	56.90	3.60	29.43	2.82	14.72	1.31	15.70	1.31	14.72	131.45

[1] F represents a fully loaded truck, and E an empty truck.

Each vehicle passed the bridge in the driving lane ten times at 90 km/h, five times at 70 km/h, and three times at 30 km/h. Two trucks performed seventy-two passages in two nights, which is approximately 50% of the recommended passages by COST 323 [18].

Then, the B-WIM analysis used the measurement result from the E_MG1 and E_MG2 sensors, and the strain IL was extracted. No displacement IL was extracted since the measured displacement response under the calibration vehicles was only used to validate the updated FE model, and not in the B-WIM and FEMU parts.

2.2.2. Extraction of the Strain Influence Line (IL) from the Strain Measurements

B-WIM refers to a method that uses an instrumented bridge or culvert to weigh-in-motion the passing vehicles. The B-WIM analysis is an inverse-type problem where the structural response (mid-span strains) is measured and the traffic load causing this response is calculated [19]. Most operational B-WIM algorithms, including the one in this study, work on static assumptions and follow the principles proposed by Moses [20]. The key parameter in the B-WIM analysis is the IL, a function that describes the response of a structure at a given point under a moving unit load. IL illustrates how various load effects, like displacements and strains, change under the moving traffic loads.

Several methods of calculating ILs exist [21]; the method used in this paper has been described in detail in [16]. The following is a short recap of the method and the adjustments required for its use in FEMU. The goal of B-WIM is to solve a system of equations, defined in (1) as:

$$s(t_j) = \sum_{i=0}^{N} A_i I\left(v_i\left(t_j - t_i\right)\right);\ j = 1 \ldots M \tag{1}$$

where $s(t_j)$ is the average value of the strain signals from sensors at M different times, A_i is the unknown axle weight, $I(x)$ is the known strain IL, v_i is the measured axle velocity,

t_i is the arrival time of an individual axle, N is the number of axles, and M is the number of measurements, which must be greater than or equal to N. The strain IL is specified in advance. Thus, the equation is linear in the unknown terms, meaning that relatively simple methods suffice to obtain the axle weights.

The same equation can be used to calculate the strain IL by treating the function $I(x)$ as an unknown, in addition to axle loads. Cubic splines are used to model the strain ILs. Splines are curves of the third order, smooth in derivatives and continuous in second derivatives, thereby matching the characteristics of observed strain ILs. The solved system is not linear in the unknown terms, necessitating iterative methods.

Figure 8 demonstrates the principle of strain IL modelling for a hypothetical three-span bridge, for the strain sensor located at the mid-span of the inner span. The strain IL is defined by the three types of points. The white points represent supports, the abscissas are defined by geometry, and the ordinates are 0. The exception is point M, located at the measurement point and whose ordinate is also optimised. The grey points define the radius d/2 of the rounded cap that improves the fit between the measured and modelled responses. Finally, the optional black points A through F can fine-tune the match. Their x-coordinates are selected, and y-coordinates are optimised. The ordinates of the curve between the control points are obtained with cubic spline interpolation.

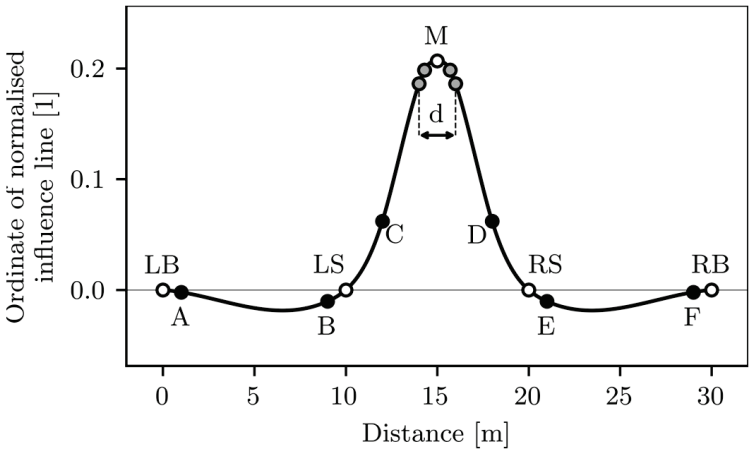


Figure 8. Hypothetical three-span bridge strain influence line (IL), approximated with cubic splines (adapted from [16]). The ordinates of the IL are obtained with cubic spline interpolation between the white (LB, LS, M, RS, RB), grey and black (A, B, C, D, E, F) control points.

This study required an adaptation to the original method for calculating the strain IL. As this technique can be applied to random traffic, monitoring its shape through time and detection allows for possible changes in bridge behaviour [16]. Since the axle loads of the vehicles from random traffic are unknown, the absolute strain IL value cannot be calculated. Instead, the strain IL is normalised so that the integral between points LS and RS is equal to 1, and the "raw" axle loads, calculated from the equation, adapt to this. Finally, one or more calibration vehicles with known axle loads cross the bridge several times. The ratio between raw and actual loads is calculated for each run, and the mean value of all results is taken as a calibration factor that converts raw into actual loads.

Calculating the strain IL with known axle loads, as in this study, allows for avoiding normalisation, as the actual influence of a unit axle on the bridge is needed. The known axle loads of the calibration vehicles were taken, and the strain IL height adapted itself during calculations.

Strain ILs were extracted separately for vehicle type and load (V1F, V1E, V2F, and V2E) and for vehicle speed (30, 70, and 90 km/h). Overall, 12 strain ILs were generated for each sensor. Figure 9 shows the strain ILs for sensors E_MG1 (a) and E_MG2, with blue,

red, magenta, and green colours denoting V1F, V1E, V2F, and V2E vehicles, respectively. The mean (μ) and mean ± standard deviation ($\mu \pm \sigma$) values are shown with dashed and grey lines, respectively.

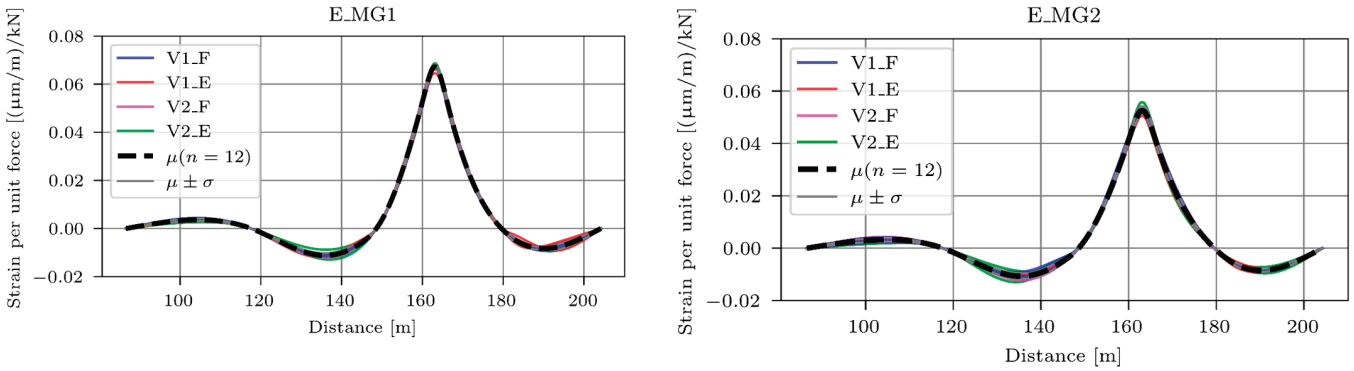


Figure 9. E_MG1 (**a**) and E_MG2 (**b**) strain ILs showing the (in)dependence of vehicle load and type.

Similarly, Figure 10 shows the generated strain ILs for sensors E_MG1 (Figure 10a) and E_MG2 (Figure 10b), with red, green, and blue colours denoting 30, 70, and 90 km/h speeds, respectively.

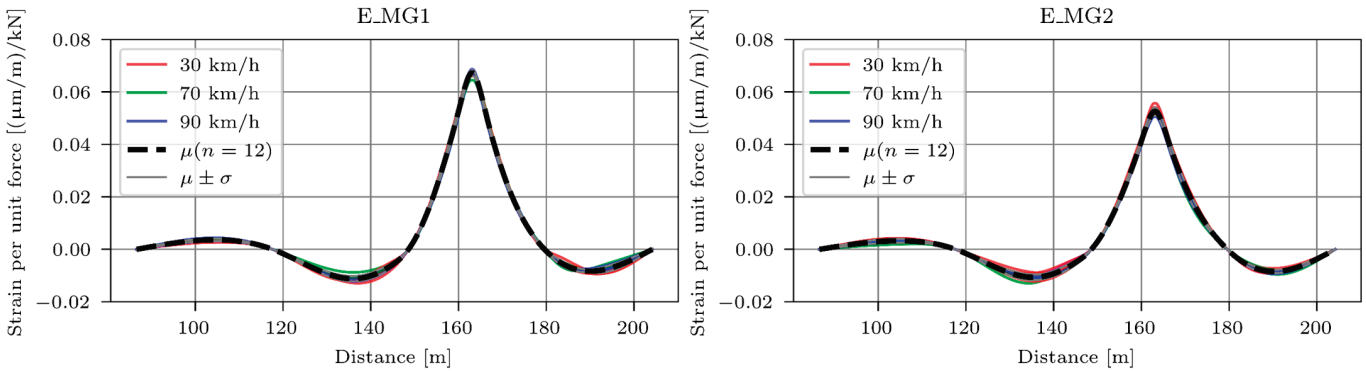


Figure 10. E_MG1 (**a**) and E_MG2 (**b**) strain ILs showing the speed (in)dependence.

Figures 9 and 10 indicate that vehicle type, load, and speed have a minimal impact (less than ±5% deviation of the maximum strain IL values, compared with the maximum values of the mean strain IL) on the strain IL's shape and magnitude. Consequently, the mean values of E_MG1 and E_MG2 strain ILs were used for the FEMU.

2.2.3. Ambient and Traffic-Induced Vibration Test

Operational modal analysis (OMA) was performed from the 60 min long signal, captured after the last passage of the calibration vehicle, the second night at 3:00 AM. Only a few passenger cars crossed the bridge in that time window. ARTeMIS Modal Pro 7.2 software [22] with the enhanced frequency domain decomposition (EFDD) method was used to estimate the modal parameters. The 66% overlap and 4096-point data samples resulted in approximately 0.06 Hz frequency resolution. Figure 11 shows the singular spectral density values for the limited range from 0 to 10 Hz. The coloured markers denote the detected modes used in the FEMU study, and the nearby text denotes the frequency values.

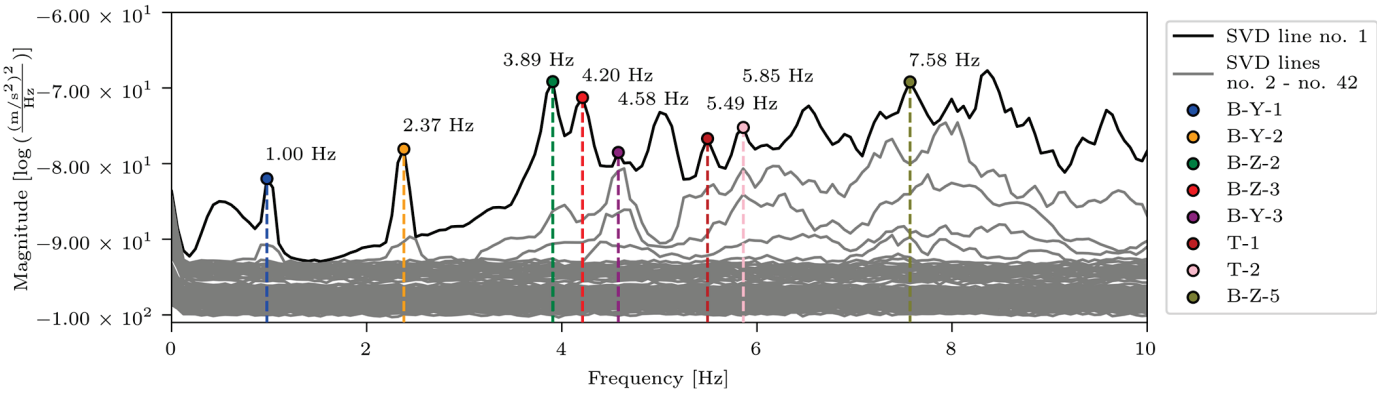


Figure 11. Singular spectral density values. Coloured markers denote the detected modes used in the FEMU study.

Eight modes were identified and considered in the FEMU. Modes are named by their shape (B for bending, T for torsion), direction (Y for movement in Y, Z for movement in vertical direction), and harmonics (1 for first harmonic, etc.). Mode name 'B-Y-1', for example, represents the first bending mode in the Y direction. Not all modes, represented by evident peaks, were considered. Their significance was decided based on their complexity, shape observation, modal assurance criterion (MAC) value, ability to distinguish them from the nearby modes, and whether they could be automatically detected and paired with measured modes. Table 2 shows natural frequencies and corresponding mode shapes from the ambient and traffic-induced vibration test. Red indicates the highest, and blue the lowest displacement magnitudes. Semi-transparent grey colour denotes the undeformed geometry.

Table 2 and Figure 12 demonstrate a strong similarity between B-Y-1, B-Y-2, and B-Y-3 modes, between B-Z-2 and B-Z-3 modes, and the T-1 and T-2 modes. This is expected, since they represent the primary movement in a similar direction.

Table 2. Natural frequencies and corresponding mode shapes from the ambient and traffic-induced vibration test. Red indicates the highest magnitude of displacements, while blue indicates the lowest. Semi-transparent grey colour denotes the undeformed geometry.

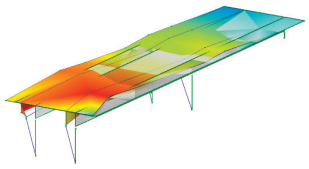
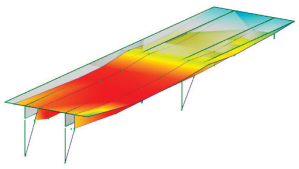
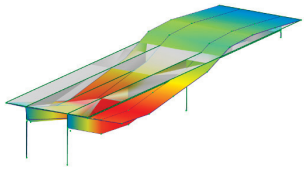
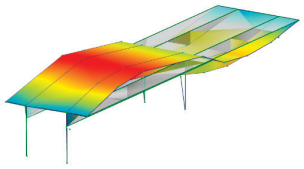
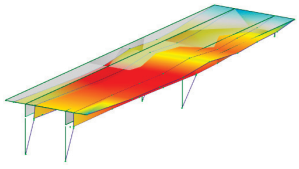
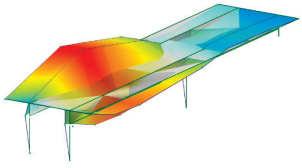
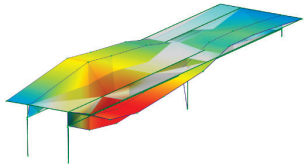
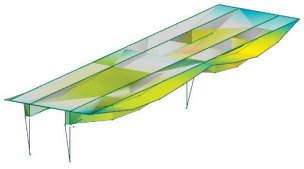
B-Y-1	**B-Y-2**	**B-Z-2**	**B-Z-3**
1.00 Hz	2.37 Hz	3.89 Hz	4.20 Hz
			
B-Y-3	**T-1**	**T-2**	**B-Z-5**
4.58 Hz	5.49 Hz	5.85 Hz	7.58 Hz
			

Figure 12 shows the auto-modal assurance criterion (Auto-MAC) matrix for the experimental mode shapes.

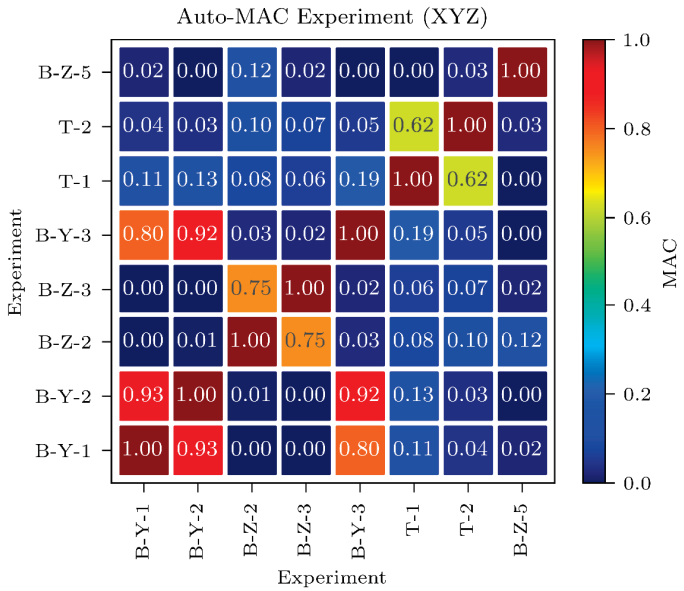


Figure 12. Auto-MAC matrix for the experimental mode shapes.

2.3. Finite Element (FE) Model

The bridge FE model was developed in Abaqus/CAE 2023 [23] software. All structural elements of the superstructure and piers were modelled using 20-node quadratic (C3D20R) hexahedral and 8-node linear (C3D8R) hexahedral elements, respectively. The approximate global mesh size was set to 0.50 m. Two analyses were conducted: modal analysis for extracting natural frequencies and mode shapes, and static analysis to determine the strain ILs. A 3D view and a detailed view of the pier–main girder and main girder–cross girder connections are shown in Figure 13a–d. Throughout this paper, the FE model, with properties from the design documentation, is denoted as the *initial FE model*.

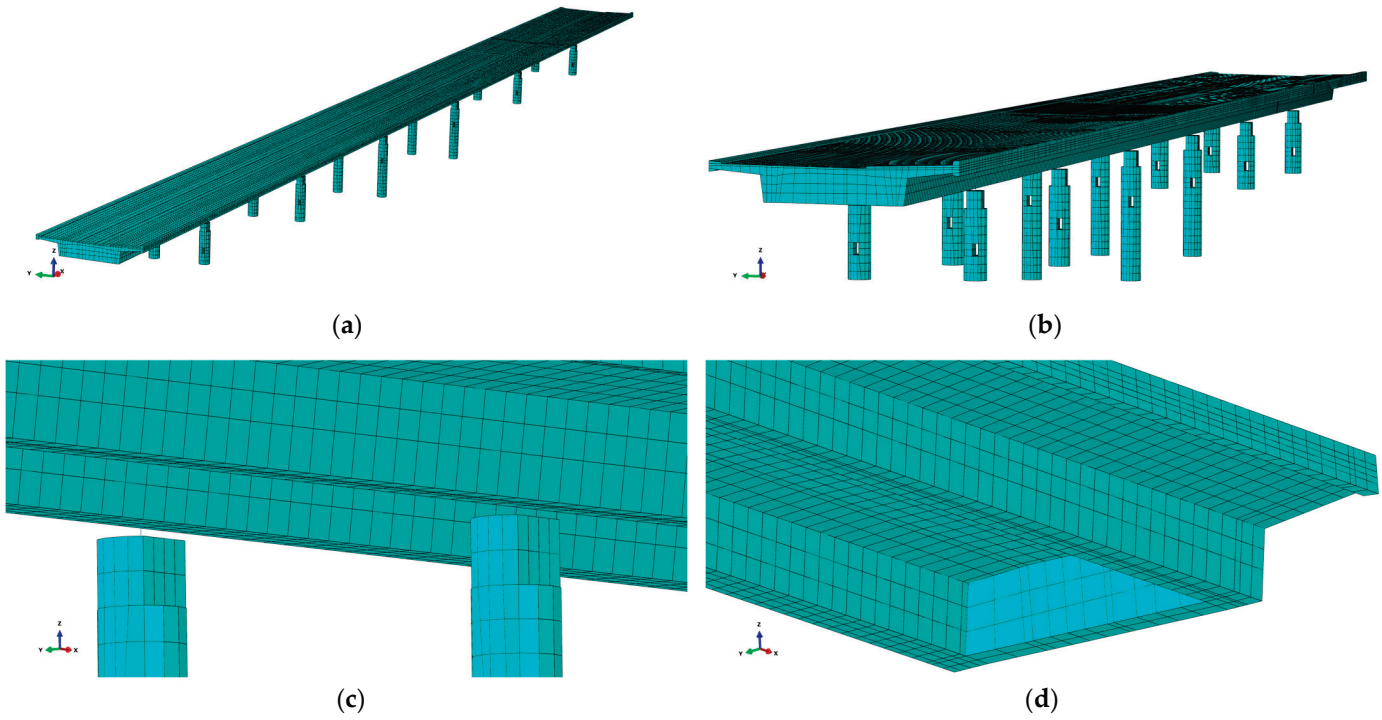


Figure 13. Finite element (FE) model of the bridge in the Abaqus/CAE 2023 software: 3D view of the entire bridge (**a**,**b**), detailed view near pier–main girder connection (**c**) and detailed view of the cross girder near abutments (**d**).

2.3.1. Geometry and Materials

The FE model was based on the geometry outlined in the design documents [24–27]. No in situ measurement data were used to construct the initial FE model. The edge beams and slab geometry were minimally simplified to design the finite element mesh. An isotropic elastic material was used for all elements. The material properties according to the design documentation [24–27] are shown in Table 3. Young's modulus and density for selected elements were modified to consider the element's weakening (holes in the SLAB5 element) and the effect of the attached non-structural elements.

Table 3. Material properties of structural elements according to design documentation [24–27].

Element	Abbreviation	Young's Modulus (GPa)	Poisson Ratio	Density (t/m^3)
Asphalt	ASPH	8.00	0.35	2.582
Edge beam 1	EB1	31.00	0.20	2.710
Edge beam 2	EB2	31.00	0.20	2.580
Main girder 1	MG1	35.00	0.20	2.500
Main girder 2	MG2	35.00	0.20	2.500
Slab 1	SLAB1	35.00	0.20	2.500
Slab 2	SLAB2	35.00	0.20	2.500
Slab 3	SLAB3	35.00	0.20	2.500
Slab 4	SLAB4	35.00	0.20	3.573
Slab 5	SLAB5	14.59	0.20	1.177
Pier (bottom part) [1]	PIER_BOTTOM	31.00	0.20	2.500
Pier (upper part, bearing region) [1]	PIER_TOP	34.00	0.20	2.500
Cross girder	CG	35.00	0.20	2.500

[1] PIER_BOTTOM represents the bottom parts, and PIER_TOP represents the top parts (bearing region) of all pier pairs: P1, P2, P3, P4, P5, and P6.

2.3.2. Interactions and Boundary Conditions

Piers were connected to the superstructure with elastomeric bearings modelled as wires (spring–dashpot assemblies). "Cartesian + Rotation" connector sections were assigned to these wires (assemblies), which connected reference points on the pier–girder contact surfaces. Stiffness properties were obtained from the design documentation [27] and are shown in Table 4. Unidirectional pot bearings, which connected the superstructure to the abutments, were not modelled as wires. Instead, the bearing surface was assigned a boundary condition with restrained movements in the Y and Z directions. A fixed boundary condition, which restrains displacements in all directions, was assigned to the bottom surfaces of all piers.

Table 4. Properties of bearings according to design documentation [27].

Bearing	Position (Abutment, Pier)	Translational Stiffness (kN/m)		Vertical Stiffness (kN/m)	Rotational Stiffness (kNm)
		X Direction	Y Direction		
Elastomeric bearing type 1	P1, P6	3.18×10^3	3.18×10^3	1.77×10^6	3.41×10^4
Elastomeric bearing type 2	P2, P3	3.61×10^3	3.61×10^3	2.01×10^6	3.90×10^4
Elastomeric bearing type 3	P4, P5	4.19×10^3	4.19×10^3	2.33×10^6	4.55×10^4
Unidirectional pot bearing	ABUT1, ABUT2	Free	Rigid	Rigid	Free (<0.01°)

2.4. Comparison of the Initial FE Model and Measurements

2.4.1. Strain IL

Strain ILs were calculated for longitudinal (E11) strains at the E_MG1 and E_MG2 positions. Since only the driving lane vehicle crossings were considered, the strain ILs were obtained with two pairs of 0.5 kN point loads (representing the vehicle wheels) varied across the last three spans, starting at the beginning of S5 and ending at the end of S7, at the expansion joint. The strain ILs were calculated for point loads spaced approximately 1.0 m apart, representing 92 static analyses required to extract each strain IL. Lastly, the modelled strain IL was discretised to 0.01 m with a cubic interpolator for the comparison with the measured strain IL. Figure 14 displays the E_MG1 (**a**) and E_MG2 (**b**) strain ILs of the initial FE model, the related measured strain ILs, and the differences between the two.

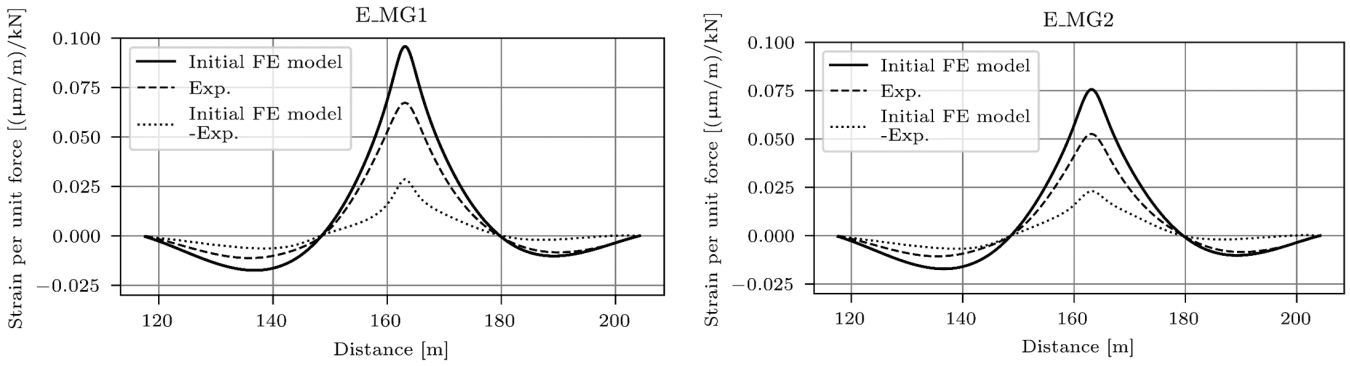


Figure 14. Strain ILs of the initial FE model and measured strain IL for E_MG1 (**a**) and E_MG2 (**b**).

As expected, the modelled strain ILs overestimated the measured ones, with the peaks exceeding the measured values by approximately 45% for both sensors.

2.4.2. Natural Frequencies and Mode Shapes

Table 5 shows the natural frequencies and mode shapes of the initial FE model. Only the modes considered for the FEMU are shown. Each has two figures. The upper shows the entire structure, and the lower shows the last two spans (S7, S8). Since the accelerometers were only installed in spans S7 and S8, the measured mode shapes are available only for those two spans. The purpose of the lower figure is to easily compare the modelled and measured responses in spans S7 and S8, as shown in Table 2.

Table 5. Natural frequencies and mode shapes of the initial FE model considered for the FEMU. The red colour indicates the highest, and blue the lowest displacement magnitude.

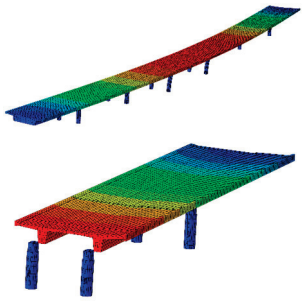
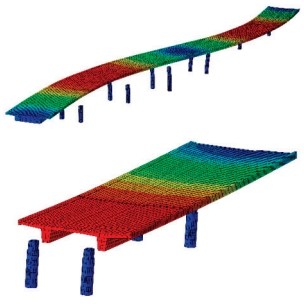
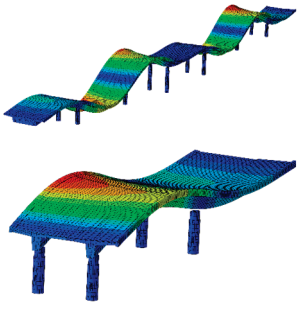
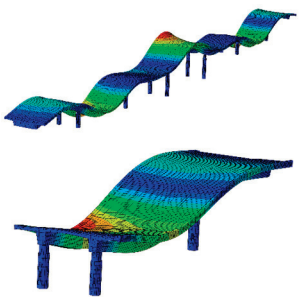
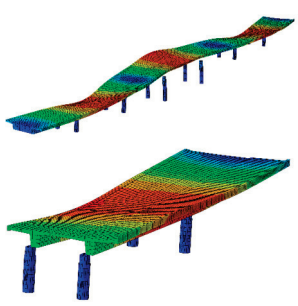
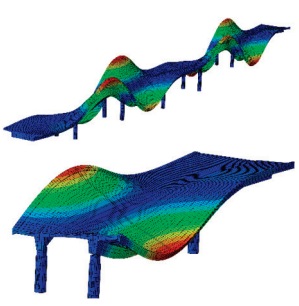
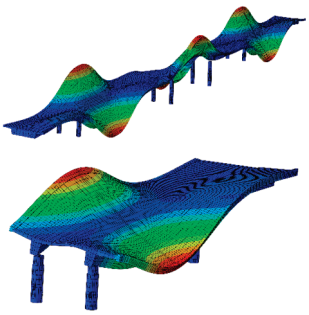
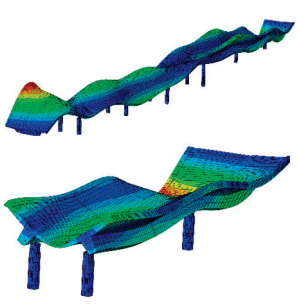
B-Y-1	**B-Y-2**	**B-Z-2**	**B-Z-3**
0.72 Hz	2.01 Hz	3.79 Hz	4.41 Hz
			

Table 5. *Cont.*

B-Y-3	T-1	T-2	B-Z-5
4.16 Hz	4.98 Hz	5.28 Hz	6.89 Hz
			

2.5. Finite Element Model Updating (FEMU): Error-Domain Model Falsification (EDMF)

For the FEMU, the EDMF methodology was employed instead of traditional approaches such as Bayesian model updating or residual minimisation. Introduced in 2013 for bridge load testing [28], EDMF is a structural identification methodology that leverages the falsification concept. Outlined by [28], it has deep roots in scientific methods, formalised in the 1930s by Karl Popper, who asserted that scientific models cannot be entirely verified by data, but can only be falsified. Using this framework, EDMF determines plausible values for FE model variables based on experimental field data and defined uncertainty levels. The methodology involves creating various FE model instances, each characterised by a unique set of variable values. These are then assessed by comparing the model's predictions with actual sensor data collected during experiments. Models that deviate beyond the set uncertainty thresholds are deemed falsified, narrowing the range of potential variable values.

According to [29], using falsification thresholds makes EDMF robust against the assumptions typically made about the correlation of uncertainties and incorporates adjustments for model biases based on engineering heuristics. This approach has been proven to offer more accurate identification and predictions, particularly where there is considerable systematic uncertainty, outperforming traditional methods like Bayesian model updating and residual minimisation. Its efficacy and growing acceptance are evidenced by its application in nine bridge-related studies, four on buildings, and two on geotechnical projects from 2015 to 2022 [29].

3. Results

3.1. Sensitivity Study

A deterministic sensitivity study was performed to understand the impact of individual structural elements and the boundary conditions on the natural frequencies and strain ILs. Based on its results, variables to be updated were selected. List of variables considered in the sensitivity analysis with the description is shown in Table 6.

Table 6. List of variables considered in the sensitivity analysis with the description.

Element/Variable/Property	Lower Value 1	Upper Value 1	Description
BC_FIXED_LEFT	DY = DZ = 0 (same as design)	DX = DY = DZ = 0	Movements in X direction are restrained at the left abutment's bearings
BC_FIXED_ RIGHT.	DY = DZ = 0 (same as design)	DX = DY = DZ = 0	Movements in X direction are restrained at the right abutment's bearings
BC_FIXED_LEFT&RIGHT	DY = DZ = 0 (same as design)	DX = DY = DZ = 0	Movements in X direction are restrained at the left and right abutment's bearings
ASPH, EB1, EB2, MG1, MG2, SLAB1, SLAB2, SLAB3, SLAB4, SLAB5, PIER_BOTTOM, PIER_TOP, CG	0.75 × design	1.25 × design	Young's modulus change

1 Design values from [24–27].

3.1.1. Natural Frequencies

The J_f objective function measures the similarity of modelled and measured natural frequencies. The lower it is, the lower the difference between the modelled and measured frequencies. It is defined as:

$$J_f = \sum_{i=1}^{n} \left(\frac{f_{i,\text{num}} - f_{i,\text{exp}}}{f_{i,\text{exp}}} \right)^2, \tag{2}$$

where $f_{i,\text{num}}$ and $f_{i,\text{exp}}$ are the ith matching mode pair of the natural frequencies from the FE model experiment, respectively. n is the overall number of natural frequencies considered. According to [30], this is the "normalised" J_2 type objective function.

3.1.2. Strain IL

The J_{IL} objective function measures the difference between the modelled and the mean measured strain IL. The lower it is, the more similar the compared strain ILs are. J_{IL} is defined separately for E_MG1 and E_MG2. Despite comparing two vectors (strain ILs), it is a scalar value. By definition, it is equal to the root-mean-square error (RMSE):

$$J_{\text{IL}} = \text{RMSE} = \sqrt{\frac{\sum_{j=1}^{m} \left(\text{IL}_{\text{num},j} - \text{IL}_{\text{exp},j} \right)^2}{m}}, \tag{3}$$

where $\text{IL}_{j,\text{num}}$ is the j-th ordinate of the modelled strain IL and $\text{IL}_{\text{exp},j}$ is the j-th ordinate of the mean measured strain IL IL_{exp}. m is the number of ordinate values considered and IL_{exp} is the mean measured strain IL (from all passages). J_{IL} can be interpreted as an average difference between the modelled and measured strain IL.

The sensitivity study results for the variation in the boundary conditions (bearings) and structural elements Young's modulus on the relative change in the objective function J_f are shown in Figure 15. Those for the variation of boundary conditions (bearings) and structural elements Young's modulus on the relative change of the objective function $J_{\text{IL,E\_MG1}}$ and $J_{\text{IL,E\_MG2}}$ are shown in Figure 16a,b.

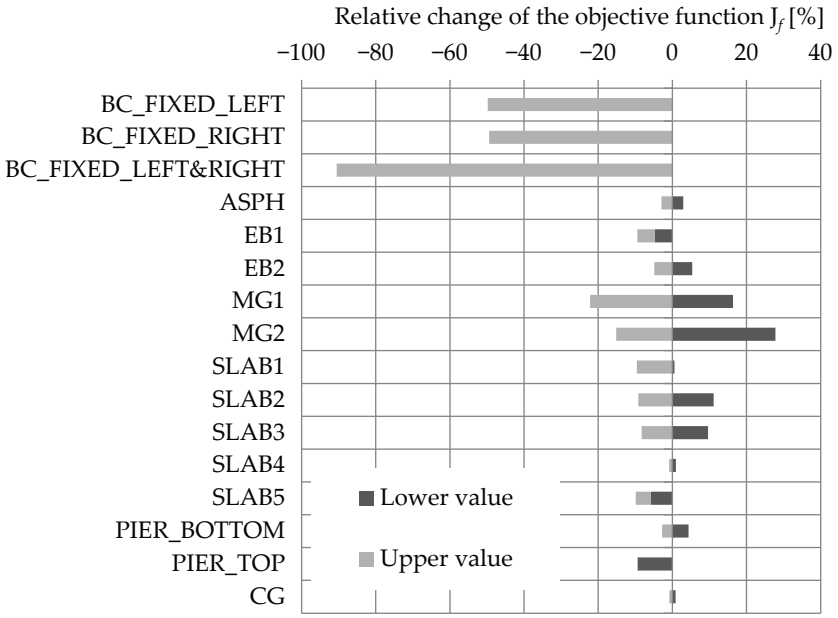


Figure 15. The sensitivity study results for the variation in boundary conditions (bearings) and structural elements' Young's modulus values on the relative change in the objective function J_f.

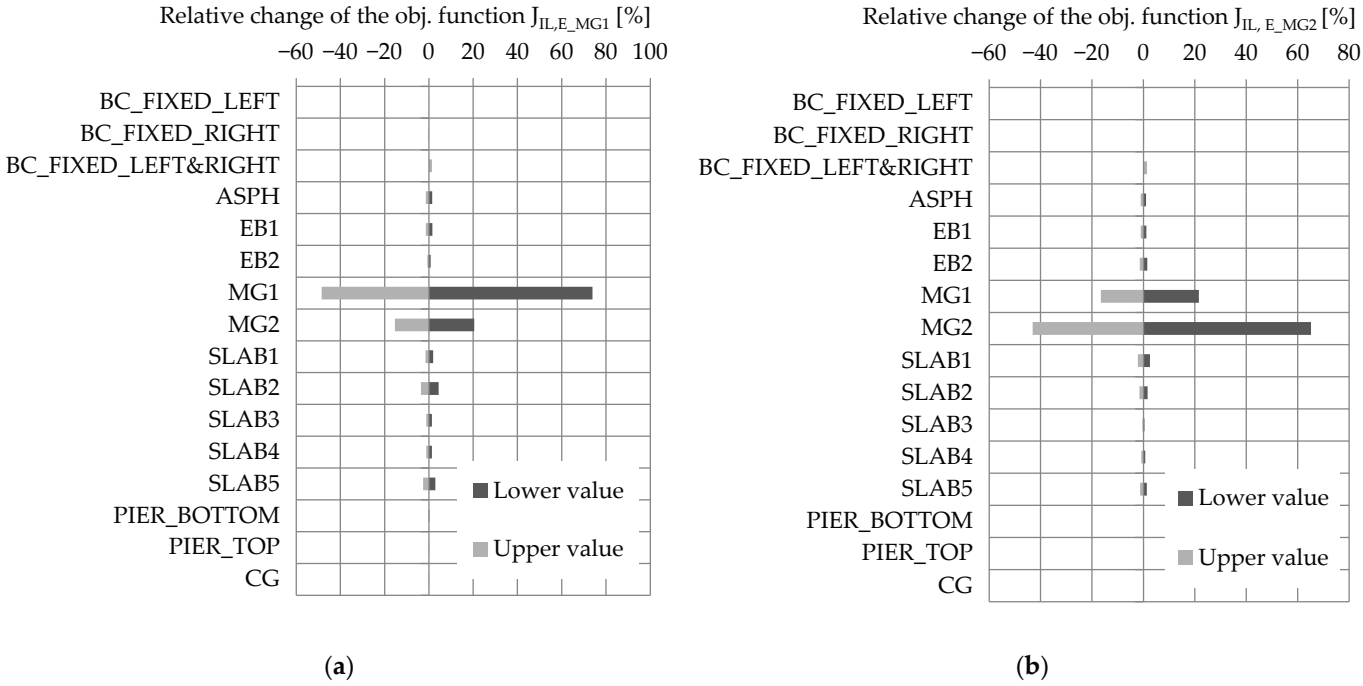


Figure 16. The sensitivity study results for the variation in boundary conditions (bearings) and structural elements' Young's modulus values on the relative change in the objective function J_{IL,E_MG1} (**a**) and J_{IL,E_MG2} (**b**).

Based on the sensitivity study results, it was decided to update the boundary conditions and Young's modulus of structural elements. For the mass, it was decided to estimate it as accurately as possible and keep it fixed to ensure that its increase did not decrease stiffness and vice versa (for the frequency-based FEMU). The Young's modulus values of MG1 and MG2 were updated through "Young's modulus adjustment factors" α_{MG1} and α_{MG2}. Those factors were defined as a correction factor, relative to the designed Young's modulus (shown in Table 3). A value of 1.00, for example, denotes no change in the Young's modulus and value of 1.20 denotes a 20% increase in the designed Young's modulus. All other structural elements were grouped into the 'OTHER' group, and their Young's modulus was updated by the same percentage through the α_{OTHER} Young's modulus adjustment factor.

It is crucial to note that the objective of FEMU, as outlined by [28], is not to adjust FE model variables to align the predicted and measured values better. Instead, model-based system identification employs physics-based models to deduce variable values. Consequently, the variables chosen for FEMU do not reflect the actual properties of structural elements, such as Young's modulus (adjustment factor). Instead, they should be viewed to consolidate the structural properties into a single variable. This distinction is important to remember, particularly when analysing the absolute values of the updated variables.

3.2. Updated FE Model

This chapter provides a comprehensive summary of the EDMF results, commencing with the frequency-based EDMF as illustrated in Figure 17, followed by the MAC-based EDMF depicted in Figure 20. Subsequently, a combined analysis of frequency- and MAC-based EDMF is shown in Figure 21. Finally, the strain-based EDMF results are presented in Figure 22. In these figures, experimental values are denoted by red markers, red horizontal lines indicate thresholds, candidates are represented in blue, and models that have been falsified are noted in grey. RMSE and MAC values are not measured, but calculated from modelled and measured responses. Therefore, the experimental values were denoted as 0

for RMSE values and 1.00 for MAC, representing the perfect match between the FE model and measurements.

3.2.1. Frequency-Based EDMF

In the frequency-based EDMF shown in Figure 17, all eight frequencies were considered. Thresholds for all frequencies were set as a multiplier of the experimental values; in this case, the [0.80, 1.20] interval, representing the $0.80 \cdot f_{i,\mathrm{exp}}$ as the lower bound and $1.20 \cdot f_{i,\mathrm{exp}}$ as the upper bound. The candidates had frequencies within ±20% of the measured values for this case. For a good correlation between the FE model and measurements, the relative difference between frequencies should be less than 5% [31]. In the initial phases of this study, it was necessary to apply threshold values somewhat higher than usual to identify viable candidates. While this may seem unrealistic, it was essential to obtain any candidates at all. Although the thresholds were subsequently reduced to 5% or less in later steps, we retained this stage to illustrate how the process of FEMU using EDMF was structured to facilitate the identification of the mode with the greatest deviation, and that finally guided us towards understanding the underlying cause. Note that, although strain IL-based (RMSE values) and MAC-based outputs (MAC values) are shown in this EDMF plot, in this case, they do not determine the candidates because of the large thresholds.

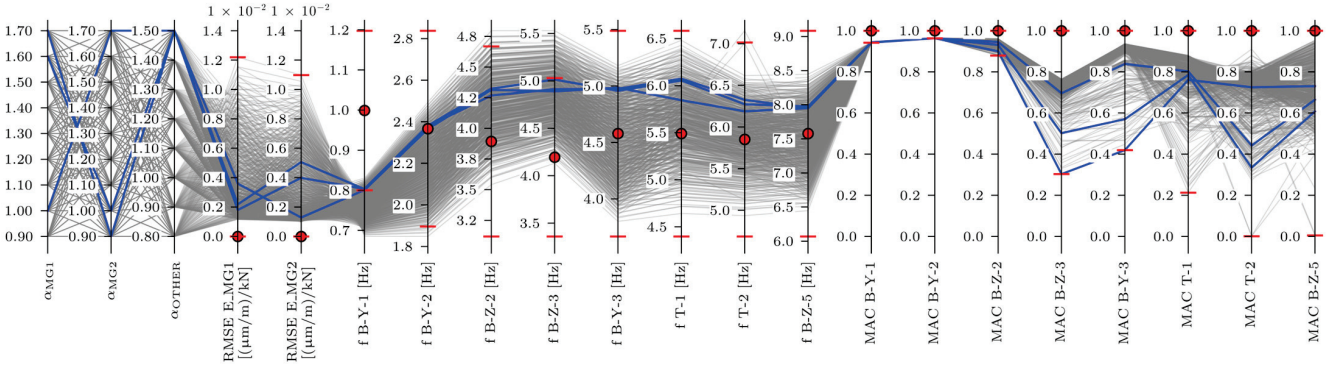


Figure 17. Frequency-based EDMF results. Experimental values are denoted by red markers, red horizontal lines indicate thresholds, candidates are represented in blue, and models that have been falsified are noted in grey.

B-Y-1 frequencies were underestimated and B-Z-3 overestimated compared with the measurements, as shown in Figure 17. Analysis of the EDMF's outputs was performed, where mean values of the modelled frequencies were compared with the experimental values, as shown in Figure 18.

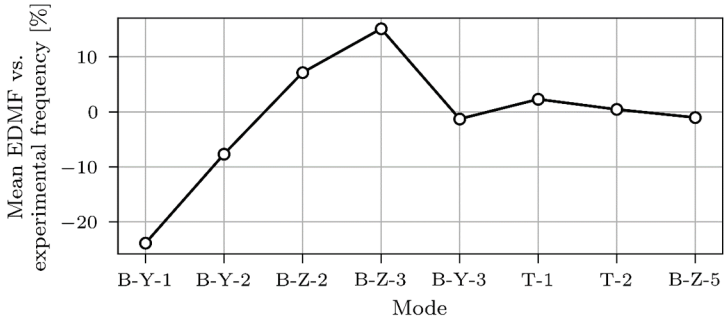


Figure 18. Difference between mean modelled (EDMF) and experimental frequencies.

The greatest absolute deviation between the mean modelled and measured values of frequencies was observed for B-Y-1 and B-Z-3 (Figure 18). Recalling the sensitivity study

results, fixed boundary conditions importantly reduce the objective function for natural frequencies and could significantly influence the B-Y-1 frequency. Contrary, fixed boundary conditions have a negligible effect on the strain ILs' objective functions. In the following, all analyses were performed on the FE model with fully fixed boundary conditions, where all degrees of freedom were constrained for bearings at both abutments.

The investigation of B-Z-3 overestimation revealed that the reason was the unreliable mode pairing strategy, which often paired the modelled B-Z-3 with the experimental B-Z-4 mode. By using the EDMF approach, it is possible to identify suspicious outputs caused by, for example [32], faulty sensors. A similar process was followed in this study, where the B-Z-3 mode was eliminated for all following analyses. Although still present in the EDMF plots, the B-Z-3 mode was excluded by setting the falsification threshold range for the B-Z-3 frequency between the minimum and maximum values of the modelled frequencies, allowing all FE models to pass through the B-Z-3 frequency thresholds. Figure 19 shows the frequency-based EDMF analysis on the FE models with fully restrained bearings at abutments and with B-Z-3 frequency eliminated. The threshold for all frequencies was set to [0.975, 1.025], allowing the frequencies to deviate to ±2.5%.

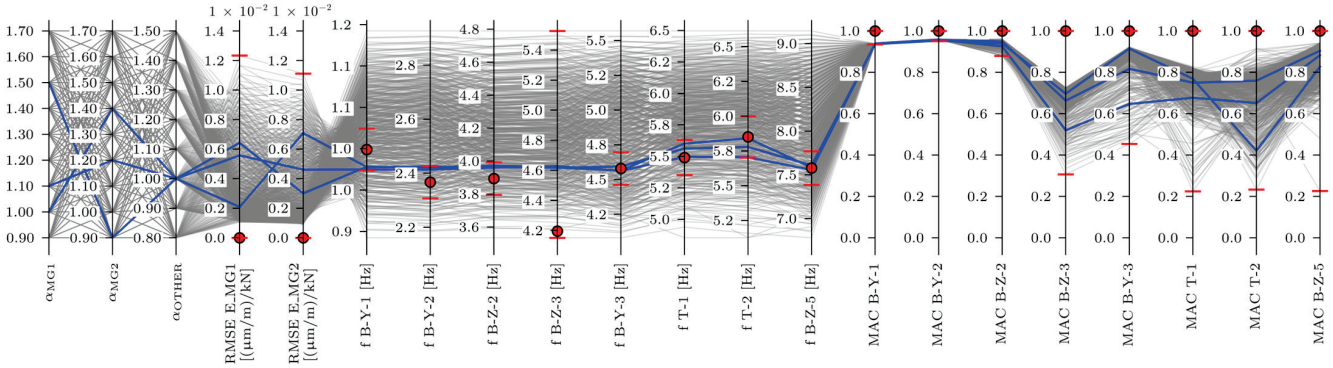


Figure 19. Frequency-based EDMF results. B-Z-3 frequency is not considered. Experimental values are denoted by red markers, red horizontal lines indicate thresholds, candidates are represented in blue, and models that have been falsified are noted in grey.

Considering fully restrained bearings at the abutments was essential for improving the B-Y-1 frequency results. This approach showed a minimal impact on the E_MG1 and E_MG2 strain IL responses, as illustrated in Figure 18. Previous studies, such as those referenced in [30,33], have also documented limited or restrained movements in bearings during ambient vibration tests. Although this effect was not measured directly, it was observed that clogged expansion joints and corroded bearings, as shown in Figure 4, limit movement, which is contrary to the original design specifications. Therefore, the assumption of fully restrained bearings at the abutments was considered reasonable, but should be studied in more detail in future research, for example, to model them as springs and change their stiffness gradually.

After considering fixed boundary conditions and eliminating the B-Z-3 frequency, the frequency-based EDMF results indicated large α_{MG1} ([1.00, 1.50]) and α_{MG2} ([0.90, 1.40]) ranges, while α_{OTHER} was equal to 1.00. Additionally, some candidates with a high α_{MG1} value had a small α_{MG2} value, which is not in line with the engineering judgement. Given that MG1 and MG2 are visually in similar conditions, it is expected that α_{MG1} and α_{MG2} would be comparable and higher than α_{OTHER} due to the many prestressing tendons. Those results are similar to the findings from another viaduct [34], where some candidates had a high–low stiffness trend for main girders, despite expectations that they would be comparable. After additional measurement data were added to the EDMF, that trend aligned with the engineering expectations.

3.2.2. MAC-Based EDMF

Figure 20 shows the MAC-based EDMF results. For the well-correlated modes, the MAC values should be greater than 0.90 [31], and for 'acceptable', 0.80 [35]. For MACs, the upper value of the thresholds was set to 1.00 for all modes, representing the scenario of perfectly similar modelled compared with the measured mode shape. The lower thresholds were set to 0.80 for all modes except for B-Z-3, which was, as already mentioned, removed from all analyses.

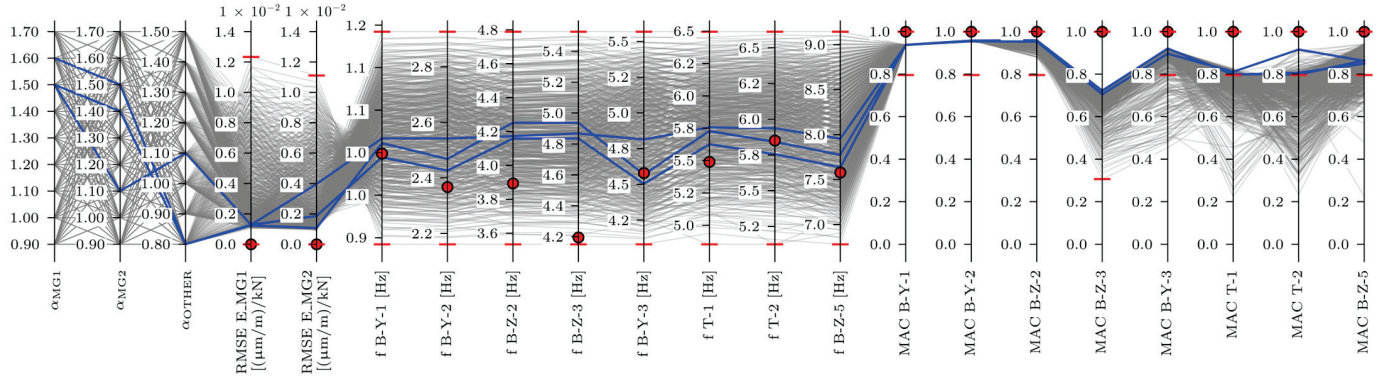


Figure 20. MAC-based EDMF results. Experimental values are denoted by red markers, red horizontal lines indicate thresholds, candidates are represented in blue, and models that have been falsified are noted in grey.

The MAC-based EDMF results fell into ranges [1.50, 1.60] for α_{MG1}, [1.10, 1.50] for α_{MG2}, and [0.80, 1.10] for α_{OTHER}.

3.2.3. Frequency & MAC-Based EDMF

The MAC values of some modes never exceeded the 0.90 value. There may have been several reasons for this [36], the sparse and/or improperly distributed sensor layout concerning the geometric complexity of the tested structure [37] being among the most likely. Despite that, it was expected that MAC criteria would improve results once added to the frequency-based EDMF. Particularly because the low MAC values also indicated incorrectly paired modelled and measured modes. As such, it would complement the frequency-based EDMF with more reliable candidates. Figure 21 shows the frequency and MAC-based EDMF results. The threshold for frequencies was set to [0.95, 1.05]. The upper thresholds for MAC were set to the absolute value of 1.00, and the lower thresholds to 0.78.

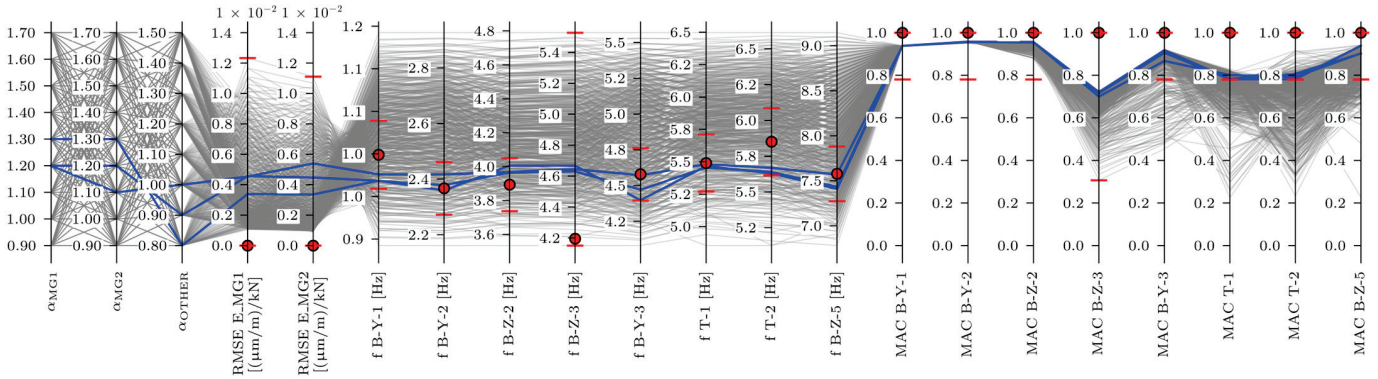


Figure 21. Frequency and MAC-based EDMF results. Experimental values are denoted by red markers, red horizontal lines indicate thresholds, candidates are represented in blue, and models that have been falsified are noted in grey.

The frequency and MAC-based EDMF produced a narrower range for α_{MG1} ([1.20, 1.30]) and α_{MG2} ([1.10, 1.30]), compared with the frequency-based EDMF. Both values were comparable and higher than α_{OTHER} ([0.80, 1.00]), which is in line with engineering expectations.

3.2.4. Strain IL-Based EDMF

Figure 22 shows the strain IL-based EDMF. The bottom thresholds for strains were set to 0, representing the perfect match between the measured and modelled strain IL. The upper thresholds were set iteratively, such that three candidates were obtained. All candidates had RMSE E_MG1 and RMSE E_MG2 values lower than 96% for all FE models.

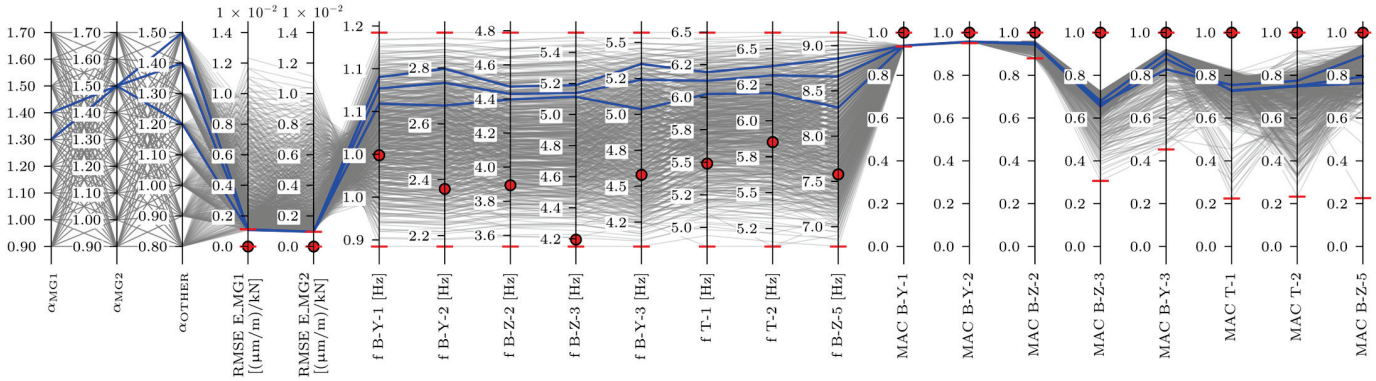


Figure 22. Strain IL-based EDMF results. Experimental values are denoted by red markers, red horizontal lines indicate thresholds, candidates are represented in blue, and models that have been falsified are noted in grey.

The final candidates produced by the strain-based EDMF had α_{MG1} and α_{MG2} values in the narrow range of [1.30, 1.40] and 1.50, respectively. They are both comparable with the results from the Ravbarkomanda viaduct study [34], where the stiffness of the main girders increased by up to 50%. The values of α_{OTHER} were in the range [1.20, 1,50].

3.2.5. Comparison of EDMF Results

Table 7 presents outputs; RMSE values for E_MG1 and E_MG2 sensors, and natural frequencies and mode shapes for the initial FE model and all four EDMF analyses. The measured values are added for comparison. 'Bottom' and 'Upper' denote both range thresholds the candidates provided. The RMSE values for both sensors were set to 0, and the MAC values for all mode shapes were set to 1.00. For each output, the cell value in a row that deviated most from the measured value is coloured red, and the one closest to the measured value is green. B-Z-3 frequencies and mode shapes are coloured grey because they were not considered in the EDMF study. Again, the results of all EDMF studies were calculated in the FE model with all restrained degrees of freedom at the ABUT1 and ABUT2 bearings. In contrast, the initial FE model enabled longitudinal movements.

The comparison of the EDMF results in Table 7 yielded the following conclusions:

- Setting bearings ABUT1 and ABUT2 to fixed improved the B-Y-1 and B-Y-2 modelled vs. measured frequency values;
- Frequency-based EDMF primarily improved the frequency values; a minor improvement was also seen for E_MG1 and E_MG2 strain ILs. The MAC values decreased;
- MAC-based improved MAC values, improvement in E_MG1 and E_MG2 strain ILs was greater than that in the frequency-based EDMF;

- Frequency and MAC-based EDMF improved frequencies and MACs, closely matching the results of frequency-based EDMF (for frequencies) and MAC-based EDMF (for MAC values), while both strain ILs did not align more closely with the measured ones;
- Strain-based EDMF only improved both strain ILs. Frequency and MAC values were even worse than for the initial FE model.

Table 7. Outputs: measured, initial FE mode, after frequency-based EDMF, after MAC-based EDMF, after frequency and MAC-based EDMF, and after strain IL-based EDMF. Red colour denotes the greatest and green the lowest deviation from the experimental values. Grey colour denotes the B-Z-3 mode that was not considered in the EDMF study.

Output	Experiment	Initial FE Model [1]	Frequency-Based		MAC-Based		Frequency and MAC-Based		Strain IL-Based	
			Bottom	Upper	Bottom	Upper	Bottom	Upper	Bottom	Upper
RMSE E_MG1 ((μm/m)/kN)	0	0.00821	0.00208	0.00642	0.00123	0.00128	0.00339	0.00456	0.00107	0.00112
RMSE E_MG2 ((μm/m)/kN)	0	0.00776	0.00300	0.00709	0.00107	0.00396	0.00336	0.00540	0.00095	0.00096
f B-Y-1 (Hz)	1.00	0.72	0.97	0.98	0.99	1.02	0.97	0.98	1.06	1.09
f B-Y-2 (Hz)	2.37	2.01	2.41	2.42	2.43	2.54	2.36	2.42	2.67	2.80
f B-Z-2 (Hz)	3.89	3.79	3.96	3.97	4.16	4.25	3.96	4.01	4.40	4.47
f B-Z-3 (Hz)	4.20	4.41	4.62	4.63	4.84	4.94	4.63	4.67	5.11	5.19
f B-Y-3 (Hz)	4.58	4.16	4.56	4.59	4.50	4.81	4.40	4.57	5.03	5.35
f T-1 (Hz)	5.49	4.98	5.50	5.60	5.63	5.76	5.46	5.48	6.02	6.19
f T-2 (Hz)	5.85	5.28	5.70	5.84	5.76	5.94	5.63	5.67	6.19	6.38
f B-Z-5 (Hz)	7.58	6.89	7.56	7.61	7.64	7.95	7.41	7.57	8.32	8.86
MAC B-Y-1	1.00	0.94	0.94	0.94	0.94	0.94	0.94	0.94	0.94	0.94
MAC B-Y-2	1.00	0.96	0.95	0.96	0.95	0.96	0.96	0.96	0.96	0.96
MAC B-Z-2	1.00	0.95	0.93	0.95	0.95	0.96	0.95	0.96	0.94	0.95
MAC B-Z-3	1.00	0.76	0.52	0.70	0.71	0.72	0.70	0.72	0.65	0.68
MAC B-Y-3	1.00	0.93	0.65	0.91	0.90	0.92	0.87	0.92	0.83	0.90
MAC T-1	1.00	0.83	0.68	0.77	0.80	0.81	0.78	0.80	0.73	0.75
MAC T-2	1.00	0.78	0.42	0.76	0.80	0.92	0.78	0.81	0.75	0.77
MAC B-Z-5	1.00	0.86	0.83	0.90	0.85	0.86	0.90	0.94	0.76	0.89

[1] All FE models except for the initial FE model had fixed ABUT1 and ABUT2 bearings.

Table 8 presents the updated variables for all EDMF studies performed. The initial values of 1, obtained from the initial FE model, are added for comparison.

Table 8. Comparison of EDMF results: updated variables.

FEMU Results	α_{MG1}	α_{MG2}	α_{OTHER}
Initial FE model	1.0	1.0	1.0
Frequency-based	1.0–1.5	0.9–1.4	1.0
MAC-based	1.5–1.6	1.1–1.5	0.8–1.1
Frequency and MAC-based	1.2–1.3	1.1–1.3	0.8–1.0
Strain IL-based	1.3–1.4	1.5	1.2–1.5

Comparing the values from Tables 7 and 8 yielded the conclusion that combining frequencies and MACs into EDMF was reasonable because it has significantly narrowed the range of the candidates' variables. The updated approximately 25 and 20% increases in the MG1 and MG2 main girders' stiffnesses and 10% decrease in the stiffnesses of all other elements are also in line with the expectations. Some updated MAC values are still lower than 0.90, and it should be noted that future research is needed to investigate the cause. The strain IL-based EDMF narrowed the MG1 and MG2 stiffness increases to more reasonable values of 35 and 50%. The α_{OTHER} range, however, remained wide as the E_MG1 and E_MG2 strain ILs were not sensitive to OTHER elements.

The strain IL-based EDMF generally resulted in approximately 10–15% higher values of frequencies (Figure 22) than those from the frequency and MAC-based EDMF (Figure 21)

or measured ones. A similar trend can be seen for the RMSE values from the frequency and MAC-based EDMF. They were higher than the strain IL-based EDMF values, because the MG1 and MG2 stiffnesses were underestimated. Figure 23 compares the strain ILs of the initial FE model with the frequency and MAC-based and strain IL-based updated models for E_MG1 (Figure 23a) and E_MG2 (Figure 23b).

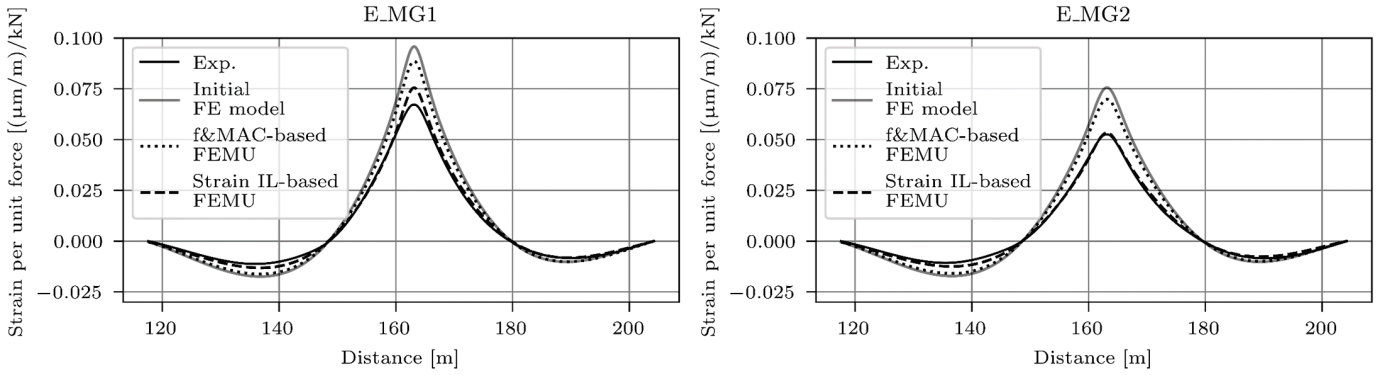


Figure 23. E_MG1 (**a**) and E_MG2 (**b**) strain ILs: comparison of measured, initial, frequency and MAC-based, and strain IL-based updated models.

The initial FE model overestimated the maximum modelled E_MG1 IL strains by 43% compared with the measured values. The frequency and MAC-based updated FE model overestimated the measured strains by 32%, and the strain IL-based FE updated model by 12%. For E_MG2 IL strains, the corresponding overestimations were 44%, 33%, and almost none, respectively.

Discrepancies between the modal (frequency, MAC)-based and static (strain, displacement)-based FEMU have already been reported, for example, by [30,38,39]. Despite using the advanced FE model with 3D finite elements and reliable measurement data in a controlled environment, this study could not eliminate these discrepancies. A potential cause could be that we measured a more global response with acceleration than with strain or displacement measurements under traffic load. The captured mode shapes, shown in Table 2, showed global behaviour in all directions, while for strain and displacement measurements, the bridge mainly deformed only in the vertical direction in S5, S6, and S7 spans. This means that the structural elements contributed differently to the modal and the static (strain, displacement) responses, which was already shown in the sensitivity analysis. This should be studied more in the future, along with the impact of non-structural components, like railings and pipes, and assumptions regarding mass.

3.3. Validation of the Updated FE Models with Measured Strains and Displacements Under Calibration Vehicle Passages

3.3.1. Strains

This section compares the measured and modelled E_MG1 and E_MG2 strains under V2_F vehicle crossings. The entire strain histories are presented, and not just the strain ILs for the E_MG1 and E_MG2 sensors. Figures 24 and 25 compare the responses of E_MG1 and E_MG2 sensors, respectively. First, the strain records of three crossings at approximately 30 km/h are shown; the colours denote the exact measured speed. The mean of the three maximum values is shown with a marker. Then, three responses are added for the initial (α_{MG1} = 1.00, α_{MG2} = 1.00, α_{OTHER} = 1.00), frequency and MAC-based (one of the candidates with α_{MG1} = 1.20, α_{MG2} = 1.10, α_{OTHER} = 1.00), and strain IL-based updated FE models (one of the candidates with α_{MG1} = 1.30, α_{MG2} = 1.50, α_{OTHER} = 1.40).

The strain IL-based FEMU did, and the frequency and MAC-based FEMU did not significantly improve the strain response at E_MG1 and E_MG2. The initial FE model overestimated the maximum measured E_MG1 strains for 51%, the frequency and MAC-based updated FE model by 40%, and the strain IL-based FE updated model by 19%. For E_MG2 strains, the corresponding values were 49%, 38%, and 6%. These values resemble the overestimations of the strain ILs, shown in Figure 23.

A similar conclusion can be drawn for strains and displacements. The strain-IL-based FEMU improved the displacement response even more than the strain response. The initial FE model overestimated maximum measured D_MG1 vertical displacements by 36%, frequency and MAC-based by 28% and strain IL-based FE updated model by 5%. For D_MG2 vertical displacements, the corresponding values were 35%, 25%, and −2%.

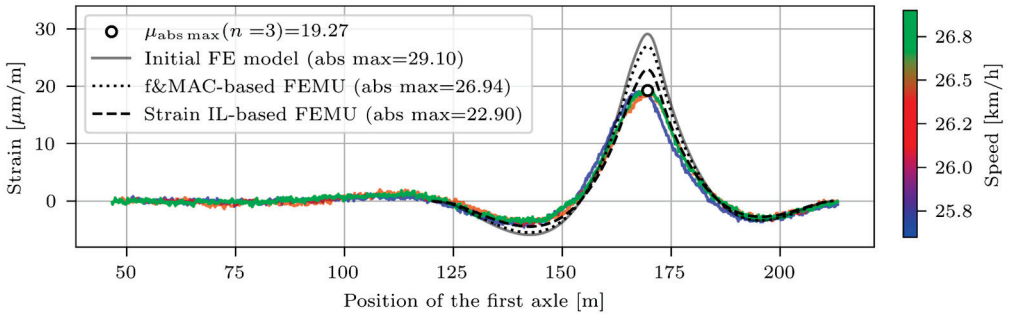


Figure 24. Comparison of E_MG1 strains under V2_F passages: measurements (30 km/h), initial, frequency and MAC-based, and strain IL-based updated FE models.

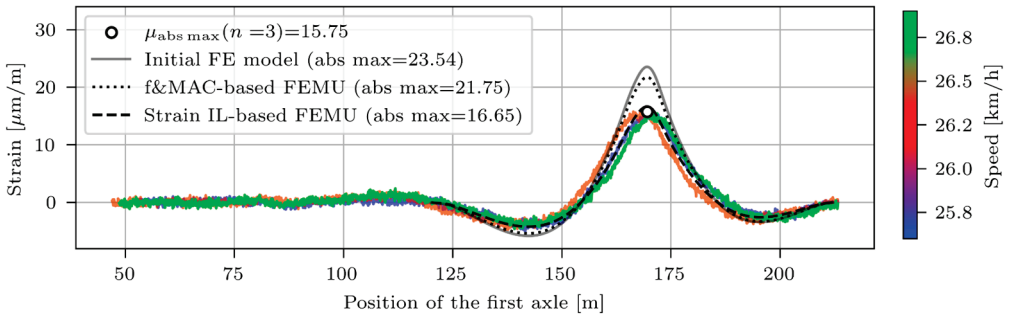


Figure 25. Comparison of E_MG2 strains under V2_F passages: measurements (30 km/h), initial, frequency and MAC-based, and strain IL-based updated FE models.

3.3.2. Displacements

To validate the results, Figures 26 and 27 compare the measured and modelled D_MG1 and D_MG2 vertical displacements under the crossings of the V2_F vehicle. The displacements were not considered in the FEMU. Thus, this validation is completely independent.

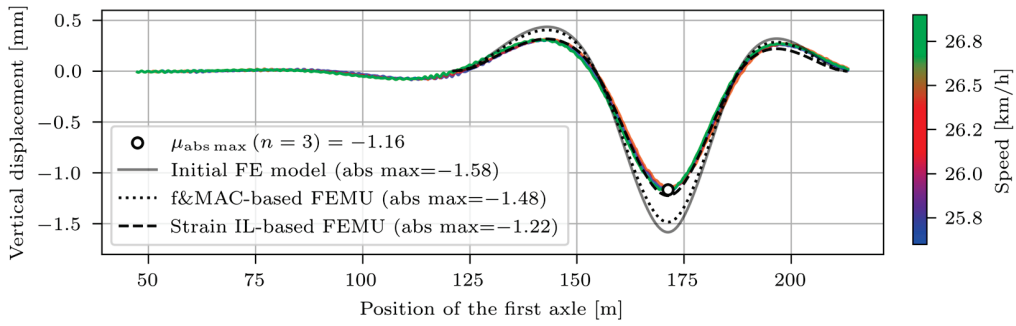


Figure 26. Comparison of D_MG1 displacements under V2_F crossings: measurements (30 km/h), frequency and MAC-based, and strain IL-based updated FE models.

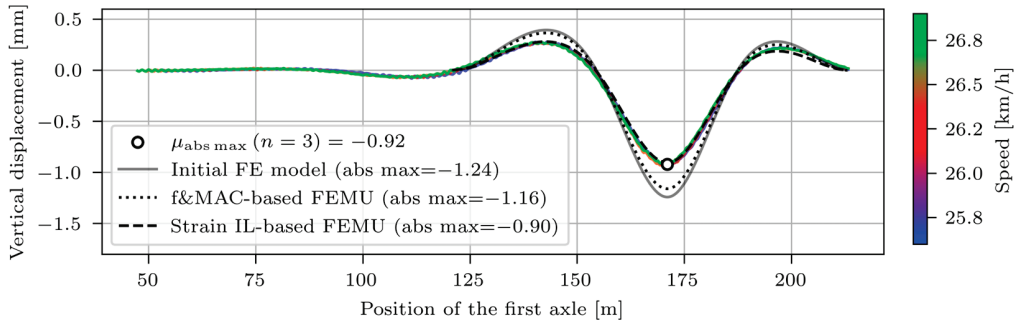


Figure 27. Comparison of D_MG2 displacements under V2_F crossings: measurements (30 km/h), frequency and MAC-based, and strain IL-based updated FE models.

4. Conclusions

The Tomačevo case study bridge serves as a B-WIM and SHM living laboratory, designed to develop and test new technologies, sensors, and methodologies. Data from this bridge demonstrated that measured strain ILs, a by-product of B-WIM measurements, offer new opportunities for leveraging B-WIM results in FEMU and SHM applications. Strain ILs have been shown to enhance acceleration and MAC-based FEMU results for multi-span concrete bridges, particularly when assessing bridge responses under traffic loads. This finding was validated through an independent comparison of measured vertical mid-span displacements during calibration vehicle crossings, showing strong agreement between the results of the measurements and the strain IL-based updated model.

The EDMF methodology was applied to conduct four independent FEMU studies: frequency-based, MAC-based, frequency and MAC-based, and strain IL-based. Three key variables were updated: α_{MG1}, α_{MG2}, and α_{OTHER}, representing Young's modulus adjustment factors for the two main girders (MG1 and MG2) and all other structural elements, respectively. Combining frequency and MAC-based methods proved more effective than using them separately, yielding a narrower range for α_{MG1} and α_{MG2}, compared with the frequency-based EDMF. The frequency and MAC-based EDMF led to moderate stiffness increases of 25% (range 20–30%) and 20% (range 10–30%) for MG1 and MG2, respectively. In contrast, the strain IL-based approach resulted in more pronounced increases of 35% (range 30–40%) and 50%. For other structural elements, the two methods diverged: while the frequency and MAC-based approach suggested a 10% decrease (range from −20% to 0%), the strain IL-based method indicated a 35% (range from 20–50%) increase in stiffness.

FEMU must be applied cautiously, particularly when relying solely on modal parameters, as their misinterpretation can lead to incorrect adjustments and inaccurate bridge response predictions. This study reinforces the value of incorporating strain ILs in FEMU to improve model accuracy and enhance agreement between simulated and measured bridge behaviour under traffic loads. These findings expand the potential applications of B-WIM in both FEMU and SHM.

As FEMU methodologies evolve, advancements in sensor technology and computational techniques are driving progress in structural assessment and monitoring. Future research should focus on understanding discrepancies between different FEMU approaches, refining strain IL extraction under extreme traffic conditions, and integrating FEMU into long-term SHM frameworks. These developments will further improve FEMU's reliability and broaden its applications in bridge performance assessment.

Author Contributions: Conceptualisation, D.H., A.Ž., P.Č. and A.A.; formal analysis, D.H., J.K. and P.Č.; methodology, D.H., A.Ž., P.Č. and A.A.; software, D.H., J.K. and P.Č.; investigation, D.H., J.K., A.Ž. and A.A.; resources, D.H., A.A., A.Ž. and P.Č.; data curation, D.H.; writing—original draft preparation, D.H., A.Ž., P.Č. and A.A.; writing—review and editing, D.H., J.K., A.Ž. and P.Č.;

visualisation, D.H. and A.Ž.; supervision, A.Ž., P.Č. and A.A.; project administration, A.Ž., P.Č. and A.A.; funding acquisition, A.Ž., P.Č. and A.A. All authors have read and agreed to the published version of the manuscript.

Funding: The authors acknowledge the financial support from the Slovenian Research and Innovation Agency: Young Researcher Funding Programme No. 53694, Research core funding No. P2-0260 and P2-0273 and Infrastructure funding I0-0032.

Data Availability Statement: The finite element models and the data from the case study are available upon request from the corresponding author.

Acknowledgments: We appreciate the research and insights gained from the Tomačevo Bridge Living Laboratory, established through the collaboration of the Slovenian National Building and Civil Engineering Institute (ZAG), Cestel, and Dewesoft. We also acknowledge the involvement of colleagues from the Section for Bridges at ZAG in the experimental campaign. Additionally, we acknowledge the support of the Interreg Central Europe project BIM4CE for contributing to the activities described in this paper. We thank the Ministry of Infrastructure, Directorate of the Republic of Slovenia for Infrastructure (DRSI), which allowed access to the bridge for the establishment of the Tomačevo Bridge Living Laboratory.

Conflicts of Interest: The authors declare no conflicts of interest.

References

1. Žnidarič, A.; Pakrashi, V.; OBrien, E.J.; O'Connor, A. A Review of Road Structure Data in Six European Countries. *Proc. Inst. Civ. Eng.-Urban Des. Plan.* **2011**, *164*, 225–232. [CrossRef]
2. Wikipedia Contributors. List of Bridge Failures. Available online: https://en.wikipedia.org/w/index.php?title=List_of_bridge_failures&oldid=1268499764 (accessed on 31 January 2025).
3. World Bank; Bolt, J.; van Zanden, J.L. Maddison Project Database 2023; Maddison Database 2010—With Major Processing by Our World in Data. Global GDP over the Long Run—World Bank, Maddison Project Database, Maddison Database—Historical Data. Available online: https://ourworldindata.org/grapher/global-gdp-over-the-long-run (accessed on 31 January 2025).
4. Mottershead, J.E.; Friswell, M.I. Model Updating In Structural Dynamics: A Survey. *J. Sound Vib.* **1993**, *167*, 347–375. [CrossRef]
5. Hester, D.; Koo, K.; Xu, Y.; Brownjohn, J.; Bocian, M. Boundary Condition Focused Finite Element Model Updating for Bridges. *Eng. Struct.* **2019**, *198*, 109514. [CrossRef]
6. Ticona Melo, L.R.; Malveiro, J.; Ribeiro, D.; Calçada, R.; Bittencourt, T. Dynamic Analysis of the Train-Bridge System Considering the Non-Linear Behaviour of the Track-Deck Interface. *Eng. Struct.* **2020**, *220*, 110980. [CrossRef]
7. Wang, H.; Li, A.; Li, J. Progressive Finite Element Model Calibration of a Long-Span Suspension Bridge Based on Ambient Vibration and Static Measurements. *Eng. Struct.* **2010**, *32*, 2546–2556. [CrossRef]
8. Bertola, N.J.; Smith, I.F.C. A Methodology for Measurement-System Design Combining Information from Static and Dynamic Excitations for Bridge Load Testing. *J. Sound Vib.* **2019**, *463*, 114953. [CrossRef]
9. Xiao, F.; Mao, Y.; Tian, G.; Chen, G.S. Partial-Model-Based Damage Identification of Long-Span Steel Truss Bridge Based on Stiffness Separation Method. *Struct. Control Heal. Monit.* **2024**, *2024*, 5530300. [CrossRef]
10. Calò, M.; Ruggieri, S.; Buitrago, M.; Nettis, A.; Adam, J.M.; Uva, G. An ML-Based Framework for Predicting Prestressing Force Reduction in Reinforced Concrete Box-Girder Bridges with Unbonded Tendons. *Eng. Struct.* **2025**, *325*, 119400. [CrossRef]
11. OBrien, E.; Quilligan, M.J.; Karoumi, R. Calculating an Influence Line from Direct Measuremetns. *Proc. Inst. Civ. Eng. Bridge Eng.* **2005**, *159*, 31–34.
12. Yan, W.-J.; Yuen, K.-V. A New Probabilistic Frequency-Domain Approach for Influence Line Extraction from Static Transmissibility Measurements under Unknown Moving Loads. *Eng. Struct.* **2020**, *216*, 110625. [CrossRef]
13. Frøseth, G.; Rønnquist, A.; Cantero, D.; Øiseth, O. Influence Line Extraction by Deconvolution in the Frequency Domain. *Comput. Struct.* **2017**, *189*, 21–30. [CrossRef]
14. Li, J.-A.; Feng, D.; Li, Z.; Zhang, H. Bridge Influence Line Identification Using an Adaptive Enhanced Variational Mode Decomposition. *Eng. Struct.* **2025**, *326*, 119561. [CrossRef]
15. Žnidarič, A.; Kalin, J.; Kreslin, M. Improved Accuracy and Robustness of Bridge Weigh-in-Motion Systems. *Struct. Infrastruct. Eng.* **2017**, *14*, 13. [CrossRef]
16. Žnidarič, A.; Kalin, J. Using Bridge Weigh-in-Motion Systems to Monitor Single-Span Bridge Influence Lines. *J. Civ. Struct. Health Monit.* **2020**, *10*, 743–756. [CrossRef]
17. *DEWESoft DewesoftX*, Version 2023.5. Available online: https://dewesoft.com/products/dewesoftx (accessed on 26 December 2023).

18. Jacob, B.; OBrien, E.J.; Jehaes, S. (Eds.) *Weigh-in-Motion of Road Vehicles: Final Report of the COST 323 Action*; LCPC: Paris, France, 2002.
19. Žnidarič, A. Influence of Number and Quality of Weigh-in-Moiton Data on Evaluation of Load Effects on Bridges. Ph.D. Thesis, University of Ljubljana, Ljubljana, Slovenia, 2017.
20. Moses, F. Weigh-in-Motion System Using Instrumented Bridges. *J. Transp. Eng.* **1979**, *105*, 233–249. [CrossRef]
21. Zheng, X.; Yang, D.H.; Yi, T.H.; Li, H.N. Development of Bridge Influence Line Identification Methods Based on Direct Measurement Data: A Comprehensive Review and Comparison. *Eng. Struct.* **2019**, *198*, 109539. [CrossRef]
22. Solution, S.V. ARTeMIS Modal Pro. Available online: https://www.svibs.com/artemis-modal-pro/ (accessed on 26 December 2023).
23. *Dassault Systemes User Assistance*; R2023x; Dassault Systèmes: Vélizy-Villacoublay, France, 2023.
24. *Technical Report About the General Project of the Tomačevo Bridge*; Industrijski projektni zavod Zagreb: Zagreb, Croatia, 1980. (In Croatian)
25. *Cross Section of the Tomačevo Bridge*; Industrijski projektni zavod Zagreb: Zagreb, Croatia, 1980. (In Croatian)
26. *Detail of the Sidewalk of the Tomačevo Bridge*; Industrijski projektni zavod Zagreb: Zagreb, Croatia, 1980. (In Croatian)
27. *Static Analysis of the Tomačevo Bridge*; Industrijski projektni zavod Zagreb: Zagreb, Croatia, 1980. (In Croatian)
28. Goulet, J.-A.; Smith, I.F.C. Structural Identification with Systematic Errors and Unknown Uncertainty Dependencies. *Comput. Struct.* **2013**, *128*, 251–258. [CrossRef]
29. Pai, S.G.S.; Smith, I.F.C. Methodology Maps for Model-Based Sensor-Data Interpretation to Support Civil-Infrastructure Management. *Front. Built Environ.* **2022**, *8*, 801583. [CrossRef]
30. Schlune, H.; Plos, M.; Gylltoft, K. Improved Bridge Evaluation through Finite Element Model Updating Using Static and Dynamic Measurements. *Eng. Struct.* **2009**, *31*, 1477–1485. [CrossRef]
31. Jiménez-Alonso, J.F.; Naranjo-Perez, J.; Pavic, A.; Sáez, A. Maximum Likelihood Finite-Element Model Updating of Civil Engineering Structures Using Nature-Inspired Computational Algorithms. *Struct. Eng. Int.* **2021**, *31*, 326–338. [CrossRef]
32. Cao, W.-J.; Koh, C.G.; Smith, I.F.C. Enhancing Static-Load-Test Identification of Bridges Using Dynamic Data. *Eng. Struct.* **2019**, *186*, 410–420. [CrossRef]
33. Hekič, D.; Kosič, M.; Kalin, J.; Žnidarič, A.; Anžlin, A. Challenges of Implementing Bridge Weigh-in-Motion on a Century-Old Steel-Riveted Railway Bridge. In *Bridge Maintenance, Safety, Management, Digitalization and Sustainability*; CRC Press: Boca Raton, FL, USA, 2024; pp. 1429–1436.
34. Hekič, D.; Ribeiro, D.; Anžlin, A.; Žnidarič, A.; Češarek, P. Improved Finite Element Model Updating of a Highway Viaduct Using Acceleration and Strain Data. *Sensors* **2024**, *24*, 2788. [CrossRef] [PubMed]
35. Ewins, D.J. Model Validation: Correlation for Updating. *Sadhana* **2000**, *25*, 221–234. [CrossRef]
36. Allemang, R. The Modal Assurance Criterion—Twenty Years of Use and Abuse. *Sound Vib.* **2003**, *37*, 14–23.
37. Rainieri, C.; Fabbrocino, G. *Operational Modal Analysis of Civil Engineering Structures, An Introduction and a Guide for Applications*; Springer: New York, NY, USA, 2014; ISBN 978-1-4939-0767-0.
38. Solís, M.; He, L.; Lombaert, G.; De Roeck, G. Finite Element Model Updating of a Footbridge Based on Static and Dynamic Measurements. In Proceedings of the 4th International Conference on Computational Methods in Structural Dynamics and Earthquake Engineering, Kos Island, Greece, 12–14 June 2013; pp. 1432–1449. [CrossRef]
39. Anžlin, A.; Hekič, D.; Kalin, J.; Kosič, M.; Ralbovsky, M.; Lachinger, S. *Assets4rail Deliverable D3.3: Improved Fatigue Consumption Assessment Through Structural and On-Board Monitoring*; European Comission: Brussels, Belgium, 2020.

Disclaimer/Publisher's Note: The statements, opinions and data contained in all publications are solely those of the individual author(s) and contributor(s) and not of MDPI and/or the editor(s). MDPI and/or the editor(s) disclaim responsibility for any injury to people or property resulting from any ideas, methods, instructions or products referred to in the content.

applied sciences

MDPI

Article

Dynamic Inversion Method for Concrete Gravity Dam on Soft Rock Foundation

Guanglin Yin [1,2], Chaoning Lin [1,*], Taozhen Sheng [3], Wenbo Xue [1], Tongchun Li [1] and Siyu Chen [4,5,*]

[1] College of Water Conservancy and Hydropower Engineering, Hohai University, Nanjing 210024, China; guanglin-yin@sac-china.com (G.Y.); 241302020021@hhu.edu.cn (W.X.); ltchhu@163.com (T.L.)
[2] NanJing Hohai Nanzi Hydropower Automation Co., Ltd., Nanjing 210032, China
[3] Center for Big Data and Smart Water, Nanjing Hydraulic Research Institute, Nanjing 210029, China; hhustz@126.com
[4] Dam Safety Management Department, Nanjing Hydraulic Research Institute, Nanjing 210029, China
[5] Dam Safety Management Center of the Ministry of Water Resources, Nanjing 210029, China
* Correspondence: linchaoning@hhu.edu.cn (C.L.); siyuchen@nhri.cn (S.C.)

Featured Application: This study provides a novel approach for assessing the long-term safety of the concrete gravity dam on a soft rock foundation. The proposed dynamic inversion method, based on an improved particle swarm optimization algorithm, enables accurate identification of time-dependent parameter deterioration in dam foundations. The proposed method provides practical solutions for real-time dam health monitoring, stability assessment, and maintenance optimization, enabling more reliable safety evaluations and informed engineering decisions.

Abstract: This study presents a dynamic inversion method for the concrete gravity dam on a soft rock foundation, aiming to accurately characterize the time-dependent trend of the dam's mechanical properties. Conventional static inversion methods often overlook temporal variations in material behavior, particularly the long-term weakening of soft rock foundations under environmental influences. To address this limitation, an improved particle swarm optimization (PSO) algorithm is developed for dynamic parameter inversion, combining real-time monitoring data with finite element modeling to evaluate the time-varying elastic modulus of the foundation. The results reveal an exponential decay in the foundation's elastic modulus (from 4.67 GPa to approximately 3.83 GPa), while the dam body maintains a stable modulus of 20.74 GPa. Comparative analyses demonstrate that the dynamic inversion approach, which accounts for time-dependent parameter degradation, significantly improves the displacement prediction accuracy of the dam. The results highlight the critical importance of incorporating temporal mechanical property variations in inversion analyses to ensure reliable structural assessments and enhance long-term dam safety management.

Keywords: dynamic inversion; concrete gravity dam; soft rock foundation; particle swarm algorithm; dam displacement

1. Introduction

The concrete dam plays a crucial role in hydraulic engineering and is widely utilized in reservoirs, hydropower plants, and flood control projects worldwide [1,2]. Ensuring the safe operation and stability of concrete dams requires a thorough understanding of their physical and mechanical properties. Among these, the elastic modulus is a fundamental mechanical parameter that characterizes the extent of material deformation under

external loads [3,4]. However, for the rock mass forming the foundation of a gravity dam, mechanical parameters obtained from laboratory tests on small specimens or limited field samples often lack representativeness and reliability due to the inherent heterogeneity of the rock mass (e.g., the influence of joints and fissures) [5]. Consequently, the inversion of mechanical parameters through feedback analysis of field monitoring data has become a crucial approach [6].

Among traditional optimization-based inversion methods, Wang et al. [7] employed the simplex method to invert the comprehensive mechanical parameters of surrounding rock in a hydropower station, while Wu Xianghao et al. [8] used the simplex method to determine the creep characteristics of a milled concrete dam. With advancements in artificial intelligence, various intelligent optimization algorithms have been introduced into inversion analysis. For instance, Niu Jingtai et al. [9] applied a chaotic genetic algorithm to invert the transverse isotropic deformation and asymptotic parameters of a milled concrete dam. Wan Zhiyong et al. [10] integrated an optimization method based on homogeneous design with a BP neural network to address the complex multi-parameter inversion problem for both the dam and its foundation. Li Wei et al. [11] compared the performance of different machine learning models and proposed the XGBoost algorithm for inverting stockpile model parameters using dam deformation monitoring data. However, current research on dam parameter inversion has largely focused on static analysis methods. During the operational period, the dam is subjected to multiple multi-physics interactions, including hydraulic pressure, thermal cycling, and other environmental factors. These coupled loading conditions induce progressive degradation of foundation rock properties, particularly affecting strength and deformation parameters [12,13]. This time-dependent material deterioration is especially significant in the soft rock foundation due to the inherent structural vulnerability and higher susceptibility to environmental factors [14]. Recent investigations on time-dependent behaviors of geotechnical structures, such as bridge pile foundations in soft soil, have demonstrated the necessity of accounting for creep mechanisms and consolidation effects in long-term performance evaluations [15].

Dynamic inversion refers to an iterative updating process where structural parameters are continuously adjusted based on time-dependent monitoring data, thereby capturing the evolutionary trends of structural characteristics. Compared to static inversion, dynamic inversion offers superior capability in tracking time-varying structural parameters through continuous data assimilation, but requires higher computational costs and more sophisticated algorithms. While static inversion provides efficient one-time estimation, it fails to capture temporal parameter evolution and may yield less accurate results for long-term monitoring. Liu et al. introduced a Bayesian optimization framework combined with deep learning to invert dynamic material parameters of high arch dams under discharge excitation, demonstrating the potential of probabilistic methods in dynamic assessment [16]. Tian et al. proposed an improved Autoformer-based deep learning model for multistep and multifeature deformation prediction of the concrete dam, achieving higher accuracy in capturing long-term temporal patterns and varying environmental factors [17]. Additionally, Su et al. developed a dynamic deformation prediction model for dams based on a time attention mechanism, enhancing the model's ability to focus on temporal features and improving prediction accuracy [18]. Liu et al. presented an LSTM-based anomaly detection model for arch dam deformation, effectively identifying abnormal structural behavior through predictive modeling [19]. Moreover, a study by Zhang et al. [20] introduced a hybrid SSA–LSTM model, combining the sparrow search algorithm with long short-term memory networks to optimize model parameters and improve the accuracy of dam deformation predictions. These studies highlight a growing trend toward integrating

data-driven techniques with numerical simulations to better reflect the time-varying nature of dam behavior.

This study proposes an improved particle swarm optimization (PSO) method for dynamic parameter inversion for the gravity dam on a soft rock foundation. In contrast to conventional static inversion methods, the proposed method systematically incorporates real-time monitoring data to characterize the time-dependent degradation of the foundation's elastic modulus. A finite element model is established to simulate the dam response under operational conditions, with inversion results rigorously validated against field displacement measurements. The principal novelty of this work resides in its explicit consideration of time-dependent material property deterioration within the inversion framework, enabling more realistic characterization of the dam behavior. The results provide valuable insights for the long-term safety assessment and maintenance of gravity dams, advancing the field of structural health monitoring for hydraulic infrastructures.

2. Inversion Methods for Mechanical Parameters of Concrete Gravity Dam

The estimation of mechanical parameters of dam concrete and bedrock usually relies on laboratory test data. However, such experimentally determined parameters often demonstrate significant discrepancies with in situ conditions due to scale effects and long-term environmental exposure. To address this limitation, inversion analysis methodology integrates numerical modeling with prototype monitoring data to accurately identify the time-dependent mechanical properties of dam–foundation systems [21,22].

The basic principles and methods for identifying the elastic modulus are as follows:

Divide the dam and dam base into two areas Ω_1, Ω_2.

Define the average elastic modulus and Poisson's ratio of the materials in the two regions as E_c, E_r, μ_r, μ_c, respectively. In the elastic phase, the equilibrium equations of the whole structure are shown in Equation (1):

$$[K]\{\delta_H\} = \{R_H\} \tag{1}$$

$[K]$ is the overall strength matrix, which can be written as Equations (2) and (3):

$$[K] = \sum_{e_j \in \Omega_1} [C]_{e_j}^T [K]_{e_j} [C]_{e_j} + \sum_{e_j \in \Omega_2} [C]_{e_j}^T [k]_{e_j} [C]_{e_j} \tag{2}$$

$$[k]_{e_j} = \iiint_{\Omega_j} [B]^T [D][B] d\Omega = E \iiint_{\Omega_j} [B]^T f(\mu)[B] d\Omega = E\left[\overline{k}\right]_{e_j} \tag{3}$$

where $[D] = Ef(\mu)$ is the elasticity matrix; $[B]$ is the cell geometry matrix; $[C]_{e_j}$ is the strength transformation matrix of cell e_j.

Since $E = \begin{cases} E_c, & e_j \in \Omega_1 \\ E_r, & e_j \in \Omega_2 \end{cases}$, Equation (2) can be written in the following form:

$$\begin{aligned} [K] &= E_c \left\{ \sum_{e_j \in \Omega_1} [C]_{e_j}^T \left[\overline{k}\right]_{e_j} [C]_{e_j} + R \sum_{e_j \in \Omega_2} [C]_{e_j}^T \left[\overline{k}\right]_{e_j} [C]_{e_j} \right\} = \\ & E_c \cdot f(L, \mu_r, \mu_c, \frac{E_r}{E_c}) \end{aligned} \tag{4}$$

where $R = \frac{E_r}{E_c}$; L is the geometry of the dam.

If $\frac{E_r}{E_c}$ is certain, μ_r and μ_c are unchanged, then $[\overline{K}] = f(L, \mu_r, \mu_c, \frac{E_r}{E_c})$. Equation (4) can be rewritten as Equation (5):

$$[K] = E_c[\overline{K}] \tag{5}$$

Simplification is given as Equation (6):

$$\{\delta_H\} = \{\overline{\delta}_H\}/E_c \tag{6}$$

where $\{\overline{\delta}_H\} = [\overline{K}]^{-1}\{R_H\}$.

From Equation (6), the displacement of the dam body $\{\delta_H\}$ induced by the reservoir water pressure is inversely proportional to E_c when the ratio of the concrete and bedrock modulus of the dam body is a certain value under the reservoir water force.

The dam's safety monitoring displacement is used as the target variable for inversion analysis. The objective function of the parameter inversion optimization problem is defined as the weighted sum of squares of the residuals between the finite element computed displacement and the measured displacement at the monitoring points. This approach aims to determine the basic parameter that most closely reflects actual conditions. The flowchart of the parameter inversion process is shown in Figure 1. This flowchart systematically outlines the iterative optimization framework, beginning with the initialization of observed data and finite element inputs, followed by stochastic parameter generation and displacement computation. The adaptive feedback loop, driven by the objective function evaluation and termination criteria, ensures continuous refinement of parameters until convergence. Notably, the integration of real-time monitoring data with numerical simulations highlights the algorithm's capability to bridge empirical observations and theoretical models. While the flowchart provides a clear procedural structure, future enhancements could explicitly incorporate time-dependent parameter updating steps to better align with the dynamic inversion methodology proposed in this study.

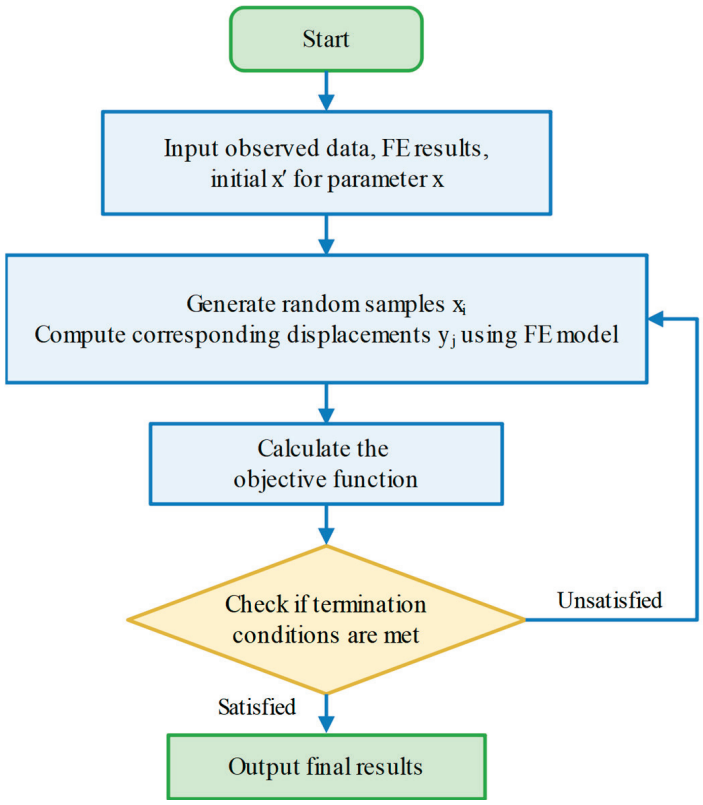


Figure 1. Flowchart of inversion analysis.

3. Improved Particle Swarm Optimization Algorithm

3.1. Particle Swarm Algorithm Fundamentals

The particle swarm algorithm [23] is a global optimization evolutionary algorithm inspired by the collective behaviors of birds, such as feeding, migration, and flocking. It is known for its fast convergence and strong optimization capability. In this algorithm, the target solution of the optimization problem is abstracted as the feeding target of a bird flock, while potential solutions are represented as birds searching for food in a multidimensional space. To simplify the model, the flock is replaced with massless particles, each characterized by only two attributes: spatial position and evolutionary velocity [24].

In the search space, a particle's position represents its current solution to the optimization problem. The algorithm evaluates each solution using a fitness function to determine its quality. Two key positions influence the optimization speed of each particle: the best solution found by an individual particle over time and the best solution found by any particle in the swarm. Through continuous iterations updating particle positions and velocities, the algorithm gradually converges to the optimal solution [25].

Individuals in the particle swarm (PSO) algorithm are called particles, and each swarm consists of N particles randomly initialized in a D dimensional search space. During the search process, each particle i is represented by two vectors, i.e., the velocity vector $v_i = [v_{i1}, v_{i2}, \ldots, v_{iD}]$ and the position vector $X_i = [x_{i1}, x_{i2}, \ldots, x_{iD}]$. Each particle i updates its velocity and position using its personal historical best position $Pbest_i = [\, pbest_{i1}, \, pbest_{i2}, \ldots, \, pbest_{iD}]$, and the global best position found so far. For simplicity, Pb_i is used to refer to $Pbest_i$ and Pg is used to refer to $Gbest$. The update formulas for v_i and X_i are shown in Equations (7) and (8):

$$V_{id}^{t+1} = \omega V_{id}^{t} + c_1 r_1 \left[Pb_{id}^{t} - X_{id}^{t} \right] + c_2 r_2 \left[Pg_{d}^{t} - X_{id}^{t} \right] \tag{7}$$

$$X_{id}^{t+1} = X_{id}^{t} + V_{id}^{t+1} \tag{8}$$

where V_{id}^{t} and X_{id}^{t} denote the velocity and position of the i particle at the t iteration in the d-th dimension; Pb_{id}^{t} is the best position searched by the i particle at the t iteration in the d-th dimension, and Pg_{d}^{t} is the best position searched by the whole swarm at the t iteration. t and $t+1$ are the current and next iterations, respectively. ω are the inertia weights, and c_1 and c_2 represent the acceleration coefficients of the particles with Pb_{id}^{t} and Pg_{d}^{t} weights, respectively. r_1 and r_2 are random numbers in the range [0, 1]. The personal historical best position and global best position of each particle are updated in each iteration using Equations (9) and (10), respectively:

$$Pb_{id}^{t+1} = \begin{cases} X_{id}^{t+1}, f\left(X_{id}^{t+1}\right) \le f\left(Pb_{id}^{t}\right) \\ Pb_{id}^{t}, f\left(X_{id}^{t+1}\right) > f\left(Pb_{id}^{t}\right) \end{cases} \tag{9}$$

$$Pg_{d}^{t+1} = \begin{cases} Pg_{d}^{t}, f\left(Pg_{d}^{t}\right) \le \min_i\left(f\left(Pb_{id}^{t+1}\right)\right) \\ Pb_{id}^{t+1}, f\left(Pg_{d}^{t}\right) > \min_i\left(f\left(Pb_{id}^{t+1}\right)\right) \end{cases} \tag{10}$$

In the above equation, f is the objective function of the optimization problem, and Pb_{id} and Pg_{d} are updated as an example for taking the minimum value. Thus, the particle velocity update equation (Equation (8)) consists of three components. The first is the inertia of the particle, which represents its tendency to maintain its previous velocity and is referred to as "memory". The second component reflects the particle's own knowledge, while the third accounts for information exchange and cooperation among particles, known

as "socialization". Although the standard particle swarm algorithm can be applied to robotic arm path planning, it has several limitations. For instance, a constant inertia weight is not conducive to balancing local and global searches. Additionally, as iterations progress, particles tend to converge to a local optimal solution, reducing population diversity and increasing the risk of the algorithm becoming trapped in a local optimum [26].

3.2. Improvement Strategy

The particle swarm optimization (PSO) algorithm differs from genetic algorithms in that it does not involve crossover or mutation operations. Instead, it relies solely on particle velocity to perform the search. During iterative evolution, only the information from the optimal particle is shared with other particles, resulting in a fast search speed. Additionally, PSO has a simple structure, requires fewer adjustable parameters, and is easy to implement in engineering applications. It employs real-number encoding, where the number of variables in the problem directly corresponds to the number of dimensions in the particle space, ensuring a direct representation of the optimization problem.

A key challenge in PSO is balancing global and local search capabilities, which remains a crucial issue in optimization [27]. To address this, an adaptive inertia weight parameter is introduced to enhance the algorithm's performance. By adjusting inertia weights dynamically based on particle positions during the search process, the optimized PSO algorithm improves convergence toward the global optimum while reducing the risk of being trapped in a local optimum. The fundamental process of the algorithm is as follows.

Assuming that the number of kinetic–elastic modulus regions to be inverted is m and that an initial population is formed by n particles, the initial population of particles E in $n \times m$ space is Equation (11):

$$E = \begin{bmatrix} E_{11} & E_{12} & \cdots & E_{1m} \\ E_{21} & E_{22} & \cdots & E_{2m} \\ \vdots & \vdots & \cdots & \vdots \\ E_{n1} & E_{n2} & \cdots & E_{nm} \end{bmatrix} \tag{11}$$

If the velocity $v_i = (v_{i1}, v_{i2}, \cdots, v_{im})$ and position $x_i = (x_{i1}, x_{i2}, \cdots, x_{im})$ of the first i particle in the population, after determining the initialized particle population information, the adaptation value $J(E_i)$ of each particle is calculated and the individual extreme value $P_i = (P_{i1}, P_{i2}, \cdots, P_{im})$ and global extreme value $g_i = (g_{i1}, g_{i2}, \cdots, g_{im})$ of the i-th particle in the population are determined at the same time. The particle determines the running direction and velocity of the next generation through its own experience and the experience of the group; for the $k+1$ generation of particles, the velocity and position of the particle are updated as Equation (12) according to the following equation:

$$\begin{cases} v_{id}^{k+1} = \omega v_{id}^{k} + c_1 r_1 \left(P_{id}^{k} - x_{id}^{k} \right) + c_2 r_2 \left(g_{d}^{k} - x_{id}^{k} \right) \\ x_{id}^{k+1} = v_{id}^{k} + v_{id}^{k+1} \\ \omega = \begin{cases} \omega_{\min} - \frac{(\omega_{\max} - \omega_{\min})(J_t - J_{\min})}{J_{arg} - J_{\min}} & , J_t \le J_{arg} \\ \omega_{\max} & , J_t > J_{arg} \end{cases} \end{cases} \tag{12}$$

where c_1, c_2 is the learning factor; r_1, r_2 are uniform random numbers in the range of [0, 1]; v_{id}^{k}, x_{id}^{k} are the velocity and position of the particle i in the d-th dimension of the k-th iteration; P_{id}^{k} is the position of the particle i in the d-th dimension of the smallest individual adaptation value; g_{d}^{k} is the position of the particle in the d-th dimension of the smallest population adaptation value; ω is the inertia weights; $\omega_{\min}$, $\omega_{\max}$ are the minimum and maximum of the inertia weights; J_t represents the real-time adaptation value of the particle;

J_{arg}, $J_{\min}$ are the average and minimum fitness values, respectively, across all particles in the current iteration. When the number of iterations or the stop condition is reached, the search is stopped and the optimal value is output; otherwise, the search will continue to iterate and update the particles until the search reaches a value that satisfies the convergence criterion.

4. Engineering Examples

4.1. Overview of the Project

A hydropower dam pivot project is located in Cambodia. The main structure consists of a 112 m high roller-compacted concrete gravity dam, a five-gate spillway at the top of the dam, a PH3 diversion structure, a PH3 powerhouse, and a switching station. According to the 500-year flood design and the calibration of the Probable Maximum Flood (PMF), the reservoir's key water levels are as follows: a calibration flood level of 151.88 m, a design flood level of 150.00 m, a normal storage level of 150.00 m, and a dead water level of 130.00 m. The reservoir has a total capacity of 717.3 million m^3, with a dead water capacity of 354.2 million m^3, and the capacity of the reservoir below the normal storage level of 681.3 million m^3. The dam has a crest elevation of 153.00 m and a base elevation of 41.00 m, with a maximum height of 112.00 m. The dam crest is 6.0 m wide. The upstream face is vertical above 84 m, while below this elevation, it has a slope of 1:0.3. The downstream face has a slope of 1:0.75, with a slope break at 145.00 m.

To monitor horizontal displacement, a total of eight inverted plumb lines were installed at elevations of 153 m, 120 m, 88 m, 60 m, and 43 m on both the left and right banks of the dam. These instruments were designated as IP1–IP8, with displacement observations beginning on 21 March 2011. IP7 and IP8 were added in January 2014 and installed by July 2014, and their initial values were recorded. In 2018, additional plumb lines were installed in dam sections 4# and 7#, including IP9, PL1-1, PL1-2, and PL1-3 in section 4#, as well as IP10 and PL2 in section 7# (with IP6 as the reference point).

The dam foundation's horizontal displacement is monitored using inverted plumb lines, which detect displacement in both the downstream and cross-river directions. The monitoring system consists of 10 inverted plumb line holes distributed across different elevations: IP7 in section 5 at the 43.00 m corridor, IP8 in section 6 at the 60.00 m corridor, IP5 and IP6 in sections 3 and 7 at the 88.00 m corridor, IP3 and IP4 in sections 2 and 9 at the 120.00 m corridor, and IP1 and IP2 at the 153.00 m elevation on the dam crest in sections 1 and 10.

Additionally, in 2018, new inverted plumb lines were added to sections 4# (IP9) and 7# (IP10). The monitoring layout is illustrated in Figure 2. The foundation's inverted displacement was observed from baseline values recorded before reservoir impoundment. However, displacement data from the construction period are incomplete and not fully reflected. Since IP7 and IP8 were installed later as supplementary instruments, only post-2014 monitoring data are available. Initial values for IP9 and IP10 were recorded on 7 June 2018.

In this paper, the measured data of IP6, IP10, and PL2 installed at dam section 7 are used for inversion analysis. The dam section 7# is equipped with three plumb lines for monitoring the displacement in the upstream–downstream direction. A normal plumb line (PL2) was installed at a 153 m elevation. Two inverted plumb lines (IP10 and IP6) were installed at 120 m and 88 m elevations. The plumb line allows for measuring relative displacement between the two ends of the plumb line. For a normal plumb line, the upper end of the wire is fixed at the top of the dam, while a heavy weight is damped at its lower end. For an inverted plumb line, the plumb wire is fixed at the lower end, and the upper end of the wire is linked to a float submerged in a water box in the observation area. Observations are recorded digitally.

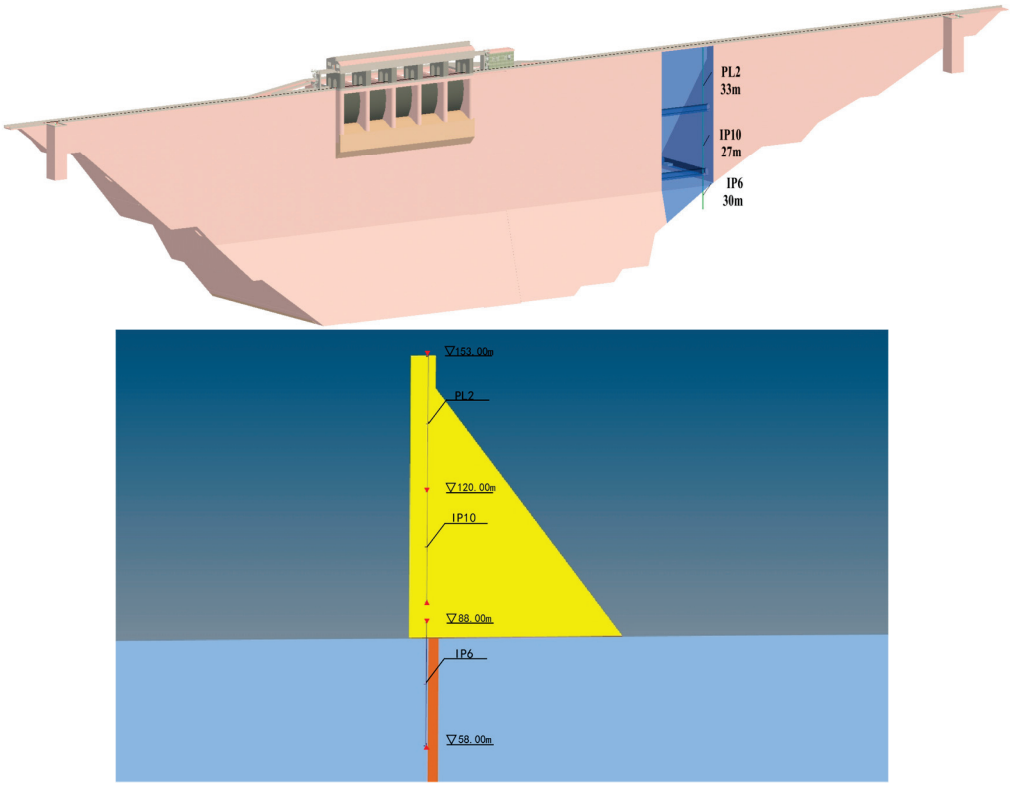


Figure 2. Arrangement of deformation monitoring of section 7# of a gravity dam.

4.2. Finite Element Model and Calculation Parameters

In this study, the 7# section of the prototype dam was selected as the reference for the finite element numerical analysis. A two-dimensional finite element model was developed using HyperMesh for preprocessing and mesh generation. The finite element mesh includes 908 elements and 983 nodes. Based on the geometric and structural characteristics of the prototype and the arrangement of observation points, the FEM was established with the upstream dam foundation as the coordinate origin. The dam has a height of 69 m, and the foundation extends approximately twice the maximum dam height both upstream and downstream. Different structural regions were categorized and processed accordingly, dividing the model into three main components: the dam body, the dam foundation, and the curtain. The x-axis represents the downriver direction, while the y-axis corresponds to the vertical direction. The finite element discretization utilizes plane quadrilateral elements with four nodes. In the numerical simulation, normal displacement constraints are imposed on the peripheral boundaries of the foundation, while full fixity conditions are applied at the base. The external load includes the upstream water pressure. According to tests, the densities of the dam body and foundation are taken as 2.4 g/cm^3 and 2.57 g/cm^3, respectively. Moreover, it is already verified that the load–displacement response of the concrete dam is not highly influenced by the Poisson ratio; thus, the Poisson ratios of the dam body and foundation are taken as 0.167 and 0.25, respectively. The finite element model is illustrated in Figure 3.

The described FEM was implemented by GeHoMadrid, an FE program that was jointly developed between Technical University of Madrid (Spain) and Hohai University (China) [28]. The program was developed in Fortran and incorporates the PARDISO package for solving highly complicated and sparse equations. It is commonly used to solve complex structural, fluid, and multi-physics problems in geotechnical and hydraulic engineering.

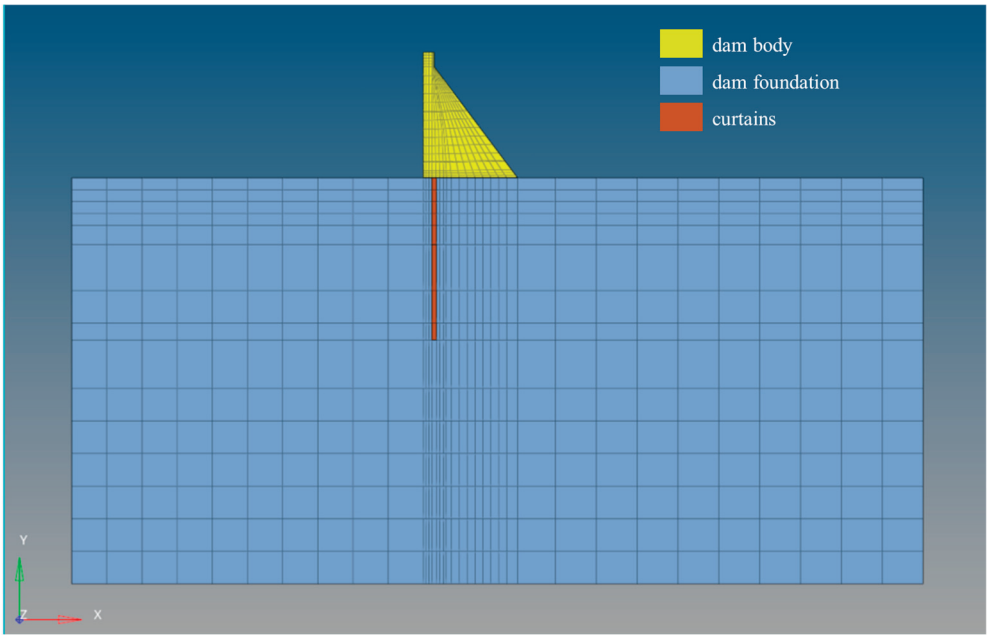


Figure 3. Two-dimensional finite element model of dam section 7#.

4.3. Comparison and Discussion

Dam section #7 is taken as a representative example in this study. The observed displacements of the plumb lines IP6, IP10, and PL2 in section #7 are shown in Figures 4–6. Observations were recorded monthly from 26 June 2018 to 26 December 2023, for a total of 66 measurements. In the improved particle swarm algorithm, the population size is taken as 30; the maximum number of iterations is 30; the inertia weight maximum and minimum values are taken as $\omega_{max} = 0.8$, $\omega_{min} = 0.2$; the learning factor $c_1 = c_2 = 1.5$, $e_1 = 0.8$, $e_2 = 0.4$. According to the preliminary calculations, the ranges of values of the mechanical parameters are set as $E \in [17\ \text{GPa}, 25\ \text{GPa}]$ for the dam body and $E \in [2\ \text{GPa}, 6\ \text{GPa}]$ for the dam foundation. The inversion results are 20.74 GPa for the dam body and 4.67 GPa for the dam foundation. The fitted displacements based on the calibration numerical model are shown in Figures 4–6.

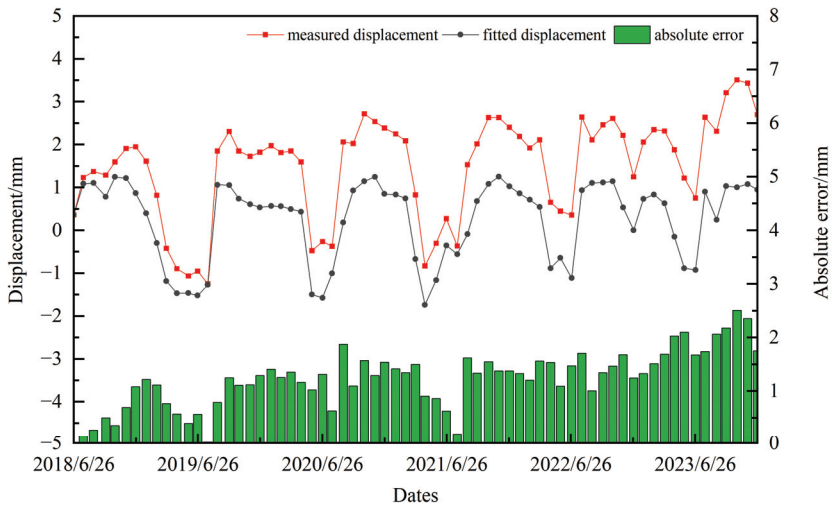


Figure 4. The measured and fitted displacements of IP6 (static inversion analysis).

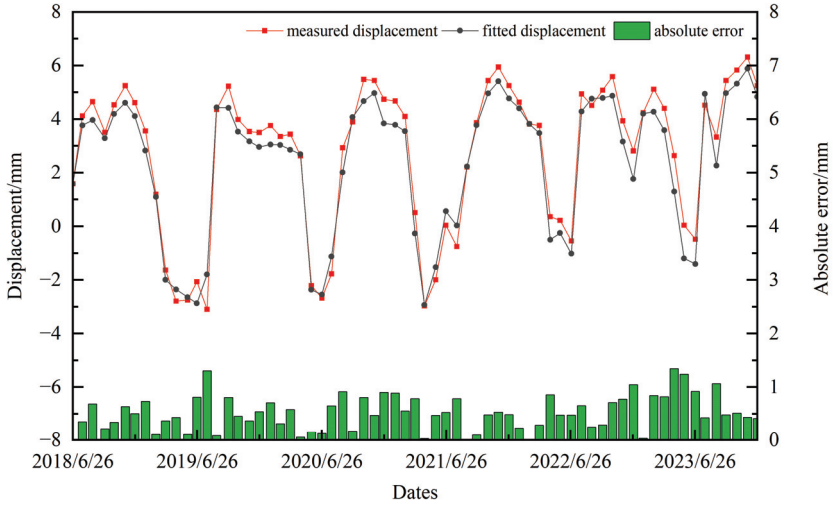


Figure 5. The measured and fitted displacements of IP10 (static inversion analysis).

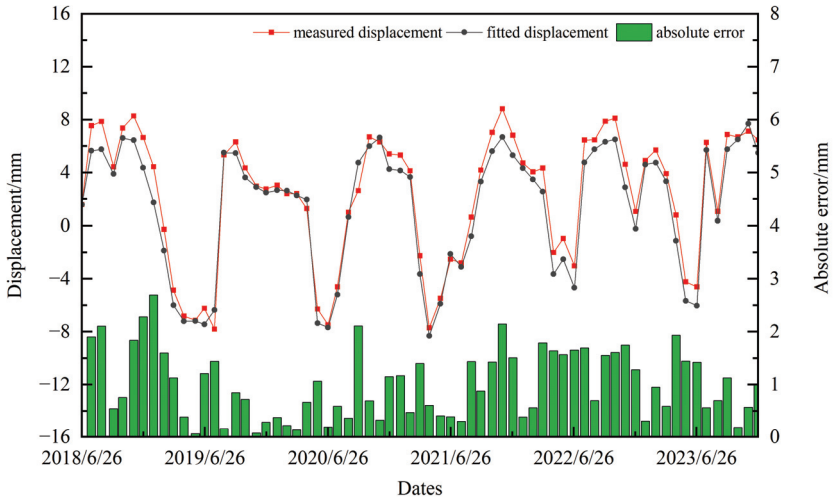


Figure 6. The measured and fitted displacements of PL2 (static inversion analysis).

The general consistency between measured and inverted displacement trends across most monitoring points can be observed from the figures. However, a larger discrepancy is noted at measurement points especially near the dam foundation.

Based on the fitted results of the static parameter inversion, it is initially inferred that parameter weakening occurs in the dam foundation, while the dam body remains in an elastic working condition. Therefore, the elastic modulus of the dam body is determined to be 20.74 GPa based on the static inversion results. The dynamic inversion analysis incorporated field data from three positioned monitoring points (IP6, IP10, and PL2) in dam section 7#. The calculation results reveal a clear temporal degradation pattern in the mechanical properties of the dam foundation, which was quantitatively characterized through curve fitting. Figure 7 presents the time-dependent reduction in the elastic modulus of the dam foundation.

The time-varying functions of material parameters, such as those of geotechnical bodies and concrete, are typically modeled using exponential or logarithmic functions [29,30]. The time-dependent reduction in the elastic modulus of the dam foundation is fitted as the equation $y = 1.075 \cdot e(-0.114 \cdot x) + 3.829$. The time-dependent elastic moduli obtained from the dynamic inversion analysis are sequentially implemented in the finite element program to compute theoretical displacements. The fitted displacements compared against field measurements are shown in Figures 8–10.

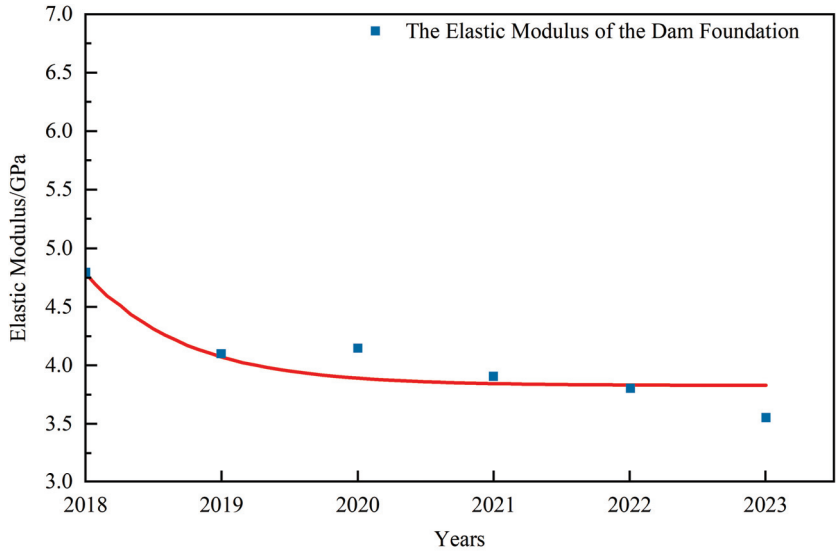


Figure 7. The time-dependent reduction in the elastic modulus of the dam foundation (2018–2023).

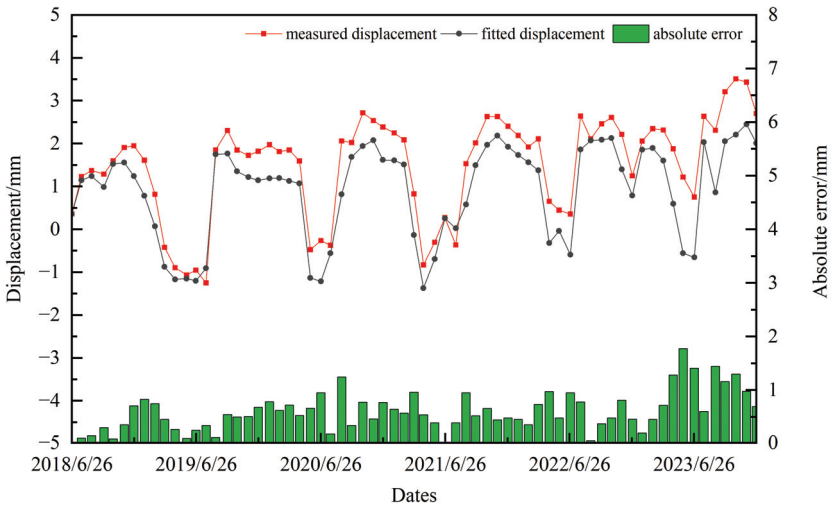


Figure 8. The measured and fitted displacements of IP6 (dynamic inversion analysis).

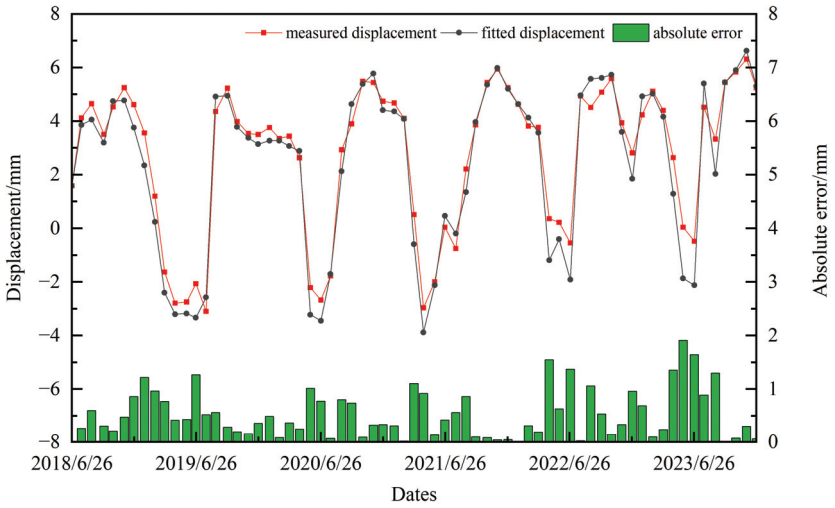


Figure 9. The measured and fitted displacements of IP10 (dynamic inversion analysis).

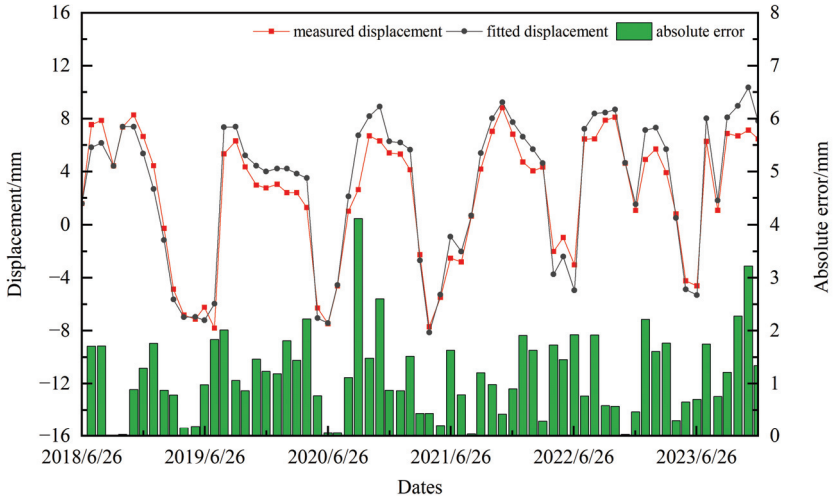


Figure 10. The measured and fitted displacements of PL2 (dynamic inversion analysis).

The measured and simulated displacement time series exhibit strong agreement across all monitoring points (Figures 8–10), demonstrating the effectiveness of the dynamic inversion analysis. In addition, two statistical metrics, the Mean Absolute Error (MAE) and Root Mean Square Error (RMSE), are employed to quantitatively evaluate the model performance, as defined in Equations (13) and (14):

$$RMSE = \sqrt{\frac{1}{N}\sum_{i=1}^{N}(\hat{x}_i - x_i)^2} \tag{13}$$

$$MAE = \frac{1}{N}\sum_{i=1}^{N}|\hat{x}_i - x_i| \tag{14}$$

where N is the number of sequences; $\hat{x}_i$ and x_i are the fitted and measured values of the displacement, respectively.

The results are shown in Tables 1 and 2.

Table 1. The evaluation results of the static inverse analysis.

Evaluation Indicators	IP6	IP10	PL2
RMSE/mm	1.344	0.614	1.193
MAE/mm	1.230	0.521	1.000

Table 2. The evaluation results of the dynamic inversion analysis.

Evaluation Indicators	IP6	IP10	PL2
RMSE/mm	0.707	0.701	1.401
MAE/mm	0.604	0.530	1.150

The calculation results indicate that the fitting accuracy of the measurement points at the dam foundation is significantly improved in the dynamic inversion model compared to the static inversion model. Although the errors of measurement points at the dam body are slightly larger than those of the static inversion model, the overall prediction errors remain lower than those of the static inversion model. The primary sources of error can be attributed to two factors. First, the observed data contain random errors due to limitations in measurement instrument accuracy and environmental influences. Second, the

numerical model itself introduces inherent errors arising from simplified assumptions and uncertainties in mechanical parameters. This suggests that parameter weakening occurs at the dam foundation and that the weakening trend gradually stabilizes. These results demonstrate time-dependent stiffness degradation in the dam foundation, with the rate of modulus reduction decreasing asymptotically over time.

5. Conclusions

This study presents a comprehensive investigation into the long-term deformation behavior of concrete gravity dams on soft rock foundations, with a focus on dynamic parameter inversion using an improved particle swarm optimization (PSO) algorithm. The conclusions are as follows:

(1) The inversion analysis successfully quantified the elastic moduli of the dam body and foundation, while capturing the time-dependent degradation of the foundation's elastic modulus through an exponential decay model. The identified mechanical parameters provide a critical baseline for evaluating the structural performance and long-term safety of the dam.

(2) The improved PSO algorithm, incorporating adaptive inertia weight, achieves robust global optimization with stable convergence. Integrated with finite element modeling and real-time monitoring data, the inversion framework enables high-precision displacement predictions of the concrete dam.

(3) The proposed dynamic inversion method has exhibited significant effectiveness in assessing the long-term performance of the concrete gravity dam constructed on a soft rock foundation. To further advance the research, Bayesian updating theory will be introduced to systematically quantify the uncertainties in both monitoring data and numerical models, with the ultimate objective of establishing reliable risk warning indicators.

Author Contributions: Methodology, T.L.; Software, C.L. and T.L.; Validation, T.S. and W.X.; Data curation, G.Y.; Writing—original draft, G.Y. and C.L.; Writing—review and editing, W.X. and S.C.; Project administration, C.L. All authors have read and agreed to the published version of the manuscript.

Funding: This research was funded by the National Key Research and Development Program of China (No. 2022YFC3005403), the National Natural Science Foundation of China (Nos. 52309151 and 52309157), the Open Research Fund of Key Laboratory of Reservoir and Dam Safety Ministry of Water Resources (No. YK323007), and the Science and Technology Project of Power Construction Corporation of China (No. DJ-HXGG-2022-02).

Data Availability Statement: The data presented in this study are available on request from the corresponding author.

Conflicts of Interest: Author Guanglin Yin was employed by the company NanJing Hohai Nanzi Hydropower Automation Co., Ltd. The remaining authors declare that the research was conducted in the absence of any commercial or financial relationships that could be construed as a potential conflict of interest.

References

1. Chen, S.; Lin, C.; Gu, Y.; Sheng, J.; Hariri-Ardebili, M.A. Dam Deformation Data Preprocessing with Optimized Variational Mode Decomposition and Kernel Density Estimation. *Remote Sens.* **2025**, *17*, 718. [CrossRef]
2. Xiang, Y.; Su, H.; Wu, Z. Inversion of Physico-Mechanical Parameters Based on Dam Safety Monitoring Data. *J. Water Resour.* **2004**, *35*, 98–102. [CrossRef]
3. Lin, C.; Chen, S.; Hariri-Ardebili, M.A.; Li, T. An Explainable Probabilistic Model for Health Monitoring of Concrete Dam via Optimized Sparse Bayesian Learning and Sensitivity Analysis. *Struct. Control Health Monit.* **2023**, *2023*, 2979822. [CrossRef]
4. Huang, Y.; Huang, G.; Wu, Z.; Shen, Z. Optimized Inversion of Time-Varying Parameters of Concrete Dams Based on Deformation Monitoring Data. *J. Rock Mech. Eng.* **2007**, *26*, 2941–2945.

5. Lin, C.; Li, T.; Chen, S.; Yuan, L.; van Gelder, P.; Yorke-Smith, N. Long-term viscoelastic deformation monitoring of a concrete dam: A multi-output surrogate model approach for parameter identification. *Eng. Struct.* **2022**, *266*, 114553. [CrossRef]
6. Lin, C.; Du, X.; Chen, S.; Li, T.; Zhou, X.; van Gelder, P.H.A.J.M. On the multi-parameters identification of concrete dams: A novel stochastic inverse approach. *Int. J. Numer. Anal. Methods Geomech.* **2024**, *48*, 3792–3810. [CrossRef]
7. Wang, P.; Zhu, W.; Wang, K. Simplex Shape Method and Its Application to Inversion analysis of Perimeter Rock Deformation in Guangzhu Power Station. *Geotech. Mech.* **1991**, *12*, 57–66.
8. Wu, X.; Wu, Z.; Gu, C.; Shen, Z.; Shu, Y. Inversion analysis Method of Creep of Crushed Concrete Arch Dam. *Dam Obs. Civ. Test.* **2000**, *24*, 22–24, 35.
9. Niu, J. Inversion analysis of Mechanical Parameters of Crushed Concrete Dam Based on Chaotic Genetic Algorithm. *South-to-North Water Divers. Water Sci. Technol.* **2012**, *10*, 140–143.
10. Wan, Z.; Huang, Y.; Zhu, Z.; Wang, T.; Jing, J.; Xiao, L. Inversion Analysis of Mechanical Parameters During Operation Period of Crushed Concrete Dam in Alpine Area. *Water Conserv. Hydropower Technol.* **2017**, *48*, 50–55.
11. Li, W.; Liu, Q.; Shi, E.; Guo, W. Parameter Inversion and Application of South Water Modeling for Rockfill Based on XGBoost Algorithm. *J. Water Resour. Water Transp. Eng.* **2023**, 111–120. [CrossRef]
12. Sun, T.; Chen, Y.; Chen, J.; Yang, B.; Tan, C. Stability Modeling of Typical Dam Foundation of Daitengxia Lock and Dam. *J. Undergr. Space Eng.* **2022**, *18*, 179–189.
13. Tang, M.; Duan, B.; Zhang, L.; Chen, J.; Yang, B. Experimental Study on Geomechanical Modeling of Overall Stability of High Gate Dam on Deep and Thick Overburden. *Hydropower Gener* **2017**, *43*, 105–109.
14. Tian, Y.; Chen, W.; Tian, H.; Zhao, M.; Zeng, C. Study on the Design of Buffer Layer Letting Pressure Support Considering the Time-Dependent Weakening of Soft Rock Strength. *Geotech* **2020**, *41* (Suppl. S1), 237–245.
15. Li, S.; Wei, L.; Niu, J.; Deng, Z.; Wu, B.; Qian, W.; He, F. Time-Dependent Deviation of Bridge Pile Foundations Caused by Adjacent Large-Area Surcharge Loads in Soft Soils and Its Preventive Measures. *Front. Struct. Civ. Eng.* **2024**, *18*, 184–201. [CrossRef]
16. Liu, B.; Li, H.; Wang, G.; Huang, W.; Wu, P.; Li, Y. Dynamic Material Parameter Inversion of High Arch Dam under Discharge Excitation Based on the Modal Parameters and Bayesian Optimised Deep Learning. *Adv. Eng. Inform.* **2023**, *56*, 102016. [CrossRef]
17. Tian, K.; Yang, J.; Cheng, L. Deep Learning Model for the Deformation Prediction of Concrete Dams under Multistep and Multifeature Inputs Based on an Improved Autoformer. *Eng. Appl. Artif. Intell.* **2024**, *137*, 109109. [CrossRef]
18. Yan, S.; Jiayuan, F.; Chuan, L. Prediction Model of Dam Structure Dynamic Deformation Based on Time Attention Mechanism. *J. Hydroelectr. Eng.* **2022**, *41*, 72–84.
19. Liu, C.; Pan, J.; Wang, J. An LSTM-Based Anomaly Detection Model for the Deformation of Concrete Dams. *Struct. Health Monit.* **2023**, *23*, 1914–1925. [CrossRef]
20. Madiniyeti, J.; Chao, Y.; Li, T.; Qi, H.; Wang, F. Concrete Dam Deformation Prediction Model Research Based on SSA–LSTM. *Appl. Sci.* **2023**, *13*, 7375. [CrossRef]
21. Su, H.; Li, J.; Wu, Z. Optimization of inversion analysis of dam and foundation physico-mechanical parameters. *J. Water Resour.* **2007**, *S1*, 129–134.
22. Lin, C.; Li, T.; Chen, S.; Lin, C.; Liu, X.; Gao, L.; Sheng, T. Structural identification in long-term deformation characteristic of dam foundation using meta-heuristic optimization techniques. *Adv. Eng. Softw.* **2020**, *148*, 102870. [CrossRef]
23. Kennedy, J.; Eberhart, R. Particle Swarm Optimization. In Proceedings of the ICNN'95-International Conference on Neural Networks, Perth, WA, Australia, 27 November–1 December 1995; IEEE: Piscataway, NJ, USA, 1995; Volume 4, pp. 1942–1948.
24. Ocampo, E.; Liu, C.-H.; Kuo, C.-C. Performance Analysis of Partitioned Step Particle Swarm Optimization in Function Evaluation. *Appl. Sci.* **2021**, *11*, 2670. [CrossRef]
25. Wang, D.; Tan, D.; Liu, L. Particle Swarm Optimization Algorithm: An Overview. *Soft Comput.* **2018**, *22*, 387–408. [CrossRef]
26. Rini, D.P.; Shamsuddin, S.M.; Yuhaniz, S.S. Particle Swarm Optimization: Technique, System and Challenges. *Int. J. Comput. Appl.* **2011**, *14*, 19–26. [CrossRef]
27. Shi, Y.; Eberhart, R. A Modified Particle Swarm Optimizer. In Proceedings of the IEEE International Conference on Evolutionary Computation Conference, Anchorage, AK, USA, 4–9 May 1998; pp. 69–73.
28. Fernandez-Merodo, J.A.; Castellanza, R.; Mabssout, M.; Pastor, M.; Parma, M. Coupling transport of chemical species and damage of bonded geomaterials. *Comput. Geotech.* **2007**, *34*, 200–215. [CrossRef]
29. Cheng, X. Time-Varying Reliability Analysis Model and Reliability Calculation Method for Rocky Slope Anchoring Project. Ph.D. Thesis, Hunan University, Changsha, China, 2010.
30. Peng, H.; Liu, D.; Tian, B. Time-Varying Modeling of Safety and Reliability of Concrete Gravity Dams. *Hydropower Gener.* **2009**, *35*, 77–79.

Disclaimer/Publisher's Note: The statements, opinions and data contained in all publications are solely those of the individual author(s) and contributor(s) and not of MDPI and/or the editor(s). MDPI and/or the editor(s) disclaim responsibility for any injury to people or property resulting from any ideas, methods, instructions or products referred to in the content.

applied sciences

MDPI

Article

Research on Cracking Mechanism and Crack Extension of Diversion Tunnel Lining Structure

Hui Xie [1,2], Haoran Wang [1,2,*], Xingtong Zou [3], Yongcan Chen [1,2], Zhaowei Liu [1,2], Liyi Yang [1] and Kang Liu [2]

[1] Sichuan Energy Internet Research Institute, Tsinghua University, Chengdu 610039, China; xiexieh@163.com (H.X.); yangliyi20251005@163.com (L.Y.)
[2] State Key Laboratory of Hydroscience and Engineering, Tsinghua University, Beijing 100084, China; liu-k21@mails.tsinghua.edu.cn
[3] School of Emergency Managment, Xihua University, Chengdu 610039, China; z1329496475@163.com
* Correspondence: thuwhr@163.com

Abstract: Tunnel systems are often confronted with issues such as cracks, water seepage, and exposed tendons, all of which compromise their structural integrity. This study utilizes an advanced robotic system equipped with a 3D laser scanner to capture data on visible lining defects. By analyzing the distribution of defects across various tunnel segments, we explore the mechanisms underlying structural cracks. Finite element software is employed to assess stress, deformation, and crack progression within the tunnel linings. The result found that the diversion tunnel's segments exhibit notable variations: 66.0% of the defects are concentrated in the upper flat section, while 34.0% are found in the inclined shaft segment. Cracks, primarily located in the vault area, characterize these defects. Under water pressure, stress deformation in the intact lining follows a linear escalation pattern. Specifically, after the formation of cracks measuring 0.1 m, 0.2 m, and 0.3 m, circumferential stresses increase by approximately 4.50%, 9.10%, and 15.10%, respectively. Numerical simulations reveal significant stress concentration near the cave entrance at the upper flat break. Crack propagation at the arch crown is found to pose a greater risk than at the sides of the arch waist. These findings offer valuable scientific insights and practical implications for improving safety and enabling intelligent monitoring of power station tunnels.

Keywords: diversion tunnels; apparent defects; cracking mechanism; stress deformation; crack extension

1. Introduction

With the continuous advancement of water conservancy and hydropower technologies, a large number of hydraulic tunnels have been constructed to support efficient water management, energy generation, and power supply. However, prolonged operation often leads to structural degradation. If such damage is not detected and addressed in a timely manner, it can pose serious threats to the safety and reliability of the infrastructure [1–5]. Manual inspection methods face several limitations, including high operational risk, extended inspection times, and potential inaccuracies in data acquisition. With the rapid development of advanced equipment and information technologies, the integration of artificial intelligence (AI) tools for tunnel scanning and defect detection has become increasingly important [6–10]. By analyzing the spatial distribution and formation mechanisms of tunnel defects, this study identifies key patterns that are critical for maintaining long-term structural integrity. These findings contribute to a better understanding of potential vul-

nerabilities and provide valuable guidance for proactive maintenance strategies, thereby enhancing the safety and resilience of hydraulic tunnel infrastructure.

Currently, investigations into defects within diversion tunnels predominantly concentrate on model testing, theoretical examinations, and computational simulations. Lin, C.J. et al. [11] studied the influence of crack location, Enhanced Safety Factors of Lining Structures: A Study Based on Crack Model Analysis and the Influence of Depth and Host Rock Resistance; according to Liu, C. et al. [12], the analysis of the lining cracking, conducted through rigorous model testing, revealed that the primary cause was the excessive tensile stress leading to cracks at the arch top and arch footing. Additionally, the side walls experienced significant localized pressure, contributing to their failure; Lu, A. et al.'s [13] study meticulously examined the cracking phenomena in the lining using field-measured pressure data from model tests. It explored the underlying causes, patterns, and distinctive characteristics of observed lining fractures; in a study by Li, G.D. et al. [14], the photoelastic patch method was employed to examine the cracking patterns, stability, and destabilizing damage in a concrete four-point shear beam test. This investigation covered various sizes and locations of cracks, revealing their expansion rules and characteristics comprehensively; Du, Jiaji's [15] study employed cloud interferometry to examine the propagation dynamics of fractures in concrete during a three-point shear beam test; Li, Z.H. et al.'s [16] research introduced an advanced computational framework to assess fractures in lining masonry, drawing upon the principles of fracture mechanics. This innovative approach was subsequently juxtaposed with existing methodologies for analyzing cracks in similar structures, highlighting its unique contributions and enhanced accuracy; Khan, G. et al. [17] proposed a calculation model for the cracks of lining masonry based on the theory of fracture mechanics, analyzing the analysis of the cracks of lining masonry. Based on the fracture mechanics theory, Chen, S.'s [18] study introduced a novel model for calculating lining cracks, and conducted a comparative analysis on how various depths and angles of cracks influence the stability of lining structures; Karami, M. et al.'s [19] study delved into the influence of internal water pressure, tunnel radius, and lining thickness, among other variables, on the fracture patterns of the lining, employing advanced fracture calculation methodologies; Wang, G. et al. [20] proposed a structural methodology grounded in the longitudinal bending stiffness of a cracked lining, and conducted an exhaustive analysis on the impact of both isolated and multiple cracks on the mechanical attributes of tunnel linings. Chen, J.X. et al. [21], based on fracture mechanics theory, developed a sophisticated model for evaluating cracked linings. This model enables us to meticulously analyze the intricate stress and deformation characteristics inherent in mixed cracked lining systems; Peng, Z.T. et al.'s [22] study delved into the influence of reinforcement and surrounding rock conditions on the quantity and width of cracks by developing a numerical model focused on lining crack formation; Du, J.M. et al.'s [23] research focused on analyzing the maximal principal stresses, as well as the stresses at crack tips across varying depths of cracks within different components of lining structures, employing advanced numerical simulation techniques; Xu, Z.L.'s [24] study delved into the stress and deformation characteristics of cracks situated at critical junctions such as the arch summit, midsection, and base by constructing a sophisticated numerical model. This model incorporated both non-destructive and cracked linings, leveraging advanced finite element analysis techniques to simulate real-world conditions with enhanced precision. Lu, S. et al.'s [25] study delved into the characteristics, distribution patterns, and propagation mechanisms of fractures under varying conditions of surrounding rock loads, structural imperfections, and additional influencing factors; Lei, Y.M. et al.'s [26] study employed an integrated finite element-discrete element approach to meticulously simulate and analyze the distribution patterns and propagation dynamics of cracks within linings, considering variations in

their locations, extents of influence, and magnitudes of applied loads. This investigation aimed at unraveling the intricate mechanisms governing crack evolution under diverse loading scenarios and geometrical configurations, thereby enhancing our understanding of structural integrity and failure modes in complex engineered systems.

Previous research has primarily focused on the stress characteristics and propagation behavior of cracks in lining structures. However, studies involving actual defect detection data from diversion tunnels remain limited, and the differences in lining defects and their underlying formation mechanisms are not yet well understood. This study utilizes inspection data collected from the diversion tunnel of a hydropower station in the Dadu River Basin to investigate the mechanisms of crack formation and patterns of crack propagation in the lining structure. The results aim to enhance the operational safety and efficiency of hydropower stations while contributing to the development of intelligent defect detection technologies.

2. Engineering Background

2.1. Tunnel Inspections

This study focuses on a power station located in the Dadu River Basin that includes a barrage, flood relief structures on either side of the river, and a diversion power generation system. The station features four parallel pressure pipelines designed to optimize water flow for energy generation. The pressure pipes are situated within the thin to medium-thick, and further thickening to massive laminated dolomitic greywacke and metamorphic greywacke formations, ranging from the 9th to 12th layer of the Lower Devonian System. This positioning covers various segments such as upper flat, upper curved, inclined, lower curved, and lower flat areas, all embedded within the microsilver rock strata, and the peripheral rocks are preliminarily classified as III1 to III2 types. Given the intricate environmental conditions of the diversion tunnel, including total darkness, standing water, jet streams, and sediment accumulation, we employ our custom-designed robot. This advanced robot is outfitted with a 3D laser scanner and high-definition microlight camera equipment. The inspection apparatus is carefully lowered into the tunnel using a specialized aerial basket, allowing for comprehensive scanning and examination of the tunnel's lining surface. Here are the detailed steps involved in the robotic inspection process of the diversion tunnel:

Step 1: Gather comprehensive data on hydrological information for both flow and project areas from the commissioning of the diversion tunnel to the present. Step 2: The robot was deployed outside the tunnel for an inspection mission, navigating its way into the tunnel's interior. It was equipped with high-definition cameras, 3D laser scanners, and lighting to capture detailed images and 3D point cloud coordinates of the tunnel. After completing the inspection, the robot returned by the same route it entered. Due to the challenging conditions—namely, darkness, lack of adequate lighting, and a slippery cave environment—the lower flat section of the water pump ceased functioning, failing to pump water up to 1.5 m or more. As a result, the inspection could only be conducted on the upper flat section and the inclined section of the tunnel (see Figures 1 and 2).

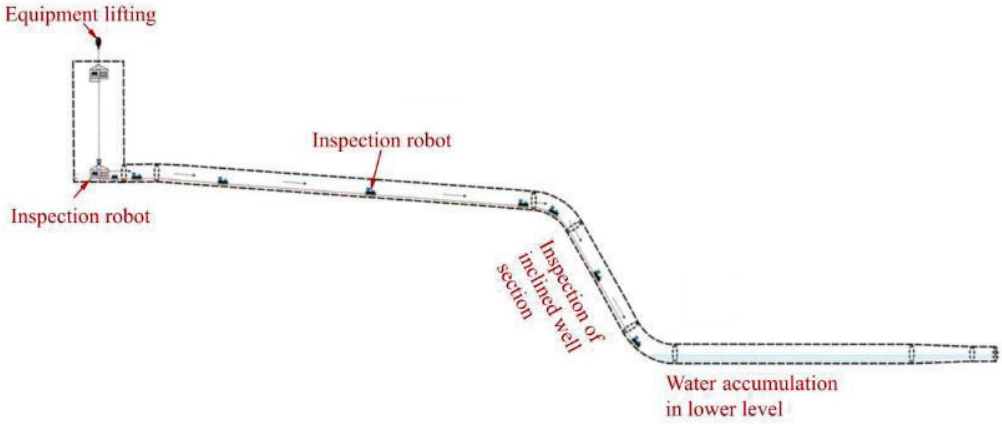
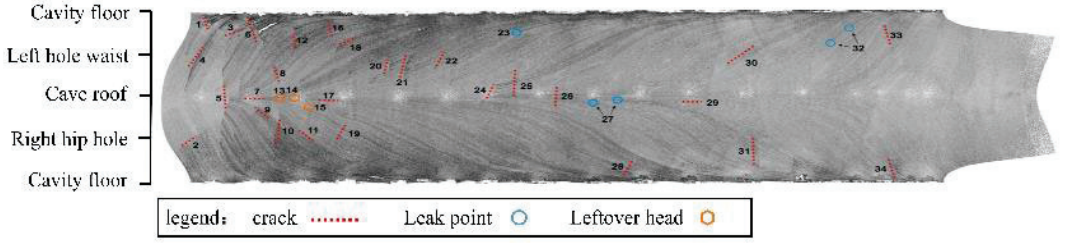


Figure 1. Schematic diagram of the inspection path and implementation process.

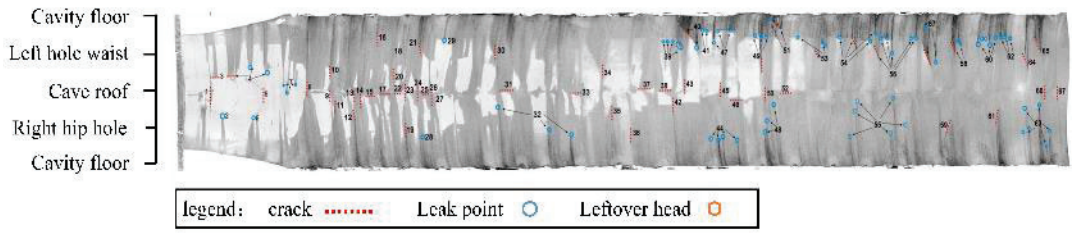


Figure 2. Map of site operations.

Step 3: Following a thorough inspection, we generate a comprehensive tunnel and a LIDAR. This allows us to pinpoint and measure any visible defects on the laser image. Subsequently, the LIDAR orthophoto is meticulously edited to incorporate this defect information (see Figure 3).



(**a**) Upper flat section



(**b**) Inclined section

Figure 3. Infographic of diversion tunnel defects.

Step 4: Result interpretation. Utilizing data gathered from the robotic assessment, defects undergo meticulous quantitative analysis. Subsequently, both mechanical and sim-

ulation models of the tunnel are devised to elucidate the underlying mechanical principles governing the spatial and geometric distribution patterns of the observed cracks.

From Figure 4, The inspection data reveals a total of 101 imperfections, comprising 77 fissures ranging from 0.38 m to 11.88 m; additionally, there are 21 instances of concrete seepage and three residual protruding rebar ends, the longest measuring up to 0.12 m. The diversion tunnel's structural segments exhibit considerable variation in defect types. The upper flat section alone harbors 67 deficiencies, constituting 66.0% of the total defects tally, predominantly manifested as cracks accompanied by water seepage, with calcium deposits encircling most fissures, and minor water discharge observed. The primary cause is water seepage, with most cracks accompanied by calcium precipitation and fine water outflow. There are 34 defects in the inclined shaft section, accounting for 34.0% of the total number of defects. The distribution characteristics along the axial direction of the tunnel show that cracks are more concentrated in the upper-level section, particularly within the 0–40 m interval, indicating a higher risk area for the diversion tunnel.

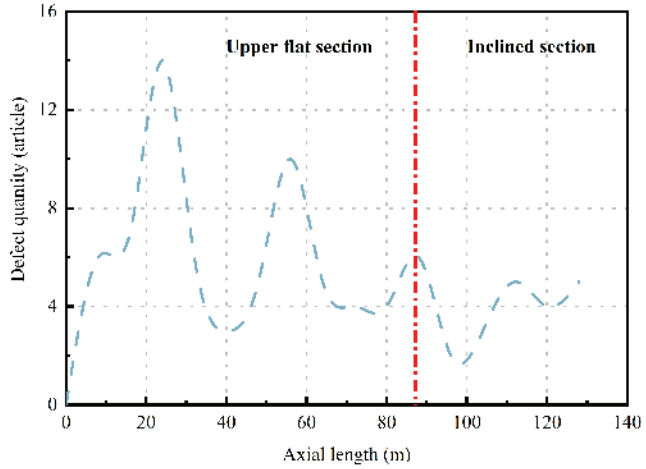


Figure 4. Characteristic distribution of the number of cracks along the axis of the tunnel.

2.2. Characterization of Defects Based on the Gray Correlation Method

The gray correlation approach evaluates the impact of defects on various structural components, facilitating a quantitative assessment and comparison of system evolution and trends. It determines correlation levels based on geometric similarity of parameter curves; higher resemblance indicates stronger correlation. The computation details follow [27].

The defects in different structural sections of the diversion tunnel are selected as the reference sequence $X_0 = \{x_0(k), k = 1, 2 \ldots m\}$, and the cracks and leaks in different locations are selected as the comparison sequence $Xi = \{xi(k), k = 1, 2 \ldots m\}$, and the cracks and leaks at different locations are compared with the sequence $Xi = \{x_i(k), k = 1, 2 \ldots m, i = 1, 2 \ldots n\}$.

The compositional data series homogenization process is as follows:

$$Y_0 = \frac{x_0(k)}{\overline{x_0}}, k = 1, 2, 3 \cdots\cdots n, \text{ where : } \overline{x_0} = \frac{1}{n}\sum_{k=1}^{n} x_0(k) \quad (1)$$

$$Y_i = \frac{x_i(k)}{\overline{x_i}}, k = 1, 2, 3 \cdots\cdots n, \text{ where : } \overline{x_i} = \frac{1}{n}\sum_{k=1}^{n} x_i(k) \quad (2)$$

where Y_0 denotes the reference sequence priming process; Yi denotes the comparison sequence priming process.

Calculate the correlation coefficient of each point of the comparison sequence to each point of the reference sequence:

$$\begin{cases} \xi_i(k) = \frac{\mathrm{m}+\rho\ M}{\Delta_i(k)+\rho\ M} \\ m = \min\limits_i \min\limits_k \Delta_i(k) \quad i = 1,2,\ldots,n,\ k = 1,2,\ldots,m \\ M = \max\limits_i \max\limits_k \Delta_i(k) \\ \Delta_i(k) = |Y_0(k) - Y_i(k)| \end{cases} \tag{3}$$

In the formula, ξi(k) indicates the correlation coefficient; ρ indicates the resolution coefficient, ρ ∈ (0, +∞), and the larger value of the resolution will be smaller, usually taking the value of 0.5; Δi(k) indicates the degree of proximity; *m* indicates the absolute value of the smallest difference in the smallest difference in the difference in distance between points *I* ∈ (1, 2, … n) and X0(k) on the curve Xi(k); *M* indicates the absolute value of the largest difference in the largest difference in the difference in distance between points *I* ∈ (1, 2, … n) and X0(k) on the curve Xi(k).

The degree of correlation between the reference sequence and the comparison sequence is as follows:

$$r_i = \frac{1}{n}\sum_{k=1}^{n} \zeta_i(k) \tag{4}$$

where r_i represents the degree of association, when $0.5 \leq r_i \leq 1$, the reference sequence is associated with the comparison sequence, and the larger the value, the higher the degree of association; when $0 \leq r_i \leq 0.5$, the reference sequence is not associated with the comparison sequence.

The main defect correlation coefficients of the diversion tunnels were calculated by Equation (4), and the results are shown in Table 1.

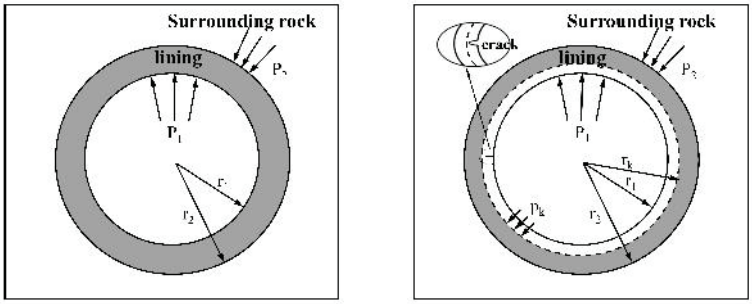
Table 1. Correlation of major defects in diversion tunnels.

Position	Vault Crack	Waist Crack	Soffit Leakage	Arch Girdlet Leakage
Upper flat section	1	0.88	0.62	0.91
Inclined section	0.99	0.88	0.62	0.91

From the table, it is evident that the correlation of major defects in both the upper-level section and the inclined shaft section exceeds 0.5. Particularly, the correlation among roof cracks, waist cracks, and waist leakage is notably high, while the correlation for roof leakage remains average. This suggests that a high incidence of cracks within the tunnel predominates as the primary defect type. In contrast, the number of leaks is relatively low and does not pose severe damage. The emergence of these cracks correlates with the extent of constraints on lining deformation [28,29]. Cracks will form in lining structures under stress during deformation, regardless of internal or external constraints. Thus, the impact of roof cracks on tunnel safety must be prioritized in practical engineering applications.

3. Research on Lining Cracking and Deformation Mechanism

Diversion tunnels show various structural flaws due to multiple factors like rock characteristics, material quality, design, construction, concrete mix, and maintenance. This paper focuses on the stress and deformation of intact and fractured linings under hydraulic pressure using a mechanical model (Figure 5) and thick-walled cylinder theory with several theoretical assumptions:



(**a**) Force analysis of non-destructive lining(**b**) Force analysis of cracked lining

Figure 5. Schematic force diagram of the diversion tunnel.

(1) The reinforced concrete lining and surrounding rock act as impermeable elastomers, adhering to Hooke's law for displacement and deformation, ensuring structural integrity and stability; (2) The rock body's exterior is devoid of any external load, experiencing solely the force of gravity; (3) The inner surface of the lining is subjected to water pressure, which manifests as a form of surface force; (4) The concrete lining and the surrounding rock structure are intimately linked, exhibiting no tendency for relative sliding.

3.1. Mechanical Characteristics of Non-Destructive Lining Structures

Figure 6 illustrates the force model of the lining under water pressure. Given that the lining is primarily subjected to uniform internal water pressure, the mechanical model can be simplified to an axial stress model. This simplification is based on the inverse solution method in elastic mechanics theory [30]; it is postulated that the stress function varies solely with the radial coordinate, r, and remains invariant to the polar angle. The specific form of this relationship is articulated as follows:

$$\phi = \phi(r) \tag{5}$$

Then the stress expression is as follows:

$$\begin{cases} \sigma_r = \frac{1}{r}\frac{d\phi}{dr} \\ \sigma_\theta = \frac{d^2\phi}{dr^2} \\ \tau_{r\theta} = \tau_{\theta r} = 0 \end{cases} \tag{6}$$

where σ_r denotes radial stress; σ_θ denotes circumferential stress; and τrθ and τθr denote shear stress.

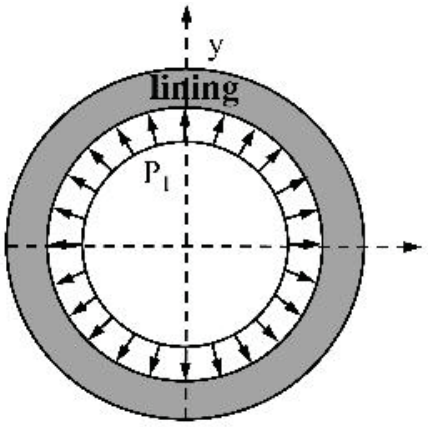


Figure 6. Lining force diagram under water pressure.

From Figure 7, The compatibility equation expressed in terms of the stress function can be simplified as follows:

$$\left(\frac{d^2}{dr^2}+\frac{1}{r}\frac{d}{dr}\right)^2\varphi=0 \tag{7}$$

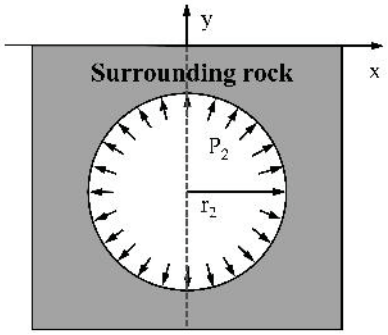


Figure 7. Force diagram of surrounding rock under water pressure.

This is a fourth-order ordinary differential equation that provides the general solution of the stress function for the axisymmetric stress state as follows:

$$\phi = A\ln r + Br^2\ln r + Cr^2 + D \tag{8}$$

where A, B, C, and D denote arbitrary constants.

Bringing Equation (8) into Equation (6) yields the stress component as follows:

$$\begin{cases} \sigma_{\mathrm{r}} = \frac{A}{r^2} + B(1+2\ln r) + 2C \\ \sigma_\theta = \frac{A}{r^2} + B(3+2\ln r) + 2C \\ \tau_{r\theta} = \tau_{\theta r} = 0 \end{cases} \tag{9}$$

However, the displacement component is expressed as follows:

$$\begin{cases} u_{\mathrm{r}} = \frac{1}{E}[-(1+\mu)\frac{A}{r} + 2(1-\mu)Br(\ln r - 1) + \\ \qquad (1-3\mu)Br + 2(1-\mu)Cr] + I\cos\phi + K\sin\phi \\ u_\theta = \frac{4Br\phi}{E} + Hr - I\sin\phi + K\cos\phi \end{cases} \tag{10}$$

where u_r and u_θ denote radial and circumferential displacements, respectively; A, B, C, H, I, and K denote constants; and E and μ denote the modulus of elasticity and Poisson's ratio of the material, respectively.

In the thick-walled cylinder problem, since the closed cylinder is a multicontinuum, the displacement singular value condition needs to be considered. Also, because it is axisymmetric, the tangential displacement is zero, i.e., $u_\theta = 0$, so $B = H = I = K = 0$ in Equations (2)–(6).

Assuming that the inner diameter of the cylinder is, the outer diameter is, the internal pressure is, and the external pressure is, the boundary conditions and contact conditions are as follows:

$$\begin{cases} \sigma_r|_{r=r_1} = -p_1 \\ \sigma_r|_{r=r_2} = -p_2 \\ \tau_{r\theta}|_{r=r_1} = \tau_{\theta r}|_{r=r_2} = 0 \end{cases} \tag{11}$$

The boundary conditions are brought into Equations (9) and (10), and the coefficients A and C are obtained with the following expressions:

$$\begin{cases} A = \frac{r_1^2 r_2^2 (p_2 - p_1)}{r_2^2 - r_1^2} \\ C = \frac{r_1^2 p_1 - r_2^2 p_2}{2(r_2^2 - r_1^2)} \end{cases} \tag{12}$$

The lining stresses and displacements are obtained by bringing Equation (12) into Equations (9) and (10) with the following expression:

$$\begin{cases} \sigma_r = \frac{p_1 r_1^2 - p_2 r_2^2}{r_2^2 - r_1^2} + \frac{r_1^2 r_2^2 (p_2 - p_1)}{r_2^2 - r_1^2} \frac{1}{r^2} \\ \sigma_\theta = \frac{p_1 r_1^2 - p_2 r_2^2}{r_2^2 - r_1^2} - \frac{r_1^2 r_2^2 (p_2 - p_1)}{r_2^2 - r_1^2} \frac{1}{r^2} \qquad r_1 \le r \le r_2 \\ u_r = \frac{1+\mu_c}{E_c (r_2^2 - r_1^2)} \left\{ \left[(1 - 2\mu_c) r^2 + r_2^2 \right] p_1 r_1^2 - \right. \\ \qquad \left. \left[(1 - 2\mu_c) r^2 + r_1^2 \right] p_2 r_2^2 \right\} \end{cases} \tag{13}$$

where σ_r denotes the radial stress of the lining; σ_θ denotes the tangential stress of the lining; u_r denotes the displacement of the lining; r_1 denotes the inner radius of the lining; r_2 denotes the outer radius of the lining; E_c and μ_c denote the modulus of elasticity and Poisson's ratio of the concrete lining, respectively; p_1 denotes the pressure of water in the tunnel; and p_2 denotes the additional pressure.

For the surrounding rock surface acting under uniform water pressure, the stress and displacement of the surrounding rock under water pressure can be calculated using the principles of elastic mechanics, with its formula being as follows:

$$\begin{cases} \sigma_r = -\frac{r_2^2}{r^2} p_2 \\ \sigma_\theta = \frac{r_2^2}{r^2} p_2 \qquad r_2 \le r \le \infty \\ u_r = \frac{1+\mu_d}{E_d} \frac{r_2^2}{r} p_2 \end{cases} \tag{14}$$

where σ_r denotes the radial stress of the surrounding rock; σ_θ denotes the tangential stress of the surrounding rock; u_r denotes the displacement of the surrounding rock; r_2 denotes the radius of the tunnel; E_d and μ_d denote the modulus of elasticity and Poisson's ratio of the surrounding rock, respectively.

By applying the displacement condition at the contact interface between the surrounding rock and the lining, Equations (13) and (14) are utilized to determine the interaction force between the outer wall of the lining and the surrounding rock under internal water pressure. The resultant expression is as follows:

$$p_2 = p_1 \frac{2(1 - \mu_c^2) E_d r_1^2}{(1 + \mu_d) E_c (r_2^2 - r_1^2) + (1 + \mu_c) E_d \left[r_1^2 + (1 - \mu_c) r_2^2 \right]} \tag{15}$$

The Geological Investigation Report outlines the specific geometrical and material characteristics of the diversion tunnel, which are as follows: inner radius r_1 = 4.25 m; outer radius r_2 = 5.25 m; lining modulus of elasticity E_c = 30 GPa; lining Poisson's ratio μ_c = 0.25; peripheral rock modulus of elasticity E_d = 10 GPa; peripheral Poisson's ratio μ_d = 0.3; and water pressure = 0~1.35 MPa. The stress deformation diagrams of the non-destructive lining are shown in Figure 8, which shows a positive growth trend of cyclic stress and displacement. As shown in Figure 8, the stress and displacement of the undamaged lining are shown to be positively increasing, which indicates that the lining is currently in the stage of elastic deformation, i.e., the lining can effectively resist deformation through the annular stress when it is subjected to the water pressure.

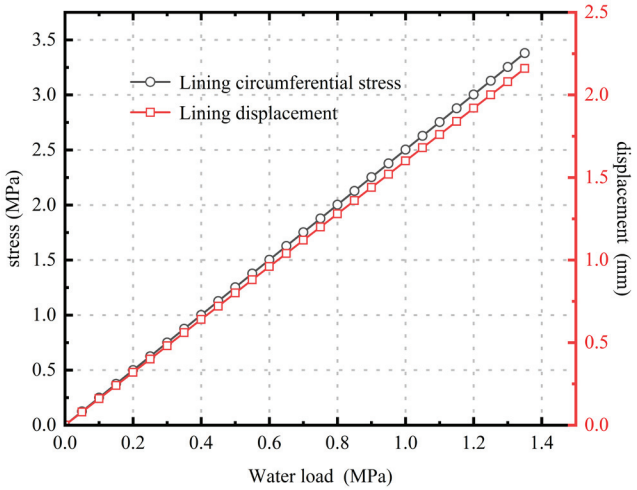


Figure 8. Stress-deflection diagram for non-destructive lining.

3.2. Mechanical Characteristics of Crack Lining Structures

Given that the surrounding rock remains in an elastic stress state without any damage following the emergence of cracks in the lining, according to the principles of elasticity, the plane differential equation for the axisymmetric plane problem in polar coordinates [30] can be expressed as follows:

$$\frac{\partial \sigma_r}{\partial r} + \frac{\sigma_r - \sigma_\theta}{r} = 0 \tag{16}$$

The lining structure produces cracks with tangential stresses $\sigma_\theta = 0$, and the stress balance equation is then expressed as follows:

$$\frac{\partial \sigma_r}{\partial r} + \frac{\sigma_r}{r} = 0 \tag{17}$$

Integrating Equation (18) yields from the boundary conditions $\sigma_r|_{r=r_1} = -p_1$:

$$\sigma_r = -\frac{r_1}{r} p_1 \quad r_1 \le r \le r_2 \tag{18}$$

Therefore, the stress in the cracked lining can be expressed as follows:

$$\sigma_{r_k} = -\frac{r_1}{r_k} p_1 \quad r_1 \le r_k \le r_2 \tag{19}$$

where σ_{rk} denotes the radial stress of the cracked lining; r_k denotes the radius of the cracked lining; r_1 denotes the inner radius of the lining; and p_1 denotes the water pressure in the tunnel.

It is presumed that the lining at the location where no crack has formed remains in an elastic condition, with the water pressure on its surface being pk = −rk. The structural stresses and displacements of the undamaged lining are derived using Equation (6) along with the provided expression:

$$\begin{cases} \sigma_r = \frac{p_k r_k^2 - p_2 r_2^2}{r_2^2 - r_k^2} + \frac{r_k^2 r_2^2 (p_2 - p_k)}{r_2^2 - r_k^2} \frac{1}{r^2} \\ \sigma_\theta = \frac{p_1 r_k^2 - p_2 r_2^2}{r_2^2 - r_k^2} - \frac{r_k^2 r_2^2 (p_2 - p_k)}{r_2^2 - r_k^2} \frac{1}{r^2} \qquad r_k \le r \le r_2 \\ u_r = \frac{1+\mu_c}{E_c (r_2^2 - r_k^2)} \left\{ \left[(1-2\mu_c) r^2 + r_2^2 \right] p_1 r_k^2 - \right. \\ \qquad \left. \left[(1-2\mu_c) r^2 + r_k^2 \right] p_2 r_2^2 \right\} \end{cases} \tag{20}$$

where σ_r denotes the radial stress at the lining without cracks; σ_θ denotes the tangential stress at the lining without cracks; u_r denotes the displacement at the lining without cracks; E_c and μ_c denote the modulus of elasticity and Poisson's ratio of the concrete lining, respectively; p_1 denotes the water load in the tunnel; and p_2 denotes the additional pressure.

The stresses and displacements of the surrounding rock subjected to water pressure can be determined through elastodynamic analysis, utilizing the provided expression:

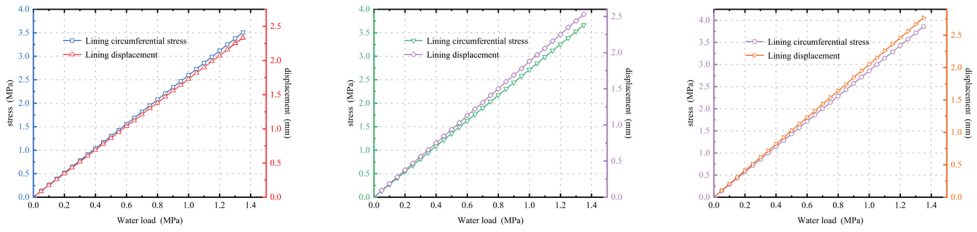
$$\begin{cases} \sigma_r = -\frac{r_2^2}{r^2} p_2 \\ \sigma_\theta = \frac{r_2^2}{r^2} p_2 \qquad r_2 \le r \le \infty \\ u_r = \frac{1+\mu_d}{E_d} \frac{r_2^2}{r} p_2 \end{cases} \tag{21}$$

where σ_r denotes the radial stress of the surrounding rock; σ_θ denotes the tangential stress of the surrounding rock; u_r denotes the displacement of the surrounding rock; r_2 denotes the radius of the tunnel; and E_d and μ_d denote the modulus of elasticity and Poisson's ratio of the surrounding rock, respectively.

In the same vein, Equations (21) and (22) are employed to determine the interaction force between the outer wall of the lining and the surrounding rock under the influence of internal water pressure. This force is represented as follows:

$$p_2 = p_k \frac{2(1-\mu_c^2)E_d r_k^2}{(1+\mu_d)E_c(r_2^2 - r_k^2) + (1+\mu_c)E_d\left[r_k^2 + (1-\mu_c)r_2^2\right]} \tag{22}$$

Based on the Geological Investigation Report for the diversion tunnel, we computed stresses and deformations of the crack lining structure under hydraulic pressure. As shown in Figure 9, there is a linear progression in both annular stress and displacement of the crack lining. With increasing crack depth, stress and displacement magnitudes escalate. This is due to stress transmission and deformation effects from water pressure, with cracks compromising the lining structure. Compared to an unblemished lining, the circumferential stress of the lining increased by approximately 4.50% with 0.1 m cracks, 9.10% with 0.2 m cracks, and 15.10% with 0.3 m cracks. A cracked lining fails to distribute stress evenly, reducing its resistance to water pressure interference and leading to heightened circumferential stress near the cracks. Over time, this stress concentration further degrades the lining structure.



(**a**) 0.1 m crack (**b**) 0.2 m crack (**c**) 0.3 m crack

Figure 9. Stress deformation diagram for defective lining.

3.3. Mechanical Characteristics of Different Structural Segments

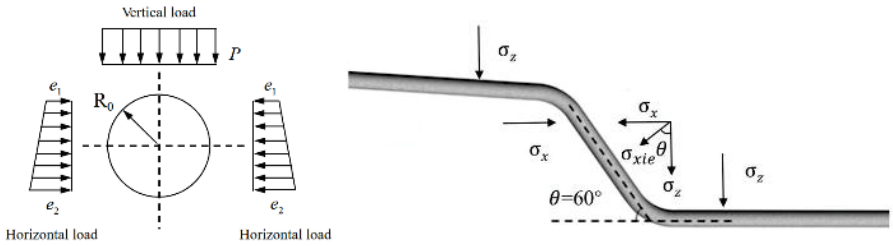
The text describes the features of lining cracks in axial coordinates. The diversion tunnel includes an upper flat section, an inclined shaft section, and a lower flat section. Data show a notable difference in defect numbers between the upper flat and inclined shaft sections. This difference stems from the unique force characteristics of each structural segment, affecting defect formation and distribution.

Figure 10 presents a detailed schematic diagram illustrating the comprehensive force analysis of the diversion tunnel. This analysis is meticulously computed in accordance with

the guidelines stipulated by the Road Tunnel Design Code and incorporates fundamental principles of rock mechanics theory to ensure accuracy and reliability [31]. In this context, the distinction between shallow and deeply buried tunnels is delineated by employing a formula that calculates the load equivalent height:

$$\begin{cases} H_p = 2.5h_q \\ \mathrm{h}_q = \frac{q}{\gamma} \end{cases} \tag{23}$$

where H_p denotes the dividing depth between deep and shallow buried tunnels; h_q denotes the load equivalent height; γ denotes the weight of the surrounding rock; and q denotes the vertical pressure of the surrounding rock.



(**a**) Force analysis of lining section (**b**) Lining structure section force analysis diagram

Figure 10. Schematic diagram of the overall force analysis of the lining.

Given that the deepest burial point of the diversion tunnel in this project exceeds the critical depth Hp as stipulated by Equation (23), it is categorized as a deeply embedded tunnel. Consequently, the lining structure of the diversion tunnel experiences vertical stress corresponding to the pressure exerted by the surrounding rock mass of the tunnel:

$$\sigma_z = \gamma h = \gamma \times 0.45 \times 2^{\mathrm{s}-1} w \tag{24}$$

where σ_z denotes the vertical pressure; γ denotes the perimeter rock capacity; s denotes the perimeter rock level; w denotes the width influence coefficient, $w = 1 + i\ (B - 5)$; B denotes the width of the tunnel; and i is taken as 0.1 when $B > 5$ m.

The lining structure is subjected to horizontal pressure, which is expressed as follows:

$$\begin{cases} e_1 = q\tan^2(45^\circ - \frac{\varphi_c}{2}) \\ e_2 = (q + \gamma h)\tan^2(45^\circ - \frac{\varphi_c}{2}) \\ \sigma_x = \frac{(e_1+e_2)}{2} = K_0\sigma_Z \\ K_0 = \frac{\mu}{1-\mu} \end{cases} \tag{25}$$

In the formula, e_1, e_2 indicates the horizontal pressure of surrounding rock from the top to the bottom of the tunnel arch; e indicates the horizontal mean pressure; h indicates the height of the tunnel; φ_c indicates the friction angle of surrounding rock, and the value of 65° is taken in this project; K_0 indicates the lateral pressure coefficient of surrounding rock, and the value of 0.43 is taken in the calculation of this project; and μ indicates the Poisson's ratio of surrounding rock.

The architecture of the upper flat and inclined shaft segments mainly addresses vertical pressure from the surrounding rock at the diversion tunnel's apex. Lateral pressures are evenly distributed, neutralizing each other. Thus, the focus is on vertical pressure impact. Due to lining inclination, the pressure on the vertical face of the inclined shaft segment is articulated as follows [32]:

$$\sigma_{xie} = \sigma_z \cos\theta < \sigma_z \tag{26}$$

where σ_{xie} denotes the component of pressure in the vertical direction, and θ denotes the angle between the inclined shaft section and the horizontal line.

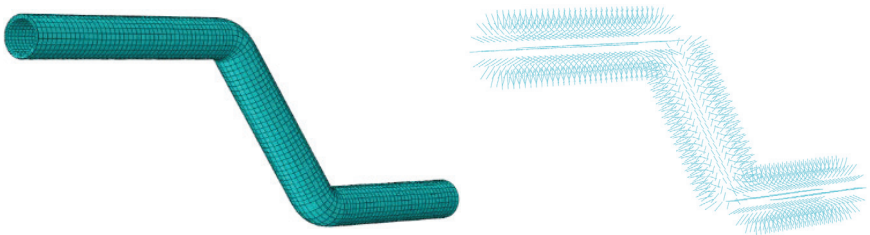
The shaft's angle relative to the horizontal creates a vertical stress component that reduces perpendicular pressure on the surrounding rock. This leads to fewer defects in the inclined shaft compared to the upper level, as confirmed by defect inspection data from both sections of the diversion tunnel.

4. Numerical Simulation and Analysis of Diversion Tunnels

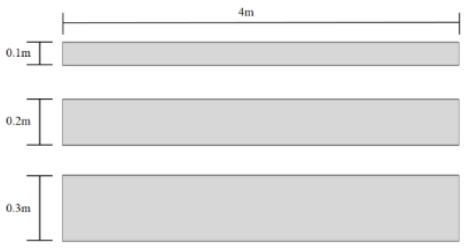
Numerical analysis is less costly and faster. To further verify the results of the field tests, the continuous medium software ABAQUS (Version ABAQUS-2023) was used to continue the numerical model analysis.

4.1. Three-Dimensional Modeling

Based on actual test conditions, this paper investigates the stress and strain response of the diversion tunnel lining structure using a 3D numerical model. Based on a comprehensive review of the existing literature and a detailed analysis of the engineering geological structure, a sophisticated three-dimensional simulation model of the diversion tunnel has been developed. The model is configured with comprehensive mechanical and seepage parameters: elastic modulus E = 50 GPa, Poisson's ratio ν = 0.24, uniaxial compressive strength UCS = 110 MPa, tensile strength σ_t = 7 MPa, internal friction angle $\phi = 32^\circ$, permeability coefficient $k = 1 \times 10^{-7}$ m/s, and porosity n = 0.05. Figure 11 shows that the model's geometric dimensions are precisely defined: the upper flat section spans 87.4 m, the inclined shaft section measures 58.3 m, and the lower flat section extends 55.3 m. The tunnel has a diameter of 10.5 m and a lining thickness of 1.0 m, supported by rebar at intervals of every 2 m. Longitudinal cracks are prioritized for investigation due to the specific structural configuration and loading conditions of the lining, while circumferential cracks are excluded from this study [33]. When formulating the model with cracks, crack components are set with an average length of 4 m and varying depths of 0.1 m, 0.2 m, and 0.3 m. The tunnel lining utilizes an elastic–plastic model based on actual engineering values. Material parameter values are detailed in Table 2. A vertical load is applied to the top of the lining (see Equation (24)), a horizontal load to the left and right boundaries (see Equation (25)), and a water load from 0 to 1.35 MPa inside the lining.



(**a**) Lining models (**b**) Rebar modeling



(**c**) Cracked component modeling

Figure 11. Diversion tunnel component models.

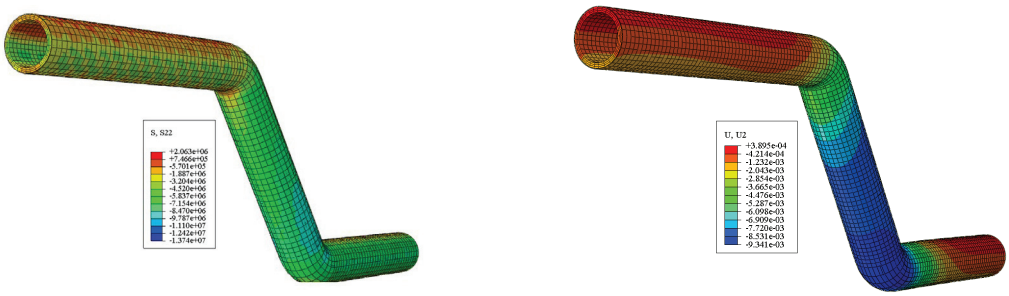
Table 2. Table of values for each parameter.

Type	Unit Weight (kN·m^{-3})	Modulus of Elasticity (GPa)	Poisson's Ratio	Angle of Internal Friction (°)	Cohesion (MPa)	Tensile Strength (MPa)	Breaking Energy (N/M)
Surrounding rock	27.5	5.38	0.30	45	1.20		
Lining	25	30.0	0.25	-	-	1.43	114.35
Shotcrete	25	31.5	0.20	-	-	1.57	
Anchor bolt	78	200.0	0.20	-	-		

4.2. Simulation Results

4.2.1. Deformation Characteristics of Non-Destructive Lining Structures

Figure 12 shows the simulated circumferential stress deformation of the lining. A negative sign indicates compression, and a positive sign indicates tension. In Figure 12a, the lining displays varying stress levels, with the vault in tension. The maximum tensile stress exceeds 1.43 MPa, raising the risk of tensile cracking. The pressure on both sides of the cave waist is significant, but the peak compressive stress is below the concrete's compressive strength, indicating a low risk of compression fractures. Figure 12b shows that the lining near the entrance deforms more, with greater displacement in the upper flat section than in the inclined shaft section. This suggests internal water pressure negatively impacts the lining's bearing capacity. However, the overall displacement cloud diagram shows symmetrical and minimal deformation, ensuring the lining's safety and stability remain intact.



(**a**) Circumferential stress distribution in the lining(**b**) Circumferential displacement distribution of the lining

Figure 12. Circumferential stress deformation of diversion tunnel lining cloud map.

To gain deeper insights into the distribution patterns of lining stress and displacement, we have selected specific points from both the upper flat section and the inclined shaft section. These numerical results are depicted in Figure 13, which illustrates their evolution over time through a series of curves. Figure 14 illustrates that the patterns of stress and deformation in both the lining arch and arch waist are fundamentally consistent. The displacement values across points A to E exhibit minor variations, with the maximum displacement observed at point A. This suggests a uniform deformation response of the tunnel structure as a whole, albeit with notably larger deformations nearer the entrance. Since the magnitude of the displacement value does not directly dictate the deformation characteristics of the lining, it necessitates analysis from the perspective of internal force distribution. Figure 14c illustrates that the variation in circumferential stresses at points A to C along the lining is minimal, whereas the disparity at points D to F is substantial, suggesting a relatively uniform stress distribution across the upper flat section. When compared to the section points depicted in Figure 14d, the stress alteration at the apex of the arch is more pronounced. This phenomenon may be attributed to the heightened tensile stress induced by the vertical pressure exerted by the surrounding rock at the arch's crown.

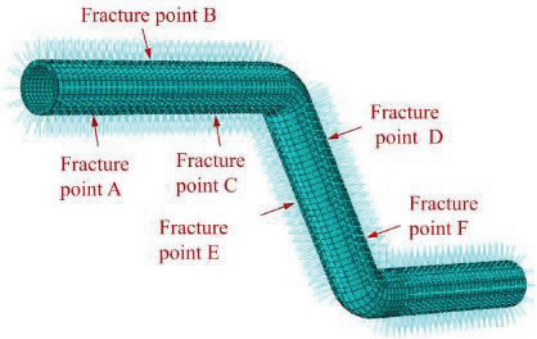
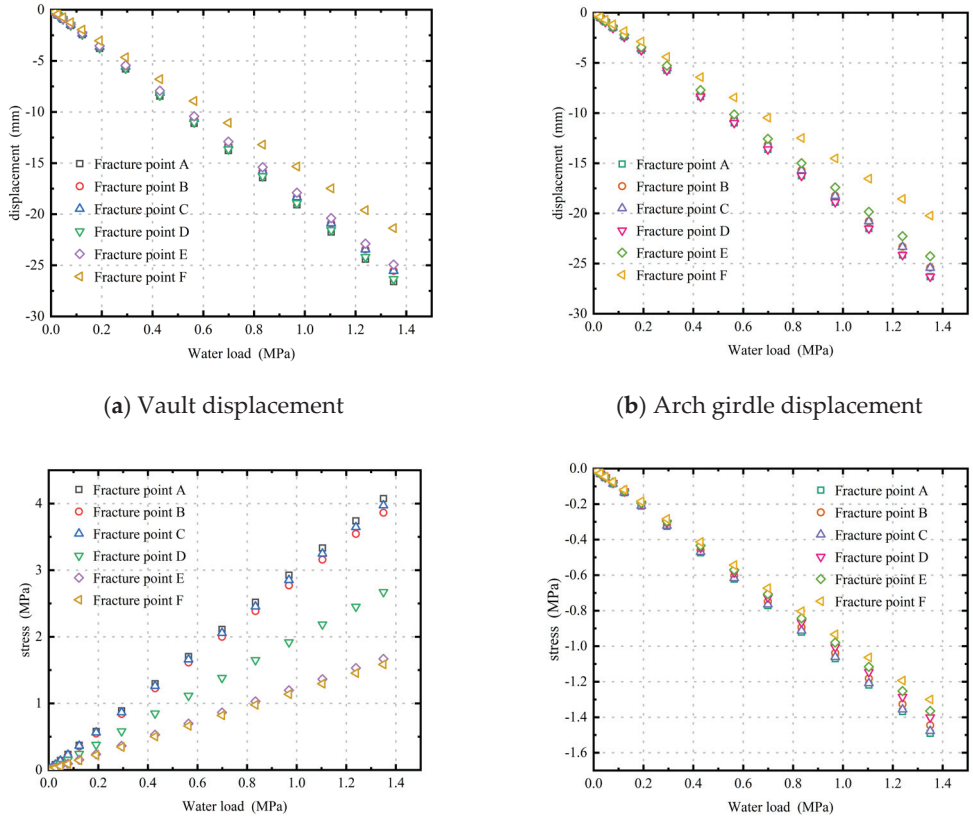


Figure 13. Schematic diagram of cross-section points of diversion tunnels.



(**a**) Vault displacement

(**b**) Arch girdle displacement

(**c**) Arch top stress

(**d**) Arch girdle stress

Figure 14. Circumferential stress deformation curve of diversion tunnel lining.

To verify the non-destructive lining model, analytical solutions are compared with simulated stress values at the annular region. Discrepancies, detailed in Table 3, show errors within a 15% margin. Despite numerical deviations, both methods concur on the overall stress trends of the lining structure, validating the theoretical computations.

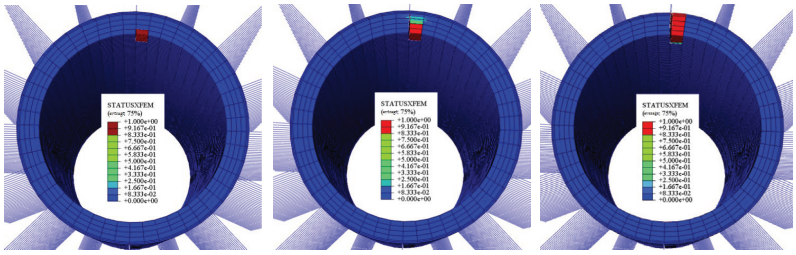
Table 3. Comparison table between theoretical and simulated results of non-destructive lining.

Water Load in the Cave (MPa)	Analytical Solution for Cyclic Stress (MPa)	Numerical Solution for the Maximum Cyclic Stress (MPa)	Error Value (%)
0.45	1.13	1.29	14.15
0.8	2.00	2.28	14.00
1.2	2.75	3.15	14.55
1.35	3.37	3.84	13.95

4.2.2. Deformation Characteristics of Cracked Lining Structures

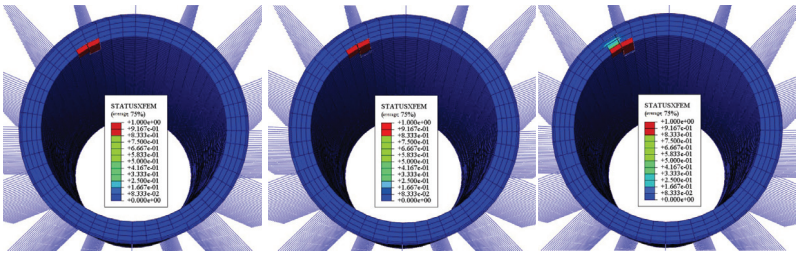
Based on the mechanical characterization of the non-destructive lining, the upper flat section with superior stress deformation properties is chosen for investigating crack propagation.

Throughout the crack expansion progression, STATUS indicates the extent of the crack. A STATUSXFEM value of one signifies complete obliteration of the lining. Figure 15 shows a fully cracked region from 0 to 90 degrees at the top of the arch, with cloud map values at the tip between zero and one, indicating imminent cracking that will spread as steps increase. Water pressure keeps the crack open, and the incremental step method simulates crack expansion by gradually decomposing the overall loading. In the initial phase (steps 0–20), cracks of 0.1 m, 0.2 m, and 0.3 m expand along depth; over time (steps 20–40), cracks penetrate through the lining, potentially causing significant fractures; beyond step 40, crack expansion shifts towards the lining wall until halted.



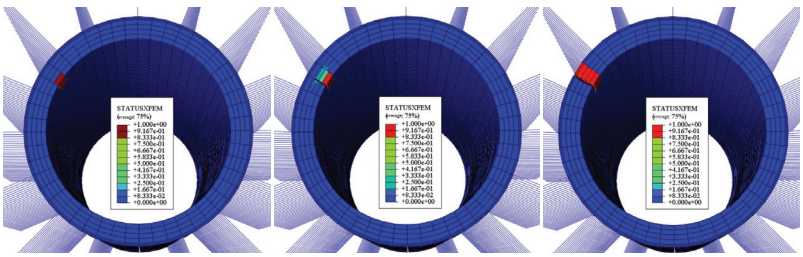
incremental step 0 incremental step 20 incremental step 40

(**a**) Expansion process of the crack located at 0° off the top of the arch figure



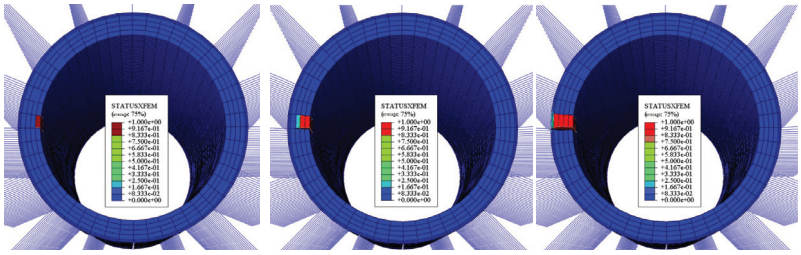
incremental step 0 incremental step 20 incremental step 40

(**b**) Expansion process of the crack located at 30° off the top of the arch figure



incremental step 0 incremental step 20 incremental step 40

(**c**) Expansion process of the crack located at 60° off the top of the arch figure



incremental step 0 incremental step 20 incremental step 40

(**d**) Expansion process of the crack located at 90° off the top of the arch figure

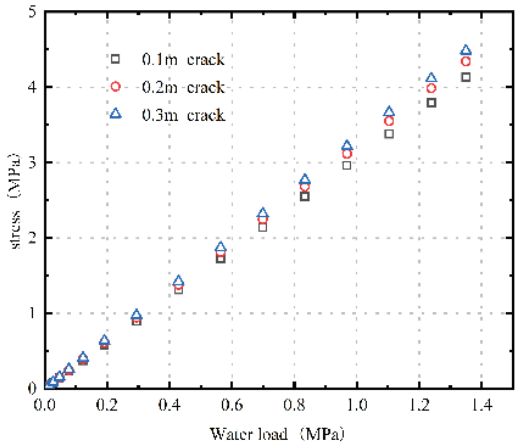
Figure 15. Diagram of the expansion process of the cracked lining.

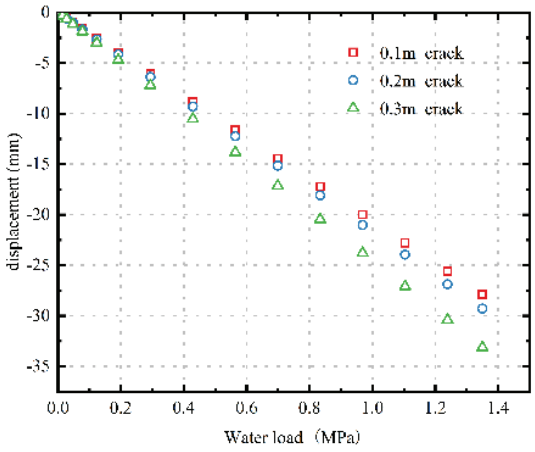
Extracting a point at the crack and recording its development with a curve, it can be seen in Figure 16b,d,f,h that the displacement value at 90° of the vault > 0° of the vault > 60° of the vault > 30° of the vault. It shows that the water pressure has a greater influence on the top of the arch at 60~90°, and the deeper the crack, the higher the displacement value. This phenomenon likely arises due to the arch waist experiencing not only heightened circumferential rock compression but also uneven hydrostatic pressure. The presence of cracks exacerbates displacement magnitudes, suggesting that the extent of displacement in a fissured lining alone does not encapsulate its deformation behavior comprehensively. Instead, an in-depth analysis of stress distribution patterns is imperative to fully grasp the nuances of lining deformation characteristics. From the stress distribution depicted in Figure 16a,c,e,g, it is evident that the circumferential stress at angles 0–30° off the vault exceeds the circumferential stress found at angles 60–90° off the vault. The data reveals a significant tensile stress concentration at the apex of the lining, with stress magnitude escalating as the crack deepens. This phenomenon can likely be attributed to heightened surrounding rock tension at the crown, which disrupts the normal stress distribution within the lining structure. Consequently, an augmented tensile force manifests at the crack periphery, leading to a more pronounced localized stress concentration as the crack progresses deeper into the structure [34].

Furthermore, to ensure the validity of the crack lining model presented above, a portion of the analytical solutions was chosen for comparison against the simulated values for the maximum annular stress. As demonstrated in Table 4, the error margins between the theoretical predictions and the simulated outcomes for crack linings at 0.1 m, 0.2 m, and 0.3 m are all within a 15% range. Although there exists some discrepancy between the two sets of calculations, the overall trend in the stress characteristics of the lining structure derived from both methods is consistent, thereby validating the reasonableness of the model assumptions.

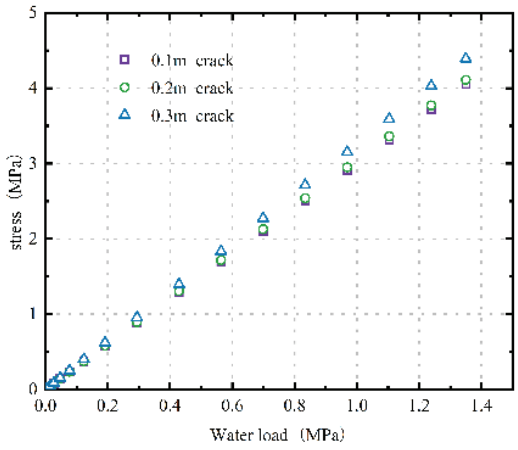
Table 4. Comparison table between theoretical and simulated results for crack lining.

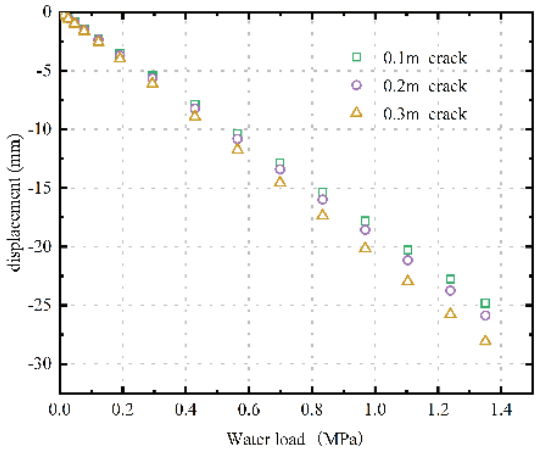
(a) Comparison of 0.1 m crack results			
Water Load in the Cave (MPa)	Analytical Solution for Cyclic Stress (MPa)	Numerical Solution for the Maximum Cyclic Stress (MPa)	Error Value (%)
0.45	1.17	1.31	11.97
0.8	2.08	2.35	12.98
1.2	2.86	3.28	14.68
1.35	3.51	4.03	14.81
(b) Comparison of 0.2 m crack results			
Water Load in the Cave (MPa)	Analytical Solution for Cyclic Stress (MPa)	Numerical Solution for the Maximum Cyclic Stress (MPa)	Error Value (%)
0.45	1.22	1.39	13.93
0.8	2.17	2.44	12.44
1.2	2.99	3.42	14.38
1.35	3.66	4.19	14.48
(c) Comparison of 0.3 m crack results			
Water Load in the Cave (MPa)	Analytical Solution for Cyclic Stress (MPa)	Numerical Solution for the Maximum Cyclic Stress (MPa)	Error Value (%)
0.45	1.29	1.45	12.40
0.8	2.29	2.57	12.27
1.2	3.14	3.57	13.69
1.35	3.86	4.38	13.47



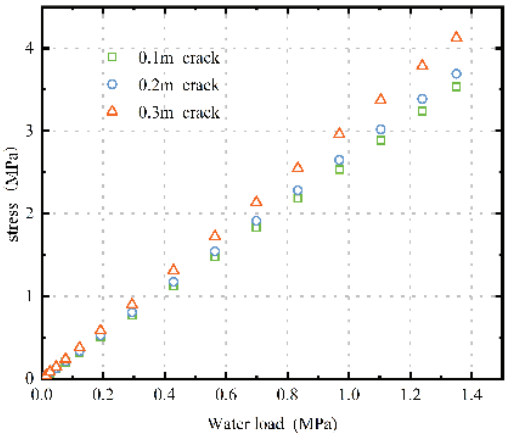


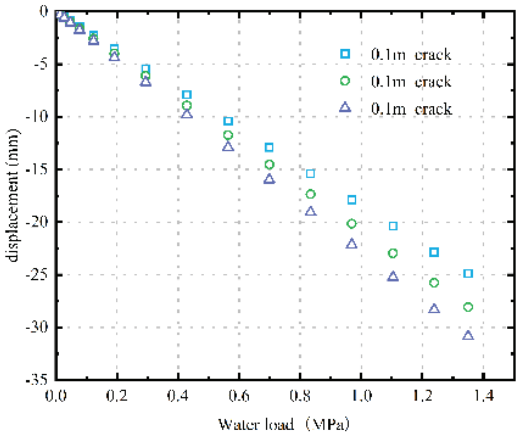
(**a**) Stress changes where the crack is located at 0° off the top of the arch (**b**) Change in displacement with the crack located at 0° off the top of the arch





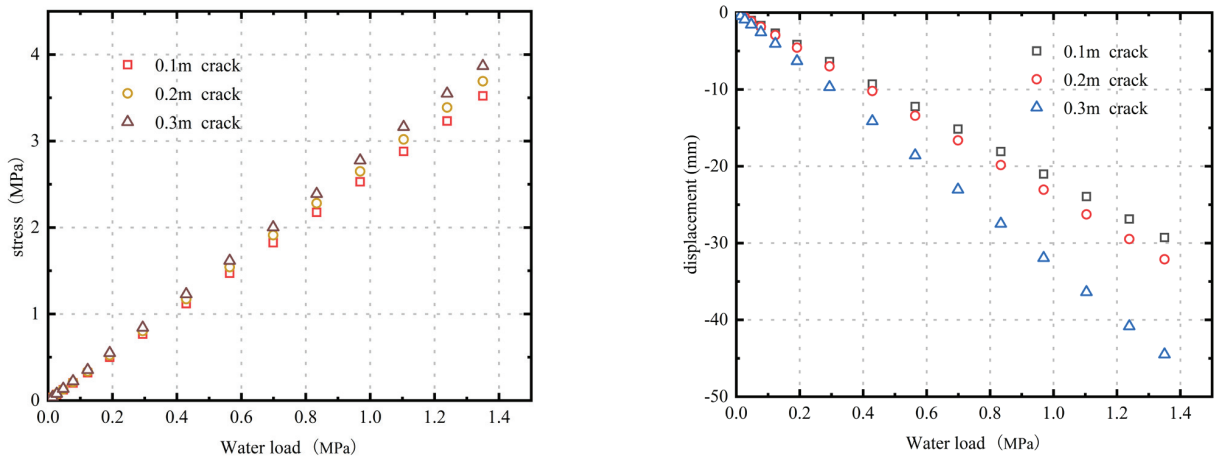
(**c**) Stress changes where the crack is located at 30° off the top of the arch (**d**) Change in displacement with the crack located at 30° off the top of the arch





(**e**) Stress changes where the crack is located at 60° off the top of the arch (**f**) Change in displacement with the crack located at 60° off the top of the arch

Figure 16. *Cont.*



(**g**) Stress changes where the crack is located at 90° off the top of the arch (**h**) Change in displacement with the crack located at 90° off the top of the arch

Figure 16. Circumferential stress deformation curve of cracked lining of diversion tunnel.

5. Conclusions

This study investigates the inspection results of a diversion tunnel in a hydropower station located in the Dadu River Basin, with a focus on the formation mechanisms and simulation analysis of lining cracks. The main conclusions are summarized as follows:

(1) Tunnel lining inspections reveal significant spatial variation in defect distribution across different structural sections. The upper horizontal section exhibits a markedly higher frequency of defects compared to the inclined shaft, with most defects concentrated near the tunnel crown. Cracks at the crown are identified as having a more pronounced impact on structural safety.

(2) A two-dimensional axial force model was developed based on elastic mechanics for both intact and cracked linings. The analysis indicates a rising trend in both hoop stress and displacement. The presence of cracks at varying depths results in localized stress concentrations, potentially accelerating long-term structural degradation. The inclined shaft demonstrates a lower tendency for defect formation under stress, which aligns with field inspection findings.

(3) A three-dimensional finite element model was employed to simulate stress distribution. The results show that the undamaged lining in the upper horizontal section is subjected to greater circumferential stress than that in the inclined shaft. For cracked linings, circumferential stress is higher in the arch range of 0–30° than in 60–90°, indicating that cracks in the upper arch pose a greater threat to structural integrity. The simulation results are consistent with theoretical predictions, with deviations maintained within an acceptable error margin of 15%.

Author Contributions: Conceptualization, H.X., X.Z. and K.L.; Methodology, H.X. and H.W.; Formal analysis, L.Y.; Investigation, H.X., Z.L. and K.L.; Writing—original draft, H.X., H.W., Y.C. and Z.L.; Visualization, Y.C.; Supervision, X.Z.; Funding acquisition, H.W. All authors have read and agreed to the published version of the manuscript.

Funding: This work was supported by the National Key R&D Program of China (No. 2022YFB4703404), the National Natural Science Foundation of China (No. U21A20157), and the Sichuan Science and Technology Program (No. 2023YFS0410).

Institutional Review Board Statement: Not applicable.

Informed Consent Statement: Not applicable.

Data Availability Statement: Some or all data, models, or code that support the findings of this study are available from the corresponding author upon reasonable request.

Conflicts of Interest: The authors declare that they have no known competing financial interests or personal relationships that could have appeared to influence the work reported in this paper.

References

1. Yu, J.; Zhong, D.H.; Ren, B.Y.; Tong, D.W.; Hong, K. Probabilistic Risk Analysis of Diversion Tunnel Construction Simulation. *Comput. Aided Civ. Infrastruct. Eng.* **2017**, *32*, 748–771. [CrossRef]
2. McAdams, M.; Wang, J. Gunnison Tunnel: Engineering History of an Early American Reclamation Project. *J. Perform. Constr. Facil.* **2013**, *27*, 826–835. [CrossRef]
3. Liu, K.; Chen, Y.C.; Wang, H.R.; Xie, H.; Liu, Z.W. Reducing inconsistencies of FAHP in structural safety assessment of diversion tunnels. *Appl. Soft Comput.* **2023**, *146*, 14. [CrossRef]
4. He, Y.P.; Sun, X.J.; Zhang, M.X. Investigation on the Deformation of Segment Linings in Cross-Fault Tunnel Considering the Creep Behavior of Surrounding Rock during Construction-Operation Period. *Buildings* **2022**, *12*, 1648. [CrossRef]
5. Deng, J.; Xiao, M. Dynamic response analysis of concrete lining structure in high pressure diversion tunnel under seismic load. *J. Vibroeng.* **2016**, *18*, 1016–1030. [CrossRef]
6. Yao, J.; Wang, Y.; Feng, D. Application of Signal Imaging Analysis Technology in Prediction and Treatment of Water Inrush in Diversion Tunnel. *Trait. Du Signal* **2022**, *39*, 1729–1736. [CrossRef]
7. Xia, M.P.; Li, H.B.; Jiang, N.; Chen, J.L.; Zhou, J.W. Risk Assessment and Mitigation Evaluation for Rockfall Hazards at the Diversion Tunnel Inlet Slope of Jinchuan Hydropower Station by Using Three-dimensional Terrestrial Scanning Technology. *KSCE J. Civ. Eng.* **2023**, *27*, 181–197. [CrossRef]
8. Wu, Y.; Li, Y.Z.; Qiao, W.G.; Fan, Z.W.; Zhang, S.; Chen, K.; Zhang, L. Water Seepage in Rocks at Micro-Scale. *Water* **2022**, *14*, 2827. [CrossRef]
9. Hao, X.J.; Feng, X.T.; Yang, C.X.; Jiang, Q.; Li, S.J. Analysis of EDZ Development of Columnar Jointed Rock Mass in the Baihetan Diversion Tunnel. *Rock Mech. Rock Eng.* **2016**, *49*, 1289–1312. [CrossRef]
10. Dong, L.H.; Chen, J.D.; Song, D.Q.; Wang, C.W.; Liu, X.L.; Liu, M.X.; Wang, E.Z. Application of Long-Range Cross-Hole Acoustic Wave Detection Technology in Geotechnical Engineering Detection: Case Studies of Tunnel-Surrounding Rock, Foundation and Subgrade. *Sustainability* **2022**, *14*, 16947. [CrossRef]
11. Lin, C.J.; Wang, X.T.; Li, Y.; Zhang, F.K.; Xu, Z.H.; Du, Y.H. Forward Modelling and GPR Imaging in Leakage Detection and Grouting Evaluation in Tunnel Lining. *KSCE J. Civ. Eng.* **2020**, *24*, 278–294. [CrossRef]
12. Liu, C.; Zhang, D.L.; Zhang, S.L. Characteristics and treatment measures of lining damage: A case study on a mountain tunnel. *Eng. Fail. Anal.* **2021**, *128*, 13. [CrossRef]
13. Lu, A.; Yan, P.; Lu, W.B.; Li, X.F.; Liu, X.; Luo, S.; Huang, S.L.; Grasselli, G. Crack propagation mechanism of smooth blasting holes for tunnel excavation under high in-situ stress. *Eng. Fract. Mech.* **2024**, *304*, 19. [CrossRef]
14. Li, G.D.; Ren, Z.Y.; Yu, J.J. Mixed-Mode I-II Fracture Process Zone Characteristic of the Four-Point Shearing Concrete Beam. *Materials* **2020**, *13*, 3203. [CrossRef]
15. Du, J. A Fracture Mechanics Study of Concrete Failure. Ph.D. Thesis, University of Washington, Seattle, WA, USA, 1988.
16. Li, Z.H.; Gong, Y.J.; Chen, F.J. Simulation of mixed mode I-II crack propagation in concrete using toughness-based crack initiation-propagation criterion with modified fracture energy. *Theor. Appl. Fract. Mech.* **2023**, *123*, 16. [CrossRef]
17. Khan, G.; Ahmed, A.; Liu, Y.; Tafsirojjaman, T.; Ahmad, A.; Iqbal, M. Phase field model for mixed mode fracture in concrete. *Eng. Fract. Mech.* **2023**, *289*, 15. [CrossRef]
18. Chen, S.; Yang, Z.; Liu, S.; Li, L.F.; Zheng, Y.B.; Yuan, Y. Numerical simulation and analysis of crack disease in tunnel lining structure. *Front. Mater.* **2022**, *9*, 17. [CrossRef]
19. Karami, M.; Kabiri-Samani, A.; Nazari-Sharabian, M.; Karakouzian, M. Investigating the effects of transient flow in concrete-lined pressure tunnels, and developing a new analytical formula for pressure wave velocity. *Tunn. Undergr. Space Technol.* **2019**, *91*, 13. [CrossRef]
20. Wang, G.; Fang, Q.; Du, J.M.; Wang, J. Semi-analytical solution for internal forces of tunnel lining with multiple longitudinal cracks. *J. Rock Mech. Geotech. Eng.* **2023**, *15*, 2013–2024. [CrossRef]
21. Chen, J.X.; Hu, T.T.; Hu, X.; Jia, K. Study on the influence of crack depth on the safety of tunnel lining structure. *Tunn. Undergr. Space Technol.* **2024**, *143*, 16. [CrossRef]
22. Peng, Z.T.; Fang, Q.; Ai, Q.; Jiang, X.M.; Wang, H.; Huang, X.C.; Yuan, Y. Identifying the dominant influencing factors of secondary lining cracking risk in an operating mountain tunnel. *Int. J. Struct. Integr.* **2024**, *15*, 731–756. [CrossRef]
23. Du, J.M.; Shu, Y.H.; Xu, G.W.; He, C.; Yao, C.F. Study on the influence of geo-stress field on the fracture pattern of secondary tunnel lining. *Eng. Fail. Anal.* **2023**, *152*, 28. [CrossRef]

24. Xu, Z.L.; Chen, J.X.; Luo, Y.B.; Zhu, H.Y.; Liu, W.W.; Shi, Z.; Song, Z.G. Geomechanical model test for mechanical properties and cracking features of Large-section tunnel lining under periodic temperature. *Tunn. Undergr. Space Technol.* **2022**, *123*, 15. [CrossRef]
25. Lu, S.; Sun, Z.Y.; Zhang, D.L.; Liu, C.; Wang, J.C.; Huangfu, N.Q. Numerical modelling and field observations on the failure mechanisms of deep tunnels in layered surrounding rock. *Eng. Fail. Anal.* **2023**, *153*, 27. [CrossRef]
26. Lei, Y.M.; Yang, X.H.; Liu, Q.S.; Liu, H.; Chu, Z.F.; Wen, J.T.; Huang, Y.H. An enhanced polar-based GPGPU-parallelized contact detection algorithm for 3D FDEM and its application to cracking analysis of shield tunnel segmental linings. *Tunn. Undergr. Space Technol.* **2024**, *148*, 22. [CrossRef]
27. Li, L.Y.; Liu, Z.; Du, X.L. Improvement of Analytic Hierarchy Process Based on Grey Correlation Model and Its Engineering Application. *Asce-Asme J. Risk Uncertain. Eng. Syst. Part A Civ. Eng.* **2021**, *7*, 12. [CrossRef]
28. Lang, L.; Zhu, Z.M.; Zhang, X.S.; Qiu, H.; Zhou, C.L. Investigation of crack dynamic parameters and crack arresting technique in concrete under impacts. *Constr. Build. Mater.* **2019**, *199*, 321–334. [CrossRef]
29. Peng, J.X.; Hu, S.W.; Zhang, J.R.; Cai, C.S.; Li, L.Y. Influence of cracks on chloride diffusivity in concrete: A five-phase mesoscale model approach. *Constr. Build. Mater.* **2019**, *197*, 587–596. [CrossRef]
30. Mittelstedt, C.; Becker, W. Efficient computation of order and mode of three-dimensional stress singularities in linear elasticity by the boundary finite element method. *Int. J. Solids Struct.* **2006**, *43*, 2868–2903. [CrossRef]
31. Xie, H.P.; Lu, J.; Li, C.B.; Li, M.H.; Gao, M.Z. Experimental study on the mechanical and failure behaviors of deep rock subjected to true triaxial stress: A review. *Int. J. Min. Sci. Technol.* **2022**, *32*, 915–950. [CrossRef]
32. Li, C.B.; Yang, D.C.; Xie, H.P.; Ren, L.; Wang, J. Size effect of fracture characteristics for anisotropic quasi-brittle geomaterials. *Int. J. Min. Sci. Technol.* **2023**, *33*, 201–213. [CrossRef]
33. Zhang, N.; Zhu, X.J.; Ren, Y.F. Analysis and Study on Crack Characteristics of Highway Tunnel Lining. *Civ. Eng. J. Tehran* **2019**, *5*, 1119–1123. [CrossRef]
34. Rodríguez, C.A.; Rodríguez-Pérez, Á.M.; López, R.; Hernández-Torres, J.A.; Caparrós-Mancera, J.J. A Finite Element Method Integrated with Terzaghi's Principle to Estimate Settlement of a Building Due to Tunnel Construction. *Buildings* **2023**, *13*, 1343. [CrossRef]

Disclaimer/Publisher's Note: The statements, opinions and data contained in all publications are solely those of the individual author(s) and contributor(s) and not of MDPI and/or the editor(s). MDPI and/or the editor(s) disclaim responsibility for any injury to people or property resulting from any ideas, methods, instructions or products referred to in the content.

applied sciences

MDPI

Article

Edge-Enhanced CrackNet for Underwater Crack Detection in Concrete Dams †

Xiaobian Wu [1,2], Weibo Zhang [1], Guangze Shen [1,3] and Jinbao Sheng [1,3,*]

[1] Nanjing Hydraulic Research Institute, Nanjing 210029, China; xbwu@nhri.cn (X.W.); wbzhang@nhri.cn (W.Z.); gzshen@nhri.cn (G.S.)
[2] NHRI R&D Tech Group Co., Ltd., Nanjing 210029, China
[3] Dam Safety Management Center of the Ministry of Water Resources, Nanjing 210029, China
* Correspondence: jbshen@nhri.cn; Tel.:+86-025-85828600
† This paper is an extension of a conference paper. Edge Enhanced Underwater CrackNet for Dam Underwater Crack Detection. In Proceedings of the International Symposium "Common Challenges, Shared Future, Better Dams" ICOLD-CIGB 2025, Chengdu, China, 16–23 May 2025.

Featured Application: This study provides an underwater image enhancement method that effectively improves the detection performance of crack recognition algorithms under complex flow field and low-illumination underwater conditions and provides a new solution for concrete crack detection algorithms applied to dam surfaces under deep-water conditions.

Abstract: Underwater crack detection in dam structures is of significant importance to ensure structural safety, assess operational conditions, and prevent potential disasters. Traditional crack detection methods face various limitations when applied to underwater environments, particularly in high dam underwater environments where image quality is influenced by factors such as water flow disturbances, light diffraction effects, and low contrast, making it difficult for conventional methods to accurately extract crack features. This study proposes a dual-stage underwater crack detection method based on Cycle-GAN and YOLOv11 called Edge-Enhanced Underwater CrackNet (E^2UCN) to overcome the limitations of existing image enhancement methods in retaining crack details and improving detection accuracy. First, underwater concrete crack images were collected using an underwater remotely operated vehicle (ROV), and various complex underwater environments were simulated to construct a test dataset. Then, an improved Cycle-GAN image style transfer method was used to enhance the underwater images. Unlike conventional GAN-based underwater image enhancement methods that focus on global visual quality, our model specifically constrains edge preservation and high-frequency crack textures, providing a novel solution tailored for crack detection tasks. Subsequently, the YOLOv11 model was employed to perform object detection on the enhanced underwater crack images, effectively extracting crack features and achieving high-precision crack detection. The experimental results show that the proposed method significantly outperforms traditional methods in terms of crack detection accuracy, edge clarity, and adaptability to complex backgrounds, effectively improving underwater crack detection accuracy (precision = 0.995, F1 = 0.99762, mAP@0.5 = 0.995, and mAP@0.5:0.95 = 0.736) and providing a feasible technological solution for intelligent inspection of high dam underwater cracks.

Keywords: dam safety; small-object detection; underwater crack detection

1. Introduction

Currently, China has the largest number of high dams, with 588 dams over 70 m, 233 dams over 100 m, and 23 dams over 200 m. Thus, high dam safety is a major challenge for national water safety and public safety. Cracks are one of the most common structural defects in such underwater engineering facilities during long-term operation. They can lead to reduced structural strength, water leakage, and even catastrophic consequences, posing a serious threat to safety. In some cases, the cracks exist underwater, which is even more challenging, as mature methods for above-water detection cannot be directly applied. Therefore, determining methods for early detection and precise evaluation of cracks both above and below water is of critical importance for ensuring the stability of these engineering structures.

Traditional crack detection methods mainly rely on draining reservoirs to clear interference factors combined with manual inspections to clearly observe underwater structural defects [1,2], an approach that is both time-consuming and economically costly and requires a considerable amount of human resources, potentially having a negative impact on the ecological environment in certain cases. It is also not suitable for high dams and large reservoirs. In contrast, modern detection methods primarily rely on divers or portable detection equipment for underwater visual inspections, with saturation diving required for high dams, which is both dangerous and costly. Moreover, divers often lack professional knowledge of hydraulic engineering, lowering the reliability of their detection results. Most recently, with the advancements in ROVs and underwater imaging technologies, the possibility of intelligent inspection for underwater cracks has emerged. However, traditional image-processing methods perform poorly in complex underwater environments, and their detection accuracy and adaptability are severely limited [3]. Therefore, research on crack defect detection models in complex underwater environments is of great significance.

One of the core challenges in underwater crack detection tasks is the low quality of underwater images. Due to the influence of various disturbance fields in the underwater environment (such as flow fields and hydrodynamic fields), underwater images often exhibit significant motion blur and light diffraction effects. Additionally, the absorption and scattering of light in water result in reduced image contrast, color distortion, and detail blurring, which severely affects the performance of crack detection models [4]. Therefore, underwater image enhancement techniques have become a fundamental research direction for improving the accuracy of underwater crack detection. Traditional underwater image data enhancement algorithms, such as histogram equalization [5] and homomorphic filtering [6], are relatively simple, but have poor robustness, making them unsuitable for image enhancement tasks in high dam underwater multi-field disturbance environments. In recent years, with the rapid development of machine learning [7] and deep learning technologies [8], neural network-based image enhancement methods have made significant progress in the field of image processing [9,10]. Recent unpaired enhancement approaches (e.g., WaterGAN [11], Shallow-uwnet [12], UColor [13], PUIE-Net [14]) and datasets show that paired data are not strictly required, but these methods focus mainly on perceptual quality rather than preserving crack features for detection. Meanwhile, modern detectors such as YOLOv8–v11 demonstrate strong robustness, though pipelines that explicitly constrain edge/high-frequency cues for underwater cracks remain scarce. For example, Wang Yue et al. [15] proposed a multi-scale attention and contrast learning-based underwater image enhancement algorithm, which effectively extracts multi-level image features by combining an encoder–decoder structure with multi-scale channel pixel attention modules. The improvements achieved in PSNR and SSIM metrics were 4.4% and 2.8%, respectively, significantly improving image clarity. Additionally, Du Feiyu et al. [16] proposed a domain-adaptive underwater image enhancement method combining convolutional neural

networks with a multi-head attention mechanism and adversarial learning to achieve image enhancement under unsupervised conditions. Although these methods achieved good results in restoring visual quality, they focus more on enhancing the overall visual effect of the image rather than preserving and enhancing crack details, such as crack boundaries, which may lead to blurred crack edges or feature loss, thereby affecting subsequent crack detection accuracy. In other words, current underwater enhancement pipelines rarely optimize for crack-salient edges and high-frequency cues, leaving a gap between visually pleasing restoration and useful feature retention for detectors. Furthermore, existing underwater image enhancement models require paired images for training [17,18], but paired underwater crack images are difficult to obtain as they require the use of ROVs for image collection, making it challenging to create paired image datasets for model training.

In the field of underwater crack detection, traditional crack detection methods, such as Markov random fields [19] and Sobel operators [20], rely on edge detection algorithms in their image processing techniques. Although these methods perform well in simple scenarios, they are highly sensitive to noise and easily affected by background interference and optical artifacts in complex underwater environments, making it difficult to effectively extract crack features. In recent years, with the continuous development of object detection technologies, deep learning-based models have achieved significant progress in underwater crack detection. For instance, Shi et al. proposed a method called CrackYOLO [21], based on the YOLOv5 model, which introduces a feature fusion module, a Res2C3 feature extraction module, and a BCAtt attention mechanism, significantly improving crack detection performance. It achieved 94.3% mAP and a detection speed of 151 FPS in underwater crack detection tasks. Moreover, Mao Yingchi et al. [22] proposed a multi-task enhanced crack image detection method (ME-Faster R-CNN) based on Faster R-CNN, which improves the regional proposal network (RPN) and introduces the multi-source adaptive balancing TrAdaBoost method, effectively improving the detection capability for multiple targets and small target cracks. In experiments, it achieved an 82.52% average intersection over union (IoU) and 80.02% average precision (mAP), an improvement of 1.06% and 1.56%, respectively, compared to traditional Faster R-CNN methods. Additionally, Huang et al. [23] tackled the inherent limitations of redundant architectural components and deficient multi-scale feature extraction in the canonical YOLOv5 framework by introducing an enhanced model that synergistically integrates attention mechanisms with the Complete-IoU (CIoU) loss [24], thereby substantially elevating real-time detection accuracy. Concurrently, a refined YOLOv8-derived architecture was developed, which exhibits markedly superior robustness and detection fidelity when confronted with the severe visual degradations characteristic of the underwater domain, thereby advancing the state of the art in marine object detection [25]. These research outcomes show that deep learning-based object detection methods can effectively handle complex underwater crack detection tasks in various fields and achieve a good balance between detection speed and accuracy. However, due to the lack of underwater crack data, research on dam underwater crack detection based on object detection algorithms is relatively limited [26].

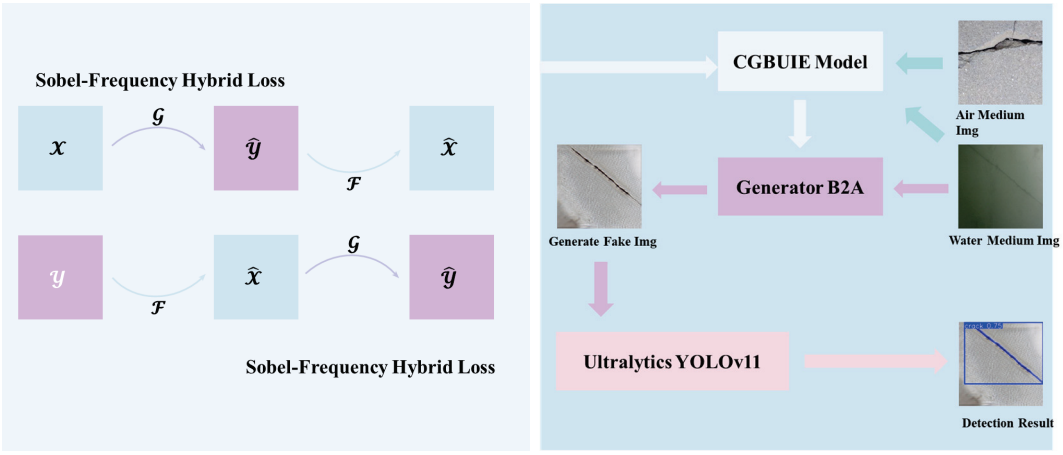
To address the deficiencies in the existing research on underwater image enhancement and crack detection, this paper proposes a dual-stage underwater crack detection method based on Cycle-GAN [27] and YOLOv11 [28] called Edge-Enhanced Underwater CrackNet (E^2UCN) in order to pay sufficient attention to crack feature details in complex underwater environments and achieve high-precision crack detection. First, during the underwater crack image collection process, we used a P200 underwater remotely operated vehicle (ROV) to capture artificial crack images in an underwater concrete tank, simulating various complex underwater scenarios, including flow field disturbances, optical diffraction, and low-contrast environments, to simulate the real environment of high dams. Next, in

the image enhancement stage, we designed a Cycle-GAN-based underwater image style transfer method named the CycleGAN-Based Underwater Image Enhancement (CGBUIE) model to improve underwater image quality and highlight crack detail features. Although hybrid GAN-based approaches such as attention-guided CycleGAN [29,30] and ESRGAN variants [31,32] have achieved impressive results in natural image enhancement, they primarily optimize for perceptual quality rather than structural crack feature preservation. In contrast, our method explicitly constrains edge and frequency information, making it more suitable for downstream crack detection tasks. Furthermore, the CGBUIE model introduces Sobel operators [33] and high-frequency transformations [34,35] in the loss function to constrain the edge information and high-frequency detail retention in the generated image, preventing crack edges from becoming blurred or details from being lost. The Sobel operator extracts prominent edge information from the image, while high-frequency transformations enhance crack texture features, enabling the enhanced image to achieve both visual style transfer to an above-water environment and crack boundary and detail retention at the feature level [36–38]. Finally, in the crack detection stage, we first trained the YOLOv11 model on an above-water concrete crack dataset so it could learn key crack features and prominent edge features, then applied the trained model to the enhanced underwater crack images generated by the CGBUIE model for accurate underwater crack detection. During the detection process, YOLOv11, with its optimized network architecture and multi-scale feature extraction capability, is able to better capture the subtle features and irregular edges of cracks, particularly in cases where the cracks are small and complex in shape [39]. Unlike existing underwater image enhancement approaches, which mostly emphasize overall image clarity, our method explicitly integrates the Sobel operator and high-frequency Fourier constraints into CycleGAN, ensuring the preservation of crack edges and the fine textures critical for subsequent detection. The enhanced underwater crack images not only significantly improved the visibility of cracks but also provided high-quality input for the model, enabling fast and accurate crack localization and classification in complex underwater environments. Experimental results showed that the proposed method performs well in terms of crack edge clarity, object localization accuracy, and adaptability to complex backgrounds.

The novelty of E^{2}UCN lies in its dual-stage architecture: (i) an enhanced CycleGAN that incorporates Sobel and Fourier constraints to explicitly preserve crack-specific features during the style transfer process, and (ii) its integration with YOLOv11 for robust crack detection. This was further substantiated by comprehensive ablation studies. The remainder of this paper is organized as follows: Section 2 describes the proposed E^{2}UCN and its edge-/texture-aware enhancement. Section 3 presents the datasets, annotation protocols, and ablation design, discusses the results, uncertainties, and analysis. Section 4 concludes with the study's contributions and limitations.

2. Proposed Method

The E^{2}UCN framework, the CGBUIE model, and the YOLOv11 model used in this study will be described in detail in this section. Specifically, the E^{2}UCN model is shown in Figure 1.



(**a**) (**b**)

Figure 1. The architecture of the proposed model: (**a**) structural diagram of E^{2}UCN; (**b**) structural diagram of CGBUIE.

2.1. CycleGAN-Based Underwater Image Enhancement Model

Based on the style transfer functionality of CycleGAN, this study combines Sobel operators and high-frequency filtering to perform style transfer between underwater crack images and above-water crack images, aiming to enhance the images. The core idea of CycleGAN is to map between different domains through unsupervised learning without paired training data. This enables its widespread application in underwater crack detection, particularly when large annotated datasets are unavailable. CycleGAN achieves this goal by introducing two generators and two discriminators. Generators are used to generate images similar to the target style, while discriminators judge the difference between the generated image and the real image, thereby guiding the generator to optimize its generation effect.

In CycleGAN (https://github.com/junyanz/CycleGAN, accessed on 9 September 2025), generator G_x maps source domain images to target domain images. Meanwhile, generator G_y maps target domain images back to the source domain. Discriminators D_x and D_y are used to distinguish generated images from real images, thus guiding the generator to optimize its style transfer effect. The aim is to minimize the difference between generated and real images while ensuring that the generated image can restore the original image after being mapped back. This process is achieved by introducing cyclic consistency loss based on the adversarial loss of the original GAN.

Adversarial loss is used to train the generator to produce realistic images, forcing the generated images to "fool" the discriminator. For generator G_x, the goal is to minimize the following loss function:

$$L_{GAN}(G_x, D_y, x, y) = \mathbb{E}_{\{y \sim p_{data}(y)\}}[\log D_y(y)] + \mathbb{E}_{\{x \sim p_{data}(x)\}}[\log(1 - D_y(G_x(x)))], \quad (1)$$

where x and y are real images from the source and target domains, $G_x(x)$ is the image generated by generator G_x, and D_y is the discriminator.

To ensure that the generated image can still restore the original image after being mapped back, CycleGAN introduces cyclic consistency loss. For generators G_x and G_y, their goals are defined as follows:

$$L_{Cycle}(G_x, D_y, x, y) = \mathbb{E}_{\{y \sim p_{data}(x)\}}[G_y(G_x(x)) - x_1] + \mathbb{E}_{\{x \sim p_{data}(y)\}}[G_x(G_y(y)) - y_1], \quad (2)$$

This loss uses the L1 norm to measure the difference between the generated image and the original image, forcing the generated image to maintain the structural features of the source image. Therefore, the total loss function of the original CycleGAN is as follows:

$$L_{CycleGAN} = L_{GAN}(G_x, D_y, x, y) + L_{GAN}(G_y, D_x, y, x) + \lambda_{cycle} L_{Cycle}(G_x, D_y, x, y), \quad (3)$$

where λ_{cycle} is the weight balancing adversarial loss and cyclic consistency loss.

However, experiments have shown that the style transfer images generated by the original CycleGAN, focusing mainly on style transfer (e.g., color, contrast of the above-water images), fail to retain the edge information and texture details of the image. To enhance the edge details of the style-transferred images, this paper introduces the E^{2}UCN model.

The Sobel operator extracts edge information from an image by computing the gradients and is effective in retaining the image's edge features. Here, based on the original CycleGAN, the basic principle of the Sobel operator is applied and further improved to construct Sobel loss. First, the Sobel operator is applied to compute the gradients of the input image, obtaining the gradients in the horizontal (x) and vertical (y) directions. Specifically, the Sobel operator used in this paper is as follows:

$$Sobel_x = \begin{bmatrix} -1 & 0 & 1 \\ -2 & 0 & 2 \\ -1 & 0 & 1 \end{bmatrix}, Sobel_y = \begin{bmatrix} -1 & -2 & -1 \\ 0 & 0 & 0 \\ 1 & 2 & 1 \end{bmatrix}, \quad (4)$$

where $Sobel_x$ and $Sobel_y$ are the convolution kernels of the Sobel filter in the x and y directions, respectively. The gradients calculated by the two operators can be represented as follows:

$$\nabla_{x,y}(i,j) = \sum_{m=0}^{2} \sum_{n=0}^{2} I(i+m, j+n) \cdot sobel_{x,y}(m,n), \quad (5)$$

where i and j represent the pixel positions in the image, and $\nabla x(\cdot)$ and $\nabla y(\cdot)$ represent the gradients in the x and y directions, respectively. Then, the gradient magnitude of the image is calculated to represent the edge information of the restored image. The specific formula is as follows:

$$\nabla(i,j) = \sqrt{\nabla_x(i,j)^2 + \nabla_y(i,j)^2 + \varepsilon}, \quad (6)$$

where ε is a small constant to avoid numerical instability when the gradient is zero.

The Sobel loss proposed in this paper measures the gradient magnitude difference between the generated image and the real image using the L1 norm, comparing the edge differences in both the x and y directions between the generated image and the original image to simulate the edge enhancement effect of the Sobel operator. The specific formula is as follows:

$$L_{sobel} = \mathbb{E}_{x \sim P_{data}(x)}[\nabla G_x(x) - \nabla x_1], \quad (7)$$

where $G_x(x)$ is the generated image, x is the real image, and $\nabla G_x(x)$ and ∇x are the gradients of the generated image and the real image, respectively.

By constructing Sobel loss, CycleGAN is forced to preserve the edge information of the real image during the image generation process, better retaining the crack edge features in the image and improving the accuracy of subsequent object detection tasks. However, while the generated image with Sobel loss retains the edge features of the cracks, there is still a significant amount of blurring and loss of the internal texture information of the cracks. Therefore, to further enhance the texture information in the image, and enable the subsequent object detection model to recognize and extract cracks from the image, this paper constructs a high-frequency loss function. Specifically, by using the Fourier transform and other high-frequency transformations, the image can be converted from the spatial

domain to the frequency domain, allowing for better extraction and retention of high-frequency information such as textures and edges. Based on this, in the CGBUIE model, a high-frequency loss function is used to compare the high-frequency information between the real image and the generated image, preserving and enhancing the texture information.

In detail, the original image x and the generated image G_x are first transformed from the spatial domain to the frequency domain using the fast Fourier transform. Assuming the discrete image signal is Ω, the specific formula is as follows:

$$\mathcal{F}(\Omega(h,w)) = \sum_{n=0}^{N-1} \Omega[n] e^{-i2\pi \frac{hwn}{N}}, \tag{8}$$

where N is the signal length, n is the time index, and k is the frequency index. After applying the fast Fourier transform, the original image and the generated image are represented as $\mathcal{F}_{real}(h,w)$ and $\mathcal{F}_{fake}(h,w)$, respectively. High-frequency components are extracted by applying a high-frequency filter to remove low-frequency parts of the frequency domain signal, and the absolute value is taken to retain the magnitude of the high-frequency components, i.e., the texture details in the original image. The specific rule is as follows:

$$H(h,w) = \begin{cases} |\mathcal{F}(\Omega(h,w))|, if\ h < cutoff\ or\ w < cutoff \\ 0,\ otherwise \end{cases}, \tag{9}$$

where h and w represent the height and width in the frequency domain, i.e., the dimensions of the frequency domain, and $cutoff$ is a manually set threshold for determining the high-frequency filtering threshold. Finally, the L1 norm loss is calculated between the original image and the generated image based on the magnitude of the high-frequency components to further enhance the texture details of the generated image. The formula is as follows:

$$L_{HF} = \mathbb{E}_{x \sim P_{data}(x)}[H(G_x(x)) - H(x)_1]. \tag{10}$$

Therefore, the overall loss function of the E^{2}UCN model proposed in this paper, called Sobel-Frequency Hybrid Loss (SFHLoss), can be expressed as follows:

$$SFHLoss = L_{GAN}(G_x, D_y, x, y) + L_{GAN}(G_y, D_x, y, x) + L_{cycle}(G_x, D_y, x, y) + L_{sobel} + L_{HF} \tag{11}$$

By adding Sobel loss and high-frequency loss, the edge and texture details of the image are effectively preserved, which helps the subsequent object detection model accurately extract the crack locations.

2.2. YOLOv11 Model

After image enhancement, images with enhanced texture details are obtained. Subsequently, this study uses the YOLOv11 (https://github.com/ultralytics/ultralytics, accessed on 9 September 2025), model for automatic underwater crack detection. YOLOv11, based on the previous generations of the YOLO model, significantly improves detection accuracy and speed through various innovations and optimizations, demonstrating excellent performance, particularly in the detection of fine targets such as cracks. The specific model architecture is shown in Figure 2.

The core structure of YOLOv11 includes the C3k2 module, the SPPF module, the C2PSA module, and a lightweight design. These innovations enable YOLOv11 to efficiently process the enhanced underwater crack images and achieve accurate crack localization and classification.

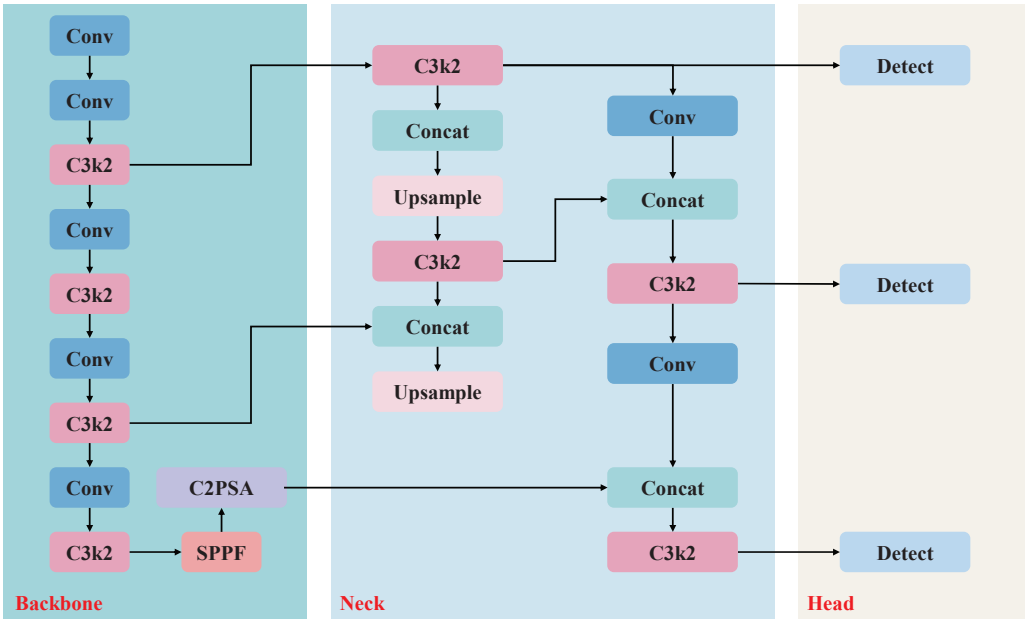


Figure 2. The architecture of YOLOv11.

First, the C3k2 module in YOLOv11 adopts an improved CSP (Cross-Stage Partial) structure, which optimizes the feature extraction process by using smaller convolution kernels (e.g., 3×3 kernels). The C3k2 module splits the input feature map into two parts, performs convolution on each part, and then merges them. This design effectively reduces the number of parameters while maintaining feature extraction capabilities. Next, the SPPF (Spatial Pyramid Pooling—Fast) module, another key component of YOLOv11, quickly merges feature maps of different scales through multi-scale pooling. This module significantly enhances the network's ability to detect targets of different sizes, which is particularly relevant as scale differences are common in crack images. By aggregating global features, the SPPF module improves the model's detection accuracy. It generates multi-level feature maps through pooling operations at different scales and ultimately merges these feature maps into a global feature representation, thus enhancing the network's sensitivity to multi-scale information in crack images.

Furthermore, the Convolutional block with the Parallel Spatial Attention (C2PSA) module introduced by YOLOv11 further optimizes the extraction of spatial features. The C2PSA module uses parallel spatial attention mechanisms to focus on key areas in the image (such as the edges of cracks or the cracks themselves), effectively improving the model's recognition ability against complex backgrounds. The C2PSA module combines both channel attention and spatial attention mechanisms, and, through multi-head attention, it further enhances the feature expression capabilities, allowing YOLOv11 to more accurately localize cracks.

To enhance the model's lightweight design, YOLOv11 introduces the MobileViT backbone network and depthwise separable convolutions (DWConv), significantly reducing the computational load and the number of parameters while maintaining high accuracy. MobileViT combines the advantages of convolutional neural networks (CNN) and Transformers, enabling efficient information encoding and fusion to capture complex features in crack images while maintaining a low computational overhead. This design makes YOLOv11 suitable for resource-constrained devices such as embedded systems and drones, meeting the demand for crack detection on edge devices.

The loss function of YOLOv11 consists of three main components: classification loss (L_{cls}), bounding box regression loss (L_{box}), and distribution focal loss (L_{dfl}). L_{cls} mainly

optimizes the prediction of object categories, L_{box} is used to optimize the prediction of object locations, and L_{dfl} optimizes the confidence of the bounding boxes.

Through this multi-task loss function optimization strategy, YOLOv11 can effectively balance accuracy and speed in crack detection tasks, particularly showing high accuracy and robustness in detecting small cracks in complex backgrounds.

3. Experimental Analysis

In this section, the data collection process and experimental setup are introduced. A series of experiments, including quantitative comparisons of image enhancement and crack detection metrics, detection result images, and ablation studies, is used to validate the effectiveness of the proposed E^{2}UCN.

3.1. Data Collection and Experimental Setup

The underwater image dataset used in this study was collected from the physical model pool at the Tangtu Experimental Base of the Nanjing Hydraulic Research Institute. The test pool dimensions are 11.0 m × 5.9 m × 4.2 m (*length* × *width* × *depth*), with a depth of 3.4 m below the ground surface and a surrounding wall height of 0.8 m, and the pool's sidewalls are reinforced with carbon-fiber fabric. The pool contains an underwater tunnel and a dam test scenario with concrete of grade C30. The underwater tunnel dimensions are 6 m × 4 m × 3.3 m (*length* × *width* × *height*), with typical defects set inside. The tunnel is 3.0 m wide and 2.08 m high, providing sufficient space for robotic operations, as shown in Figure 3.

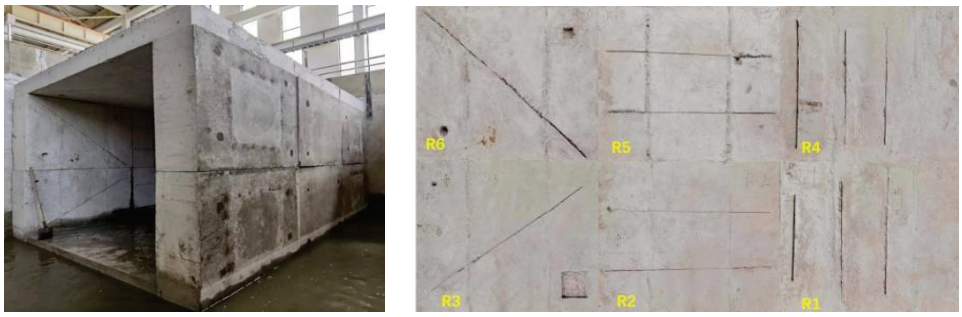


Figure 3. Schematic diagram of the construction layout of the test platform and the cracked wall. Specially, R1–R6 represent six different types of cracks with varying orientations.

During the data collection process, the mini underwater P200 robot "Qianjiao" (Manufacturer: Qianxin Innovation Technology Co., Ltd.; City: Shenzhen; Country: China) was used to capture underwater optical images. The original video data were processed into eight typical images with a size of 256 × 256 pixels, simulating various lighting and visual conditions, including normal light, low contrast, light scattering, and non-uniform lighting, as shown in Figure 4a.

The dataset used for training YOLOv11 was the Roboflow crack dataset, which was collected by researchers working on transportation and public safety. The dataset contains 4029 different static images of cracks divided into training, testing, and validation sets, each with corresponding labels. For the CycleGAN training, 10 underwater crack images and 26 above-water crack images were collected, among which 8 typical underwater images (with scattering, insufficient illumination, and blur) were selected for testing. In addition, the dataset for validation contained 11 images, covering cracks with diverse widths, depths, and orientations and several real underwater crack images. Although the number of self-collected underwater images was limited, representative cases with scattering, blurring, and color distortion were selected to ensure diversity in crack characteristics. The experiments

were conducted on a high-performance personal computer equipped with an NVIDIA RTX 3080ti 12GB GPU and an AMD5800X CPU. All models were constructed and tested using PyTorch version 1.10.0. During network training, the high-frequency filtering parameter $cutoff$ was set to 10.

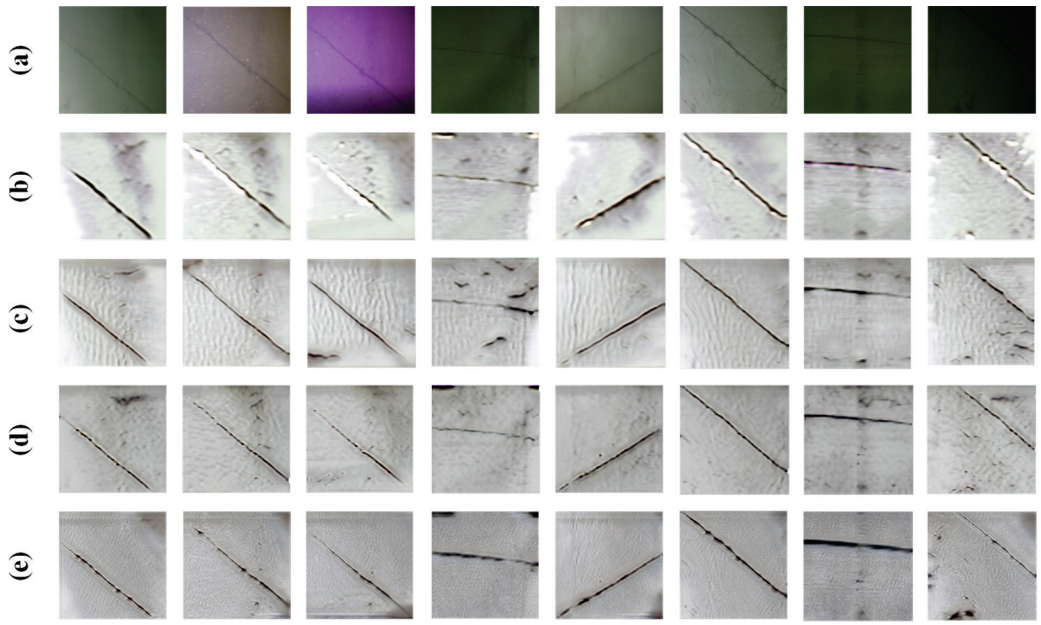


Figure 4. Image enhancement results, where (**a**) is the original image, (**b**) is the image generated using the original CycleGAN model, (**c**) is the image generated after using SobelLoss, (**d**) is the image obtained using high-frequency loss, and (**e**) is the image obtained using SobelLoss and high-frequency loss.

3.2. Experimental Results and Analysis

To validate the effectiveness of the CGBUIE model, several ablation experiments were designed [40–42]. First, the original CycleGAN was used for the style transfer of underwater images. Then, Sobel operators and high-frequency loss were added, and subjective evaluation of the resulting images compared to the designed CGBUIE model was performed. The enhanced results from different models are shown in Figure 4. The images were then input into the trained YOLOv11 model for detection. During the evaluation process, precision, recall, mAP (mean average precision), F1-score, and other metrics were recorded for each case to comprehensively evaluate the performance of YOLOv11 with different input images. Visual comparisons were also made between the original and enhanced images in terms of crack detection, analyzing the enhancement method's effect on detection accuracy and feature recognition. The specific methods and corresponding experimental results are shown in the table below.

Table 1 shows the models used for target detection, where the checked boxes represent the models used in this experiment, and the first row, with no checked boxes, represents the use of the original underwater crack images. From the experimental results, it can be seen that the image enhancement methods significantly affect the performance of YOLOv11 in underwater crack detection. Firstly, Sobel operators primarily enhance the edge information of the image, which helps YOLOv11 achieve better detection results in crack edge localization. However, although Sobel operators improve edge clarity, they may lose some texture and detail information when enhancing the edges, leading to relatively poor performance in complex textured regions. Therefore, although the recall is very high, the mAP50-95 shows a certain decline, reflecting the model's performance in broader detection areas, which may be affected, thus reducing overall detection performance.

Table 1. Ablation experiment module design and evaluation metrics.

CycleGAN	SobelLoss	HFLoss	Detection Evaluation Indicators				
			Precision	Recall	F1-Score	mAP50	mAP50-95
			0.93	0.875	0.902	0.876	0.565
√			0.994	1	0.930	0.982	0.624
√	√		0.869	1	0.996	0.991	0.548
√		√	0.993	1	0.997	0.993	0.72
√	√	√	0.995	1	0.997	0.995	0.732

Secondly, high-frequency loss focuses on enhancing the details and high-frequency information in the image, particularly the finer parts of cracks. Compared with Sobel operators, the high-frequency loss image enhancement method is better at preserving the fine texture information of cracks, thus improving detection precision and recall. However, high-frequency enhanced images may also introduce some noise, particularly in more complex backgrounds, leading to minor errors in the detection boxes. Nevertheless, the improvements in the F1-score and mAP50 indicate that high-frequency loss has a significant effect on detail restoration.

Overall, the goal of image enhancement is to improve detection performance by enhancing edge clarity and restoring details, and, when Sobel operators and high-frequency loss are combined, their advantages complement each other toward achieving that goal. In other words, Sobel operators effectively enhance edges but may lose details, while high-frequency loss restores details but may introduce noise. Therefore, using both methods together maximizes the retention of crack feature information in the enhanced underwater images, effectively improving YOLOv11's overall performance in crack detection, particularly for small cracks and complex backgrounds, with precision, recall, and F1-scores reaching near-perfect levels.

The changes in the loss function and performance metrics during YOLOv11 training are shown in Figure 5, with the ground truth illustrated in line (a). The detection results after applying different enhancement models are shown in Figure 6.

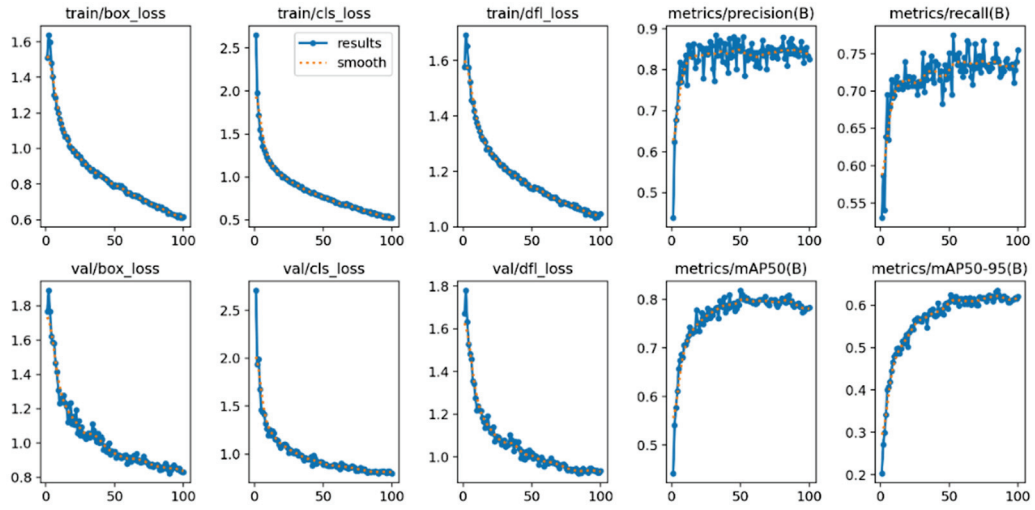


Figure 5. Loss function curve and performance index variation curve after training YOLOv11 on the Crack-Seg dataset.

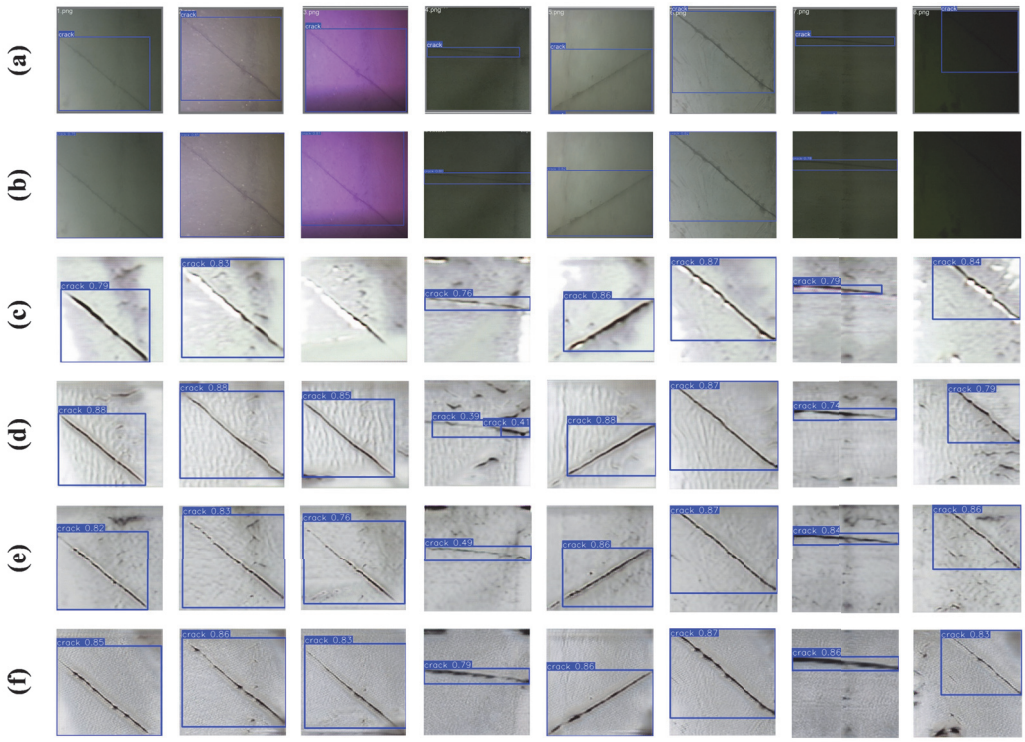


Figure 6. Target detection results, where (**a**) is the ground truth, (**b**) is the original image detection results, (**c**) is the images generated by the original CycleGAN model detection results, (**d**) is the images generated by SobelLoss detection results, (**e**) is the images generated by high-frequency loss detection results, and (**f**) is the images generated by SobelLoss and high-frequency loss detection results.

It can be observed that YOLOv11 exhibits some deficiencies in the original images (Figure 6b), particularly when the crack details are blurry or the background is complex. In these cases, the detection confidence is generally lower, and crack localization accuracy is affected. Specifically, the original image, due to its blurry details and low contrast, poses challenges for YOLOv11 in accurately detecting cracks.

With the application of the original CycleGAN model for style transfer (Figure 6c), the detection results of YOLOv11 showed significant improvement. CycleGAN enhanced the overall image clarity, particularly improving the representation of edges and textures, which effectively increased the model's crack localization accuracy. The enhanced image's improved details and contrast allowed YOLOv11 to more accurately identify cracks, with a significant increase in detection confidence, reflecting the positive impact of image enhancement on detection results.

After further introducing SobelLoss (Figure 6d), YOLOv11's crack detection performance improved further. The Sobel operator enhanced the image's edge details, significantly improving the clarity of the crack contours, and the model's precision in crack localization was improved. However, despite the positive effect of Sobel on edge enhancement, its ability to preserve image texture information is relatively weak, which may lead to the loss of details in small cracks, affecting detection accuracy. Some false positives and missed detections were still observed, suggesting that, while edge enhancement is beneficial, detail restoration remains a challenge for the model.

When high-frequency loss is applied for image enhancement (Figure 6e), focusing on the high-frequency components of the image, the fine details and subtle features of the cracks are more effectively restored, improving YOLOv11's ability to recognize small cracks. The enhanced image made crack detection more precise, and confidence increased, particularly for low-contrast and complex backgrounds, where the model demonstrated

stronger robustness. However, excessive high-frequency enhancement could introduce background noise, causing instability in some areas of the detection results, highlighting the sensitivity of the enhancement method to background interference.

Finally, the combination of SobelLoss and high-frequency loss (Figure 6f) demonstrated the best crack detection performance. This combination not only strengthened the edge details of the image but also effectively restored more texture information, making crack localization more precise, and the image details richer. YOLOv11 performed at its best with these enhanced images, with its overall detection precision and recall being significantly improved. By integrating both edge enhancement and detail restoration, the model's adaptability to complex environments was significantly improved, and detection confidence was generally higher, further validating the superiority of combining SobelLoss and high-frequency loss for enhancing image detail restoration and model robustness.

In addition to YOLOv11, we conducted comparative experiments with YOLOv5 and YOLOv8 to provide a broader reference for detection performance. As summarized in Table 2 and Figure 7, all three models benefited from the proposed image enhancement strategy. YOLOv5 achieved a precision of 0.91 and a recall of 1.0, resulting in an F1-score of 0.953, with mAP@0.5 = 0.876 and mAP@0.5:0.95 = 0.752. YOLOv8 exhibited higher overall precision and recall (1.0 and 0.995, respectively), yielding an F1-score of 0.997, and the highest mAP@0.5 value of 0.995, although its performance at stricter IoU thresholds (mAP@0.5:0.95 = 0.685) was comparatively lower. YOLOv11 attained balanced and robust performance, with precision = 0.995, recall = 1.0, F1-score = 0.998, and mAP@0.5 = 0.995, while maintaining a competitive mAP@0.5:0.95 of 0.732.

Table 2. Comparative experiments and corresponding evaluation metrics. The highest score of each evaluation metric is highlighted in bold.

Model Name	Detection Evaluation Indicators				
	Precision	**Recall**	**F1-Score**	**mAP50**	**mAP50-95**
YOLOv5	0.91	**1**	0.953	0.876	**0.752**
YOLOv8	**1**	0.995	0.997	0.995	0.685
YOLOv11	0.995	**1**	**0.998**	**0.995**	0.732

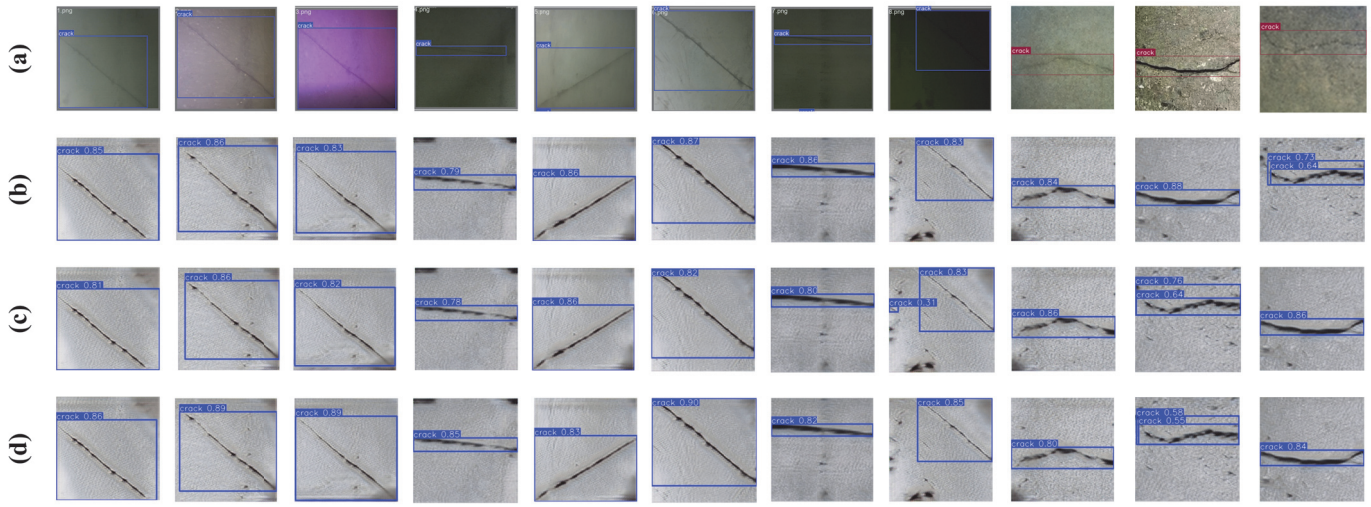


Figure 7. Target detection results, where (**a**) is the ground truth, (**b**) is the YOLOv11 results, (**c**) is the YOLOv5 results, and (**d**) is the YOLOv8 results.

These results show that, although YOLOv8 achieved the highest detection accuracy under lenient IoU criteria, YOLOv11 demonstrated superior robustness in handling small and irregular crack patterns, reflected in its higher F1-score and improved performance at

more stringent IoU thresholds compared to YOLOv8. Therefore, YOLOv11 was selected as the primary detection model in this study. More comprehensive comparisons with other detectors, such as Faster R-CNN and Transformer-based architectures, will be explored in future work to further validate the generality of the proposed approach.

4. Conclusions

This study combines the advantages of image style transfer, detail restoration, and edge enhancement, fully leveraging the complementary effects of Sobel operators and high-frequency filtering. A CycleGAN-based underwater image enhancement method (the CGBUIE model) was proposed, which effectively improves the edge and detail information of the generated images by introducing Sobel operators and high-frequency filtering as loss functions. Specifically, by training on underwater crack images and above-water crack images, the style transfer of underwater images to above-water image styles was achieved, enhancing image visibility and detail expression while improving the robustness of the crack detection model. On this basis, YOLOv11 was used to train the model on the Crack-Seg dataset, constructing a detection model capable of effectively recognizing cracks. The experimental results show that the enhanced underwater crack images significantly improved YOLOv11's detection performance, detection confidence, and accuracy with complex backgrounds and in low-contrast conditions. Specifically, on a real underwater validation set, E^2UCN achieved precision = 0.995, F1 = 0.99762, mAP@0.5 = 0.995, and mAP@0.5:0.95 = 0.736.

In summary, the primary contribution of this work lies in the integration of Sobel operators and high-frequency Fourier constraints into the CycleGAN framework, which ensures the preservation of critical crack-related details during the enhancement process. Together with YOLOv11, this creates a powerful and reliable system for underwater crack detection in challenging environments.

However, this study has certain limitations. The underwater dataset used is relatively small, with only three real underwater images supplementing the dataset. This limited dataset size restricts the diversity and robustness of the model, which may affect its performance in more varied scenarios. Future research should focus on expanding this dataset to increase its diversity and improve the model's generalization capabilities.

Author Contributions: Methodology, X.W. and J.S.; software, W.Z. and X.W.; validation, W.Z.; investigation, X.W. and W.Z.; resources, X.W. and G.S.; writing—original draft preparation, W.Z.; writing—review and editing, X.W. All authors have read and agreed to the published version of the manuscript.

Funding: This work was funded by the the National Key R&D Program of China under Grant (No. 2022YFC3005401), the National Natural Science Foundation of China under Grant (No. 52309159), the National Natural Science Foundation of China—Joint Fund under Grant (No. U23B20150), the Jiangsu Province Youth Science and Technology Talent Support Program under Grant (No. JSTJ-2024-082), the Scientific Research Fund of Nanjing Hydraulic Research Institute under Grant (No. Y724001), the Technology Talent and Platform Program of Yunnan Province under Grant (No. 202405AK340002),and the Science and Technology Projects of China Huaneng Group under Grant HNKJ20-H46.

Institutional Review Board Statement: Not applicable.

Informed Consent Statement: Not applicable.

Data Availability Statement: The data presented in this study are available from the author on request.

Acknowledgments: This paper is an extension of a conference paper. Edge Enhanced Underwater CrackNet for Dam Underwater Crack Detection. In Proceedings of the International Symposium "Common Challenges, Shared Future, Better Dams" ICOLD-CIGB 2025, Chengdu, China, 16–23 May 2025 [43].

Conflicts of Interest: Author X.W. was employed by the company NHRI R&D Tech Group Co., Ltd. The remaining authors declare that the re-search was con-ducted in the absence of any commercial or financial relationships that could be construed as a potential conflict of interest.

References

1. Gong, X.N.; Zhang, C.S.; Jia, J.S. *Dam Danger Assessment and Risk Reinforcement Technology*; China Construction Industry Press: Beijing, China, 2021. (In Chinese)
2. Xiang, Y.; Wang, Y.; Chen, Z.; Dai, B.; Chen, S.; Shen, G. Underwater defect detection and diagnosis assessment for high dams: Current status and challenges. *Adv. Water Sci.* **2024**, *35*, 153–164.
3. Raveendran, S.; Patil, M.D.; Birajdar, G.K. Underwater image enhancement: A comprehensive review, recent trends, challenges and applications. *Artif. Intell. Rev.* **2021**, *54*, 5413–5467. [CrossRef]
4. Akkaynak, D.; Treibitz, T. Sea-thru: A Method for Removing Water from Underwater Images. In Proceedings of the IEEE/CVF Conference on Computer Vision and Pattern Recognition (CVPR), Long Beach, CA, USA, 15–20 June 2019; pp. 1682–1691.
5. Pizer, S.M.; Amburn, E.P.; Austin, J.D.; Cromartie, R.; Geselowitz, A.; Greer, T.; ter Haar Romeny, B.; Zimmerman, J.B.; Zuiderveld, K. Adaptive histogram equalization and its variations. *Comput. Vis. Graph. Image Process.* **1987**, *39*, 355–368. [CrossRef]
6. Chen, L.; Liang, X.; Peng, Q.; Liu, W. Adaptive homomorphic filtering algorithm for low illumination image enhancement. *Comput. Sci. Appl.* **2023**, *13*, 450–457. (In Chinese) [CrossRef]
7. Li, C.; Zhang, W.; Zhang, Y.; Chen, Z. Adaptively Dictionary Construction for Hyperspectral Target Detection. *IEEE Geosci. Remote Sens. Lett.* **2023**, *20*, 5502005. [CrossRef]
8. Wang, Y.; Xiang, Y.; Dai, B.; Li, J. Dam early warning model based on structural anomaly identification and dynamic effect variables selection. *Structures* **2025**, *74*, 108507. [CrossRef]
9. Habib, A.; Yildirim, U. Distribution of strong input energy in base-isolated structures with complex nonlinearity: A parametric assessment. *Multidiscip. Model. Mater. Struct.* **2023**, *19*, 324–340. [CrossRef]
10. Habib, A.; Barakat, S.; Al-Toubat, S.; Junaid, M.T.; Maalej, M. Developing machine learning models for identifying the failure potential of fire-exposed FRP-strengthened concrete beams. *Arab. J. Sci. Eng.* **2025**, *50*, 8475–8490. [CrossRef]
11. Li, J.; Skinner, K.A.; Eustice, R.M.; Johnson-Roberson, M. WaterGAN: Unsupervised generative network to enable real-time color correction of monocular underwater images. *IEEE Robot. Autom. Lett.* **2017**, *3*, 387–394. [CrossRef]
12. Naik, A.; Swarnakar, A.; Mittal, K. Shallow-uwnet: Compressed model for underwater image enhancement (student abstract). In Proceedings of the AAAI Conference on Artificial Intelligence, Online, 2–9 February 2021; Volume 35, pp. 15853–15854.
13. Lin, P.; Wang, Y.; Li, Y.; Fan, Z.; Fu, X. Underwater color correction network with knowledge transfer. *IEEE Trans. Multimed.* **2024**, *26*, 8088–8103. [CrossRef]
14. Fu, Z.; Wang, W.; Huang, Y.; Ding, X.; Ma, K. Uncertainty inspired underwater image enhancement. In *Computer Vision—ECCV 2022, 17th European Conference, Tel Aviv, Israel, 23–27 October 2022*; Springer Nature: Cham, Switzerland, 2022; pp. 465–482.
15. Wang, Y.; Fan, H.; Liu, S.; Tang, Y. Underwater Image Enhancement Based on Multi-scale Attention and Contrastive Learning. *Laser Optoelectron. Prog.* **2024**, *61*, 0437008. (In Chinese)
16. Du, F.; Wang, H.; Yao, H.; Chen, X. Domain-Adaptive Underwater Image Enhancement Algorithm. *Comput. Mod.* **2024**, 55–60. (In Chinese) [CrossRef]
17. Li, J.; Skinner, K.; Eustice, R.M.; Johnson-Roberson, M. WaterGAN: Unsupervised Generative Network to Enable Real-time Color Correction of Monocular Underwater Images. *arXiv* **2017**, arXiv:1702.07392. [CrossRef]
18. Islam, M.J.; Xia, Y.; Sattar, J. Fast underwater image enhancement for improved visual perception. *IEEE Robot. Autom. Lett.* **2020**, *5*, 3227–3234. [CrossRef]
19. Hambon, J. Electronical imaging of structural concrete: Investigation by Bayesian stationary wavelet field. *Electron. Imaging* **2009**, *9*, 764–773.
20. Gao, Y.; Wang, Y.; Zhou, D. The Image Recognition, Automatic Measurement and Seam Tracking Technology in Arc Welding Process. In Proceedings of the 2010 8th World Congress on Intelligent Control and Automation, Jinan, China, 7–9 July 2010; pp. 2327–2332.
21. Shi, P.; Shao, S.; Fan, X.; Xin, Y.; Zhou, Z.; Cao, P.; Li, X.; Zhu, S. CrackYOLO: Towards efficient dam crack detection for underwater scenes. *Pattern Anal. Appl.* **2024**, *27*, 105. (In Chinese) [CrossRef]
22. Mao, Y.; Ping, P.; Chen, J.; Chen, H. Crack Detection with Multi-task Enhanced Faster R-CNN Model. In Proceedings of the IEEE International Conference on Image Processing, Online, 25–28 October 2020; pp. 1234–1238.

23. Huang, B.; Kang, F.; Tang, Y. Real-Time Crack Detection Method for Concrete Dams Based on Object Detection. *J. Tsinghua Univ. (Sci. Ed.)* **2023**, *63*, 1078–1086. [CrossRef]
24. Zheng, Z.; Wang, P.; Liu, W.; Li, J.; Ye, R.; Ren, D. Distance-IoU Loss: Faster and Better Learning for Bounding Box Regression. In Proceedings of the the AAAI Conference on Artificial Intelligence, New York, NY, USA, 7–12 February 2020; pp. 12993–13000.
25. Huang, J.; Fang, C.; Zheng, X.; Liu, J. YOLOv8-UC: An Improved YOLOv8-Based Underwater Object Detection Algorithm. *IEEE Access* **2024**, *12*, 172186–172195. [CrossRef]
26. Liu, C.; Li, H.; Wang, S.; Zhu, M.; Wang, D.; Fan, X.; Wang, Z. A dataset and benchmark of underwater object detection for robot picking. In Proceedings of the 2021 IEEE International Conference on Multimedia & Expo Workshops (ICMEW), Shenzhen, China, 5–9 July 2021; IEEE: Piscataway, NJ, USA, 2021; pp. 1–6.
27. Zhu, J.-Y.; Park, T.; Isola, P.; Efros, A.A. Unpaired Image-to-Image Translation using Cycle-Consistent Adversarial Networks. In Proceedings of the 2017 IEEE International Conference on Computer Vision (ICCV), Venice, Italy, 22–29 October 2017; pp. 2242–2251.
28. Zhang, Y.; Wu, K.; Fang, K. Comprehensive Performance Evaluation of YOLOv11: Advancements, Benchmarks, and Real-World Applications. *arXiv* **2024**, arXiv:2411.18871.
29. Tang, H.; Liu, H.; Xu, D.; Torr, P.H.S.; Sebe, N. AttentionGAN: Unpaired Image-to-Image Translation Using Attention-Guided Generative Adversarial Networks. *IEEE Trans. Neural Netw. Learn. Syst.* **2023**, *34*, 1972–1987. [CrossRef]
30. Hou, M.; He, X.; Dou, F.; Zhang, X.; Guo, Z.; Feng, Z. Semi—Supervised image super-resolution with attention CycleGAN. *IET Image Process.* **2022**, *16*, 1181–1193. [CrossRef]
31. Wang, X.; Yu, K.; Wu, S.; Gu, J.; Liu, Y.; Dong, C.; Qiao, Y.; Change Loy, C. Esrgan: Enhanced super-resolution generative adversarial networks. In Proceedings of the European Conference on Computer Vision (ECCV) Workshops, Munich, Germany, 8–14 September 2018.
32. Wei, Z.; Huang, Y.; Chen, Y.; Zheng, C.; Gao, J. A-ESRGAN: Training real-world blind super-resolution with attention U-Net Discriminators. In *PRICAI 2023: Trends in Artificial Intelligence, 20th Pacific Rim International Conference on Artificial Intelligence, PRICAI 2023, Jakarta, Indonesia, 15–19 November 2023*; Springer Nature: Singapore, 2023; pp. 16–27.
33. Kanopoulos, N.; Vasanthavada, N.; Baker, R.L. Design of an image edge detection filter using the Sobel operator. *IEEE J. Solid-State Circuits* **1988**, *23*, 358–367. [CrossRef]
34. Cooley, J.W.; Tukey, J.W. An algorithm for the machine calculation of complex Fourier series. *Math. Comput.* **1965**, *19*, 297–301. [CrossRef]
35. Gonzalez, R.C.; Woods, R.E. *Digital Image Processing*, 3rd ed.; Pearson: London, UK, 2008.
36. Jiang, L.; Dai, B.; Wu, W.; Loy, C.C. Focal Frequency Loss for Image Reconstruction and Synthesis. In Proceedings of the 2021 Conference on Neural Information Processing Systems, Online, 6–14 December 2021.
37. Kim, M.W.; Cho, N.I. Wavelet-Domain High-Frequency Loss for Perceptual Quality. In Proceedings of the 2023 IEEE/CVF Winter Conference on Applications of Computer Vision (WACV), Waikoloa, HI, USA, 2–7 January 2023.
38. Wu, J.; Zhang, G.; Fan, Y. LM-CycleGAN: Improving Underwater Image Quality Through Learned Perceptual Image Patch Similarity and Multi-Scale Adaptive Fusion Attention. *Sensors* **2024**, *24*, 7425. [CrossRef] [PubMed]
39. Chen, D.; Kang, F.; Li, J.; Zhu, S.; Liang, X. Enhancement of underwater dam crack images using a multi-feature CycleGAN. *Autom. Constr.* **2024**, *167*, 105727. [CrossRef]
40. Powers, D.M.W. Evaluation: From Precision, Recall and F-Measure to ROC, Informedness, Markedness and Correlation. *J. Mach. Learn. Technol.* **2011**, *2*, 37–63.
41. Everingham, M.; Van Gool, L.; Williams, C.K.I.; Winn, J.; Zisserman, A. The PASCAL Visual Object Classes (VOC) Challenge. *Int. J. Comput. Vis.* **2010**, *88*, 303–338. [CrossRef]
42. Yacouby, R.; Axman, D. Probabilistic extension of precision, recall, and f1 score for more thorough evaluation of classification models. In Proceedings of the First Workshop on Evaluation and Comparison of NLP Systems, Online, November 2020; pp. 79–91. Available online: https://aclanthology.org/2020.eval4nlp-1.9/ (accessed on 9 September 2025).
43. Zhang, W.; Wu, X.; Xiang, Y. Edge enhanced underwater CrackNet for dam underwater crack detection. In Proceedings of the International Symposium "Common Challenges, Shared Future, Better Dams," ICOLD-CIGB 2025, Chengdu, China, 16–23 May 2025; International Commission on Large Dams: Paris, France, 2025.

Disclaimer/Publisher's Note: The statements, opinions and data contained in all publications are solely those of the individual author(s) and contributor(s) and not of MDPI and/or the editor(s). MDPI and/or the editor(s) disclaim responsibility for any injury to people or property resulting from any ideas, methods, instructions or products referred to in the content.

applied sciences

MDPI

Article

MambaUSR: Mamba and Frequency Interaction Network for Underwater Image Super-Resolution

Guangze Shen [1,†], Jingxuan Zhang [1,†] and Zhe Chen [2,*]

[1] Nanjing Hydraulic Research Institute, Nanjing 210029, China; gzshen@nhri.cn (G.S.); jxzhang@nhri.cn (J.Z.)
[2] College of Information Science and Engineering, Hohai University, Changzhou 213200, China
* Correspondence: chenzhe@hhu.edu.cn
† These authors contributed equally to this work.

Abstract: In recent years, underwater image super-resolution (SR) reconstruction has increasingly become a core focus of underwater machine vision. Light scattering and refraction in underwater environments result in images with blurred details, low contrast, color distortions, and multiple visual artifacts. Despite the promising results achieved by deep learning in underwater SR tasks, global and frequency-domain information remain poorly addressed. In this study, we introduce a novel underwater SR method based on the Vision State-Space Model, dubbed MambaUSR. At its core, we design the Frequency State-Space Module (FSSM), which integrates two complementary components: the Visual State-Space Module (VSSM) and the Frequency-Assisted Enhancement Module (FAEM). The VSSM models long-range dependencies to enhance global structural consistency and contrast, while the FAEM employs Fast Fourier Transform combined with channel attention to extract high-frequency details, thereby improving the fidelity and naturalness of reconstructed images. Comprehensive evaluations on benchmark datasets confirm that MambaUSR delivers superior performance in underwater image reconstruction.

Keywords: underwaterimage super-resolution; MambaUSR; vision state-space model; underwater image reconstruction

1. Introduction

Underwater images are frequently degraded by color distortion, low contrast, and blurred details, primarily due to the complex optical phenomena of light refraction, absorption, and scattering in aquatic environments. These degradations lead to poor visual quality, which can significantly compromise the performance of underwater robots in tasks such as object recognition, route navigation, and environmental observation. To address this issue, underwater image super-resolution (SR) reconstruction aims to generate an underwater high-resolution (HR) image from its degraded underwater low-resolution (LR) version. SR technology achieves better visual results by effectively recovering fine-grained details and high-frequency components.

Recent advancements in deep learning have fostered a wide spectrum of SR methodologies, encompassing convolutional neural networks (CNNs) [1,2], Transformers [3,4], State-Space Model (SSMs) [5,6], and Fast Fourier Transform (FFT) [7,8], all aimed at improving the performance of underwater image SR. For instance, Islam et al. [9] introduced a convolutional neural network named SRDRM tailored for underwater SR and further extended it into SRDRM-GAN by incorporating a Markovian PatchGAN as the discriminator. To facilitate more effective training of these models, they also released a large-scale dataset, called USR-248. Subsequently, Islam et al. [10] presented a deep simultaneous

enhancement and super-resolution (Deep SESR) framework, an end-to-end framework that simultaneously conducts enhancement and SR, evaluated on the UFO-120 dataset. AM-PCNet [11] established interconnections between residual and dilated modules, enabling effective merging of heterogeneous feature information. In a similar vein, MSIDN [12] was proposed to balance underwater SR accuracy with deployment efficiency in real-world applications. Yang et al. [13] developed a lightweight encoder-decoder architecture, termed LAFFNet, which integrates multiple adaptive feature fusion modules to enhance underwater image quality. Sharma et al. [14] presented Deep WaveNet, a deep CNN designed with a wavelength-guided multi-contextual architecture to address SR tasks effectively. Although CNN-based approaches have achieved notable success in underwater image restoration, their dependence on local receptive fields constrains the modeling of global context, making them less effective in addressing complex illumination variations. In contrast, recent studies have explored Transformer-based architectures, which exhibit strong potential in underwater applications by capturing long-range dependencies through multi-head self-attention. For example, Peng et al. [15] proposed a Transformer framework with a U-shaped design, aimed at strengthening the model's capacity to selectively emphasize severely attenuated color channels and spatially degraded regions. UIR-Net [16] was a concise yet efficient approach tailored to restore clear underwater images from inputs affected by substantial particulate matter and marine light interference. URSCT [17] was developed to perform joint enhancement and SR, demonstrating the superior capacity to model global context in nonhomogeneous underwater media. Despite their strengths, Transformer-based methods are challenged by the quadratic cost of self-attention as the number of patches increases, significantly limiting their scalability for underwater tasks. Figure 1 presents a local attribution map (LAM) [18] for different methods. The red regions in the CNN-based SRDRM [9] exhibit limitations, while the Mamba-based approach achieves higher DI values. This phenomenon is crucial for underwater SR tasks, as it requires both focus on critical regions and broader global modeling capabilities.

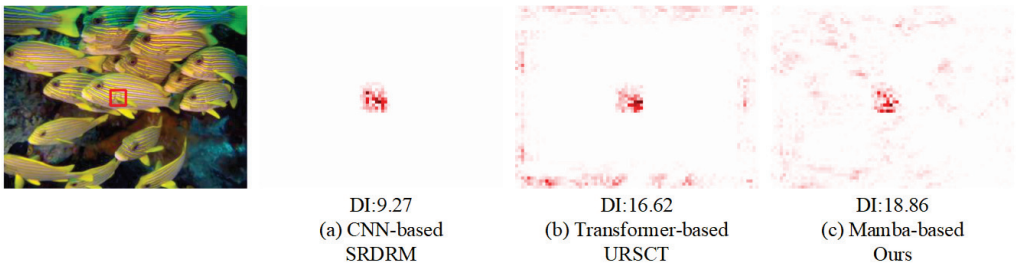


Figure 1. Comparison of LAM for (**a**) SRDRM, (**b**) URSCT, and (**c**) our MambaUSR. Our MambaUSR harvests the highest DI, maintaining local focus while modeling global dependencies.

SSM [19] has recently gained attention as a compelling alternative for capturing long-range dependencies, offering both theoretical rigor and computational. Gu and Dao [20] introduced Mamba, a foundational architecture that incorporates a selection mechanism into SSM, enabling adaptive information retention or suppression based on token-wise context along the sequence or scan path. Guan et al. [21] introduced WaterMamba, a novel method built upon SSM with linear computational complexity. This approach effectively captures pixel-wise information propagation across four spatial directions and channel-wise interactions, thereby overcoming limitations associated with pixel and channel dependency modeling. Liu et al. [22] introduced an SSM-based vision backbone network called VMamba that converts image patches into sequential representations along horizontal and vertical axes, enabling bidirectional scanning to capture structured spatial dependencies in both directions. An innovative O-shaped dual-branch network, termed

O-Mamba [23], was proposed to strengthen spatial—channel interaction and effectively exploit multi-scale features for improved representation learning. Beyond spatial modeling, frequency-domain information has recently gained attention for its ability to complement spatial features and capture global structures more effectively. Yao et al. [24] shifted their focus to the Fourier domain by integrating frequency-domain information with spatial features for the enhancement of remote sensing low-light images. Wang et al. [25] developed a spatial—frequency mutual network for face SR, leveraging information from both domains to improve reconstruction fidelity. A novel SR approach named multi-scale FFT-based attention network (MSFFTAN) [26], introduced an FFT-based residual block that integrates both image-domain and Fourier-domain branches, allowing concurrent extraction of fine-grained details and global structural information.

The above analysis suggests that existing methods have achieved notable progress in addressing SR problems. However, several key challenges remain to be explored. On the one hand, with comparable parameter counts and computational complexity, Mamba-based approaches generally achieve superior performance over the more sophisticated CNN, Transformer, and hybrid models. On the other hand, the effective integration of frequency-domain information with spatial features for underwater image SR remains an open problem. Developing efficient models that can fully leverage this complementary information across domains is, therefore, a critical direction for future research.

To alleviate the above disadvantages, we first try to apply Mamba to underwater SR and propose a novel method, dubbed MambaUSR. Specifically, we present a Frequency State-space Module (FSSM) that is composed mainly of a VSSM and a frequency-assisted enhancement module (FAEM). VSSM can effectively enhance long-range dependency modeling to enhance global contrast in underwater images. In FAEM, the FFT decomposes the features into phase and amplitude components, while channel attention highlights important information, thereby enhancing the high-frequency details of underwater images. Experimental results reveal that our MambaUSR attains comparable performance to prevailing underwater SR methods with fewer computational resources.

In short, our main contribution is reflected in three aspects:

- We present the first application of SSM to underwater SR, showcasing the potential of Mamba for efficient and effective global modeling in underwater image processing.
- We propose a frequency state-space module (FSSM) that explores long-term dependencies to resolve detail blurring and low contrast in underwater images.
- We devise a frequency-assisted enhancement module (FAEM) that integrates FFT with CA to efficiently extract high-frequency features, resulting in a more natural reconstructed image.

The remainder of this paper is organized as follows. Section 2 reviews the related work on underwater image SR and frequency-domain modeling. Section 3 details the proposed MambaUSR framework and its core components. Section 4 presents the experimental setup, ablation analyses, and quantitative as well as qualitative results. Section 5 concludes the paper.

2. Related Work

2.1. Underwater Image SR

Deep learning has substantially improved underwater image SR by enabling the extraction of rich and complex features from large-scale datasets. SRDRM [9] was a generative model based on deep residual networks for underwater SR, capable of effectively recovering the global contrast and texture of images. Building upon this, a residual-in-residual generative architecture was introduced in Deep SESR [10] to boost perceptual quality, focusing on the preservation of fine structural details and the enhancement of overall visual

realism. In PAL [27], the authors incorporated a CNN with channel-wise attention that guided the network to focus on the most salient areas. To address image degradation in nonhomogeneous media, Wang et al. [28] presented a DIMN incorporating spatial-aware attention blocks and multi-scale Transformer blocks to direct inductive bias, thereby better adapting to spatially varying degradation patterns. Pramanick et al. [29] proposed LitNet, a lightweight multi-stage network for multi-resolution image analysis. It employs a multi-resolution attention network and a multi-scale attention network to capture varying receptive fields and obtain rich feature representations. In addition to CNN-based models, Transformer architectures have also been introduced to address underwater restoration challenges. Dharejo et al. [30] employed the Swin Transformer, incorporating wavelet blocks to mitigate information loss caused by irreversible downsampling. Ren et al. [17] integrated Swin Transformer with U-Net architecture to enhance global dependency capture capabilities. More recently, Mamba-based models have demonstrated the ability to achieve efficient global modeling with reduced computational complexity. In the realm of underwater image enhancement, Guan et al. [21] put forward the WaterMamba algorithm, which effectively models and leverages multi-scale image features through spatial—channel omnidirectional selective scanning blocks. Chang et al. [31] presented a mamba-enhanced spectral-attentive wavelet network, which achieves complementary learning between the spatial and frequency domains, thereby yielding superior image restoration results. The potential of Mamba in underwater SR tasks has not yet been fully explored, to our knowledge. Unlike WaterMamba, which focuses on underwater image enhancement without explicit high-frequency reconstruction, and spectral-attentive wavelet networks, which rely on Transformer-based spectral attention for spatial—frequency coupling, the proposed MambaUSR integrates vision state-space modeling and frequency-assisted enhancement in a unified, linear-complexity framework specifically tailored for underwater SR. Compared to natural images, underwater images suffer from significant detail loss, reduced contrast, and color distortion, posing greater challenges for deep learning models in achieving high-quality reconstruction.

2.2. Fourier Transform

FFT serves as a global analysis technique that effectively captures long-term dependencies by representing signals in the frequency domain [32]. With this in mind, numerous computer vision tasks leverage FFT for frequency-domain modeling. Shao et al. [33] replaced traditional self-attention in Vision Transformers with FFT-based operations, effectively capturing both high- and low-frequency components and achieving linear computational complexity. Wang et al. [25] used FFT to implement an image-size receptive field, thus better capturing global face structure. Huang et al. [34] put forth a deep exposure correction model operating in the Fourier domain, where amplitude and phase are independently learned via dedicated branches to recover brightness and structure in low-quality images. Zhang et al. [35] utilized FFT to obtain frequency-domain information and collaborated with spatial domain information, preserving underwater image details and reducing noise. Inspired by these studies, we combine the global context capture capability of the Mamba framework with the frequency-domain representation of FFT, enabling complementary spatial—frequency information and improving the quality of underwater image reconstruction.

3. Proposed Method

3.1. Overall Network Architecture

Our proposed MambaUSR involves three stages, as shown in Figure 2. Stage 1 performs a 3 × 3 to abstract initial features. Stage 2 is the core part of our MambaUSR,

constituted by T FrequencyState-Space Groups (FSSG) for capturing high-level information features. Each FSSG is composed of G Frequency State-Space Modules (FSSMs) followed by a 3 × 3 convolution. Stage 3 assembles shallow and deep features to yield high-quality SR outputs. Given a degraded input image $I^{LR} \in \mathbb{R}^{H\times W\times 3}$, we can obtain an HR image $I^{SR} \in \mathbb{R}^{rH\times rW\times 3}$ after MambaUSR processing, where r denotes the scale factor.

$$F^0 = \mathrm{Conv}_{3\times 3}(I^{\mathrm{LR}}) \tag{1}$$

$$F^t = H^t_{\mathrm{MIEM}}(F^{t-1}) = H^t_{\mathrm{MIEM}}(H^{t-1}_{\mathrm{MIEM}}(\cdots H^1_{\mathrm{MIEM}}(F^0))) \tag{2}$$

$$I^{\mathrm{SR}} = H_{\mathrm{HU}}(F^T) + H_{\mathrm{LU}}(I^{\mathrm{LR}}) \tag{3}$$

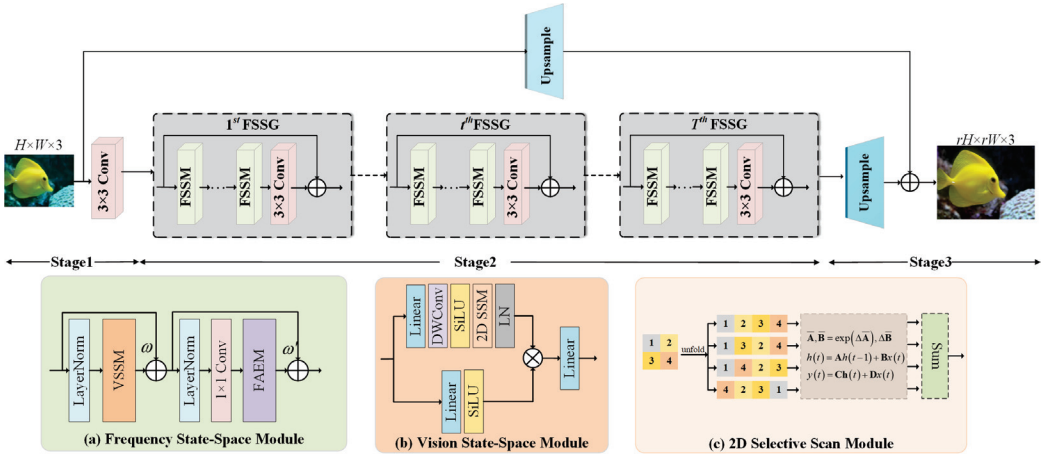


Figure 2. Overall pipeline of our proposed MambaUSR that mainly consists of T FSSGs. (**a**) Frequency State-Space Module (FSSM), (**b**) Vision State-Space Module (VSSM), (**c**) 2D Selective Scan Module (SSM).

$H_{HU}(\cdot)$ and $H_{LU}(\cdot)$ correspond to the upsampling operations of the deep features and the input LR image, respectively. Specifically, $H_{HU}(\cdot)$ integrates a 3 × 3 convolutional layer and sub-pixel convolutional layer, $H_{LU}(\cdot)$ integrates a 5 × 5 convolutional layer and a sub-pixel convolutional layer.

We optimize MambaUSR using L_1 loss. Given a training dataset $\{I^{LR}_n, I^{HR}_n\}^N_{n=1}$, where I^{HR} denotes ground truth images. The loss calculation formula is:

$$\mathcal{L}(\Theta) = \frac{1}{N}\sum_{n=1}^{N} \parallel I^{HR}_n - \mathrm{MambaUSR}(I^{LR}_n) \parallel_1 \tag{4}$$

where Θ refers to the trainable parameters of MambaUSR, and n is number of training samples (e.g., N = 1060 for USR-248 dataset and N = 1500 for UFO-120 dataset).

3.2. Frequency State-Space Modules

To better mitigate the blurring of details and color bias effects of underwater light conditions, we put forward a frequency state-space module (FSSM).

The modular design follows the literature [36] that is inspired by the Transformer architecture [37], as reported in Figure 2a. For the g-th FSSM, the input features $Z_{g-1} \in \mathbb{R}^{H\times W\times C}$ are first normalized using Layer Normalization (LN), followed by long-range dependency modeling through VSSM. Besides, a learnable parameter ϖ is used to dynamically control the information flow:

$$\bar{Z}_g = VSSM(LN(Z_{g-1})) + \varpi \cdot Z_{g-1} \tag{5}$$

where $LN(\cdot)$ represents the operation of layer normalization and $VSSM(\cdot)$ denotes the Vision State-Space Module.

Furthermore, since SSM treats the flattened feature mapping as a one-dimensional labeled sequence, the neighborhood pixels of the flattened strategy in the sequence are easily lost [35]. To address this problem, another LayerNorm is employed, followed by a 1×1 convolution layer to compensate for local features. Also, to boost the modeling capability of the VSSM while attaining rich high-frequency cues, we have designed the Frequency-Assisted Enhancement Module (FAEM), as detailed in Section 3.4. The above process can be calculated as:

$$Z_g = FAEM(Conv(LN(\bar{Z}_g))) + \varpi' \cdot \bar{Z}_g \tag{6}$$

where $FAEM(\cdot)$ denotes the operation of FAEM. ϖ' is a learnable parameter that adaptively scales the residual contribution from $\bar{Z}_g$.

3.3. Vision State-Space Module

The Vision State-Space Module (VSSM) can catch long-range dependencies utilizing a state-space equation, as illustrated in Figure 2b. The input features $\dot{Z}_g \in \mathbb{R}^{H \times W \times C}$ is handled by two parallel paths [22]. In the first path, input feature channels are initially expanded to λC by a linear layer, then processed by deep-wise convolution and the activation function SiLU, and finally processed by utilizing the 2D Selective Scan Module (2D-SSM) layer and LayerNorm. Simultaneously, the second pathway applies a linear layer and an activation function to input features. The outputs of these two paths are fused utilizing Hadamard product and then projected back to C channels using a linear layer, obtaining the final output $\ddot{Z}_g \in \mathbb{R}^{H \times W \times C}$:

$$\dot{Z}'_g = \text{LN}(\text{2D-SSM}(\text{SiLU}(\text{DWConv}(\text{Linear}(Z'_g))))) \tag{7}$$

$$\dot{Z}''_g = \text{SiLU}(\text{Linear}(\dot{Z}'_g)) \tag{8}$$

$$\ddot{Z}_g = \text{Linear}(\dot{Z}'_g \odot \dot{Z}''_g) \tag{9}$$

where $DWConv(\cdot)$ is depth-wise convolution. $\odot$ is the Hadamard product. Figure 2c reveals that the 2D-SSM module first transforms a 2D feature map into four sets of 1D sequences by scanning along four directional axes. Each sequence is then processed, leveraging discrete state-space equations to catch the global context. After this temporal modeling, the outputs from all directions are integrated and rearranged to recreate the initial 2D spatial layout. In this way, 2D-SSM can effectively preserve image spatial information and enhance feature acquisition processing.

3.4. Frequency-Assisted Enhancement Module

The complex optical properties of underwater environments often result in substantial loss of detailed information in the captured images. Therefore, we put forth the Frequency-assisted Enhancement Module (FAEM) that leverages FFT to effectively extract and enhance the high-frequency cues, making the reconstructed image more natural, as depicted in Figure 3b. Thanks to FFT, the amplitude and phase components capture the receptive field of the image size. Remarkably, the phase component provides rich structural information that can greatly help in target reconstruction. Unlike the frequency block (FRB shown in Figure 3a) proposed in the literature [25], we advocate the use of channel attention (CA) [38] instead of convolutional operations to make the network more focused on informative channels.

Firstly, the input features $\bar{Z}'_g \in \mathbb{R}^{H\times W\times C}$ are projected into frequency space utilizing FFT calculated as $fre = FFT(\bar{Z}'_g)$. Then, the amplitude and phase components are obtained separately:

$$\mathrm{A} = \mathrm{angle}(fre), \mathrm{P} = \mathrm{abs}(fre) \tag{10}$$

Subsequently, we exploit CA to strengthen informative feature representations and mitigate the impact of noise in the frequency domain. Concretely, the missing structural information in the underwater image can be effectively augmented by CA on the phase branch, which is then mapped back into the image space along $\bar{\mathrm{A}}$ with the original amplitude components using IFFT. The amplitude component leverages CA to further highlight important image intensity information, which is then mapped back into image space along $\bar{\mathrm{P}}$ with the original phase component using IFFT. The enhanced amplitude branch can be expressed as:

$$\begin{aligned} &\bar{A} = CA(A) + A \\ &\begin{cases} real = \bar{A} \times \cos(P) \\ \mathrm{imag} = \bar{A} \times \sin(P) \end{cases} \\ &fre_A = complex(real, imag) \\ &F_A = abs(IFFT(fre_A)) \end{aligned} \tag{11}$$

where $CA(\cdot)$ is the operation of channel attention. Analogously, the enhanced phase branch can be expressed as:

$$\begin{aligned} &\bar{P} = CA(P) + P \\ &\begin{cases} real = A \times \cos(\bar{P}) \\ \mathrm{imag} = A \times \sin(\bar{P}) \end{cases} \\ &fre_P = complex(real, imag) \\ &F_P = abs(IFFT(fre_P)) \end{aligned} \tag{12}$$

Finally, we integrate these two different frequency-domain features F_A and F_P with a 1×1 convolutional layer, while incorporating a skip connection to boost the training efficiency.

$$\bar{Z}''_g = Conv(F_A + F_P) + \bar{Z}'_g \tag{13}$$

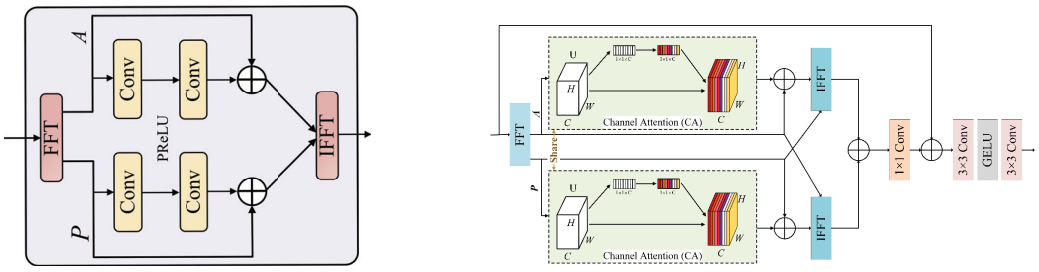
where $IFFT(\cdot)$ denotes inverse Fourier transform operation. The implementation of FAEM is depicted in Algorithm 1.

Unlike FRB (shown in Figure 3a) that applies a uniform FFT-IFFT residual mapping, FAEM performs content-adaptive spectral selection and fusion. After transforming features to the frequency domain, two lightweight branches, respectively, emphasize information-rich mid/high-frequency components and stabilize low-frequency structures. Channel attention adaptively reweights spectral bands to suppress noise-dominated frequencies caused by underwater scattering. The refined spectrum is then fused back into the spatial stream via IFFT and residual connections. Compared to FRB, this selective enhancement technique more effectively amplifies structural and textural details, yielding clearer, artifact-free reconstructions.

Algorithm 1: The implementation of Frequency-assisted Enhancement Module (FAEM)

Input: Input Feature Matrix $Z'_g \in \mathbb{R}^{H\times W\times C}$
Output: Resultant Matrix $Z''_g \in \mathbb{R}^{H\times W\times C}$

1. **Fourier Projection:** Transform the input feature Z'_s into the frequency domain using FFT: $fre = \text{FFT}(Z'_g)$;
   Obtain amplitude and phase components:
   $A = \text{angle}(fre)$, $P = \text{abs}(fre)$.
2. **Amplitude Enhancement Branch:**
   - Apply CA to the amplitude feature to obtain $\bar{A} = \text{CA}(A) + A$.
   - Reconstruct the complex frequency representation:
     $real = \bar{A} \cdot \cos(P), \quad imag = \bar{A} \cdot \sin(P)$.
   - Combine the real and imaginary parts: $fre_A = \text{complex}(real, imag)$.
   - Transform back to spatial domain: $F_A = \text{abs}(\text{IFFT}(fre_A))$.
3. **Phase Enhancement Branch:**
   - Apply CA to the phase feature to obtain $\bar{P} = \text{CA}(P) + P$.
   - Reconstruct frequency components:
     $real = A \cdot \cos(\bar{P}), \quad imag = A \cdot \sin(\bar{P})$.
   - Combine real and imaginary parts: $fre_P = \text{complex}(real, imag)$.
   - Transform back to spatial domain: $F_P = \text{abs}(\text{IFFT}(fre_P))$.
4. **Fusion and Output:** Apply a 1×1 convolution to fuse the outputs of the amplitude and phase branches and merge it with the input feature via a residual connection:
   $Z''_g = \text{Conv}_{1\times1}(F) + Z'_g$.



(**a**) Architecture of FRB (**b**) Architecture of FAEM

Figure 3. Two variants of the FFT. (**a**) FRB proposed by [25]; (**b**) FAEM proposed in this paper.

4. Experiments

4.1. Dataset and Experimental Setup

Experiments on the benchmark datasets USR-248 [9] and UFO-120 [10] are carried out to evaluate the performance of our MambaUSR. Specifically, USR-248 contains 1060 training pairs and 248 testing pairs. In this dataset, HR images are downscaled via bicubic interpolation at ×2, ×4, and ×8, and are further degraded with 20% Gaussian noise to produce the corresponding LR images. The UFO-120 dataset contains 1500 training pairs and 120 testing pairs, with downsampling performed at scaling factors of ×2, ×3, and ×4. To remain consistent with mainstream algorithms, we evaluate the proposed networks using the Peak Signal-to-Noise Ratio (PSNR), Structural Similarity Index (SSIM), and Underwater Image Quality Metric (UIQM). In this study, both FSSM and FSSG are set to 6 to acquire a lightweight network.

The optimization is performed using the Adam optimizer, with the hyperparameters set as follows: $\beta_1 = 0.9$, $\beta_2 = 0.999$, and $\varepsilon = 10^{-8}$. The learning rate is initially set to $le - 3$, reducing to half every 200 epochs. Each batch comprises 12 LR patches, each measuring 80 × 80, for the SR task. The hyperparameters mentioned above are selected empirically

to strike a balance between convergence stability and computational efficiency. All experiments are executed using PyTorch (https://pytorch.org/) on a system powered by an NVIDIA RTX 4090 GPU. To ensure transparency and reproducibility of the experiments, all results reported in this study represent the single optimal model. Results for all comparison methods are sourced from the literature [14].

4.2. Ablation Study

An ablation study is executed on the USR-248 dataset, examining the performance impact of each individual module within the proposed framework. We sequentially remove FAEM and VSSM for retraining. Notably, to further highlight the advantages of FAEM, we utilize the FRB (shown in Figure 3a) from the literature [25] for replacement, named MambaUSR w FRB. Table 1 summarizes ablation study results for our MambaUSR.

Table 1. Ablation results of individual components on UFO-120 dataset with scale factor ×4.

Model	PSNR (dB)	SSIM	UIQM
MambaUSR w FRB	24.93	0.6709	2.8179
MambaUSR w/o FAEM	25.02	0.6758	2.8208
MambaUSR w/o VSSM	24.91	0.6579	2.8107
MambaUSR	25.07	0.6853	2.8297

Effect of FAEM. When FAEM is replaced by FFT (MambaUSR w FRB), there is a slight reduction in PSNR to 24.93 and SSIM to 0.6709, indicating that FAEM is more effective than FFT in enhancing image quality and maintaining structural similarity. The UIQM score of 2.8179 in this variant also suggests a minor decrease in perceptual quality. In addition, when FAEM is completely removed (MambaUSR w/o FAEM), the PSNR marginally decreases to 25.02, but there is a slight reduction in SSIM to 0.6758, further underscoring FAEM's advantage in underwater SR tasks. This is because FAEM performs content-adaptive spectral weighting, selectively enhancing useful high-frequency information, thereby significantly improving perceived quality. Moreover, in Figure 4, we visualize the intermediate feature maps of FRB and FAEM on the 6-th FSSM of the 6-th FSSG. Compared to MambaUSR w FRB, MambaUSR supported by FAEM emphasizes richer detail and edges, particularly in textures of the nudibranch and coral images, indicating that FAEM is better at capturing local high-frequency details.

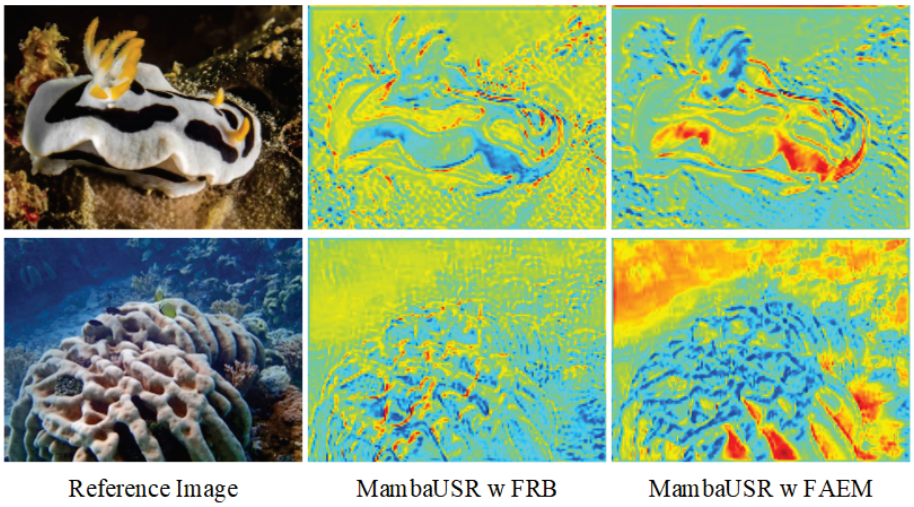


Figure 4. The feature visualization results are compared in MambaUSR with FRB and FAEM, respectively.

Effect of VSSM. The exclusion of VSSM (MambaUSR w/o VSSM) results in the lowest SSIM score among all model variations (0.6579) and a reduction in PSNR to 24.91, suggesting that VSSM is instrumental in retaining structural similarity and fine details. The UIQM score of 2.8107 further confirms that VSSM can elevate perceptual quality, highlighting its importance as a critical component for underwater SR. VSSM provides long-range dependency modeling that enforces global contour continuity and repeated-pattern alignment. SSIM is highly sensitive to such structural coherence within local windows; when VSSM is removed, edges become locally inconsistent and textures fragment. In contrast, PSNR is an average pixel error metric dominated by low-frequency content, making it less affected by such misalignments and thus exhibiting smaller variations.

Overall, the ablation study demonstrates that both FAEM and VSSM are integral to MambaUSR's performance, with FAEM offering advantages over FFT in enhancing structural and perceptual image quality, and VSSM being crucial for preserving structural details and boosting perceptual metrics.

4.3. Comparison with Underwater SR

4.3.1. Comparison on USR-248 Dataset

Our method is evaluated relative to a set of advanced approaches on the USR-248 dataset to demonstrate its effectiveness. Quantitative results of the experiments are listed in Table 2. A clear trend observed in the data is that as the scaling factor increases, the PSNR and SSIM values tend to decrease across all methods, indicating a general decline in performance as the resolution enhancement becomes more challenging. MambaUSR consistently performs well across all scales, especially for PSNR and SSIM. At a scaling factor of ×2, MambaUSR produces a PSNR of 29.75 dB and an SSIM of 0.52, which is among the highest across the methods. Similarly, for ×4 and ×8 scales, MambaUSR demonstrates strong performance, with a PSNR of 26.14 dB and 23.97 dB, respectively. In terms of computational efficiency, MambaUSR stands out as having lower FLOPs compared to many of the other high-performing models, such as ESRGAN and SRDRM, especially as the scaling factor increases. The superior performance of Mamba, particularly in maintaining a high PSNR and SSIM across all scaling factors, suggests that it is well-optimized for handling complex SR tasks while keeping computational demands low.

Figure 5 showcases representative visual reconstruction results on the USR-248 dataset. All models capture some detail at scale factor ×2, but differences in sharpness and texture retention are noticeable. Models like SRGAN and SRDRM-GAN tend to produce artifacts, especially visible in areas with complex patterns and textures, such as the scales of fish or coral structures. In contrast, MambaUSR appears to retain finer details more effectively, maintaining a closer resemblance to the HR reference images. As magnification increases to ×4 and ×8, the challenge of preserving details becomes more evident. At these higher magnifications, most models display significant blurring and loss of structure, with only EDSRGAN, SRDRM-GAN, and MambaUSR demonstrating moderate resilience. Notably, MambaUSR continues to show comparatively better detail retention and fewer distortions, particularly in intricate textures such as fish patterns and coral spots.

Table 2. Quantitative results on USR-248 dataset with scale factors ×2, ×4, and ×8. The best performance is highlighted in bold. FLOPs are computed based on an HR image of size 640 × 480.

Scale	Method	FLOPs (G)	Params (M)	PSNR (dB)	SSIM	UIQM
×2	SRCNN [39]	21.3	0.06	26.81	0.76	2.74
	VDSR [40]	205.28	0.67	28.98	0.79	2.57
	EDSRGAN [41]	273.34	1.38	27.12	0.77	2.67
	SRGAN [42]	377.76	5.95	28.05	0.78	2.74
	SRResNet [42]	222.37	1.59	25.98	0.72	–
	ESRGAN [43]	4274.68	**16.7**	26.66	0.75	2.7
	SRDRM [9]	203.91	0.83	28.36	0.80	**2.78**
	SRDRM-GAN [9]	289.38	11.31	28.55	**0.81**	2.77
	PAL [27]	203.82	0.83	28.41	0.80	–
	AMPCNet [11]	–	1.15	29.54	0.80	2.77
	Deep WaveNet [14]	21.47	0.28	29.09	0.80	2.73
	MambaUSR (ours)	93.8	2.73	**29.75**	0.52	2.75
×4	SRCNN [39]	21.3	0.06	23.38	0.67	2.38
	VDSR [40]	205.28	0.67	25.7	0.68	2.44
	EDSRGAN [41]	206.42	1.97	21.65	0.65	2.40
	SRGAN [42]	529.86	5.95	24.76	**0.69**	2.42
	SRResNet [42]	85.49	1.59	24.15	0.66	–
	ESRGAN [43]	1504.09	**16.7**	23.79	0.66	2.38
	SRDRM [9]	291.73	1.9	24.64	0.68	2.46
	SRDRM-GAN [9]	377.2	12.38	24.62	**0.69**	2.48
	PAL [27]	303.42	1.92	24.89	**0.69**	–
	AMPCNet [11]	–	1.17	25.90	0.66	**2.58**
	Deep WaveNet [14]	5.59	0.29	25.20	0.68	2.54
	MambaUSR (ours)	23.9	2.75	**26.14**	0.66	2.53
×8	SRCNN [39]	21.3	0.06	19.97	0.57	2.01
	VDSR [40]	205.28	0.67	23.58	0.63	2.17
	EDSRGAN [41]	189.69	2.56	19.87	0.58	2.12
	SRGAN [42]	567.88	5.95	20.14	0.60	2.10
	SRResNet [42]	51.28	1.59	19.26	0.55	–
	ESRGAN [41]	811.44	**16.7**	19.75	0.58	2.05
	SRDRM [9]	313.68	2.97	21.20	0.60	2.18
	SRDRM-GAN [9]	399.15	13.45	20.25	0.61	2.17
	PAL [27]	325.51	2.99	22.51	**0.63**	–
	AMPCNet [11]	–	1.25	23.83	0.62	**2.25**
	Deep WaveNet [14]	1.62	0.34	23.25	0.62	2.21
	MambaUSR (ours)	6.43	2.84	**23.97**	0.55	2.20

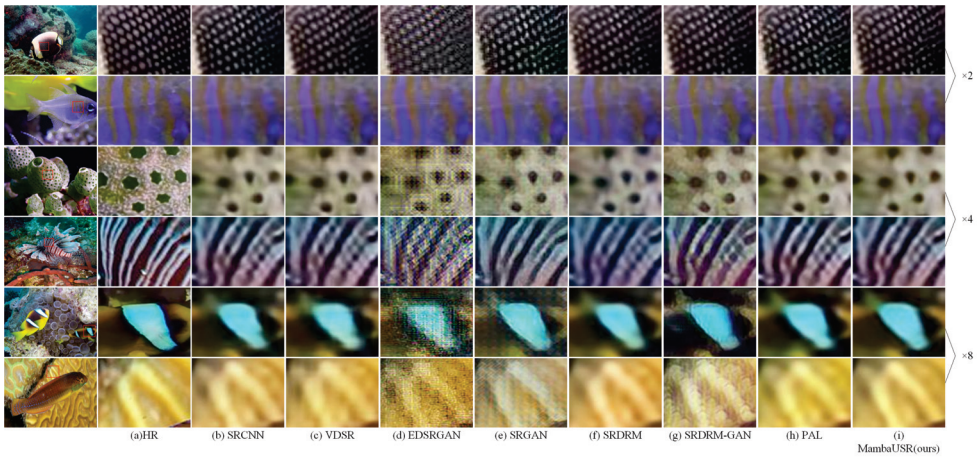


Figure 5. Visual comparison of our proposed MambaUSR against popular works on USR-248 dataset. It can be found that MambaUSR produces sharper textures and more natural colors, effectively suppressing artifacts in dense patterns.

4.3.2. Comparison on the UFO-120 Dataset

To demonstrate the efficacy of MambaUSR further, we conduct comparative experiments on the UFO-120 dataset against several representative and widely used models, as listed in Table 3. In terms of PSNR, MambaUSR demonstrates competitive performance across all scaling factors. Notably, at the ×2 scale, it achieves a PSNR of 25.76 dB, outperforming all compared methods except SRGAN (26.11 dB). For larger scale factors (×3 and ×4), MambaUSR remains consistent, outperforming most methods, particularly at ×3, where it records a PSNR of 26.15 dB, higher than SRCNN, SRDRM, and SRDRM-GAN. For SSIM, Mamba maintains a strong performance across all scaling factors, matching Deep WaveNet at ×2 (0.74) and outperforming all methods except URSCT at ×3. For UIQM, Mamba's performance is also notable, especially at ×2 and ×3, where it achieves high scores (2.93 and 2.97), closely trailing Deep WaveNet and AMPCNet. However, at scale factor ×4, its UIQM slightly decreases to 2.84. The trends observed in the data suggest that MambaUSR provides a balanced performance across all three metrics, particularly excelling in the intermediate scale factor (×3) with consistent PSNR and SSIM values. While other methods like SRGAN and Deep WaveNet achieve higher scores in specific metrics or scaling factors, Mamba offers a reliable and well-rounded performance overall, making it a robust choice for image enhancement tasks.

Figure 6 provides some of the visual reconstruction results on the UFO-120 dataset. An evident reduction in detail preservation is observed across models as the scaling factor increases from ×2 to ×4. MambaUSR consistently performs best, retaining finer details and natural textures that closely resemble the high-resolution reference images, while other models show blurring and artifacts, especially in complex textures.

Table 3. Quantitative results on UFO-120 dataset with scale factors ×2, ×3, and ×4.

Method	**PSNR (dB)**			**SSIM**			**UIQM**		
	×2	**×3**	**×4**	**×2**	**×3**	**×4**	**×2**	**×3**	**×4**
SRCNN [41]	24.75	22.22	19.05	0.72	0.65	0.56	2.39	2.24	2.02
SRGAN [42]	**26.11**	23.87	21.08	0.75	0.70	0.58	2.44	2.39	2.56
SRDRM [9]	24.62	–	23.15	0.72	–	0.67	2.59	–	2.57
SRDRM-GAN [9]	24.61	–	23.26	0.72	–	0.67	2.59	–	2.55
Deep WaveNet [14]	25.71	25.23	25.08	0.77	**0.76**	**0.74**	**2.99**	2.96	**2.97**
AMPCNet [11]	25.24	25.73	24.70	0.71	0.70	0.70	2.93	2.85	2.88
URSCT [17]	25.96	–	23.59	**0.80**	–	0.66	–	–	–
MambaUSR (ours)	25.76	**26.15**	**25.11**	0.74	0.74	0.69	2.93	**2.97**	2.84

4.3.3. Application in XLD Hydraulic Project

We apply the proposed MambaUSR to the XLD hydraulic project, further verifying its robustness and generalizability. Different underwater scenes are selected to demonstrate MambaUSR's fidelity in preserving detailed textures. Figure 7 illustrates the method's effectiveness, depicting scenes at varying heights: the first column shows a height of 98.7 m, the second 95.9 m, the third 87.7 m, and the fourth 83.1 m. To quantitatively assess performance in these real-world scenarios, we computed UIQM and UCIQE for each reconstructed image. MambaUSR achieves an average UIQM of 0.98 and UCIQE of 0.55 across all depths, indicating consistent enhancement in both perceptual quality and color balance. Even under severe degradation at a scaling factor of ×8, the model maintains stable UIQM and UCIQE values, confirming its robustness in preserving fine structural and chromatic information. In summary, the application of MambaUSR to the XLD hydraulic project demonstrates its strong adaptability and reliability in real underwater environments.

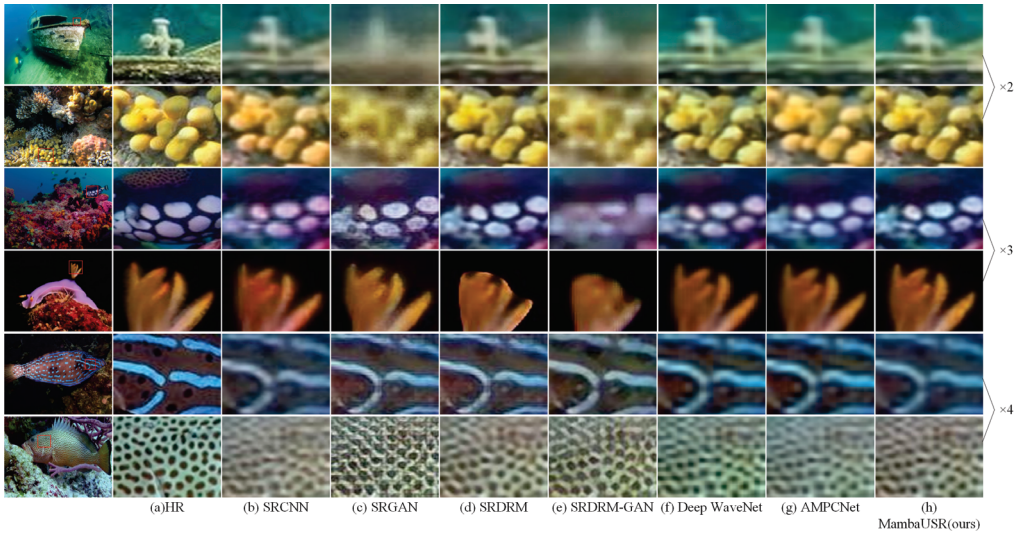


Figure 6. Visual comparison between our MambaUSR and popular networks on the UFO-120 dataset. MambaUSR reconstructs sharper edges and more natural textures than competing models.

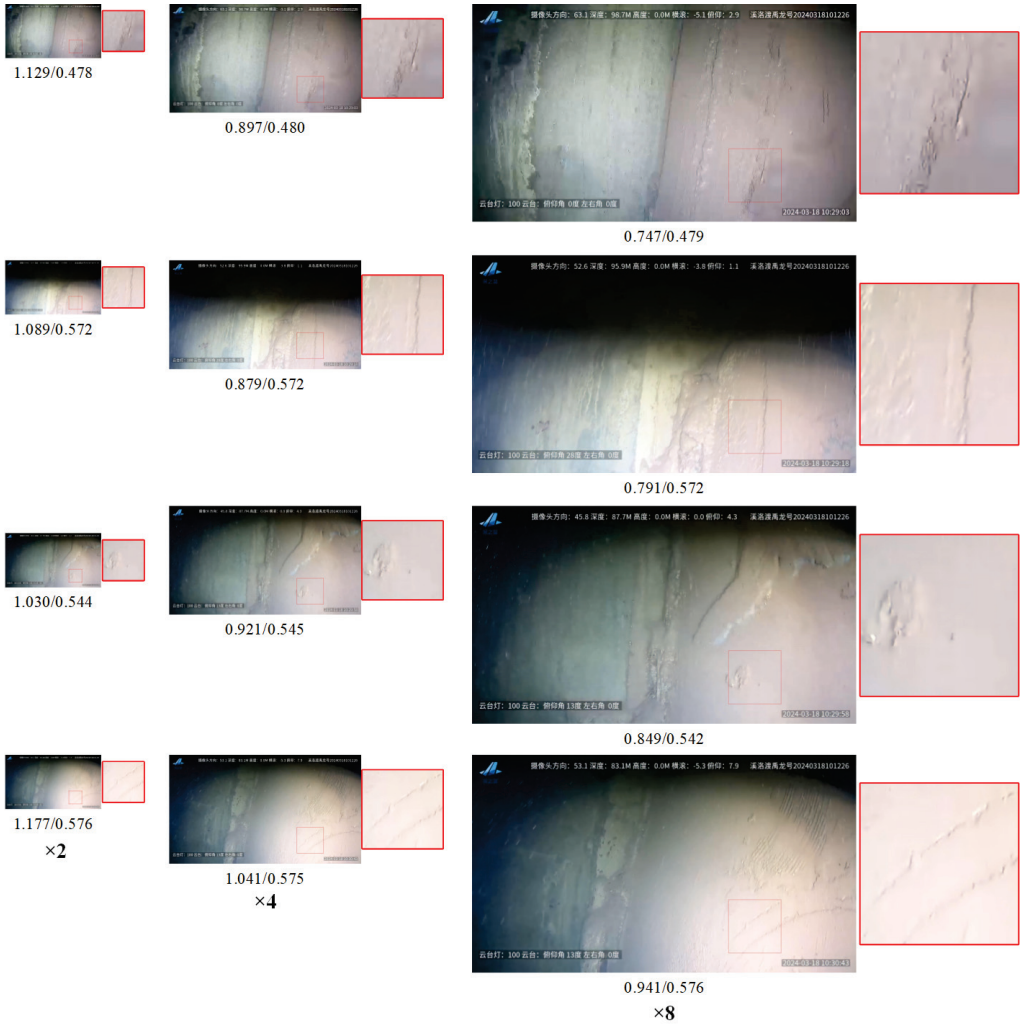


Figure 7. Application of MambaUSR in the XLD Hydraulic Project under real underwater conditions. The numerical values indicate UIQM/UCIQE scores, where higher values denote better visual quality and color fidelity.

4.4. Model Efficiency

To further demonstrate the computational efficiency of our MambaUSR, Table 4 provides the calculation results based on the RTX3060 on the USR-248 data. Compared to mainstream underwater SR methods, MambaUSR attains higher PSNR values while requiring only 6.43G FLOPS of computational effort. In terms of efficiency, MambaUSR achieves 27.34 fps, comparable to SRResNet (29.26 fps) and DeepWaveNet (28.46 fps), while outperforming most GAN-based methods. These findings demonstrate that MambaUSR successfully balances accuracy with computational cost, delivering exceptional reconstruction quality without resorting to the excessive complexity of traditional deep networks or GAN architectures.

Table 4. Computational efficiency of advanced methods on USR-248 dataset with scale factor ×8.

Method	FLOPs (G)	Params (M)	PSNR (dB)	SSIM	Average (s)	Efficiency (fps)
SRCNN	21.30	0.06	19.97	0.57	0.08496	11.77
VDSR	205.28	0.67	23.58	0.63	0.08852	11.30
EDSRGAN	189.69	2.56	19.87	0.58	0.04632	21.59
SRGAN	567.88	5.95	20.14	0.6	0.09454	10.58
SRResNet	51.28	1.59	19.26	0.55	0.03418	29.26
ESRGAN	811.44	16.7	19.75	0.58	0.09310	10.74
SRDRM	313.68	2.97	21.2	0.6	0.08940	11.19
SRDRM-GAN	399.15	13.45	20.25	0.61	0.09063	11.03
PAL	325.51	2.99	22.51	0.63	0.08068	12.39
AMPCNet	-	1.25	23.83	0.62	0.03815	26.21
Deep WaveNet	1.62	0.34	23.25	0.62	0.03514	28.46
MambaUSR (ours)	6.43	2.84	23.97	0.55	0.03657	27.34

5. Conclusions

In this work, we propose MambaUSR, a novel state-space model tailored for underwater SR, which effectively addresses blurred details, color distortion, and low contrast in underwater scenes. The proposed Frequency State-Space Module (FSSM) serves as the core of MambaUSR, where the Visual State-Space Module (VSSM) enables efficient global dependency modeling and the Frequency-Assisted Enhancement Module (FAEM) captures critical high-frequency information through FFT and channel attention. Experimental results reveal that MambaUSR significantly boosts reconstruction quality on the two benchmark datasets. On USR-248, it achieves the best PSNR performance with an improvement of at least 0.15 dB. On UFO-120, at the ×3 scale, its PSNR and UIQM improve by 0.42 dB and 0.12 dB, respectively. These results confirm the model's strong competitiveness and effectiveness compared with existing methods. In future work, we will explore incorporating depth and polarization priors to better handle complex underwater conditions and develop lightweight versions of Mamba-based methods for real-time applications.

Author Contributions: Conceptualization, Z.C.; Methodology, G.S.; Software, G.S.; Validation, G.S.; Formal analysis, J.Z.; Writing—original draft, J.Z.; Supervision, Z.C.; Funding acquisition, Z.C. All authors have read and agreed to the published version of the manuscript.

Funding: This work was supported in part by the National Key R & D Program of China under Grant 2022 YFC3005401, the Jiangsu Province Youth Science and Technology Talent Support Program under Grant JSTJ-2024-082, the National Natural Science Foundation of China under Grant 52309159 and U23B20150, the Scientific Research Fund of Nanjing Hydraulic Research Institute

under Grant Y724001, the Technology Talent and Platform Program of Yunnan Province under Grant 202405AK340002 and the Science and Technology Projects of China Huaneng Group under Grant HNKJ20-H46.

Institutional Review Board Statement: Not applicable.

Informed Consent Statement: Not applicable.

Data Availability Statement: The raw data supporting the conclusions of this article will be made available by the authors on request.

Conflicts of Interest: The authors declare no conflicts of interest.

References

1. Liu, J.; Chen, C.; Tang, J.; Wu, G.S. From Coarse to Fine: Hierarchical Pixel Integration for Lightweight Image Super-Resolution. *Proc. AAAI Conf. Artif. Intell.* **2023**, *37*, 1666–1674. [CrossRef]
2. Zhou, Z.T.; Li, G.P.; Wang, G.Z. A Hybrid of Transformer and CNN for Efficient Single Image Super-Resolution via Multi-Level Distillation. *Displays* **2023**, *76*, 102352. [CrossRef]
3. Liu, Z.; Lin, Y.T.; Cao, Y.; Hu, H.; Wei, Y.X.; Zhang, Z.; Lin, S.; Guo, B.N. Swin Transformer: Hierarchical Vision Transformer Using Shifted Windows. In Proceedings of the 2021 IEEE/CVF International Conference on Computer Vision (ICCV), Montreal, QC, Canada, 10–17 October 2021; pp. 10012–10022.
4. Lu, Z.S.; Liu, H.; Li, J.C.; Zhang, L.L. Efficient Transformer for Single Image Super-Resolution. *arXiv* **2021**, arXiv:2108.11084.
5. Yang, C.H.; Chen, Z.H.; Espinosa, M.; Ericsson, L.; Wang, Z.Y.; Liu, J.M.; Crowley, E.J. Plainmamba: Improving Non-Hierarchical Mamba in Visual Recognition. *arXiv* **2024**, arXiv:2403.17695.
6. Zhu, L.H.; Liao, B.C.; Zhang, Q.; Wang, X.L.; Liu, W.Y.; Wang, X.G. Vision Mamba: Efficient Visual Representation Learning with Bidirectional State Space Model. *arXiv* **2024**, arXiv:2401.09417.
7. Cheng, D.; Kou, K.I. FFT Multichannel Interpolation and Application to Image Super-Resolution. *Signal Process.* **2019**, *162*, 21–34. [CrossRef]
8. Kong, L.S.; Dong, J.X.; Ge, J.J.; Li, M.Q.; Pan, J.S. Efficient Frequency Domain-Based Transformers for High-Quality Image Deblurring. In Proceedings of the IEEE/CVF Conference on Computer Vision and Pattern Recognition, Vancouver, BC, Canada, 17–24 June 2023; pp. 5886–5895.
9. Islam, M.J.; Enan, S.S.; Luo, P.G.; Sattar, J. Underwater Image Super-Resolution Using Deep Residual Multipliers. In Proceedings of the 2020 IEEE International Conference on Robotics and Automation (ICRA), Paris, France, 31 May–31 August 2020; pp. 900–906.
10. Islam, M.J.; Luo, P.G.; Sattar, J. Simultaneous Enhancement and Super-Resolution of Underwater Imagery for Improved Visual Perception. *arXiv* **2020**, arXiv:2002.01155.
11. Zhang, Y.; Yang, S.X.; Sun, Y.M.; Liu, S.D.; Li, X.G. Attention-Guided Multi-Path Cross-CNN for Underwater Image Super-Resolution. *Signal Image Video Process.* **2022**, *16*, 155–163. [CrossRef]
12. Wang, H.; Wu, H.; Hu, Q.; Chi, J.N.; Yu, X.S.; Wu, C.D. Underwater Image Super-Resolution Using Multi-Stage Information Distillation Networks. *J. Vis. Commun. Image Represent.* **2021**, *77*, 103136. [CrossRef]
13. Yang, H.H.; Huang, K.C.; Chen, W.T. Laffnet: A Lightweight Adaptive Feature Fusion Network for Underwater Image Enhancement. In Proceedings of the 2021 IEEE International Conference on Robotics and Automation (ICRA), Xi'an, China, 30 May–5 June 2021; pp. 685–692.
14. Sharma, P.; Bisht, I.; Sur, A. Wavelength-Based Attributed Deep Neural Network for Underwater Image Restoration. *ACM Trans. Multimed. Comput. Commun. Appl.* **2023**, *19*, 1–23. [CrossRef]
15. Peng, L.T.; Zhu, C.L.; Bian, L.H. U-Shape Transformer for Underwater Image Enhancement. *IEEE Trans. Image Process.* **2023**, *32*, 3066–3079. [CrossRef]
16. Mei, X.K.; Ye, X.F.; Zhang, X.F.; Liu, Y.S.; Wang, J.T.; Hou, J.; Wang, X.L. UIR-Net: A Simple and Effective Baseline for Underwater Image Restoration and Enhancement. *Remote Sens.* **2022**, *15*, 39. [CrossRef]
17. Ren, T.D.; Xu, H.Y.; Jiang, G.Y.; Yu, M.; Zhang, X.; Wang, B.; Luo, T. Reinforced Swin-ConvS Transformer for Simultaneous Underwater Sensing Scene Image Enhancement and Super-Resolution. *IEEE Trans. Geosci. Remote Sens.* **2022**, *60*, 4209616. [CrossRef]
18. Gu, J.; Dong, C. Interpreting Super-Resolution Networks with Local Attribution Maps. In Proceedings of the IEEE/CVF Conference on Computer Vision and Pattern Recognition, Nashville, TN, USA, 20–25 June 2021; pp. 9199–9208.
19. Gu, A.; Johnson, I.; Timalsina, A.; Rudra, A.; Ré, C. How to Train Your Hippo: State Space Models with Generalized Orthogonal Basis Projections. *arXiv* **2022**, arXiv:2206.12037.
20. Gu, A.; Dao, T. Mamba: Linear-Time Sequence Modeling with Selective State Spaces. *arXiv* **2023**, arXiv:2312.00752.

21. Guan, M.S.; Xu, H.Y.; Jiang, G.Y.; Yu, M.; Chen, Y.Y.; Luo, T.; Song, Y. WaterMamba: Visual State Space Model for Underwater Image Enhancement. *arXiv* **2024**, arXiv:2405.08419.
22. Liu, Y.; Tian, Y.J.; Zhao, Y.Z.; Yu, H.T.; Xie, L.X.; Wang, Y.W.; Ye, Q.X.; Jiao, J.B.; Liu, Y.F. Vmamba: Visual State Space Model. *Adv. Neural Inf. Process. Syst.* **2024**, *37*, 103031–103063.
23. Dong, C.Y.; Zhao, C.; Cai, W.L.; Yang, B. O-Mamba: O-Shape State-Space Model for Underwater Image Enhancement. *arXiv* **2024**, arXiv:2408.12816.
24. Yao, Z.S.; Fan, G.D.; Fan, J.F.; Gan, M.; Chen, C.L.P. Spatial-Frequency Dual-Domain Feature Fusion Network for Low-Light Remote Sensing Image Enhancement. *IEEE Trans. Geosci. Remote Sens.* **2024**, *62*, 4706516. [CrossRef]
25. Wang, C.Y.; Jiang, J.J.; Zhong, Z.W.; Liu, X.M. Spatial-Frequency Mutual Learning for Face Super-Resolution. In Proceedings of the IEEE/CVF Conference on Computer Vision and Pattern Recognition, Vancouver, BC, Canada, 17–24 June 2023; pp. 22356–22366.
26. Wang, Z.; Zhao, Y.W.; Chen, J.C. Multi-Scale Fast Fourier Transform Based Attention Network for Remote-Sensing Image Super-Resolution. *IEEE J. Sel. Top. Appl. Earth Obs. Remote Sens.* **2023**, *16*, 2728–2740. [CrossRef]
27. Chen, X.L.; Wei, S.Q.; Yi, C.; Quan, L.W.; Lu, C.Y. Progressive Attentional Learning for Underwater Image Super-Resolution. In *International Conference on Intelligent Robotics and Applications*; Springer: Cham, Switzerland, 2020; pp. 233–243.
28. Wang, L.; Li, X.; Li, K.; Mu, Y.; Zhang, M.; Yue, Z.X. Underwater Image Restoration Based on Dual Information Modulation Network. *Sci. Rep.* **2024**, *14*, 5416. [CrossRef]
29. Pramanick, A.; Sur, A.; Saradhi, V.V. Harnessing Multi-Resolution and Multi-Scale Attention for Underwater Image Restoration. *Vis. Comput.* **2025**, *41*, 8235–8254. [CrossRef]
30. Dharejo, F.A.; Ganapathi, I.I.; Zawish, M.; Alawode, B.; Alathbah, M.; Werghi, N.; Javed, S. SwinWave-SR: Multi-Scale Lightweight Underwater Image Super-Resolution. *Inf. Fusion* **2024**, *103*, 102127. [CrossRef]
31. Chang, B.C.; Yuan, G.J.; Li, J.J. Mamba-Enhanced Spectral-Attentive Wavelet Network for Underwater Image Restoration. *Eng. Appl. Artif. Intell.* **2025**, *143*, 109999. [CrossRef]
32. Xiao, Y.; Yuan, Q.Q.; Jiang, K.; Chen, Y.Z.; Zhang, Q.; Lin, C.W. Frequency-Assisted Mamba for Remote Sensing Image Super-Resolution. *IEEE Trans. Multimed.* **2025**, *27*, 1783–1796. [CrossRef]
33. Shao, M.W.; Qiao, Y.J.; Meng, D.Y.; Zuo, W.M. Uncertainty-Guided Hierarchical Frequency Domain Transformer for Image Restoration. *Knowl.-Based Syst.* **2023**, *263*, 110306. [CrossRef]
34. Huang, J.; Liu, Y.J.; Zhao, F.; Yan, K.Y.; Zhang, J.H.; Huang, Y.K.; Zhou, M.; Xiong, Z.W. Deep Fourier-Based Exposure Correction Network with Spatial-Frequency Interaction. In *European Conference on Computer Vision*; Springer: Cham, Switzerland, 2022; pp. 163–180.
35. Zhang, H.P.; Xu, H.L.; Yu, X.S.; Zhang, X.Y.; Wu, C.D. Leveraging Frequency and Spatial Domain Information for Underwater Image Restoration. *J. Phys. Conf. Ser.* **2024**, *2832*, 012001. [CrossRef]
36. Guo, H.; Li, J.M.; Dai, T.; Ouyang, Z.H.; Ren, X.D.; Xia, S.T. Mambair: A Simple Baseline for Image Restoration with State-Space Model. In *European Conference on Computer Vision*; Springer: Cham, Switzerland, 2024; pp. 222–241.
37. Chen, Z.; Zhang, Y.L.; Gu, J.J.; Kong, L.H.; Yang, X.K.; Yu, F. Dual Aggregation Transformer for Image Super-Resolution. In Proceedings of the IEEE/CVF International Conference on Computer Vision, Paris, France, 1–6 October 2023; pp. 12312–12321.
38. Hu, J.; Shen, L.; Sun, G. Squeeze-and-Excitation Networks. In Proceedings of the IEEE Conference on Computer Vision and Pattern Recognition, Salt Lake City, UT, USA, 18–23 June 2018; pp. 7132–7141.
39. Dong, C.; Loy, C.C.; He, K.M.; Tang, X.O. Learning a Deep Convolutional Network for Image Super-Resolution. In *European Conference on Computer Vision*; Springer: Cham, Switzerland, 2014; pp. 184–199.
40. Kim, J.W.; Lee, J.K.; Lee, K.M. Accurate Image Super-Resolution Using Very Deep Convolutional Networks. In Proceedings of the IEEE Conference on Computer Vision and Pattern Recognition, Las Vegas, NV, USA, 27–30 June 2016; pp. 1646–1654.
41. Lim, B.; Son, S.H.; Kim, H.W.; Nah, S.J.; Lee, K.M. Enhanced Deep Residual Networks for Single Image Super-Resolution. In Proceedings of the IEEE Conference on Computer Vision and Pattern Recognition Workshops, Honolulu, HI, USA, 21–26 July 2017; pp. 136–144.
42. Ledig, C.; Theis, L.; Huszár, F.; Caballero, J.; Cunningham, A.; Acosta, A.; Aitken, A.; Tejani, A.; Totz, J.; Wang, Z.; et al. Photo-Realistic Single Image Super-Resolution Using a Generative Adversarial Network. In Proceedings of the IEEE Conference on Computer Vision and Pattern Recognition, Honolulu, HI, USA, 21–26 July 2017; pp. 4681–4690.
43. Wang, X.T.; Yu, K.; Wu, S.X.; Gu, J.J.; Liu, Y.H.; Dong, C.; Qiao, Y.; Loy, C.C. ESRGAN: Enhanced Super-Resolution Generative Adversarial Networks. In Proceedings of the European Conference on Computer Vision (ECCV) Workshops, Munich, Germany, 8–14 September 2018.

Disclaimer/Publisher's Note: The statements, opinions and data contained in all publications are solely those of the individual author(s) and contributor(s) and not of MDPI and/or the editor(s). MDPI and/or the editor(s) disclaim responsibility for any injury to people or property resulting from any ideas, methods, instructions or products referred to in the content.

MDPI AG
Grosspeteranlage 5
4052 Basel
Switzerland
Tel.: +41 61 683 77 34

Applied Sciences Editorial Office
E-mail: applsci@mdpi.com
www.mdpi.com/journal/applsci



Disclaimer/Publisher's Note: The title and front matter of this reprint are at the discretion of the Guest Editors. The publisher is not responsible for their content or any associated concerns. The statements, opinions and data contained in all individual articles are solely those of the individual Editors and contributors and not of MDPI. MDPI disclaims responsibility for any injury to people or property resulting from any ideas, methods, instructions or products referred to in the content.





Academic Open
Access Publishing

mdpi.com

ISBN 978-3-7258-9012-5